DEVELOPMENT OF ORTHOTOPIC GLIOBLASTOMA (GBM) PATIENT-DERIVED XENOGRAFT (PDX) MODELS FOR EFFICACY EVALUATION OF SORAFENIB COMBINED WITH A SYNTHETIC FLAVONOID DIMER

SU XIAOCHUN

PhD

The Hong Kong Polytechnic University

2023

The Hong Kong Polytechnic University

Department of Applied Biology & Chemical Technology

Development of Orthotopic Glioblastoma (GBM) Patient-Derived Xenograft (PDX) Models for Efficacy Evaluation of Sorafenib Combined with A Synthetic Flavonoid Dimer

SU Xiaochun

A thesis submitted in partial fulfillment of the requirements for the degree of Doctor of Philosophy

June 2023

CERTIFICATE OF ORIGINALITY

I hereby declare that this thesis is my own work and that, to the best of my knowledge and belief, it reproduces no material previously published or written, nor material that has been accepted for the award of any other degree or diploma, except where due acknowledgment has been made in the text.

_____ (Signed)

_____SU Xiaochun_____ (Name of student)

Abstract

Breast Cancer Resistance Protein (BCRP, ABCG2) and P-glycoprotein (P-gp) at the blood-brain barrier (BBB) have been proposed to efflux anticancer agents out of the brain and thereby restrict their usage on glioblastoma (GBM) clinically. Sorafenib, a tyrosine kinase inhibitor (TKI), showed promising cytotoxicity on GBM cells *in vitro*, but Phase I/II clinical trials were unsuccessful. This project mainly investigated if a novel synthetic flavonoid dimer, **Ac12Az9**, can inhibit the BCRP/ABCG2- and P-gp-mediated sorafenib efflux at the BBB to improve GBM treatment.

From an in-house library of 300-member of triazole-bridged flavonoid dimer, a potent and nontoxic dual inhibitor, **Ac12Az9**, was previously discovered with an EC_{50} of 0.9-1.4 nM and 285 nM for reversing BCRP/ABCG2- and P-gp-mediated drug resistance *in vitro*, respectively. **Ac12Az9** not only inhibited BCRP/ABCG2-mediated efflux of sorafenib, increasing intracellular sorafenib from 54% to 108% ($p < 0.001$) in MDCKII-GFP-BCRP cells, but it also blocked P-gp-mediated efflux of sorafenib in MDCKII-P-gp cells, increasing intracellular sorafenib from 70% to 78% ($p < 0.01$). The transepithelial transport assay further demonstrated that **Ac12Az9** can decrease the basolateral (B) side to apical (A) side (P*app B-to-A*) transport of sorafenib by 81% or 8% in MDCKII-GFP-BCRP or MDCKII-P-gp cell monolayers, respectively. In animal experiments, **Ac12Az9** can enhance brain penetration of sorafenib, with a 1.8-fold increase in the brain-to-plasma ratio, to a therapeutic level without causing toxicity. In an orthotopic patient-derived xenograft (PDX) model called G22-FLuc, co-administration of **Ac12Az9** and sorafenib could suppress tumor growth by 56.7% ($p = 0.13$) and prolong the life span of tumor-bearing nude mice by 47.4% ($p = 0.01$) when compared to the solvent control group.

To improve the half-life ($t_{1/2}$) of **Ac12Az9**, a chemical modification was performed. Metabolism of **Ac12Az9** resulted in a metabolite **M1** (**Ac12Az9-COOH**) that was

inactive in reversing BCRP/ABCG2- (EC_{50} = 470 nM) and P-gp- (EC_{50} > 1000 nM) mediated drug resistance *in vitro*. Esterase was proposed to be responsible for the cleavage of the ester bond of **Ac12Az9** to generate **M1**. Therefore, the chemical modification was performed by focusing on the ester linkage in **Ac12Az9**. **Ac12Az9** was subjected to an ester-based modification to produce the derivatives **D1-D11**. Compound **D6** was found to have increased plasma stability ($t_{1/2}$ = 270 min versus < 60 min for **Ac12Az9)** and good BCRP/ABCG2 modulating activity, with EC_{50}s of 1.2-1.3 nM for reversing BCRP/ABCG2-mediated topotecan (TPT) resistance *in vitro*. In a subcutaneous HEK293/R2 xenograft model, co-administration of **D6** and TPT could increase the tumor accumulation of TPT by 2-fold (p = 0.0028) compared to TPT alone.

Ac12Az9 was also found to increase the brain permeability for AZD1775, a Wee1 inhibitor. AZD1775 was not only found to be effective against GBM cells (IC_{50} = 0.59-1.14 μM) but also to be a good substrate for both BCRP/ABCG2 and P-gp. **Ac12Az9** was found to be able to reduce the BCRP/ABCG2- or P-gp-mediated efflux of AZD1775 by 143% or 63% in MDCKII-GFP-BCRP or MDCKII-P-gp cells, respectively. In PK studies, **Ac12Az9** can enhance the brain permeability of AZD1775, resulting in an increase in the brain-to-plasma ratios of 16.5 or 29 times.

In summary, **Ac12Az9**, a potent dual inhibitor of BCRP/ABCG2 and P-gp, can be used in combination with sorafenib for treating GBM. **Ac12Az9** derivative - **D6**, a specific inhibitor of BCRP/ABCG2, could potentially be used in another combination therapy for the treatment of BCRP/ABCG2-overexpressing tumors.

List of publications

Journal papers

1. Jason W Y Kan, Clare S W Yan, Iris L K Wong, **Xiaochun Su**, Zhen Liu, Tak Hang Chan, and Larry M C Chow, Discovery of a Flavonoid FM04 as a Potent Inhibitor to Reverse P-Glycoprotein-Mediated Drug Resistance in Xenografts and Improve Oral Bioavailability of Paclitaxel. International Journal of Molecular Sciences, 2022. 23(23): p. 15299.

2. Peng Li, Yunjiao He, Teng Chen, Kit-Ying Choy, Tsun Sing Chow, Iris L.K. Wong, Xinqing Yang, Wenqin Sun, **Xiaochun Su**, Tak Hang Chan, and Larry M C Chow, Disruption of SND1–MTDH Interaction by a High Affinity Peptide Results in SND1 Degradation and Cytotoxicity to Breast Cancer Cells In Vitro and In Vivo. Molecular Cancer Therapeutics, 2021. 20(1): p. 76-84.

3. Teng Chen, Julia YS Tsang, **Xiaochun Su**, Peng Li, Wenqin Sun, Iris L K Wong, Kit-Ying Choy, Xinqing Yang, Gary MK Tse, Tak Hang Chan, and Larry M C Chow, SALL4 promotes tumor progression in breast cancer by targeting EMT. Molecular Carcinogenesis, 2020. 59(10): p. 1209-1226.

4. Wenqin Sun, Iris L K Wong, Helen Ka-Wai Law, **Xiaochun Su**, Terry C F Chan, Gege Sun, Xinqing Yang, Xingkai Wang, Tak Hang Chan, Shengbiao Wan, and Larry M C Chow, In Vivo Reversal of P-Glycoprotein-Mediated Drug Resistance in a Breast Cancer Xenograft and in Leukemia Models Using a Novel, Potent, and Nontoxic Epicatechin EC31. International Journal of Molecular Science, 2023. 24(5): p. 4377.

Conference presentations and posters

Xiaochun Su, Xuesen Hu, Iris L. K. Wong, Jiahua Cui, Zhen Liu, Tak Hang Chan, and Larry M. C. Chow (2023). Dual inhibition of P-gp and BCRP by a flavonoid dimer **Ac12Az9** increases brain penetration of sorafenib to treat glioblastoma multiforme. ATP-Bing Cassette (ABC) Proteins: From Multidrug Resistance to Genetic Disease, Innsbruck, Austria.

Acknowledgment

First and foremost, I want to express my gratitude to Prof. Larry Ming-Cheung Chow, my Ph.D. supervisor, for welcoming me from a less prestigious university into his research team and allowing me to enroll in the doctoral program at Hong Kong Polytechnic University. My prior field of study was traditional Chinese medicine, but Prof. Chow showed a lot of compassion and patience for my cross-professional work. I want to thank him for teaching me the fundamentals of biology during our weekly meetings, which helps me learn more about biology. He would not immediately provide me with the solution when I ran into difficulties when conducting experiments, but he would show me the path around the problem so that I might actually learn something. I also want to thank him for providing me the chance to go to a conference abroad, which has not only given me the chance to share my research findings with a large audience on a global platform but also broadened my horizons and boosted my confidence. I want to thank him for all the assistance he gave me in editing my thesis, paper, and poster, which significantly raised the quality of my English writing and logical thinking. Finally, I want to express my gratitude to Prof. Chow for recognizing my aptitude. My years of Ph.D. studies have been a fruitful experience and a hefty harvest for me to refine and perfect myself. Additionally, I want to thank Prof. Bill Chan for consistently guiding our project. Even though Prof. Chan is a scientist who is over 80 years old, he still has a passion and drive for scientific study. His perseverance constantly inspires me to move forward without hesitation.

Dr. Iris Wong deserves a particular thank you from me as well. I appreciate her concern for me, her assistance with my experiments over the past few years, and her assistance in revising my papers and poster. Her preciseness and earnestness in her work have had a profound impact on me and have inspired me. I also want to thank Dr. Wenqin, Ms. Gege Sun, Dr. Terry Chan, and Dr. Clare Yan, not only are we lab mates, but we also have a great friendship and struggle together. Additionally, I want to thank Prof. Jiahua

Cui, Dr. Huan Zhang, Dr. Zhen Liu, Dr. Teng Chen, Dr. Peng Li, Mr. Xinqing Yang, and Dr. Xuesen Hu for their support and encouragement in the past. I also appreciate all the technical assistance provided to me by the ULS and CAF platform professionals at PolyU. Of course, I also want to express my gratitude to my incredibly close friend, Ms. Jie Lan[1], Dr. Wenxuan Yu[1], Ms. Manhui Wu[1], Dr, Longqing Li[1], and Dr. Angxin Song[1], for their support, affection, and many forms of assistance in the past, which I will always remember. I hope the future is prosperous for all of us.

Last but not least, I want to thank my family, especially my husband. I had to leave my family during the COVID-19 pandemic and stayed in Hong Kong to complete my studies. My husband took good care of our family on his own. He never blamed me for being unable to manage the responsibilities and obligations of being a mother. Instead, he carefully listened to all my concerns and worries and always gave me his full support in my academic endeavors. I would not have completed the five years of Ph.D. education without his support and love. I also want to express my gratitude to my parents, mother-in-law, and father-in-law for their care of my daughter. I cannot complete my studies in Hong Kong without their help. Thank you to my sister for her support and confidence in me. She mentioned that the gold will glow one day. I will keep refueling because I think she is right. Additionally, I want to thank my entire extended family for all their support of my family throughout my absence.

Xiaochun Su

25th May, 2023

Table of contents

List of figures

List of tables

List of abbreviation

GBM	Glioblastoma
WHO	World Health Organization
CBTRUS	Central Brain Tumor Registry of the United States
RTK	receptor tyrosine kinase
PI3K	phosphoinositol-3-kinase
Rb	retinoblastoma
EGFR	epidermal growth factor receptor
PDGFRα	platelet-derived growth factor receptor α
PTEN	phosphatase and tensin homolog
NF-1	neurofibromin 1
MDM2	murine double minute 2
MDM4	murine double minute 4
CDK4	cyclin-dependent kinase 4
IDH	isocitrate dehydrogenase
TCA	tricarboxylic acid
α-KG	α-Ketoglutarate
2-HG	2-hydroxyglutarate
RT	radiotherapy
TMZ	temozolomide
FDA	Food and Drug Administration
US	United States
OS	overall survival
MGMT	O-6 Methylguanine-DNA methyltransferase
TTFields	tumor treatment fields
PFS	progression-free survival
NCCN	National Comprehensive Cancer Network
EOR	extent of resection

PSI	patient safety index
HAC	hospital-acquired diseases
5-ALA	5-aminolevulinic-acid
SF	sodium fluorescein
ICG	indocyanine green
GTR	gross total resection
STR	subtotal resection
SRS	stereotactic radiosurgery
IGRT	image-guided radiotherapy
IMRT	intensity-modulated radiotherapy
CCNU	lomustine
BCNU	carmustine
BVZ	bevacizumab
PCV	procarbazine, lomustine, and vincristine regimen
PC	procarbazine and lomustine regimen
BBB	blood-brain barrier
MTIC	(5-(3-methyltriazen-1-yl) imidazole-4-carboxamide
MMR	mismatch repair
GSCs	glioma stem cells
SSB	single-strand break
DSB	double-strand break
BER	base excision repair
PARP	Poly (ADP-ribose) polymerase
miRNA	microRNA
ADAM	A disintegrin and metalloproteinases
ABC	ATP-binding cassette
P-gp	P-glycoprotein
hBVR	human biliverdin reductase
HMGB1	high-mobility group box 1

CAR	chimeric antigen receptor
TKI	tyrosine kinase inhibitor
CNS	central nervous system
TJ	tight junction
MRP1	multidrug resistance-associated protein 1
BCRP	breast cancer resistance protein
MDR	multi-drug resistance
GSH	glutathione
DDI	drug-drug interactions
ADME	absorption, distribution, metabolism, and excretion
PEG	polyethylene glycol
SOR	sorafenib
PTX	paclitaxel
TPT	topotecan
NMP	N-Methyl-2-pyrrolidone
CrEL	Cremophor EL
DMSO	dimethyl sulfoxide
ACN	acetonitrile
DMEM	Dulbecco's Modified Eagle Medium
RPMI	Roswell Park Memorial Institute
MEM-α	Minimum Essential Medium α
P/S	penicillin/streptomycin
FBS	fetal bovine serum
MTS	(3-(4,5-dimethylthiazol-2-yl)-5-(3-carboxymethoxyphenyl)-2-(4-sulfophenyl)-2H-tetrazolium inner salt)
PMS	phenazine methosulfate
UPLC-QqQ-MS/MS	ultra high-performance liquid chromatography coupled with triple quadrupole mass spectrometry
ESI	electrospray ionization

MRM	multiple reaction monitoring
LLOQ	lower limit of quantification
PDX	patient-derived xenograft
SD	standard deviation
SEM	standard error of the mean
IC_{50}	half-maximal inhibitory concentration
EC_{50}	half-effective concentration
FLuc	firefly luciferase
IVIS	*in vivo* imaging system
PBS	phosphate buffer saline
I.V.	intravenous
I.P.	intraperitoneal
P.O.	per os, the Latin for "by mouth"
PK	pharmacokinetics
AST	aspartate transaminase
ALT	alanine transaminase
BUN	urea nitrogen
CRE	creatinine
RCC	renal cell carcinoma
HCC	hepatocellular carcinoma
NSCLC	non-small-cell lung cancers
CDTX	cell-line-derived tumor xenograft
BLI	bioluminescence imaging
C_{max}	maximum plasma concentration
AUC_{0-t}	area under the plasma concentration-time curve from zero to the last measurable plasma concentration point
CL	clearance
PMSF	phenylmethylsulfonyl fluoride
MW	molecular weight

clogP	calculated partition coefficient
tPSA	topological polar surface area
mins	minutes
hrs	hours
q.o.d	quaque omni die, the Latin for every other day
RSD	relative standard deviation
SAR	structure-activity relationship
cm	centimeter
mm	millimeter
EC_{50}	half maximal effective concentration
IC_{50}	half maximal inhibitory concentration
IS	internal standard

Chapter 1 Introduction

1.1 Glioblastoma (GBM)

1.1.1 A grade 4 astrocytoma - GBM

Gliomas originate from abnormal growth of glial cells in the brain or spine. Glioma accounts for 24% of all primary brain and other central nervous system (CNS) tumors and 80.9% of malignant brain tumors [1]. The World Health Organization (WHO) classifies gliomas into grades 1 to 4 based on the level of malignancy of the tumor [2]. Grades 1 and 2 are low-grade malignancies, while grades 3 and 4 are extremely malignant tumors. GBM is of grade 4 astrocytoma and is the most aggressive invasive tumor.

1.1.2 Epidemiology of GBM

GBM is the most common malignant brain glioma. The latest data from the Central Brain Tumor Registry of the United States (CBTRUS) statistical report (2015-2019) [1] indicated that GBM accounted for 14.2% of all primary brain tumors and 50.1% of primary malignant brain tumors. The incidence rate in the United States was 3.26 per 100,000 population, and it increased with age, peaking between the age of 75 and 85. GBM is far more common in men than in women, and it is much more common in Caucasians than in Black people. Patients with GBM only have a 6.9% 5-year survival rate.

1.1.3 Pathogenesis of GBM

The cause of GBM is still under investigation. The known risk factors included high doses of ionizing radiation exposure [3, 4] and genetic alterations [5]. Additionally, nitrite-containing food [6], bacterial or viral infection [7], as well as other carcinogenic factors, may lead to the development of GBM.

Three main signaling pathways have been identified that are associated with GBM. They were (a) activation of receptor tyrosine kinase (RTK), RAS, and phosphoinositol-3-kinase (PI3K) pathway; (b) inactivation of p53 pathway; and (c) inactivation of retinoblastoma (Rb) pathway (**Figure 1-1**). Dysregulation of these signaling pathways is directly related to the development of GBM [8, 9]. Approximately 88% of GBM patients had activation in the RTK/RAS/PI3K signaling pathway, with the most frequently altered genes: epidermal growth factor receptor (EGFR) (amplification, 45%), platelet-derived growth factor receptor α (PDGFRα) (amplification, 13%), phosphatase and tensin homolog (PTEN) (homozygous deletion, 37%), or neurofibromin 1 (NF-1) (homozygous deletion, 18%). Approximately 87% of GBM patients had inactivation in the p53 signaling pathway. These genes included CDKN2A (homozygous deletion and mutation, 49%), TP53 (mutation and homozygous deletion, 35%), murine double minute 2 (MDM2) (amplification, 14%), or MDM4 (amplification, 7%). Finally, RB signaling disruption was found in 77% of GBM patients, usually involving CDKN2A (homozygous deletion and mutation, 52%), CDKN2B (homozygous deletion and mutation, 47%), or cyclin-dependent kinase 4 (CDK4) (amplification, 18%).

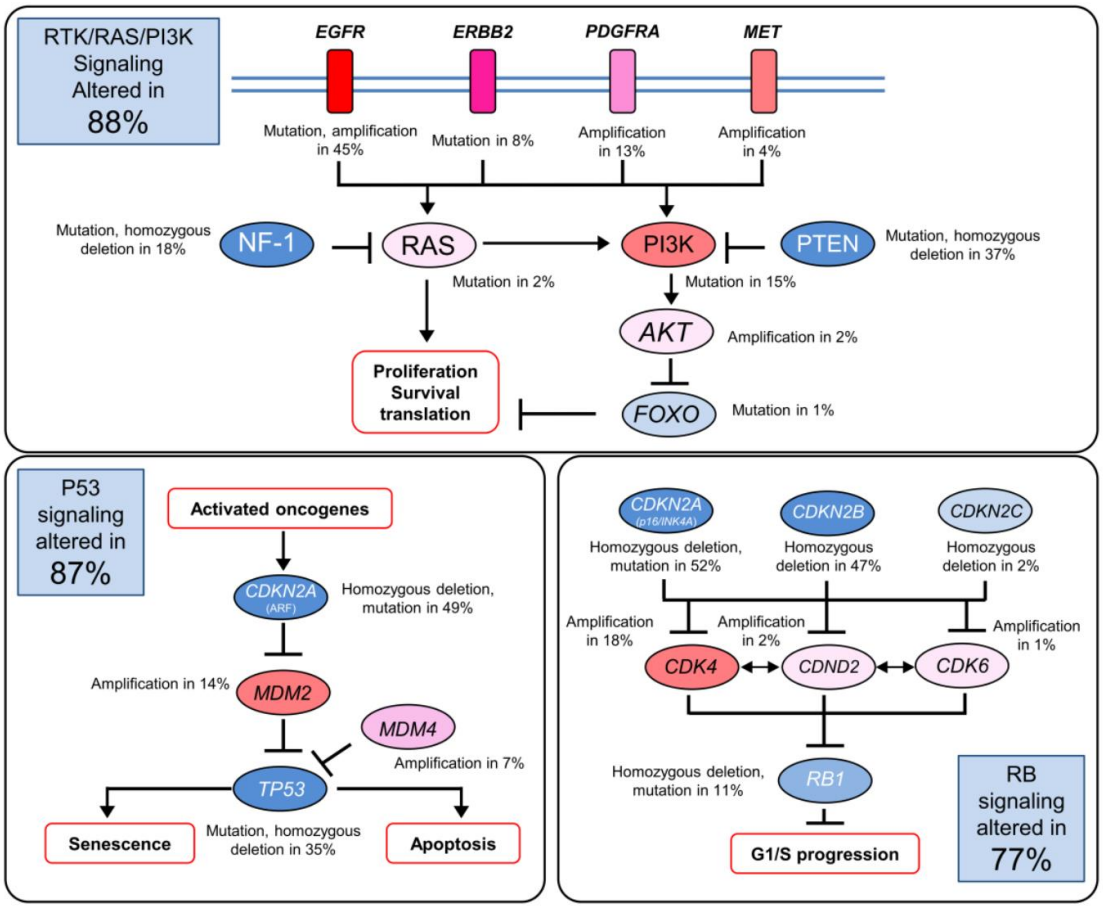

Figure 1-1 Three frequently mutated signaling pathways in GBM [10]

The three most mutated pathways in GBM were: (a) activation of RTK, RAS, and PI3K pathways; (b) p53 pathway inactivation; (c) Rb pathway inactivation. Different mutated genes were shown, including the type of mutation, and the proportion of GBMs that carry each modification. Blue represented the gene change that results in the loss of function, whereas red represented the gene change that is activated.

Another study found that 12% of GBM patients had a genetic alteration in the isocitrate dehydrogenase (IDH) [11]. Recurrent GBM patients (73%) had more IDH mutations than original GBM patients (3.7%) [12]. IDH (IDH1 and IDH2) are enzymes that are participated in the tricarboxylic acid (TCA) cycle that can catalyze the bioconversion of isocitric acid to produce α-Ketoglutarate (α-KG) and CO_2 (**Figure 1-2**). Mutations in IDH1 and IDH2 lead to the further conversion of α-KG into 2-hydroxyglutarate (2-HG) (**Figure 1-2**). Abnormal accumulation of oncometabolite 2-HG in the brain promotes tumorigenesis [13]. However, IDH-mutated GBM patients demonstrated increased median survivals [14] and higher sensitivity to chemoradiotherapy [15] compared to IDH-wild-type GBM patients. IDH mutation is therefore a significant prognostic factor for those with GBM.

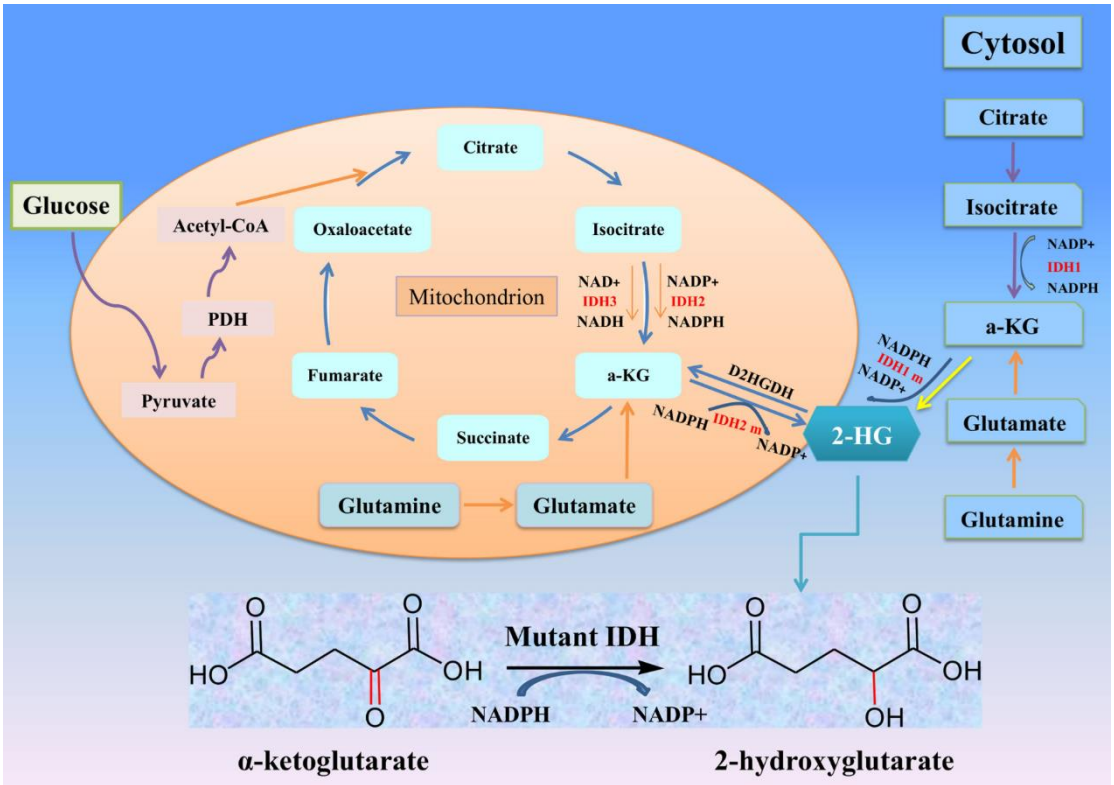

Figure 1-2 Important roles of IDHs in cellular metabolism in cancer [16]
IDH1 or IDH2 mutation can convert α-KG into 2-HG and change reduced nicotinamide adenine dinucleotide phosphate (NADPH) to NADP+.

1.2 Current standard therapy for GBM

Currently, the clinical standard of care (Stupp protocol) for patients with GBM includes maximum safe surgical removal of the brain tumor, followed by 6 weeks of postoperative radiotherapy (RT) combined with temozolomide (TMZ), and then 6 months of adjuvant TMZ chemotherapy [17].

TMZ is an oral alkylating agent that was approved by the Food and Drug Administration (FDA) of the United States in 2005 [18]. It can damage DNA and destruct tumor cells by methylating DNA at the N-7 or O-6 positions of guanine residues [19]. TMZ is usually used together with RT and is widely used for treating newly diagnosed patients with GBM. A Phase II clinical trial in 2001 first demonstrated the safety of continuous daily use of TMZ with concurrent RT in newly diagnosed patients with GBM [20]. A Phase III clinical trial further supported the efficacy of the combination of TMZ and RT in the GBM treatment, increasing the overall survival (OS) by 20.7% ($p < 0.001$) when compared to RT alone [21]. TMZ is more effective in GBM patients with O-6 Methylguanine-DNA methyltransferase (MGMT) gene promoter methylation. Another clinical trial revealed that TMZ with RT can prolong the median OS of patients with MGMT promoter methylation by 41.8% ($p = 0.007$) when compared to that of RT alone. However, this significant difference was not observed in patients with unmethylated MGMT [22]. The long-term outcomes of this trial further confirmed that MGMT gene promoter methylation can predict the sensitivity of GBM to TMZ (**Table 1-1**).

Table 1-1 Long-term survival results according to the types of treatment and MGMT status in the "Stupp trial" [23]

MGMT status	Treatment	Median OS (months)	2-year OS (%)	3-year OS (%)	4-year OS (%)	5-year OS (%)
Unmethylated	RT	11.8	1.8	0	0	0
	RT + TMZ	12.6	14.8	11.1	11.1	8.3
Methylated	RT	15.3	23.9	7.8	7.8	5.2
	RT + TMZ	23.4	48.9	27.6	22.1	13.8

FDA-approved tumor treatment fields (TTFields) were introduced in 2015 as an addition to the postoperative chemoradiotherapy regimen for GBM patients [24]. TTFields use alternating electric fields to inhibit cell division and slow tumor growth. A Phase III clinical trial [25] revealed that the median progression-free survival (PFS) increased from 4.0 months in TMZ alone to 6.7 months ($p < 0.001$) in TTF with TMZ. OS of the TTF group was also longer, with 20.9 months for TTF than that of the TMZ group of 16.0 months ($p < 0.001$).

Currently, there is no established chemotherapeutic regimen for recurrent GBM. Additional surgical resection, re-irradiation, bevacizumab, TMZ, lomustine/carmustine, or combination approaches can be used. The National Comprehensive Cancer Network (NCCN) guidelines for GBM patients were shown in **Figure 1-3**.

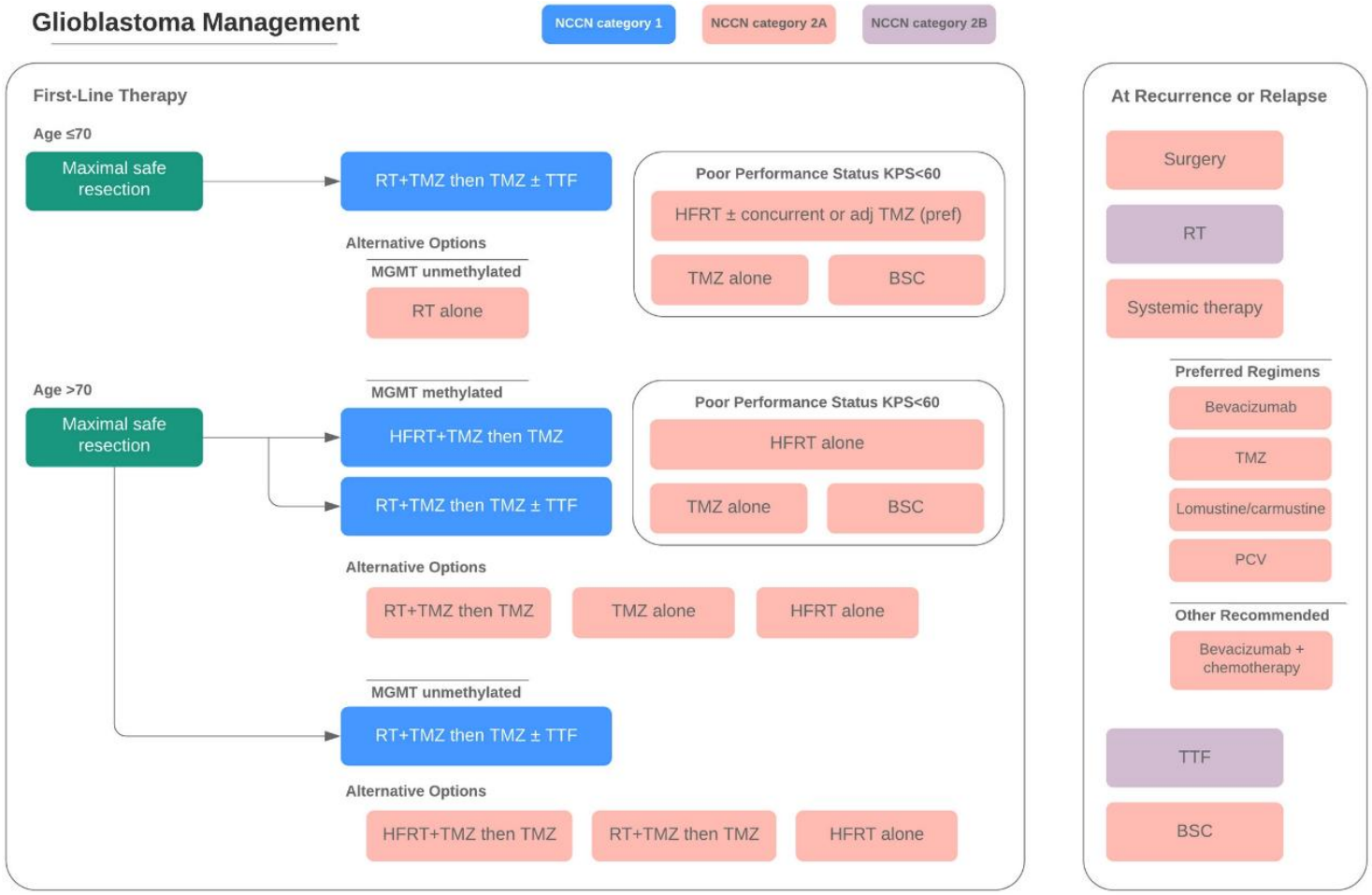

Figure 1-3 Current treatment strategy for GBM according to NCCN [26]

MGMT: O-6 Methylguanine-DNA methyltransferase; KPS: Karnofsky performance status; HFRT: hyper-fractionated radiotherapy; TMZ: temozolomide; RT: radiotherapy; TTF (TTFields): tumor treatment fields; PCV: procarbazine, lomustine, and vincristine regimen; BSC: best supportive care.

1.2.1 Surgery

Surgical resection is the primary standard treatment for GBM patients. It can remove space-occupying lesions and relieve intracranial hypertension; alleviate glioma-related symptoms, such as secondary epilepsy; obtain pathological tissue and molecular pathology study; reduce tumor burden and create the necessary conditions for further comprehensive treatment.

The extent of resection (EOR) is highly associated with the prognosis of GBM [27]. A greater degree of surgical resection can extend the life span of GBM patients. EOR > 98% is thought to be necessary for increased survival in GBM patients [28]. A retrospective study of 284 GBM patients also discovered that patients with gross total GBM removal (GTR) (EOR > 95%) had a lower incidence of patient safety index (PSI) and hospital-acquired diseases (HAC) than those with subtotal resection (STR) (EOR < 95%) ($p < 0.05$) [29].

To improve EOR, fluorescence-guided surgery is now widely used to guide the excision of GBM tumors. Different fluorescent agents, including 5-aminolevulinic-acid (5-ALA) [30, 31], sodium fluorescein (SF) [32], and indocyanine green (ICG) [33], have been demonstrated to improve resection rates and prolong PFS for GBM patients.

1.2.2 Radiation

RT has always been the mainstay of GBM treatment along with surgical resection. It uses X-rays, gamma rays, or photons to destroy GBM cells and reduce tumor size.

The time to initiation of RT is highly related to the prognosis of GBM patients. A recent study [34] determined that RT for GBM should start between 4 to 8 weeks following surgery. Delays of >8 weeks for patients with GTR and 4 weeks for patients with STR could directly lead to shorter survival.

The radiation dose is also associated with the survival rates of GBM. Conventional

radiation uses 30 fractions of 2 Gy to deliver a treatment of 60 Gy [35]. In a previous study of 420 patients with GBM, higher radiation doses (50, 55, or 60 Gy) were associated with better survival, with corresponding OS of 28 ($p < 0.001$), 36 ($p < 0.001$), or 42 ($p < 0.001$) weeks, respectively, compared to those who did not receive radiotherapy (18 weeks) [36]. Similarly, another study of 474 GBM patients also revealed that the median OS of those receiving 60 Gy was 12 months ($p = 0.007$) compared to those receiving 45 Gy of only 9 months [37]. Besides, some prospective research has revealed that radiation above 60 Gy did not further extend the survival of GBM patients [38, 39].

Recent development in radiotherapy includes whole-brain radiotherapy and moving through brachytherapy [40], stereotactic radiosurgery (SRS) [40], image-guided radiotherapy (IGRT) [41], and intensity-modulated radiotherapy (IMRT) [42]. These precision radiotherapy techniques not only enhance the treatment of lesions in GBM patients but also lessen or eliminate exposure to healthy tissues and enhance patient quality of life.

1.2.3 Chemotherapy

Chemotherapy is another main option for GBM treatment. In addition to TMZ, the US FDA also approved Lomustine (CCNU, Ceenu), Carmustine (BCNU, Gliadel Wafer), and Bevacizumab (BVZ, Avastin) in 1976 [43], 1977 [44], and 2009 [45], respectively, for the treatment of GBM.

Lomustine (CCNU, Ceenu) is a non-specific alkylating chemical that kills cells by causing DNA and RNA crosslinking. The well-known PCV chemotherapy regimen, which combines procarbazine, CCNU, and vincristine, is frequently used to treat recurrent GBM (**Figure 1-3**). A retrospective analysis revealed that the PCV regimen moderately extended the median survival for recurrent GBM following Stupp treatment, with OS at 26 weeks, PFS at 17 weeks, and 6 months of PFS at 20%, but also had a low risk of severe toxicity and a low tolerance [46]. Recently, a novel modified PC chemotherapy was developed by removing vincristine from the PCV regimen and lowering the dosage of CCNU [47]. It was demonstrated that the novel PC regimen had a better survival benefit for relapsed GBM,

with an OS of 396 days compared to 232 days (p = 0.042) in the PCV groups, and had acceptable toxicity, making it a viable alternative chemotherapy regimen [47]. Additionally, several clinical trials have also shown that the combination of CCNU with other anticancer drugs can extend the life expectancy in patients with GBM. A Phase III clinical trial has found that the median OS of GBM patients can be extended from 31.4 months in TMZ alone to 48.1 months in CCNU combined with TMZ (p = 0.0492) [48]. A meta-analysis also revealed that bevacizumab and CCNU together increased the OS (p = 0.002), PFS (p < 0.00001), and 6-month PFS (p = 0.0005) in patients with GBM [49].

Carmustine (BCNU, Gliadel Wafer) is a non-specific alkylating agent, which cross-links DNA and RNA in dividing cells to kill cancer cells. BCNU is usually prepared in a biodegradable wafer that is directly placed into the cavity left by the surgical removal of a brain tumor. Intracranial implantation of BCNU wafer enables complete and direct exposure of tumors to anticancer medications. This can achieve a better therapeutic outcome for GBM and reduce the risk of systemic toxicity [50]. A recent meta-analysis revealed that either intravenous BCNU administration or wafer implantation can significantly extend the OS of GBM patients (p < 0.0001 or p = 0.04, respectively). Moreover, BCNU and TMZ combined treatment significantly extended the OS for those with GBM compared to TMZ alone (p = 0.03) [51]. However, some studies also reported that the high cost of BCNU wafer implantation discourages its widespread use and inclusion in the standard of care [52, 53].

Bevacizumab (BVZ, Avastin) is a recombinant humanized monoclonal immunoglobulin G1 (IgG1) that can prevent the formation of new blood vessels in tumors by inhibiting the vascular endothelial growth factor (VEGF) in tumor cells. BVZ is also a preferred regimen for people with relapsed GBM (**Figure 1-3**). A retrospective analysis of 92 patients with recurrent GBM revealed that BVZ improved the median PFS and OS, with corresponding 6-, 12, or 24-month PFS rates of 55.2%, 22.9%, or 9.6% and 6-, 12-, or 24-month OS rates of 74.9%, 31.7%, or 10.1% [54]. A recent Phase II clinical trial [55] revealed that when compared to BVZ alone, BVZ plus re-RT increased the median PFS and 6-month PFS in relapsed GBM patients from 3.8 to 7.1 months (p = 0.05) and from 29.1% to 54.3% (p =

0.001), respectively. However, the median OS of patients was unaffected.

1.3 Mechanisms of TMZ resistance in GBM

Since TMZ was FDA-approved in 2005, it has been the first choice of chemotherapeutic medication for GBM treatment. TMZ is an imidazotetrazine lipophilic drug that has a high bioavailability of 100% and a strong blood-brain barrier (BBB) penetration rate. The mechanism of action of TMZ is that its active metabolite can hinder DNA synthesis by methylating DNA, which ultimately induces apoptosis. TMZ will naturally hydrolyze once within the body to create its active metabolite (5-(3-methyltriazen-1-yl) imidazole-4-carboxamide, MTIC) [56]. MTIC is further hydrolyzed to highly active methyl diazonium ion, which can methylate guanine at the O6 and N7 sites as well as adenine at the N3 site [57]. O6 site of guanine can be alkylated to create the O6-methylguanine adduct (O6-meG), which causes thymine residues to accidentally be inserted rather than cytosine. DNA mismatch repair system (MMR) identifies and cuts out the mismatched thymine, resulting in a thymic site. This blocks DNA synthesis and eventually induces apoptosis [58, 59].

Even though TMZ has good efficacy, TMZ resistance is frequently found in GBM patients. The resistance mechanisms of TMZ in GBM are shown in **Figure 1-4**. The following well-known mechanisms will be discussed: 1. DNA repair; 2. microRNAs; 3. cellular drug efflux; 4. tumor microenvironment - hypoxia; and 5. glioma stem cells (GSCs).

A

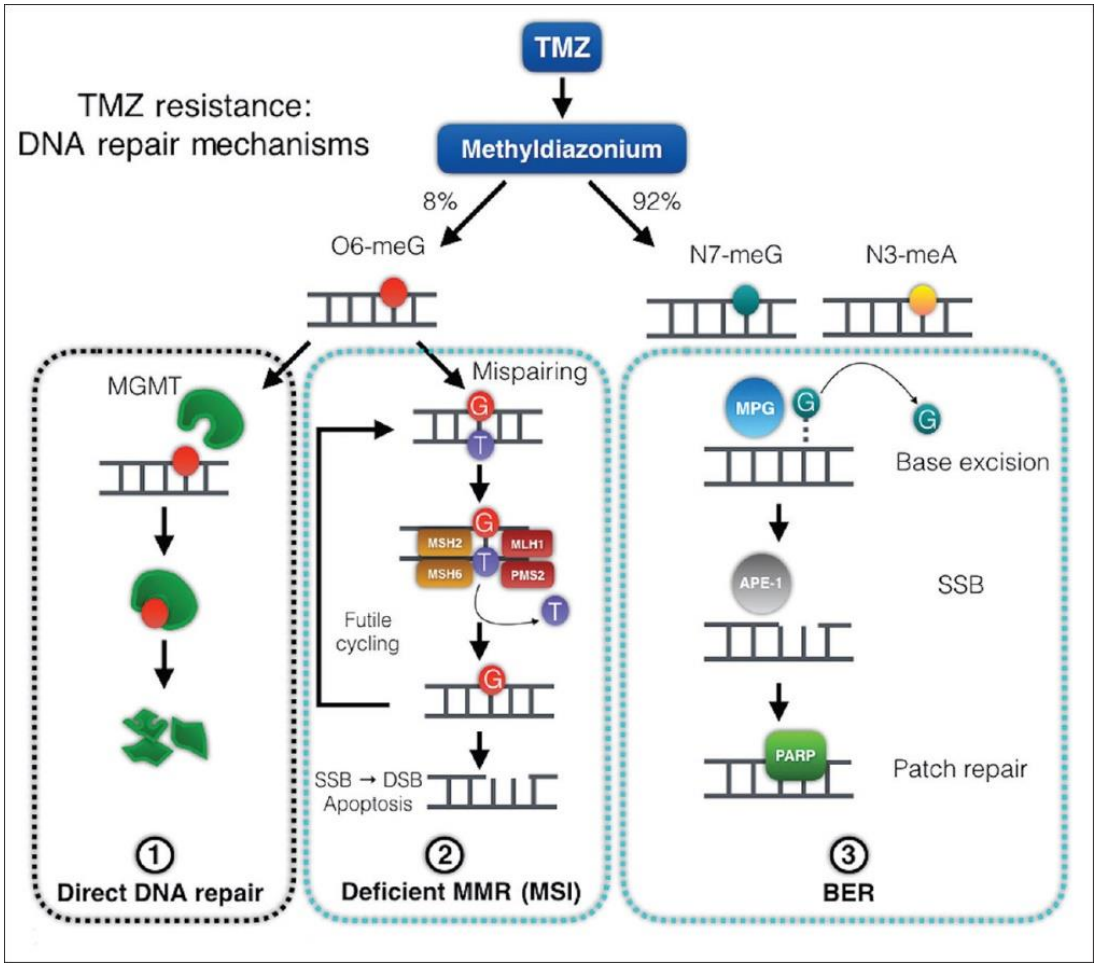
TMZ
TMZ resistance:
DNA repair mechanisms
Methyldiazonium
8%
92%
O6-meG
N7-meG
N3-meA
MGMT
Mispairing
MSH2
MLH1
MSH6
PMS2
Futile
cycling
SSB → DSB
Apoptosis
MPG
Base excision
APE-1
SSB
PARP
Patch repair
1
Direct DNA repair
2
Deficient MMR (MSI)
3
BER

B

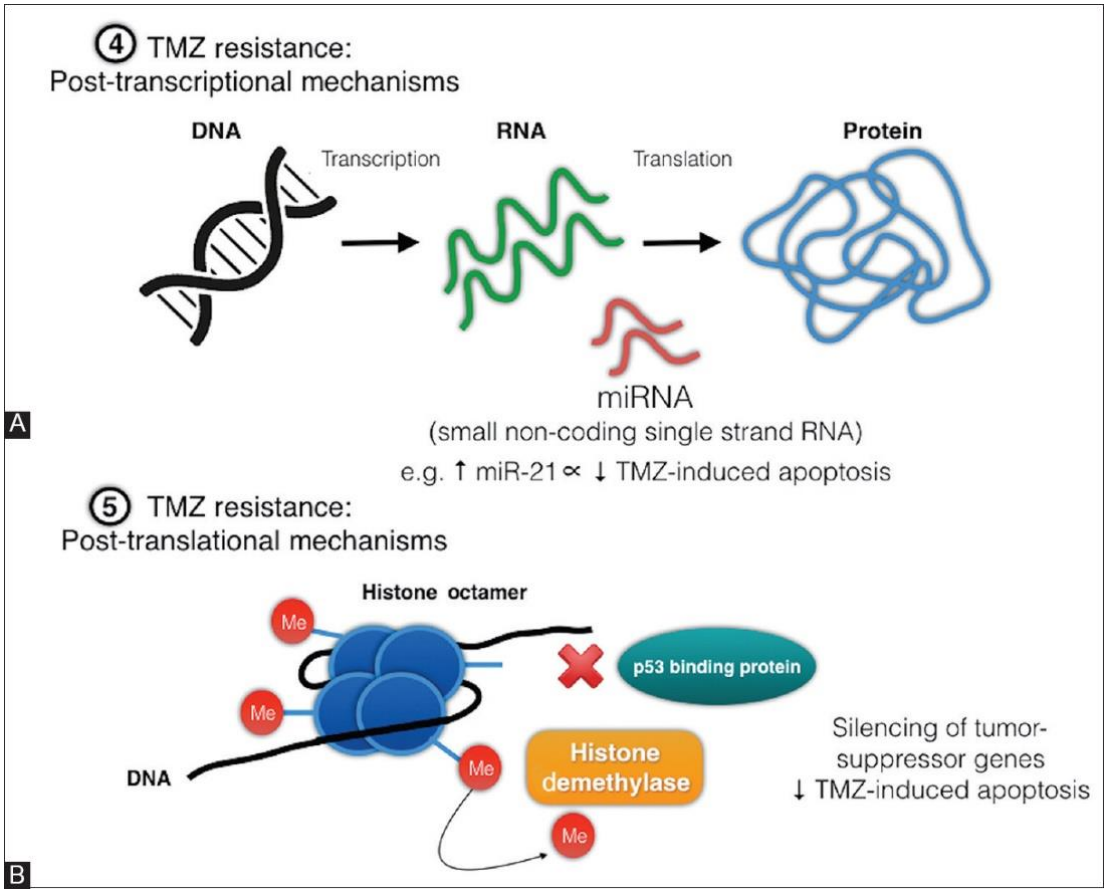
④ TMZ resistance:
Post-transcriptional mechanisms
DNA
Transcription
RNA
Translation
Protein
miRNA
(small non-coding single strand RNA)
e.g. ↑ miR-21 ∝ ↓ TMZ-induced apoptosis
A
⑤ TMZ resistance:
Post-translational mechanisms
Histone octamer
Me
Me
Me
Me
DNA
p53 binding protein
Histone demethylase
Silencing of tumor-suppressor genes
↓ TMZ-induced apoptosis
B

C

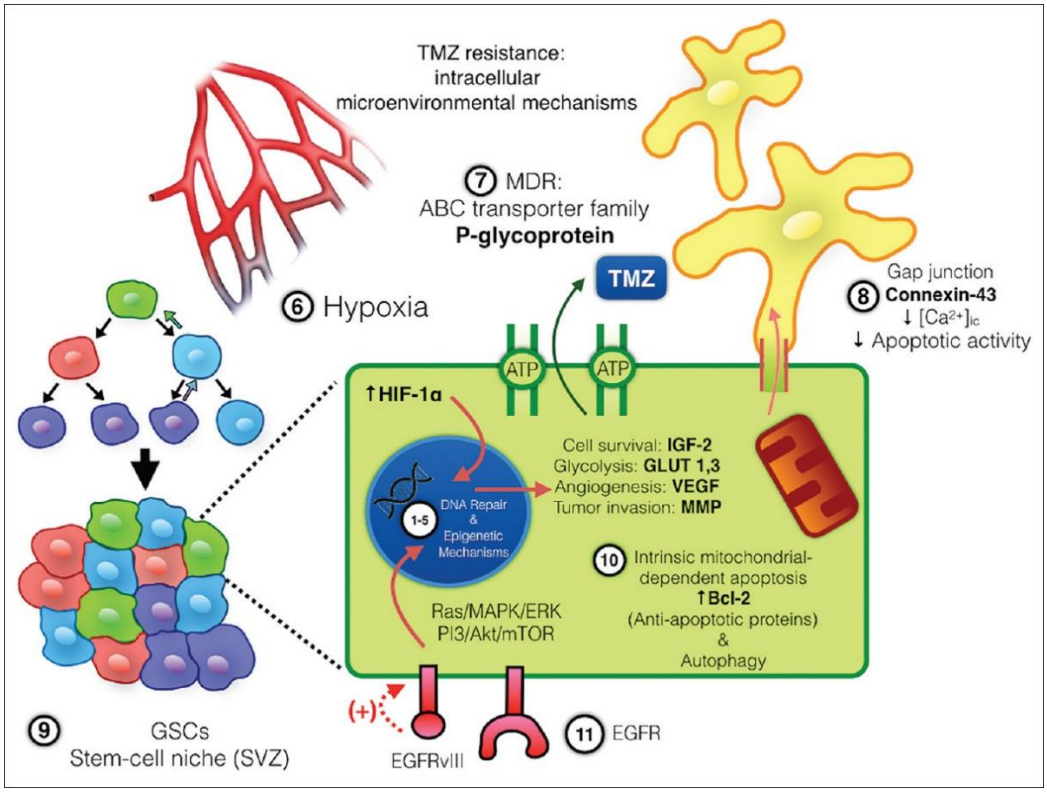

Figure 1-4 Mechanism of TMZ resistance in GBM [60]
(A) DNA repair mechanisms of TMZ resistance; (B) Epigenetic mechanisms of TMZ resistance; (C) Cellular and tumor microenvironmental TMZ resistance mechanisms.
①: Direct DNA repair; ②: Mismatch repair (MMR); ③: Base excision repair (BER); ④: Posttranscriptional mechanisms; ⑤: Posttranslational epigenetic mechanism; ⑥: Tumor microenvironment: Hypoxia; ⑦: ATP-binding cassette transporters involved cellular TMZ efflux; ⑧: Tumor microenvironment: Connexin gap junction activity; ⑨−⑪: Glioma stem cells (GSCs).

1.3.1 DNA repair

MGMT is an important enzyme in DNA repair. High MGMT expression has been demonstrated to be correlated with significant TMZ resistance in GBM patients [61]. MGMT can directly demethylate O6-meG to avoid DNA crosslinking damage and resulting in resistance to the alkylating agent (**Figure 1-4A**).

MMR is a process that fixes mismatched base pairs in the DNA double strands during the S phase of the cell cycle. As was previously mentioned, TMZ leads to a mismatch between O6-meG and thymine during DNA synthesis. The MMR system typically detects, and

excises mismatched thymine on the new strand during DNA replication, leaving O6-meG intact on the template strand and leading to DNA strand breaks. Accumulated DNA single- (SSBs) or double-strand breaks (DSBs) eventually cause cell apoptosis **(Figure 1-4A**). Numerous evidence has demonstrated that decreased or missing MMR activity would lead to TMZ resistance [62, 63].

Base excision repair (BER) is a mechanism that fixes single nucleotide modifications. BER can recognize and correct N-methylated DNA on guanine (N7-meG) and adenine (N3-meA) caused by TMZ. As shown in **Figure 1-4A**, MPG glycosylase first recognizes and removes N7-meG or N3-meA to form the AP site (apurinic/apyrimidinic site). APE-1 endonuclease cleaves the AP-site to create an SSB intermediate. Poly (ADP-ribose) polymerase (PARP) then identifies and binds to the SSB intermediate to complete the DNA repair. If TMZ-induced N3 methylation is not reversed, it will result in cell death. BER, however, can repair N3-meA, which causes cells to develop resistance to TMZ [64].

1.3.2 MicroRNAs

Non-coding RNAs - microRNAs (miRNAs) are crucial regulators of post-transcriptional gene expression [65-67]. They have the ability to bind to particular mRNAs, which will result in the degradation of the target proteins and halt translation (**Figure 1-4B**). Various miRNAs have different tumor-suppressing and carcinogenic properties [68]. Up-regulation of carcinogenic miRNAs or down-regulation of antitumor miRNAs can lead to the development of GBM or acquired resistance to chemoradiotherapy [65, 69]. Numerous evidence has demonstrated the importance of miRNAs in TMZ resistance in GBM. Some of the miRNAs implicated in TMZ resistance include miRNA-21 [70], miRNA-145 [71], miRNA-195 [72], miRNA-455-3p [73], miRNA-10a* [73], miRNA-222 [74], miRNA-26a [75], etc. For example, miRNA-145 was found to be up-regulated in GBM and can control downstream ADAMs protein (A disintegrin and metalloproteinases) to enhance TMZ resistance [71].

1.3.3 Cellular drug efflux

P-gp, a well-known ATP-binding cassette (ABC) transporter, is an essential efflux protein that transports xenobiotics out of the cell. Overexpression of P-gp has long been thought to be related to drug resistance in cancer cells. P-gp can efflux a lot of medicines from the cell, which lowers intracellular drug concentration and causes more drug failure **(Figure 1-4C)**. P-gp overexpression has been found in the chemo-resistant GBM cell lines [76]. Additionally, tissue samples from TMZ-resistant tumor patients also showed increased P-gp levels [77, 78]. As a result, inhibition or down-regulation of P-gp has been tried to lower TMZ resistance and treat GBM patients. P-gp inhibitors like PSC833, Reversan, and CP-100356 have been demonstrated to enhance TMZ-mediated cytotoxicity in GBM cell lines [76]. Down-regulating TRPC5 can also block P-gp expression, thereby reversing the TMZ resistance in TMZ-resistant cell lines [78].

1.3.4 Tumor microenvironment - hypoxia

GBM tumor has a hypoxic microenvironment, with a dioxygen (O_2) pressure as low as 1% in the deep or remote area of the tumor [79]. While hypoxia can delay tumor growth, many GBM cells manage to survive the lack of oxygen and develop increased aggressiveness and chemoresistance [80]. Hypoxia has been shown to increase TMZ-resistant GBM cells through the up-regulation of miRNA-26a mediated by hypoxia-inducible factor 1 (HIF-1) [75]. Besides, hypoxia can block the pro-apoptotic pathway to enhance the TMZ resistance in GBM. For example, hypoxia-mediated Livin (an inhibitor of apoptosis protein) was discovered to be up-regulated in GBM, and this was associated with TMZ resistance [81]. Another study also revealed that up-regulation of hypoxia-mediated hBVR (human biliverdin reductase) was linked to TMZ resistance [82].

1.3.5 Glioma stem cells (GSCs)

GSCs make up a small portion of tumor cells, but they have minimal differentiation and the capacity for self-regeneration [83]. Despite accounting for less than 1% of GBM tumors, GSCs are primarily responsible for most tumor recurrences and chemoradiotherapy resistance [84]. It is generally accepted that GSCs are the primary reason for tumor

recurrence following TMZ chemotherapy [85]. Previous studies have shown that GBM cells-secreted metabolites and cytokines can affect the capacity of GSCs to initiate tumors and thus promote TMZ resistance [86]. A recent study further found that TMZ-induced HMGB1 protein (high-mobility group box 1) upregulation can encourage the development of GSCs through the TLR2/NEAT1/Wnt/β-catenin signaling pathway, ultimately enhancing TMZ resistance in GBM patients. In addition, research has also revealed that GSCs contributed to the TMZ resistance by elevated MGMT expression [87, 88], activated anti-apoptotic mechanism [89], and activation of drug efflux [90, 91] (**Figure 1-4C**).

1.4 Targeted therapy of GBM

GBM is a malignant tumor with a very poor prognosis. Although the Stupp protocol has been around for many years as a standard treatment for GBM, GBM has not been cured. Many novel treatments are currently being investigated, including oncolytic viruses, chimeric antigen receptor (CAR) T-cells, cancer vaccines, and monoclonal antibodies, but small molecules continue to get the most attention. There were three major dysregulated signaling pathways of GBM, including the RTK/RAS/PI3K pathway, p53 pathway, and Rb pathway. These pathways have also served as the focus of GBM clinical studies over the past 20 years [92, 93].

1.4.1 RTK pathways

Approximately 88% of GBM patients had mutant RTK/RAS/PI3K signaling pathways, including EGFR (amplification, 45%), PDGFRα (amplification, 13%), or PTEN (homozygous deletion, 37%) of GBM patients [10]. Small molecule Tyrosine Kinase Inhibitors (TKIs) can block these receptor signaling pathways like EGFR, PDGFRα, or VEGF/VEGFR, preventing angiogenesis, cell proliferation, and differentiation [94]. The mechanism of action of TKIs is shown in **Figure 1-5**. Several FDA-approved TKIs for the management of other cancer types, including sorafenib [95], sunitinib [96], imatinib [97], pazopanib [98], vandetanib [99], and axitinib [100], have been investigated for treating GBM. Many of them have also been utilized in preclinical and clinical GBM studies. TKIs were successful in several preclinical studies, but clinical trials showed that they did not improve OS in patients with GBM. For example, sorafenib monotherapy demonstrated a substantial survival improvement compared to the control group ($p < 0.05$) in the orthotopic animal model using U87 cells [101]. However, clinical sorafenib therapy failed to increase survival in GBM patients [102]. The failure of TKIs in GBM treatment may be due to several issues, including different compensatory mechanisms *in vivo*, inadequate target coverage, BBB restriction, drug resistance, or poor drug safety. Many clinical trials using TKIs to treat GBM are still ongoing (ClinicalTrial.gov identifier: NCT00052208, NCT04547855, NCT03797326, etc). Combination therapy designed to attack several targets or to increase BBB permeability is predicted to improve efficacy.

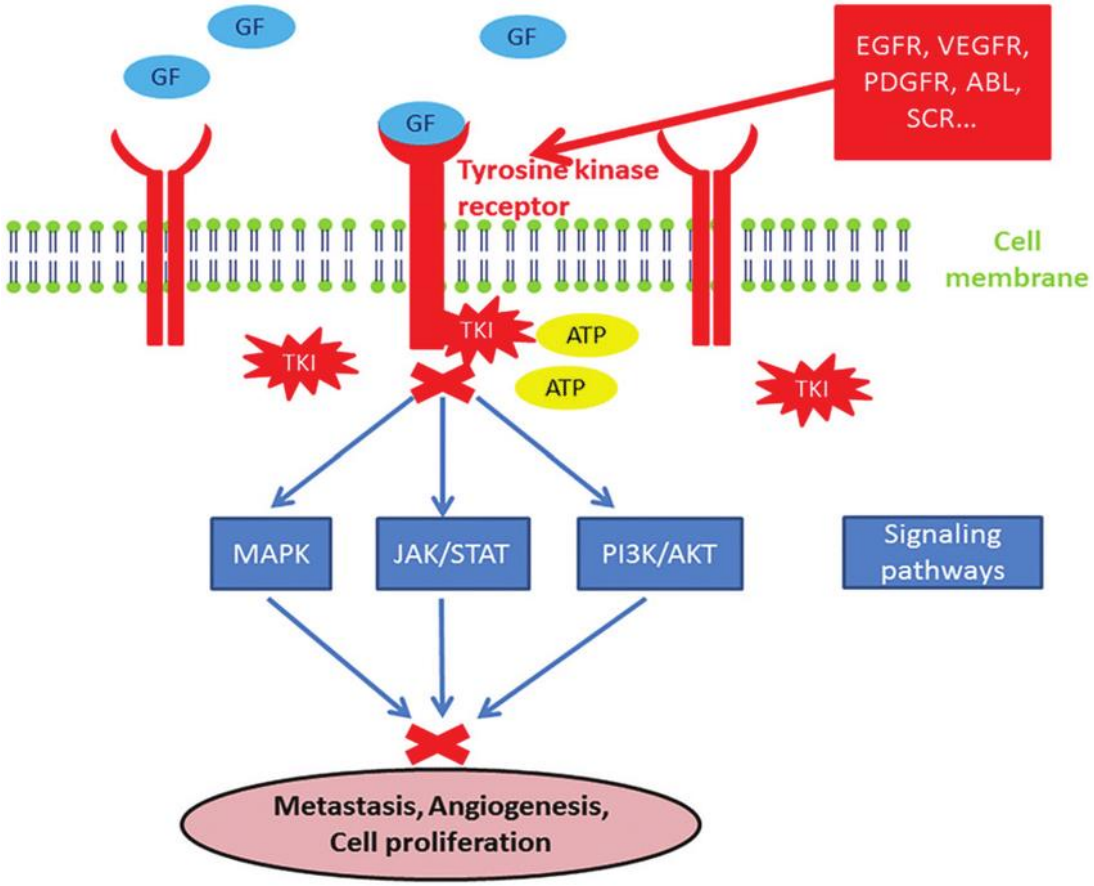

Figure 1-5 Mechanism of action of TKIs [94]
GF: growth factor; EGDR: Endothelial growth factor receptor; MAPK: mitogen-activated protein kinases; JAK/STAT: Janus kinases/Signal transducer and activation of transcription proteins, and PI3K/AKT: phosphoinositide-3-kinase/protein kinase B.

1.4.2 p53 pathway

The p53 tumor suppressor pathway was inactivated in nearly 87% of GBM patients, with CDKN2A changed in 49%, TP53 altered in 35%, MDM2 amplified in 14%, or MDM4 amplified in 7% of GBM patients [10]. Reactivation of p53 is an effective treatment strategy for GBM. On the one hand, it can stop the growth of GBM cells, and on the other side, it can inhibit the expression of MGMT in tumor cells to stop them from developing a resistance to TMZ [103]. Blocking the interaction between MDM2 and p53 is the most widely-used method for reactivating p53 [104, 105]. There are several ongoing clinical trials on MDM2 inhibitors in newly diagnosed GBM ([106], NCT03107780, and NCT05376800).

1.4.3 Rb pathway

The Rb pathway was altered in 77% of GBM patients due to CDKN2A alteration (52%), CDKN2B alteration (47%), CDK4 amplification (18%), or RB1 gene alterations (11%). Activating RB signaling with CDK inhibitors has been demonstrated to be a successful treatment option for cancer [107, 108]. Inhibitors of CDK4/6 with FDA approval have been used to treat metastatic breast cancers, including abemaciclib [109], palbociclib [110], and ribociclib [111]. Inhibiting CDK4/6 can reduce GBM cell proliferation and increase their susceptibility to TMZ by inducing apoptosis [112]. This offers a theoretical foundation for the clinical application of CDK4/6 inhibitors or a combination of TMZ in the management of relapsed GBM. Several clinical trials employing CDK4/6 inhibitors are currently being conducted on metastatic or recurrent GBM (NCT05538572, NCT04074785, and NCT03434262).

1.5 Current challenges for GBM treatment

Over the past few years, despite many efforts in new drug development, GBM treatment has not yielded the desired outcomes. The challenge comes not only from the heterogeneity of brain tumors [113, 114] but also from the presence of the BBB, which frequently hinders medications from reaching effective concentrations in the brain [115-117].

1.5.1 Tumor heterogeneity

High tumor heterogeneity is the main cause of GBM malignancy. Tumor heterogeneity typically refers to both intra-tumor heterogeneities, which refer to the difference of cells within a tumor and has a direct impact on treatment response and outcome, as well as inter-tumor heterogeneity, which describes differences in cells between tumors [118]. GBM heterogeneity is highly correlated with chemoradiotherapy tolerance and GBM relapse in GBM patients. The followings are the major contributing factors to the high heterogeneity of GBM.

Genetic heterogeneity GBM contains many different genetic mutations that may lead to the emergence of different cell types, resulting in tumor heterogeneity. Genes like EGFR, PDGFRα, PTEN, TP53, MDM2, or CDKN2A are frequently changed in GBM patients, which were mentioned in the previous section on the pathogenesis of GBM.

Glioma stem cells GSCs make up a small portion of tumor cells, but they have minimal differentiation and the capacity for self-regeneration [83]. GSCs can develop into several GBM subpopulations, such as drug-resistant variants, which adds to the heterogeneity of GBM and can potentially cause GBM relapse and tolerance to chemotherapy and radiotherapy [84]. There are numerous biomarkers for GSCs have been discovered, including CD133 (PROM-1) [119], CD44 [120], CD15 [121], CD70 (CD27L) [122], etc. These biomarkers can be used to characterize GSCs as well as act as therapeutic targets for GBM [123, 124]. For example, CD133 (+) - GSCs immunotherapy with CAR-expressing macrophages (CAR-MΦ) can reduce the recurrence rate of GBM after surgery by eliminating the CD133 (+) - GSCs left over after tumor resection [123].

Tumor microenvironment GBM microenvironment is not only made up of tumor cells. Numerous other cell types and the immune system in the brain collaborate to foster the growth of tumors, including endothelial cells, astrocytes, microglia, neurons, and immune cells. It has been demonstrated that these cell types encouraged the development, proliferation, and migration of tumors through different mechanisms [125, 126].

1.5.2 BBB and ABC transporters

BBB, which is made up of a continuous layer of endothelial cells, serves as a barrier between blood arteries and the brain [127] (**Figure 1-6**). The BBB controls the passage of different substances inside and outside the brain, shielding it from toxins and pathogens. However, this BBB feature also restricts the delivery of many drugs to the brain, which makes them ineffective for treating CNS illnesses.

Tight junction protein (TJ) and drug efflux transporters are the two main mechanisms by which the BBB can keep the drug out of the brain. TJ between endothelial cells creates a continuing intercellular barrier that prevents chemicals from moving between them paracellularly [128]. Drug efflux transporters, also known as ABC transporters, usually function as gatekeepers to pump drugs out of the brain [129]. Three primary BBB efflux transporters involve P-gp (MDR1), multidrug resistance-associated protein 1 (MRP1), and BCRP (ABCG2).

P-gp is a 170 kDa ATP-dependent efflux transmembrane protein that is encoded by the ABCB1 gene. It acts as an efflux transporter, which restricts the brain distribution of many drugs. This efflux process usually requires the consumption of ATP and results in a conformational change of P-gp [130, 131]. P-gp is highly expressed in a variety of organs, including the liver, kidneys, gastrointestinal tract, and BBB. P-gp is also discovered to be extensively expressed in a variety of cancer cells and is connected to the multi-drug resistance (MDR) mechanism, which results in treatment failure [132]. Inhibiting the transport function of P-gp can therefore increase the level of medicines that accumulate in cancer cells [133, 134]. It has been demonstrated that combining P-gp inhibitors with anti-cancer medications provides a method for overcoming MDR in cancer.

BCRP is a 72 kDa “half transporter” that is encoded by the ABCG2 gene. It functions as a homodimer or maybe a homo-oligomer to efflux various chemicals across membranes [135]. It is prevalent not only in the BBB but also in tissues like the liver, kidneys, and intestines. As a result, BCRP/ABCG2 can also affect the drug pharmacokinetics (PK) of substrate medicines by controlling intestinal absorption, renal elimination, and plasma clearance [136, 137]. Studies have revealed that BCRP/ABCG2 can work with P-gp to regulate drug transport across the BBB [138]. The double knockout or dual inhibition of both BCRP/ABCG2 and P-gp has been found to increase drug accumulation in the brain more than single inhibition or deletion of BCRP/ABCG2 or P-gp [139-141]. The combination of dual BCRP/ABCG2 and P-gp inhibitors with anticancer medications has been used as a strategy for the management of CNS disorders.

MRP1 is a 190 kDa efflux protein that is encoded by the ABCC1 gene. Unlike P-gp and BCRP/ABCG2 transport, the efflux function of MRP1 is often regulated by glutathione (GSH), with GSH co-transporting [142] or acting as a stimulus [143]. MRP1 was up-regulated in many cancer cells, contributing to MDR in cancer [144]. Inhibition of MRP1 can reverse MDR [145].

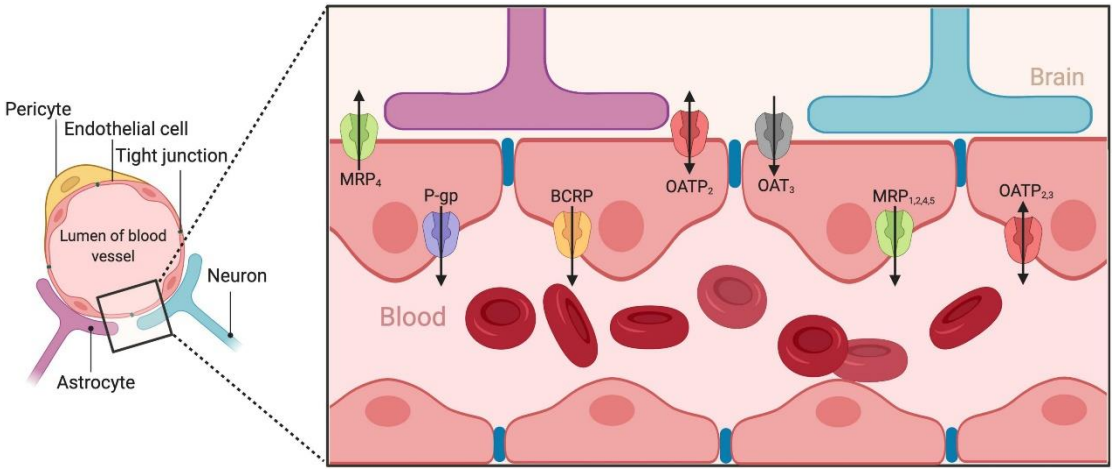

Figure 1-6 Diagram of the BBB and its transporters [146]

P-gp, BCRP/ABCG2, and MRP were efflux transporters, while OATP (organic anion transporting polypeptides) was an uptake transporter. OAT (organic anion transporter) transport smaller and hydrophilic organic anions.

1.6 Advances in the P-gp and/or BCRP/ABCG2 inhibitors

BBB has long been a challenge in the treatment of GBM. P-gp and BCRP/ABCG2, two clinically significant efflux transporters at the BBB, work in concert to prevent the entry of xenobiotics, such as pharmaceuticals, into the brain, which consequently affect their *in vivo* performance [147]. The combination of BCRP/ABCG2 and/or P-gp inhibitors with anticancer medications has been used as a strategy for the management of CNS disorders.

P-gp inhibitors have been used for a long time in conjunction with anticancer drugs to overcome MDR. Verapamil [148], quinine [149], amiodarone [150], and cyclosporine A [151] are the first generation of P-gp inhibitors that have been used with other anticancer medications to improve cancer treatment. However, the regulation of ABC membrane transporters was not the initial goal of these first-generation inhibitors [152-154]. Additionally, several of them serve as P-gp substrates [155, 156]. Thus, increasing the doses of these chemosensitizers to better inhibit the ABC transporters may have unintended consequences. The problems of the first generation of P-gp inhibitors were eliminated in the second generation, which was designed expressly to modulate ABC membrane transporters. R-Verapamil [157], VX-710 (biricodar) [158], or PSC-833 (valspodar) [159], which displayed lower toxicity and increased potency and selectivity. However, it has been discovered that the combination of these inhibitors and anti-cancer medications would cause drug-drug interactions (DDIs), altering the PK of anti-cancer medications *in vivo* and raising the risk of toxicity [160, 161]. Third-generation P-gp inhibitors were developed to address this issue. They included tariquidar [162], GF120918 (elacridar) [163], and zosuquidar [164], which had higher modulating activity on ABC transporters and minimal pharmacokinetic interactions. Clinical trials, however, have not been able to demonstrate that cancer medications improve treatment with the use of third-generation P-gp inhibitors, and some even revealed harmful effects. In addition, more studies have revealed that malignant tumors co-express several ABC transporters, which coordinate the transport of substrate in these cancers [165]. BBB was also discovered to co-express P-gp and BCRP/ABCG2 [138]. Based on this, increasing attention has been given to discover safe and effective natural compounds [166-168] or inhibitors with dual selectivity for P–gp and

BCRP/ABCG2 [169-171].

Previous research has shown that natural flavonoids in fruits and vegetables can decrease ABC transporters' ability to transport substances [172]. Since the ABC membrane transporter functions as a homodimer or homotetramer, our team investigated if a flavonoid dimer made up of two flavonoid monomers would have a higher binding affinity for the ABC transporter than a single flavonoid. Prior studies from our lab demonstrated that polyethylene glycol (PEG)-linked synthetic flavonoid homo dimers can reverse P-gp- and MRP1-mediated drug resistance in cancer cell lines [173-175]. Recently, we have developed a new library of synthetic flavonoid heterodimers based on “Click Chemistry” to discover medications that suppress both P-gp and BCRP/ABCG2. Using “Click Chemistry”, two molecular fragments can be joined together fast and effectively under benign reaction circumstances [176]. There is currently a pharmacological library with up to 300 different flavonoid dimers, and many secure and successful P-gp and/or BCRP/ABCG2 inhibitors have been identified [177, 178].

1.7 Objectives

From a library of 300 flavonoid dimers, **Ac12Az9** was selected as a strong, dual-selective inhibitor of BCRP/ABCG2 and P-gp [178]. This study further investigated the inhibition of **Ac12Az9** on both BCRP/ABCG2 and P-gp at the BBB and demonstrated that it was effective in potentiating sorafenib in treating GBM. The following elements were included in the experimental content:

1. To investigate the effect of **Ac12Az9** on the BCRP/ABCG2- or P-gp-mediated efflux and transepithelial transport of sorafenib in MDCKII-GFP-BCRP or MDCKII-P-gp cells.
2. To explore the effect of **Ac12Az9** on the PK and brain accumulation of sorafenib as well as the toxicity of this combination in BALB/c mice.
3. To create PDX models for orthotopic TMZ-sensitive or -resistant GBM to evaluate the effectiveness of **Ac12Az9** and sorafenib.
4. To identify the *in vivo* metabolite of **Ac12Az9** and modify the **Ac12Az9** structure to discover more stable, potent, and safe BCRP/ABCG2 inhibitors.
5. To study the potential of combining **Ac12Az9** with other anticancer medications in the treatment of GBM by examining its effects on the PK and brain accumulation of the Wee1 inhibitor AZD1775.

Chapter 2 Methodology

2.1 Chemicals and reagents

Sorafenib p-toluenesulfonate salt (≥ 99%) was purchased from LC Laboratories (the United States). Paclitaxel (PTX, > 98%) was purchased from Wuhan Hezhong Biochemical Manufacture Co, Ltd, Wuhan, China. Topotecan hydrochloride (TPT, 98.91%) was purchased from AbMole BioScience. Temozolomide (TMZ, > 98%) was obtained from Aladdin. Elacridar (GF120918, ≥ 99%) and regorafenib (≥ 99%) were purchased from Bio-Station Limited, Hong Kong. The synthesis of **Ac12Az9** (FD 12-9, > 98%) and **Ac3Az11** (> 98%) has been reported [178]. **Ac12Az9** derivatives, including **Ac12Az9** metabolite **M1** (84%), **Ac12Az9**-methoxy (**D1**, 95%), **Ac12Az9-methoxymethyl** (**D2**, 94%), **Ac12Az9-methyl amide** (**D3**, 91%), **Ac12Az9-trifluoromethoxy** (**D4**, 92%), **Ac12Az9-ethyl** (**D5**, 95%), **Ac12Az9-tertiary butyl** (**D6**, 94%), **Ac12Az9-chlorine** (**D7**, 96%), **Ac12Az9-fluorine** (**D8**, 93%), **Ac12Az9-para-methoxy** (**D9**, 86%), **Ac12Az9-CO_2CD_3** (**D10**, 97%), and **Ac12Az9-CD_3** (**D11**, 95%), were synthesized by Dr. Ma Cong's group (Hong Kong Polytechnic University, Hong Kong, SAR).

N-Methyl-2-pyrrolidone (NMP), Cremophor EL (CrEL), and TWEEN® 80 viscous liquid were purchased from Tin Hang Technology Limited, Hong Kong. The organic solvent, including dimethyl sulfoxide (DMSO), acetonitrile (ACN, HPLC grade,) and formic acid, were purchased from Sigma-Aldrich.

Dulbecco's Modified Eagle Medium (DMEM), Roswell Park Memorial Institute (RPMI) 1640 Medium, Minimum Essential Medium α (MEM-α), Opti-MEM™ I Reduced Serum Medium, trypsin/EDTA acid and penicillin/streptomycin (P/S) were purchased from Gibco. Fetal bovine serum (FBS) was obtained from HyClone. (3-(4,5-dimethylthiazol-2-yl)-5-(3-carboxymethoxyphenyl)-2-(4-sulfophenyl)-2H-tetrazolium inner salt)/phenazine methosulfate (MTS/PMS) was purchased from Promega. Lipofectamine™ 3000, DNA-midi™GT Plasmid DNA Purification Kit (iNtRON), and Hygromycin B were obtained

from ThermoFisher. The VivoGlo™ luciferin (*In Vivo* Grade) was purchased from Promega. Ketamine 10% and xylazine 2% were from Alfasan Diergeneesmiddelen B.V. All the colorimetric detection kits for plasma alanine transaminase (ALT), aspartate transaminase (AST), creatinine (CRE), and urea nitrogen (BUN) were purchased from Nanjing JianCheng Bioengineering Institute.

ACQUITY UPLC BEH C18 column (2.1 x 5 mm, 1.7 μm) and BEH C18 VanGuard pre-column (1.7 μm) were purchased from Waters. The sample inserts, vials, and caps used in ultra high-performance liquid chromatography coupled with triple quadrupole mass spectrometry (UPLC-ESI-QqQ-MS/MS, UPLC-MS/MS) were purchased from Tegent Technology (Hong Kong).

2.2 *In vitro* studies

2.2.1 Cell lines

The human breast cancer cell lines MDA435/LCC6 and MDA435/LCC6MDR were kindly provided by Dr. Robert Clarke (Georgetown University, United States). HEK293/pcDNA3.1 (empty vector-transfected), HEK293/R2 (BCRP/ABCG2-transfected) S1, S1M180 mitoxantrone selected, and MCF7-MX100 mitoxantrone selected cell lines were kindly provided by Dr. Kenneth To (The Chinese University of Hong Kong, Hong Kong). MCF7 was kindly provided by Prof. Thomas Leung (The Hong Kong Polytechnic University, Hong Kong). The MDCKII-WT and MDCKII-P-gp cells were generously provided by Prof. Piet Borst (the Netherlands Cancer Institute, Netherlands). MDCKII-GFP-BCRP was kindly provided by Dr. Laszlo Homolya from Semmelweis University (Hungary). A high expression level of P-gp or BCRP/ABCG2 in cells mentioned above was confirmed using a western blot (**Figure 2-1**). Human GBM cell line-U87MG-RedFluc was purchased from PerkinElmer. The frozen GBM PDX tumor tissues (G22 and G28) were kindly provided by Prof. Jann N. Sarkaria, M.D. from Mayo Clinic (Rochester, Minnesota, USA) [179].

A

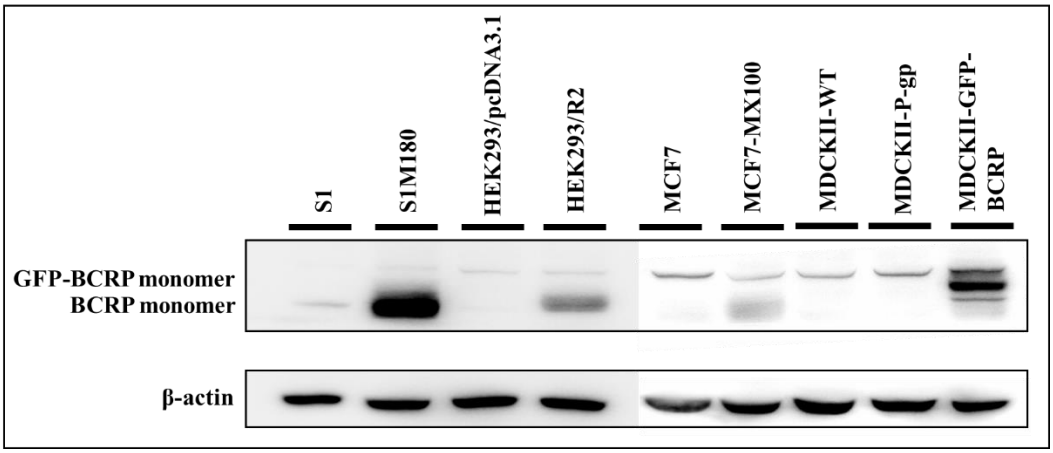

B

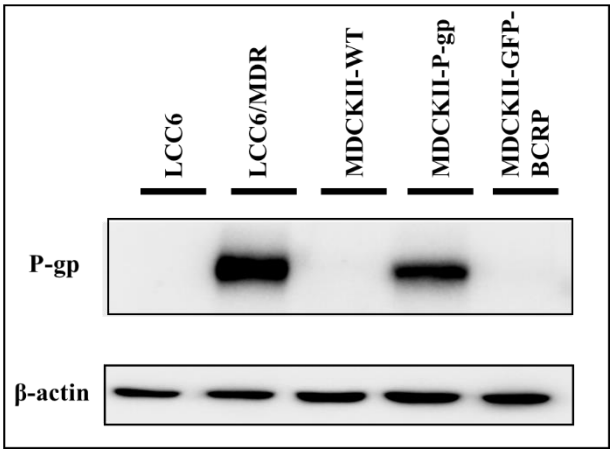

Figure 2-1 Characterization of BCRP/ABCG2 and P-gp in different cell lines
(A) Characterization of BCRP/ABCG2 in S1M180, HEK293/R2, and MDCKII-GFP-BCRP cells; (B) Characterization of P-gp in MDCKII-P-gp and LCC6MDR cells.

2.2.2 Cell culture

The cell lines were grown in the complete medium (DMEM for LCC6, LCC6MDR, HEK293FT, MDCKII-WT, MDCKII-GFP-BCRP, and MDCKII-P-gp cells; RPMI 1640 for S1, S1M180, HEK293/pcDNA3.1, HEK293/R2, MCF7, and MCF7-MX100 cells; MEM-α for U87MG-RedFluc cells) containing 10% FBS and 1% P/S (100 U/mL penicillin and 100 μg/mL of streptomycin). Short-term explant cultures from the PDX xenograft lines (G22 and G28) were established and grown in DMEM medium with 10% FBS and 1% P/S [179]. Besides, for each passage of HEK293/R2 cells, 1 mg/mL G418 was added to the

culture for selection. All the cells were kept at 37°C in a cell incubator with 5% CO_2.

2.2.3 Cell proliferation assay

A total of 4500 or 6500 cells from the following cell types were seeded into 96-well plates, including S1M180, LCC6MDR, HEK293/R2, MCF7-MX100, U87MG-RedFluc, PDX G22, G22-FLuc, G28, G28-FLuc, or TMZ-selected G28-FLuc cells, respectively. A series of concentrations of anticancer drugs, including PTX, TPT, TMZ, or sorafenib, were added into wells, respectively, with either no modulators or different modulators dosages (modulators: **Ac12Az9**, **Ac12Az9** derivatives, or GF120918). TPT concentration ranges in HEK293/R2 cells were 0, 3, 8, 25, 74, 222, 667, and 2000 nM, while in MCF7-MX100 cells, they were 0, 0.08, 0.25, 0.74, 2.22, 6.67, and 20 μM. The ranges of PTX concentration in LCC6MDR cells were 0, 1.6, 5, 15, 44, 133, and 400 nM. Sorafenib concentrations in U87MG-RedFluc and PDX GBM cells were 0, 0.027, 0.082, 0.25, 0.74, 2.2, 6.7, and 20 μM, while TMZ concentrations were 0, 3.4, 10.3, 30.9, 92.6, 277.8, 833.3, and 2500 μM. For BCRP/ABCG2-mediated drug resistance, the concentration ranges of the modulators were 0, 1.6, 8, 40, 200, and 1000 nM; for P-gp-mediated drug resistance, the concentration ranges were 0, 125, 250, 500, 1000, and 2000 nM. The final volume in each well of 96-well plates was 200 μL. After 4 days of incubation at 37°C with 5% CO_2., the cell viability was measured using the CellTiter 96 AQueous Assay (Promega). A 20:1 mixture of MTS (2 mg/mL) and PMS (0.92 mg/mL) was added to the medium. Each well received a 45 μL aliquot of the freshly made MTS/PMS combination and the plates were then incubated at 37°C for 1-2 hrs. The optical absorbance of the plate was then measured at 490 nm using a microplate absorbance reader (Bio-Rad). Each experiment was run in triplicate and at least twice. The data was provided as mean ± standard deviation (SD). Half maximal inhibitory concentration (IC_{50}) is a measure of the efficiency of an anticancer drug to inhibit cell viability by 50%. Half maximal effective concentration (EC_{50}) is a measure of the potency of modulators to reduce the IC_{50} of anticancer drugs by 50%. PRISM software was used to calculate the IC_{50} of several anticancer medications and the EC_{50} of various modulators.

2.2.4 Primary cell culturing

The frozen GBM PDX tumor tissues (G22 and G28) were kindly provided by the Mayo Clinic [179]. These samples were serially maintained between the BALB/c nude mice for two to three passages after being subcutaneously implanted into the nude mice. The G22 and G28 flank GBM tumor tissues were taken and finely minced. The tumor fragments were mixed with Trypsin-EDTA (0.25%) solution and co-incubated at 4°C for 6-16 hrs. The tumor suspension was added to an equal volume of FBS-free medium, and the mixture was filtered through a 70 μm cell strainer. The filtrate was centrifuged at 1,200 rpm for 5 mins. The red blood cells were lysed using 5 mL of a solution made of 0.64% NH_4Cl and 0.1 mM EDTA after the supernatant was removed. After that, 5 mL of FBS-free media was added to wash the cells three times until the supernatant was clear. After being resuspended in DMEM medium with 2.5% FBS and 1% P/S, the cells were transferred to a cell culture dish. After the cells had adhered to the dish, the low serum culture medium was changed to one with 10% FBS and 1% P/S.

2.2.5 Lentiviral production using Lipofectamine™ 3000 Reagent

The pCDH-CMV-MCS-EF1α-Hygro Cloning and Expression Lentivector expressing firefly luciferase (FLuc) was kindly provided by Prof. Terence Lee at Hong Kong Polytechnic University. The vector was amplified by DH-10B transformation and extracted by DNA-midiTMGT Plasmid DNA Purification Kit (iNtRON). HEK293FT cells were co-transfected with the FLuc lentivector and lentiviral packaging mix using Lipofectamine 3000 reagent. First, 2.5-3.0 x 10^6 HEK293FT cells were seeded in a 10 cm dish with only 10% FBS-containing DMEM medium. The following day, there would be a confluence of about 80%. The old medium was changed to 10 mL Opti-MEM™ I Medium two hrs before transfection. Then, two tubes-Tube A and Tube B-were made. 41 μL of Lipofectamine 3000 Transfection Reagent in Tube A was diluted with 1.5 mL of Opti-MEM™ I Medium. In Tube B, the Lentiviral Packaging Mix (10.5 μg pLP1, 10.5 μg pLP2, and 9.0 μg pVSVG) and FLuc Lentivector (10.0 μg) were combined with 35 μL P3000 Enhancer Reagent in 1.5 mL Opti-MEM™ I Medium. After that, Tubes A and B were thoroughly mixed and incubated for 15 mins at room temperature. The HEK293FT cells received a further

addition of the complexes (3 mL) for a final volume of 10 mL. The cell supernatant was harvested 24 hrs after transfection, and cellular debris was removed by centrifuging at room temperature for 10 mins at 2,000 rpm. The clarified lentiviral supernatant can be aliquoted and stored at -80°C for further use.

2.2.6 Insertion of GBM PDX with the FLuc gene

80,000 cells of G22 or G28 were seeded onto 6-well culture plates one day before lentivirus infection. The following day, there would be a confluence of about 80%. Following that, 1 mL of lentiviral supernatant (**Methodology 2.2.5**) was added to transfect the cells. The proper amount of polybrene (1 mg/mL) was simultaneously added to achieve a final concentration of 8 μg/mL, which can significantly improve the transfection efficiency by allowing lentivirus adsorption by cells. Fresh DMEM with 10% FBS was added 16 hrs after the lentiviral infection. After 48 hrs of transfection, the proper quantity of hygromycin B (50 mg/mL) was added to reach the final concentration of 400 μg/mL, which was utilized to screen the cells with successful transfection. The selection medium was changed every 3 days until the cells in the mock well were entirely dead. Finally, the transfected cells (G22-FLuc and G28-FLuc) that survived in Hygromycin B selection were collected to assess cellular luciferase activity.

2.2.7 Measurement of FLuc activity

PDX G22, G22-FLuc, G28, and G28-FLuc cells were seeded in a 24-well plate at a density gradient (3.12×10^4, 6.25×10^4, 1.25×10^5, 2.5×10^5, 5.0×10^5, and 1.0×10^6 cells/well), respectively. Each well received 10 μL of luciferin (D-Luciferin, 20 mg/mL) for a final concentration of 200 μg/mL. After 1 min of incubation protected from light, the 24-well plate was placed on the determination station, and the cellular luciferase activity was assessed using IVIS® *in vivo* imaging system (IVIS Lumina III, PerkinElmer). The imaging conditions were set at “Luminescent”, “Auto” exposure time, and “Medium” binning. The bioluminescent signal on the image of the 24-well plate was quantified in photons per second per steradian per square cm (photons/sec/sr/cm^2).

2.2.8 Drug accumulation assay

1 x 10^6 cells of MDCKII-WT, MDCKII-GFP-BCRP, or MDCKII-P-gp cells were collected in 1.5 mL Eppendorf tubes and treated with different anticancer drugs (2.5 μM of sorafenib or 1 μM of AZD1775) with or without modulators (1 μM **Ac12Az9**, **Ac12Az9** derivatives, or GF120918). The tubes were then placed at 37℃ with shaking at 250 rpm for 1 hr. 0.1% DMSO solution was used as a negative control. The cells were collected by centrifugation (1,500 rpm, 3 mins) followed by washing with ice-cold phosphate buffer saline (PBS). The cell pellets were re-suspended in 100 μL Milli-Q water and lysed through three freeze-thaw cycles (the tubes could be thawed quickly at 37℃ in a water bath and frozen again in liquid nitrogen). The intracellular drug levels were determined by UPLC-MS/MS (AcQuity, Waters).

2.2.9 Drug efflux assay

1 x 10^6 cells of MDCKII-WT, MDCKII-GFP-BCRP, or MDCKII-P-gp cells were preincubated with different anticancer drugs (2.5 μM of sorafenib or 1 μM of AZD1775) for 1 hr at 37°C with shaking at 250 rpm. After that, the cells were spun down (1,500 rpm, 3 mins) and washed with cold PBS. The cells were treated further with or without **Ac12Az9** (1 μM). At 0, 15, and 30 mins of incubation at 37℃, the cells were harvested by centrifugation (1,500 rpm, 3 mins) followed by washing with ice-cold PBS. The cell pellets were then re-suspended in 100 μL Milli-Q water and lysed through three freeze-thaw cycles (the tubes could be thawed quickly at 37℃ in a water bath and frozen again in liquid nitrogen). The level of intracellular sorafenib or AZD1775 was measured by UPLC-MS/MS. The % of drug reduction was calculated = [(drug level at final time point/drug level at 0 min) * 100%].

2.2.10 Western blot analysis

1 x 10^6 cells of S1, S1M180, HEK293/pcDNA3.1, HEK293/R2, MDCKII-WT, MDCKII-GFP-BCRP, MDCKII-P-gp, LCC6, or LCC6MDR were washed with PBS and lysed for 10 mins in 100 uL lysis buffer (RIPA Lysis Buffer: 25 mM Tris-HCl pH7.5, 150 mM NaCl, 1% NP-40, 1mM EDTA pH 8.0. Add fresh: 1 mM PMSF, and 1 x Protease Inhibitor). The

cell lysates were centrifuged at 14,000 rpm for 30 mins at 4℃. The supernatant was collected, and the protein concentration was measured by Bio-Rad Bradford reagent. The samples were mixed with 6X Protein Loading Buffer and stored at -80℃ for further use.

20 μg of protein was loaded into the gels for polyacrylamide gel electrophoresis. 5 μL of Protein Marker Ladder (PageRuler™ Prestained Protein Ladder, 10 to 180 kDa) was added into the gel electrophoresis for monitoring the progress of gel electrophoresis. Samples were further electroblotted from a protein gel onto the PVDF membrane following SDS-PAGE separation. The membrane was washed with Tris-buffered saline with 0.1% Tween® 20 Detergent (TBST) (10 mM Tris-HCl, pH 8.0, 150 mM NaCl, 0.05% Tween 20) and then blocked with 5% skimmed milk in TBST buffer for 1 hr on a shaking platform at room temperature. Then, the membranes were washed with TBST buffer, divided into two pieces at 70 kDa, and incubated with specific primary antibodies in TBST buffer overnight at 4 ℃. The primary antibody included: i. BCRP antibody (ABCG2 (BXP-21), a mouse monoclonal antibody, SANTA CRUZ BIOTECHNOLOGY, INC); ii. P-gp antibody (Mdr-1 (D-11), a mouse monoclonal antibody, Santa Cruz Biotechnology); iii. β-actin antibody (β-Actin (C4), a mouse monoclonal antibody, Santa Cruz Biotechnology). The membranes were incubated with a secondary antibody (m-IgGk BP-HRP, Santa Cruz Biotechnology) for 1 hr at room temperature, following three times of TBST wash for 10 mins each. The protein signal was detected using Chemiluminescent HRP Substrates (Immobilon) and Azure C600 (Azure Biosystems, Inc.).

2.2.11 Chemical stability of flavonoid dimers in plasma

5 μL of test compounds (**Ac12Az9** and its derivatives, 20 μg/mL in DMSO) were incubated with 100 μL of freshly prepared plasma with or without 5 mM phenylmethylsulfonyl fluoride (PMSF) for various times (0, 15, 30, 60, 120, 240, and 360 min) at 37℃. The reaction was terminated by adding a 3-fold volume of ACN. The compounds remaining in plasma were quantified by UPLC-MS/MS. The percentage of test compounds left at each time point relative to the 0-min sample was reported.

2.2.12 Analytical methods for biological samples by UPLC-ESI-QqQ-MS/MS

Agilent 6460 Liquid Chromatography-Electrospray Ionization Triple Quadrupole Mass Spectrometer (UPLC-ESI-QqQ-MS/MS, UPLC-MS/MS) was used in biological sample analysis in *in vitro* and *in vivo* studies. The chromatographic separation was conducted on Agilent 6460 Ultra Performance Liquid Chromatography (UPLC) equipped with ACQUITY UPLC BEH C18 column (2.1 x 5 mm, 1.7 μm, Waters) and BEH C18 pre-column (1.7 μm, Waters). The mobile phases consisted of (A) Milli-Q water (0.1% formic acid, v/v) and (B) ACN (0.1% formic acid, v/v).

The following gradient elution procedure was employed during separation: equilibration: 0-1 mins 10% B; elution gradient: 1-6 mins 10-95% B; regeneration: 6-8 mins 95% B then 8-8.5 mins, 95-10% B; and re-equilibration: 8.5-12 min 10% B (**Table 2-1**). The flow rate was kept at 0.3 mL/min. The column temperature was set at 26℃. The temperature of the autosampler was set at 4℃. 5 μL of the sample was injected for analysis.

Table 2-1 Gradient elution program in UPLC-MS/MS

Time (min)	Flow rate (mL/min)	Milli-Q water (0.1% formic acid, %)	ACN (0.1% formic acid, %)
0	0.3	90	10
1		90	10
6		5	95
8		5	95
8.5		90	10
12		90	10

The UPLC system was coupled online to electrospray ionization (ESI) triple quadrupole mass spectrometers (MS). Positive ion mode was used to detect the analyte. The MS parameters included a capillary voltage of 3.5 kV, sheath gas temperature of 300℃, drying gas of 8 L/min, and sheath gas flow of 11 L/min. The ion pairs for several analytes were monitored in multiple reaction monitoring (MRM) mode with optimal fragmentor voltage and collision voltage (**Table 2-2)**. The dwelling time for each MRM channel was 100 milliseconds.

Table 2-2 Retention time, ion pairs, and MS detection parameters for each analyte

Analyte	Retention time (min)	Molecular ion	Precursor ion (m/z)	Product ion (m/z)	Fragmentor (V)	Collision energy (eV)
sorafenib	5.3	$[M+H]^+$	465.1	252.1*, 270.1	110	30, 20
regorafenib (IS)	5.5	$[M+H]^+$	483.1	270.1*, 288.1	100	35, 20
AZD1775	3.2	$[M+H]^+$	501.2	483.2*, 442.2	80	25, 25
Ac12Az9	5.7	$[M+H]^+$	878.4	492.3*, 640.2	75	35, 30
M1	5.3	$[M+H]^+$	864.3	492.2*, 626.2	80	35, 30
D1	5.8	$[M+H]^+$	850.3	492.2*, 612.3	100	35, 30
D2	5.7	$[M+H]^+$	864. 2	492.1*, 626.3	100	40, 35
D3	5.1	$[M+H]^+$	877.2	492.2*, 639.2	100	40, 35
D4	6.2	$[M+H]^+$	904.3	492.2*, 639.2	100	40, 30
D5	5.9	$[M+H]^+$	892.3	492.2*, 654.3	170	35, 38
D6	6.3	$[M+H]^+$	920.2	492.2*, 626.3	140	40, 40
D7	6.1	$[M+H]^+$	912.2	492.2*, 674.3	130	40, 35
D8	5.9	$[M+H]^+$	896.4	492.2*, 658.2	100	40, 35
D9	5.9	$[M+H]^+$	908.2	492.2*, 179.1	100	40, 40
D10	5.7	$[M+H]^+$	881.3	492.3*, 643.2	100	35, 38
D11	6.0	$[M+H]^+$	853.3	492.3*, 615.3	100	40, 30
GF120918	4.1	$[M+H]^+$	564.4	252.1*, 400.2	130	40, 30
Ac3Az11 (IS)	5.3	$[M+H]^+$	674.2	418.2*	160	28

*: the product ion of analyte selected for quantification.
IS: internal standard. Regorafenib was the internal standard of sorafenib. **Ac3Az11** was the internal standard of **Ac12Az9** and its derivatives.

This UPLC-MS/MS method was validated with a wide range of linearity, satisfactory precision and accuracy, high extraction efficiency, and low matrix effect (**Table 2-3, Table 2-4)**. The intra-day and inter-day precision were shown as relative standard deviation (RSD). The intra-day and inter-day precision of sorafenib and **Ac12Az9** were less than 11.29%, while the accuracy ranged from 89.25%-107.03%. The mean extraction recoveries for sorafenib and **Ac12Az9** in murine plasma and brain homogenates ranged from 88.46%-110.72%, which were consistent over three quality control levels. The mean matrix effects varied from 93.21% to 115.83%, showing that there was no ion suppressing or enhancing effect on the detection of sorafenib and **Ac12Az9** in the biological samples.

Table 2-3 Precision and accuracy for sorafenib and Ac12Az9 in murine plasma or brain homogenate (n = 5)

Sample	Analytes	Quality controls (μg/mL)	Accuracy (%) (Mean ± SD)	Intra-day precision (RSD, %)	Inter-day precision (RSD, %)
Plasma	sorafenib	0.14	103.10 ± 2.55	2.47	4.13
		1.38	97.78 ± 2.54	2.59	4.28
		24.75	106.61 ± 10.6	9.99	10.02
	Ac12Az9	0.01	93.91 ± 2.75	2.93	6.34
		0.14	89.34 ± 3.31	3.70	5.61
		2.48	89.25 ± 4.43	4.96	3.88
Brain	sorafenib	0.03	114.30 ± 1.90	1.67	5.31
		0.28	91.27 ± 2.83	3.10	2.04
		2.2	107.03 ± 5.19	4.85	6.88
	Ac12Az9	0.03	102.92 ± 7.34	7.13	11.29
		0.28	89.50 ± 3.14	3.51	4.82
		2.2	93.77 ± 2.85	3.04	6.03

Table 2-4 Extraction recovery and matrix effect for sorafenib and Ac12Az9 in murine plasma or brain homogenate (n = 5)

Sample	Analyte	Quality controls (μg/mL)	Extraction recovery (%)	Matrix Effect (%)
Plasma	Sorafenib	0.14	103.84 ± 4.53	106.09 ± 2.79
		1.38	105.98 ± 7.78	111.01 ± 1.12
		24.75	99.32 ± 2.77	109.58 ± 5.47
	Ac12Az9	0.01	110.72 ± 4.81	108.46 ± 1.57
		0.14	103.27 ± 8.79	112.98 ± 4.52
		2.48	97.04 ± 4.12	115.83 ± 5.38
	Regorafenib (IS)	1.37	104.30 ± 6.16	110.44 ± 2.53
	Ac3Az11 (IS)	0.14	99.27 ± 5.00	109.10 ± 6.49
Brain	Sorafenib	0.03	88.46 ± 4.92	104.36 ± 6.79
		0.28	105.98 ± 4.86	96.46 ± 2.29
		2.2	101.43 ± 3.44	105.61 ± 7.57
	Ac12Az9	0.03	103.51 ± 7.01	104.36 ± 6.79
		0.28	102.60 ± 3.67	94.68 ± 3.35
		2.2	104.21 ± 4.45	93.21 ± 5.81
	Regorafenib (IS)	0.27	91.76 ± 9.21	101.47 ± 6.8
	Ac3Az11 (IS)	0.27	106.65 ± 5.42	96.47 ± 4.37

2.2.13 Pretreatment of biological samples

Cell lysate, murine plasma, tissue homogenates, or tumor homogenates were thawed at room temperature on the day of analysis. 5 μL of IS (regorafenib or **Ac3Az11**) and 100 μL of a biological sample were added in a 1.5 mL Eppendorf tube, respectively. After a brief period of vortex mixing, 300 μL of ACN was added for protein precipitation. After a 2-min vortex mixing period, samples were centrifuged at 12,000 rpm for 10 mins. The supernatant was then filtered using a 0.22 μm nylon filter, transferred to a glass vial with a micro insert, and analyzed using UPLC-MS/MS.

2.3 *In vivo* studies

2.3.1 PK studies of sorafenib, AZD1775, or modulators in mice

All animal research was carried out in line with the Cap 340 Animal License of the Department of Health in Hong Kong and was authorized by the Animal Subjects Ethics Sub-committee of The Hong Kong Polytechnic University.

Sorafenib (2.5 mg/mL) was freshly prepared using NMP, CrEL, and 5% Tween-80 (5: 5: 90). AZD1775 were dissolved in a formulation (NMP: CrEL: 5% Tween-80 = 10: 10: 80). Modulators (**Ac12Az9**, its derivatives or GF120918, 1 or 2 mg/mL), were dissolved in a formulation (NMP: CrEL: 5% Tween-80 = 10: 10: 80). The solvent must be added in sequence, and another solvent should only be added once the compound has been thoroughly dissolved or combined.

BALB/c mice (6-8 weeks) fasted for 15 hrs before treatment. Sorafenib or AZD1775 was administered to mice (n = 2-3) via oral gavage (50 mg/kg, P.O.), respectively. Modulators (**Ac12Az9**, its derivatives, or GF120918) were given intravenously (I.V.) at doses of 10 or 20 mg/kg. The combination dosing mode and interval dosing times were described in detail in different sections. Blood and tissue samples were taken at various intervals after administration (refer to the specific section for sampling time points). Blood samples in the lithium heparin tube were centrifuged at 12,000 rpm for 10 mins at 4℃ to obtain plasma. The tissues were separated, weighed, and homogenized after adding a 3-fold (w/v) volume of Milli-Q water. The concentration of sorafenib, AZD1775, or modulators was determined by the established UPLC-MS/MS.

2.3.2 Toxicity studies

The toxicity of repeated injections of sorafenib (50 mg/kg, P.O.) with or without **Ac12Az9** (20 mg/kg) was assessed in BALB/c mice. Seven groups (n = 4) of BALB/c mice (6-8 weeks) were treated every other day for nine times (q.o.d. x 9). They included: (1) untreated group, (2) sorafenib solvent (P.O.), (3) **Ac12Az9** solvent (I.V.), (4) sorafenib solvent (P.O.)

+ **Ac12Az9** solvent (I.V.), (5) sorafenib (50 mg/kg, P.O.) + **Ac12Az9** solvent (I.V.), (6) sorafenib solvent (P.O.) + **Ac12Az9** (20 mg/kg, I.V.), (7) sorafenib (50 mg/kg, P.O.) + **Ac12Az9** (20 mg/kg, I.V.). The body weight of mice was monitored during or after the treatment. If a mouse's weight drops by more than 15%, it will be considered a result of treatment-related toxicity and euthanized [180]. After completing the administration course, mice were anesthetized with ketamine (100 mg/kg) and xylazine (10 mg/kg) intraperitoneally (I.P.), and blood was then drawn from the posterior vena cava and collected in the lithium heparin tube. Blood samples were centrifuged at 4,000 rpm for 10 mins at 4℃ to obtain plasma. The hepatotoxicity and nephrotoxicity of different treatments were evaluated by measuring plasma ALT, AST, CRE, and BUN.

2.3.3 Intracranial implantation of GBM cells

GBM cells with luciferase marker were resuspended in sterile PBS at a density of 1 x 10^5 cells per μL. A total of 3 x 10^5 GBM cells was implanted intracranially in BALB/c nude mice (6-8 weeks). First, the nude mice were anesthetized by I.P. injection of ketamine (100 mg/kg) and xylazine (10 mg/kg) and placed in a stereotaxic apparatus (RWD Life Science Co., Ltd). After disinfecting the skin with ethanol, a sterile scalpel was used to make a 1 cm midline incision that ran from just below the eyes to the level of the ears. Then, a burr hole was produced 1 mm anterior and 2 mm laterally to the skull's bregma using an electric drill with a 1 mm diameter. An injection of 3 μL of cells was made into the brain through the burr hole to a depth of 3 mm using a 10 μL Hamilton syringe with a 26-G needle. The injection rate was 1 μL per min over 3 mins. To lessen the reflux of cancer cells, the needle remained in the brain for an additional min. After intracranial implantation, the wound of mice was sutured with a 4-0 polypropylene absorbable suture. After cell inoculation, the mice were returned to cages and observed until they were fully awake.

2.3.4 Subcutaneous implantation of HEK293/R2 cells

HEK293/R2 cells were resuspended in matrigel at a density of 1 x 10^7 cells per μL. A total of 1 x 10^6 HEK293/R2 cells in a volume of 100 μL were implanted subcutaneously in BALB/c nude mice (6-8 weeks). Animals with tumors of 100-150 mm^3 in size were randomly assigned to different treatment groups. Test compound dosing followed the

treatment schedule.

2.3.5 Bioluminescence imaging (BLI) of intracranial tumor growth

The size of the intracranial tumors was measured by IVIS. Mice were administered a 150 mg/kg dosage of D-luciferin (I.P.) seven to twelve days after cell implantation, following isopropanol inhalation anesthesia. Mice were then moved to the IVIS imaging chamber and positioned on the imaging station once they had complete anesthesia. The luminescence signal peaked at 25 mins after injection of D-luciferin. At that point, the image was acquired, and the region of signal on the image was encircled and measured as a unit of photon per s/cm^2 per steradian (sr). The same range of color scales were used to display each image for comparison.

2.3.6 Efficacy studies on PDX G22-FLuc and G28-FLuc in BALB/c nude mice

Tumor-bearing nude mice (6-8 weeks) were randomly assigned to several groups (n = 3-4, or 7-9 mice per group). The specific grouping was described in the main context. Each treatment group received nine or ten injections (q.o.d). The bioluminescent imaging signal of each mouse was measured every few days by IVIS. Meanwhile, the body weight of mice was also monitored during and after the treatments. All the intracranial tumor-bearing nude mice were euthanized when they reached a moribund state.

2.3.7 TPT accumulation in HEK293/R2 tumor in BALB/c nude mice

The BALB/c nude mice implanted with subcutaneous HEK293/R2 tumors were treated with either (1) TPT (6 mg/kg, I.P.) or (2) TPT (6 mg/kg, I.P.) + **D6** (20 mg/kg, I.V.). **D6** (2 mg/mL) was dissolved in a formulation (NMP: CrEL: 5% Tween-80 = 10: 10: 80). TPT (1 mg/mL) was dissolved in Milli-Q water. The I.V. injection of **D6** was administered concurrently with the I.P. dose of TPT with no time in between. The tumor was taken out two hrs after administration, washed with PBS, weighed, and homogenized by adding Milli-Q water in a 1:3 ratio. The concentration of TPT was determined by UPLC-MS/MS.

2.4 Data analysis

For the PK study, a non-compartmental analysis of sorafenib, AZD1775, or different modulators was performed by PK Solutions 2.0.3 software (Ashland, OH44805, USA) to calculate the PK parameters. PK parameters were calculated based on the drug plasma/tissue concentration-time data, including maximum concentration (C_{max}), terminal elimination rate constant (k_{el}), half-life time ($t_{1/2}$), area under the curve from the first measurable time point to the last time points ($AUC_{0\text{-}t}$), or clearance rate (CL).

Statistical differences were calculated in GraphPad Prism. The student's t-test was used to compare the means between the two groups. The survival time was calculated using the Kaplan-Meier method, and a log-rank test was employed to determine the significance of the difference. A p-value < 0.05 was considered statistically significant.

Chapter 3 Dual inhibition of BCRP/ABCG2 and P-gp by a flavonoid dimer Ac12Az9 increases sorafenib accumulation *in vitro*

3.1 Introduction

GBM is the most common malignant brain glioma. Clinical standard of care (Stupp protocol) for patients with GBM includes maximum surgical removal of the brain tumor, RT, and chemotherapy with TMZ [181]. However, TMZ resistance is frequently observed when treating GBM clinically, especially in recurrent GBM patients. As the first-line drug in GBM treatment, TMZ is an oral alkylating agent which can damage DNA and destruct tumor cells. The damage induced by TMZ, however, can be reversed by DNA repair machinery, preventing cell death. Potential mechanisms of TMZ resistance include elevated expression of MGMT, MMR deficiency, BER, etc [19].

Despite many efforts in new drug development, GBM treatment has not yielded the desired outcomes. The challenge comes not only from the complexity of brain tumors [113, 114] but also from the presence of the BBB, which frequently hinders medications from reaching effective concentrations in the brain [115-117].

TKIs have been studied as an alternative anti-GBM agent in recent years. Sorafenib (BAY 43-9006, Navara, **Figure 3-1**) was one of them. It is FDA-approved for treating renal cell carcinoma (RCC) [182] and unresectable hepatocellular carcinoma (HCC) [95]. It is a multi-kinase inhibitor that inhibits angiogenesis and proliferation of tumor cells by targeting VEGF and PDGF receptors [183]. Additionally, numerous trials have shown its efficacy in treating a variety of malignancies, including breast cancer [184], colon cancer [185], non-small-cell lung cancers (NSCLC) [186], and GBM [187].

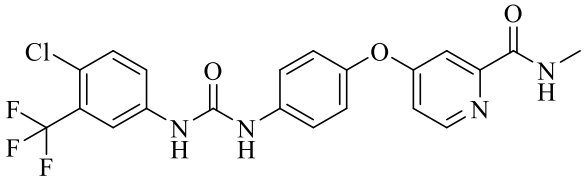

Sorafenib
Chemical Formula: $C_{21}H_{16}ClF_3N_4O_3$
Molecular Weight: 464.83

Figure 3-1 Chemical structure of sorafenib

Brain accumulation of sorafenib, however, is low with a brain-to-plasma ratio lower than 0.06 [188] due to the presence of P-gp and BCRP/ABCG2 on the endothelial cells lining the BBB [189, 190]. This may explain why sorafenib's Phase I/II clinical studies on GBM patients were unable to show any therapeutic benefit [188, 191].

BCRP/ABCG2 and P-gp at the BBB keep most xenobiotics away from the CNS by actively transporting them into blood [192]. These two transporters are working synergistically [193]. *Mdr1a/b (-/-)*, *Bcrp (-/-)*, and *Mdr1a/b (-/-)Bcrp1 (-/-)* mice displayed a 1.2-, 3.8-, and 9.7-fold increase in the brain-to-plasma ratio of sorafenib compared to wild type mice, respectively [140]. According to this finding, it may be possible to boost sorafenib levels in the brain by simultaneously inhibiting P-gp and BCRP/ABCG2.

We have previously reported a new library of 74 different synthetic flavonoid heterodimers based on "Click Chemistry" to discover novel, potent, and safe P-gp/BCRP (ABCG2) dual inhibitors [194]. Some of the most active flavonoid dimers were summarized in **Table 3-1**. Among them, **Ac12Az9** was the most potent dual inhibitor of both BCRP/ABCG2 and P-gp, with an EC_{50} of 0.9-1.4 nM for reversing BCRP/ABCG2-mediated TPT resistance in HEK293/R2 or MCF-MX100 cells, and 285 nM for reversing P-gp-mediated PTX resistance in LCC6MDR cells (**Table 3-1**). **Ac12Az9** is more selective for P-gp and BCRP/ABCG2 than verapamil or ko143, which only target one of these two transporters. **Ac12Az9** ($EC_{50,\ P\text{-}gp}$ = 285 nM or $EC_{50,\ BCRP/ABCG2}$ = 0.9 nM) had two times the P-gp inhibitory activity of verapamil ($EC_{50,\ P\text{-}gp}$ = 445.7 nM) and twelve times the BCRP/ABCG2 inhibitory activity of ko143 ($EC_{50,\ BCRP/ABCG2}$ = 11.4 nM). Additionally, **Ac12Az9** was

much less hazardous to normal L929 fibroblasts (IC_{50} > 100 M), when compared to ko143 (IC_{50} = 29.2 M) and verapamil (IC_{50} = 89.2 M). **Ac12Az9** was more effective in reversing BCRP/ABCG2-mediated TPT resistance than elacridar (GF120918), another dual P-gp/BCRP(ABCG2) selective inhibitor, with EC_{50} values of 0.9 nM of **Ac12Az9** versus 20 nM of GF120918 (**Table 3-1**). Taken together, **Ac12Az9** was a promising dual P-gp/BCRP (ABCG2) inhibitor.

This chapter investigated whether **Ac12Az9** can inhibit the BCRP/ABCG2- or P-gp-mediated efflux and transepithelial transport of sorafenib in MDCKII-GFP-BCRP or MDCKII-P-gp cells.

Table 3-1 Effects of flavonoid dimers on P-gp- or BCRP/ABCG2-modulating activity in different cell lines [194]

Modulators	IC_{50} (μM)	EC_{50} (nM) for reversing MDR		
	Cytotoxicity of modulators towards L929 cells	P-gp-mediated PTX resistance in LCC6MDR	BCRP/ABCG2-mediated TPT resistance in HEK293/R2	BCRP/ABCG2-mediated TPT resistance in MCF7-MX100
Ac12Az1	> 100	321.0 ± 43.8	51.5 ± 4.9	24.5 ± 12.0
Ac12Az2	> 50	360.0 ± 56.6	47.0 ± 19.8	18.0 ± 0.0
Ac12Az3	> 50	198.3 ± 7.6	32.8 ± 24.3	45.5 ± 44.5
Ac12Az4	> 100	325.0 ± 7.1	43.5 ± 4.2	30.5 ± 20.5
Ac12Az5	> 100	277.5 ± 81.3	35.0 ± 7.1	15.5 ± 3.5
Ac12Az7	> 100	264.0 ± 79.2	43.0 ± 4.2	17.5 ± 2.1
Ac12Az8	> 100	325.0 ± 63.6	5.2 ± 1.8	5.6 ± 2.4
Ac12Az9	**> 100**	**285.0 ± 35.4**	**0.9 ± 0.1**	**1.4 ± 1.0**
Ac12Az10	> 100	650.5 ± 49.5	20.0 ± 7.1	34.2 ± 20.8
Ac12Az11	> 100	365.0 ± 91.9	34.1 ± 32.4	39.0 ± 39.6
Ac12Az12	> 100	287.5 ± 24.7	47.0 ± 1.4	94.0 ± 36.8
verapamil	89.2 ± 8.2	445.7 ± 40.7	> 5000	ND
GF120918	> 100	1.1 ± 0.1	20.0 ± 7.1	ND
ko143	29.2 ± 1.6	1060.0 ± 120.1	11.4 ± 2.4	ND

Flavonoid dimers were evaluated for their BCRP/ABCG2- and P-gp-inhibitory properties based on their capability to reverse TPT resistance in BCRP/ABCG2-overexpressing cell line HEK293/R2 and PTX resistance in P-gp-overexpressing cell line LCC6MDR. EC_{50} represented the inhibitory activity of these flavonoid dimers, and the lower the EC_{50} values, the more potent the inhibitory activity. Cytotoxicity of modulators on normal mouse fibroblasts L929 cells was determined to evaluate the safety of the modulators. ND: Not was determined.

3.2 Results

3.2.1 Reversal activity of Ac12Az9 in P-gp- and BCRP/ABCG2-mediated drug resistance in different cell lines

The modulating activity of **Ac12Az9** on BCRP/ABCG2 and P-gp was studied in several cell lines, including BCRP/ABCG2-overexpressing cell lines HEK293/R2 and MCF7-MX100 and P-gp-overexpressing cell line LCC6MDR. Expression of BCRP/ABCG2 or P-gp was confirmed in these cell lines (**Figure 2-1**). It was found that **Ac12Az9** was a potent dual selective inhibitor of BCRP/ABCG2 and P-gp. **Ac12Az9** can modulate BCRP/ABCG2-mediated TPT resistance with an EC_{50} of 1 nM in HEK293/R2 cells (**Figure 3-2A**) or 1.6 nM in MCF7-MX100 cells (**Figure 3-2B**). It can also modulate P-gp-mediated PTX resistance with an EC_{50} of 200 nM in LCC6MDR cells (**Figure 3-2C**).

A

IC_{50}s of TPT in HEK293/R2 cells

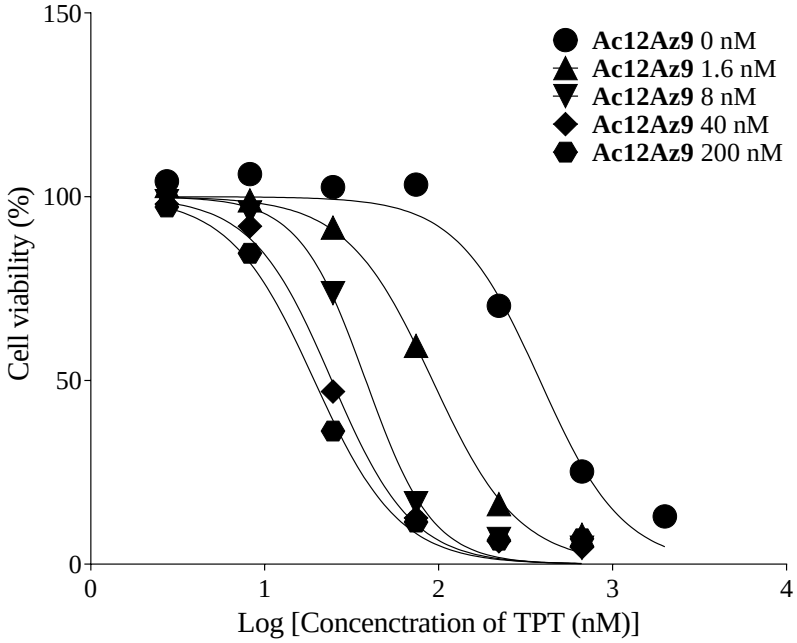

Concentration of **Ac12Az9** (nM)	IC_{50} of TPT towards HEK293/R2 cells (nM)	RF
0	382.1	1.0
1.6	92.52	4.1
8	38.16	10.0
40	24.33	15.7
200	19.28	19.8
EC_{50} of **Ac12Az9** (nM)		1.0

B

IC_{50}s of TPT in MCF7-MX100 cells

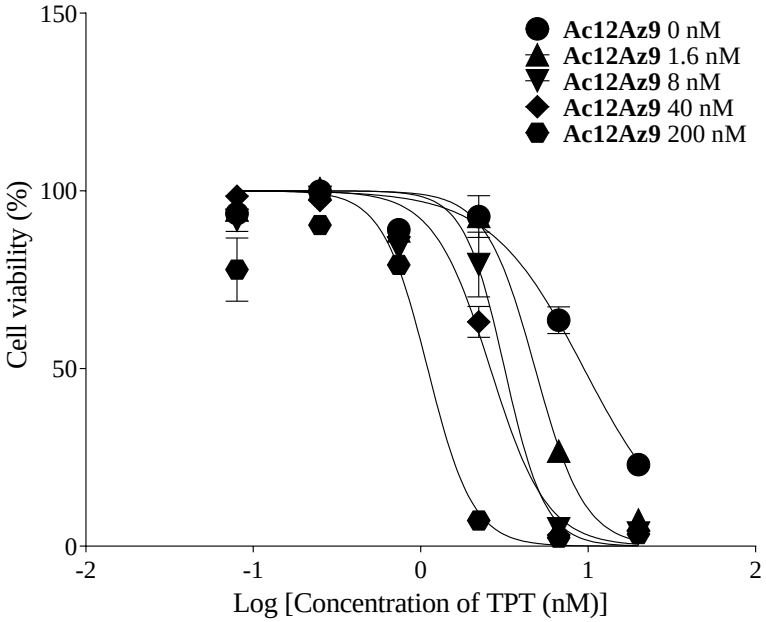

Concentration of **Ac12Az9** (nM)	IC_{50} of TPT towards MCF7-MX100 cells (μM)	RF
0	9.43	1.0
0.32	4.83	2.0
1.6	2.85	3.3
8	2.61	3.6
40	1.37	6.9
200	1.05	9.0
EC_{50} of **Ac12Az9** (nM)		1.6

C

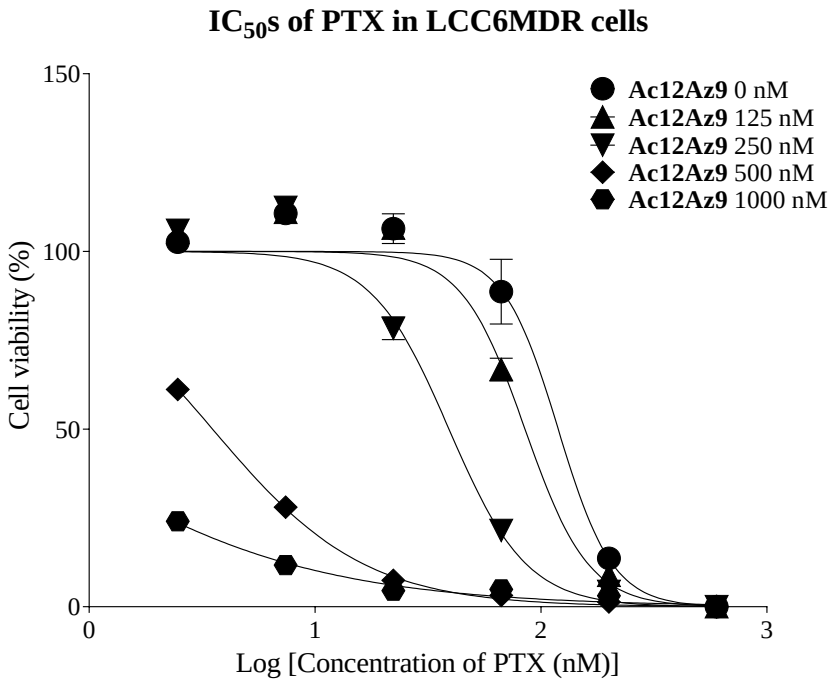

Concentration of **Ac12Az9** (nM)	IC_{50} of PTX towards LCC6MDR cells (nM)	RF
0	119.3	1.0
125	85.0	1.4
250	39.2	3.0
500	3.5	33.9
1000	0.5	238.2
EC_{50} of **Ac12Az9** (nM)		200

Figure 3-2 Dose dependence of Ac12Az9 in reversing drug resistance in LCC6MDR, HEK293/R2, or MCF7-MX100 cells

(A) Cytotoxicity of TPT against HEK293/R2 cells without or with different doses of **Ac12Az9**; (B) Cytotoxicity of TPT against MCF7-MX100 cells without or with different doses of **Ac12Az9**; (C) Cytotoxicity of PTX against LCC6MDR cells without or with different doses of **Ac12Az9**.

4500 cells of HEK293/R2, MCF7-MX100, or LCC6MDR cells were seeded into 96-well plates, respectively. Cells were treated with PTX or TPT, with either no **Ac12Az9** or different **Ac12Az9** dosages. Cell viability was measured after 4-5 days of incubation. Each sample comprised 2-3 repetitions (n = 2-3). PRISM software was used to calculate the IC_{50} of several anticancer medications and the EC_{50} of various modulators.

3.2.2 Effect of Ac12Az9 on sorafenib accumulation in MDCKII-WT, MDCKII-GFP-BCRP, or MDCKII-P-gp cells

The above results showed that **Ac12Az9** was a potent dual selective modulator of BCRP/ABCG2 and P-gp. It can reverse both BCRP/ABCG2-mediated TPT resistance and P-gp-mediated PTX resistance. Here, **Ac12Az9** was tested for its ability to increase the accumulation of sorafenib in MDCKII cells overexpressing BCRP/ABCG2 (MDCKII-GFP-BCRP cells) or P-gp (MDCKII-P-gp cells). Expression of BCRP/ABCG2 or P-gp was confirmed in these cell lines (**Figure 2-1**). Sorafenib was a substrate of BCRP/ABCG2 because MDCKII-GFP-BCRP cells accumulated 2.3-fold less sorafenib than its parental MDCKII cells ($p < 0.001$) (**Figure 3-3**). Treatment of MDCKII-GFP-BCRP cells with 1 μM of **Ac12Az9** or GF120918 increased the intracellular sorafenib accumulation by 2.4-fold ($p < 0.001$) or 2.2-fold ($p < 0.001$), respectively (**Figure 3-3**). This result suggested that **Ac12Az9** can inhibit the transport of sorafenib by BCRP/ABCG2 and restore the intracellular sorafenib concentration to the parental level in MDCKII-WT cells. There was no significant difference in sorafenib accumulation between the MDCKII-P-gp and MDCKII-WT cells (**Figure 3-3**). Treatment of MDCKII-P-gp cells with 1 μM of **Ac12Az9** or GF120918 could slightly increase the intracellular uptake of sorafenib (**Figure 3-3**). Overall, the result suggested that sorafenib was a good substrate for BCRP/ABCG2 but not for P-gp.

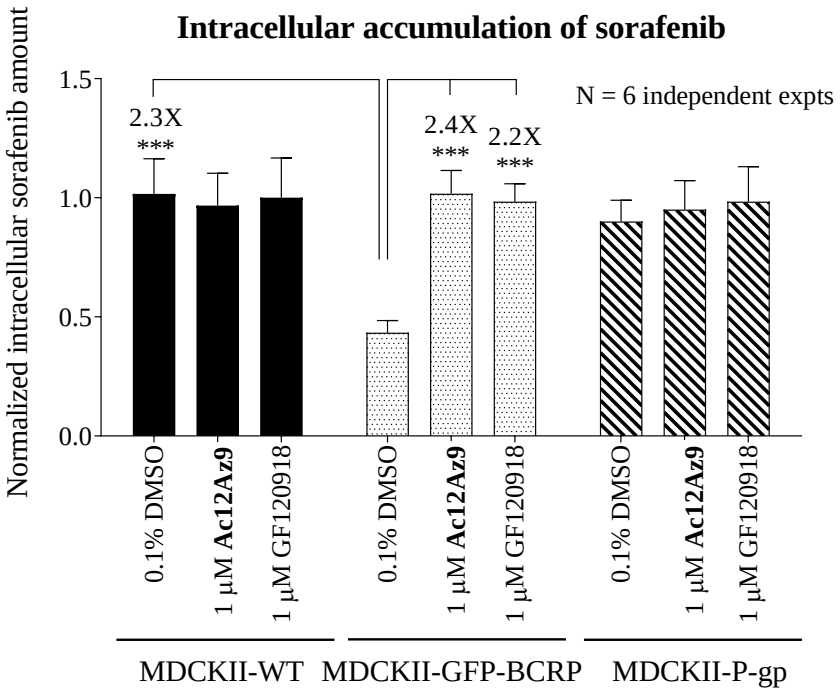

Figure 3-3 Effect of Ac12Az9 on intracellular accumulation of sorafenib in MDCKII-WT, MDCKII-GFP-BCRP, and MDCKII-P-gp cells
Cells were incubated with 2.5 μM sorafenib for 60 mins at 37°C with or without **Ac12Az9** (1 μM) or GF120918 (1 μM). 0.1% of DMSO was used as a negative control. Intracellular levels of sorafenib were determined by UPLC-MS/MS. All the data was shown as the normalized intracellular sorafenib level and presented as mean ± SD (n = 6). Student's t-test was performed in relation to MDCKII-GFP-BCRP cells that had been exposed to 0.1% DMSO. ***, $p < 0.005$.

3.2.3 Effect of Ac12Az9 on sorafenib efflux in MDCKII-WT, MDCKII-GFP-BCRP, and MDCKII-P-gp cells

In addition to accumulation, the efflux of sorafenib in MDCKII-GFP-BCRP or MDCKII-P-gp cells was also investigated. After the cells were treated with sorafenib and left in the sorafenib-free medium for 30 mins, about 92%, 54%, and 70% of sorafenib still remained in the MDCKII-WT, MDCKII-GFP-BCRP, and MDCKII-P-gp cells, respectively (**Figure 3-4**). **Ac12Az9** showed no effect on the efflux of sorafenib in MDCKII-WT cells, with the intracellular sorafenib remaining at 94%. **Ac12Az9** can inhibit the BCRP/ABCG2-mediated sorafenib efflux, raising the intracellular sorafenib from 54% to 108% ($p < 0.001$) in MDCKII-GFP-BCRP cells (**Figure 3-4**). **Ac12Az9** also blocked the P-gp-mediated sorafenib efflux in MDCKII-P-gp cells, raising the intracellular sorafenib from 70% to 78% ($p < 0.01$) (**Figure 3-4**).

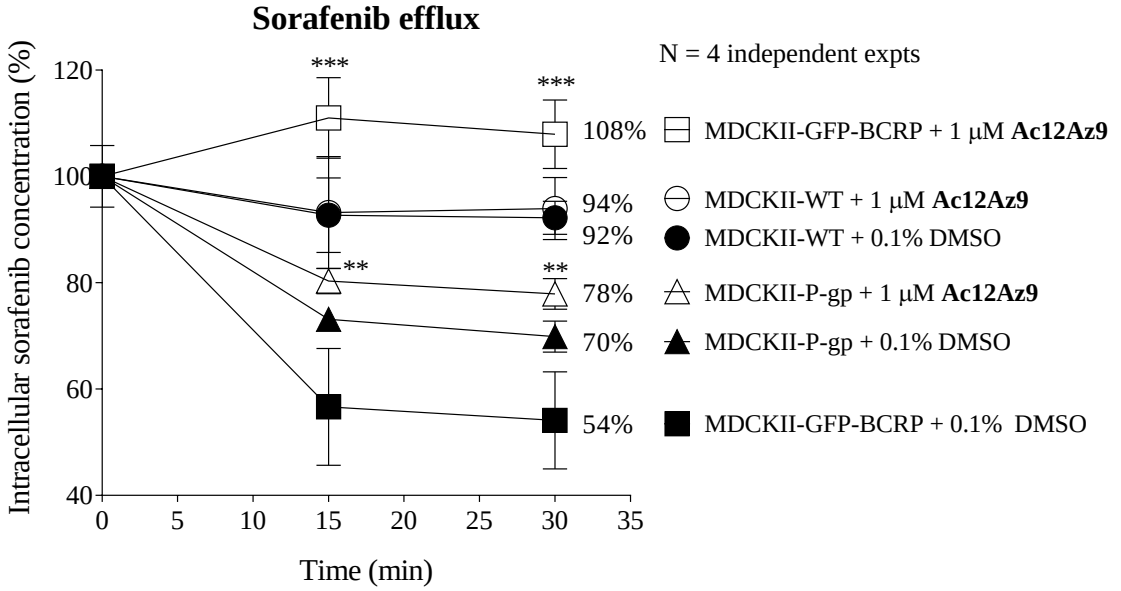

Figure 3-4 Effect of Ac12Az9 on sorafenib efflux in MDCKII-WT, MDCKII-GFP-BCRP, or MDCKII-P-gp cells

Cells preloaded with sorafenib were incubated without or with **Ac12Az9** (1 μM) at 37 °C. Cells were taken at 0, 15, and 30 mins, and UPLC-MS/MS was used to determine the intracellular sorafenib concentration. All the data was shown as the normalized percentages of intracellular sorafenib level and presented as mean ± SD (n = 4). Student's t-test was used to compare statistical differences between cells with and without **Ac12Az9** at various time points. **, $p < 0.01$, ***, $p < 0.001$.

3.2.4 Effect of Ac12Az9 on the transepithelial transport of sorafenib across MDCKII-WT, MDCKII-GFP-BCRP, or MDCKII-P-gp cells

MDCKII cells can form monolayers and the apparent permeability across such monolayers may be measured to indicate the transepithelial transport activity. The effect of **Ac12Az9** on the transepithelial transport of sorafenib was investigated in MDCKII-WT, MDCKII-GFP-BCRP, or MDCKII-P-gp cells. Part of the experiments shown here was conducted by Dr. Xuesen Hu [195].

Apparent permeability of sorafenib from apical to basal (*Papp* A-to-B) was low in all three cell lines (0.23, 0.18, and 0.10 $cm \cdot sec^{-1} \times 10^6$, respectively) (**Figure 3-5**). This was expected as both P-gp and BCRP/ABCG2 were expected to be localized at the apical side of the monolayer. In contrast, P*app* B-to-A of sorafenib was higher than P*app* A-to-B by 2.7, 18.4, and 4.8 times in MDCKII-WT, MDCKII-GFP-BCRP, and MDCKII-P-gp cells,

respectively (**Figure 3-5**). This suggested that sorafenib was a better BCRP/ABCG2 substrate than P-gp. **Ac12Az9** can reduce the BCRP/ABCG2- or P-gp-mediated *Papp* B-to-A of sorafenib by 81% ($p < 0.01$) or 8%, respectively, suggesting that **Ac12Az9** was a stronger inhibitor of BCRP/ABCG2 than P-gp (**Figure 3-5**). GF120918 can reduce the BCRP/ABCG2- or P-gp-mediated *Papp* B-to-A of sorafenib by 52% or 45%, respectively, suggesting that GF120918 was a stronger inhibitor of P-gp than BCRP/ABCG2 (**Figure 3-5**). Since sorafenib was a more effective substrate of BCRP/ABCG2 than P-gp, it was predicted that **Ac12Az9**, a potent BCRP/ABCG2 modulator, would have a higher effect on sorafenib transport in the BBB, where both BCRP/ABCG2 and P-gp were present.

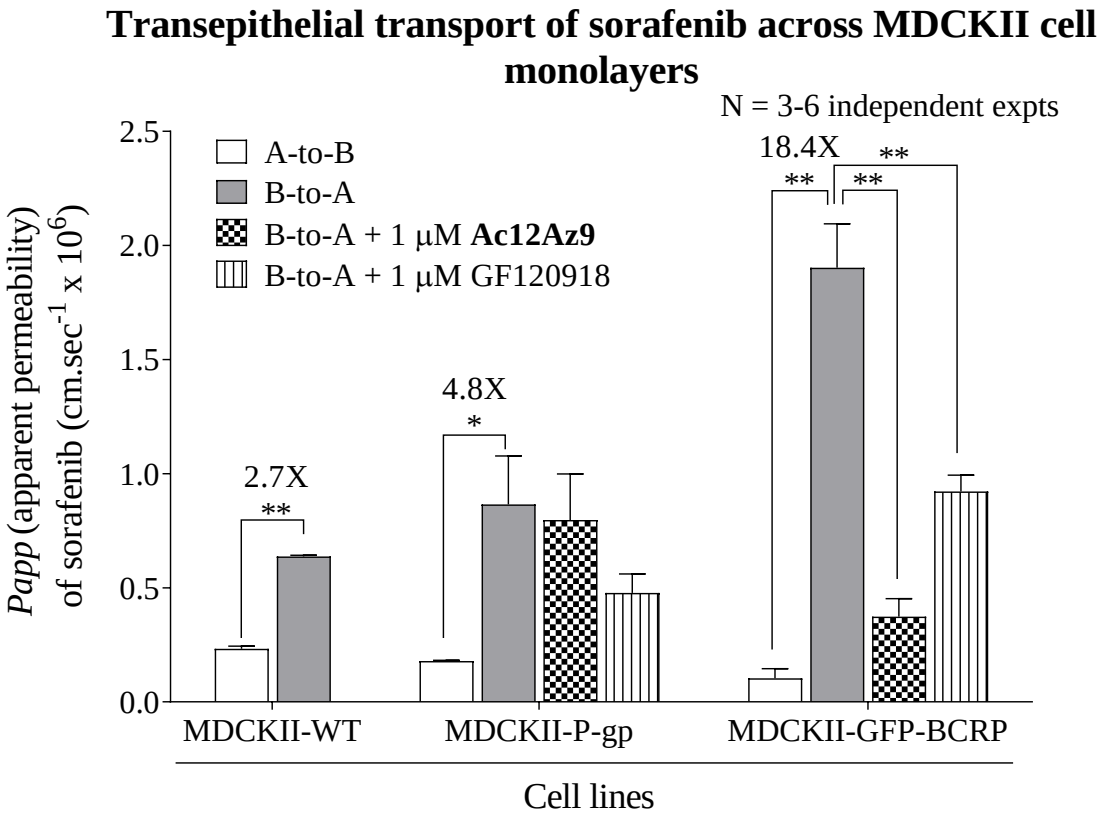

Figure 3-5 Transepithelial transport of sorafenib across MDCKII cell monolayers
First, MDCKII monolayer cells formed tight junctions with TEER > 200 Ω.cm^2. Sorafenib (20 μM) was introduced to the donor side of an MDCKII monolayer either with or without a modulator (**Ac12Az9** or GF120918, 1 μM). Samples were collected from the reception side at various time points, and the level of sorafenib was determined by UPLS-MS/MS. P*app* of sorafenib was calculated using the equation P*app* = $(dQ/dt)/A \cdot C_0$, where dQ/dt represented the sorafenib mass transfer rate, A represented the monolayer surface area corresponding to the area of the insert membrane (4.67 cm^2), and C_0 represented the sorafenib initial concentration on the donor side (10 μg/mL). Data was presented as mean ± standard error of the mean (SEM) (n = 3-6). *, $p < 0.05$; **, $p < 0.01$.

3.2.5 Effect of Ac12Az9 on the expression of BCRP/ABCG2 or P-gp in MDCKII-GFP-BCRP or MDCKII-P-gp cells

The effect of **Ac12Az9** on the expression of BCRP/ABCG2 or P-gp was investigated in MDCKII-GFP-BCRP or MDCKII-P-gp cells. BCRP/ABCG2 was expressed in MDCKII-GFP-BCRP cells but not in MDCKII-WT or MDCKII-P-gp cells, while P-gp was expressed in MDCKII-P-gp cells but not in MDCKII-WT or MDCKII-GFP-BCRP cells (**Figure 3-6A**). **Ac12Az9** had no impact on the expression of either the BCRP/ABCG2 or P-gp protein in MDCKII-GFP-BCRP or MDCKII-P-gp cells (**Figure 3-6A-C**). These findings suggested that the modulating effect of **Ac12Az9** on the accumulation, efflux, and transepithelial transport of sorafenib in MDCKII-GFP-BCRP and MDCKII-P-gp cells was not due to the downregulation of the protein expression of BCRP/ABCG2 and P-gp but was more likely due to the direct modulation of the transport function of BCRP/ABCG2 and P-gp.

A

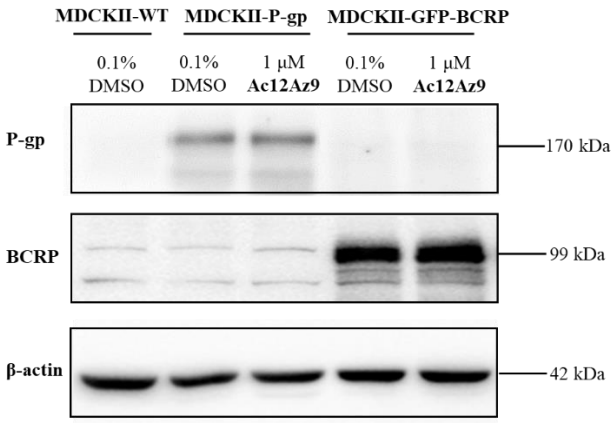

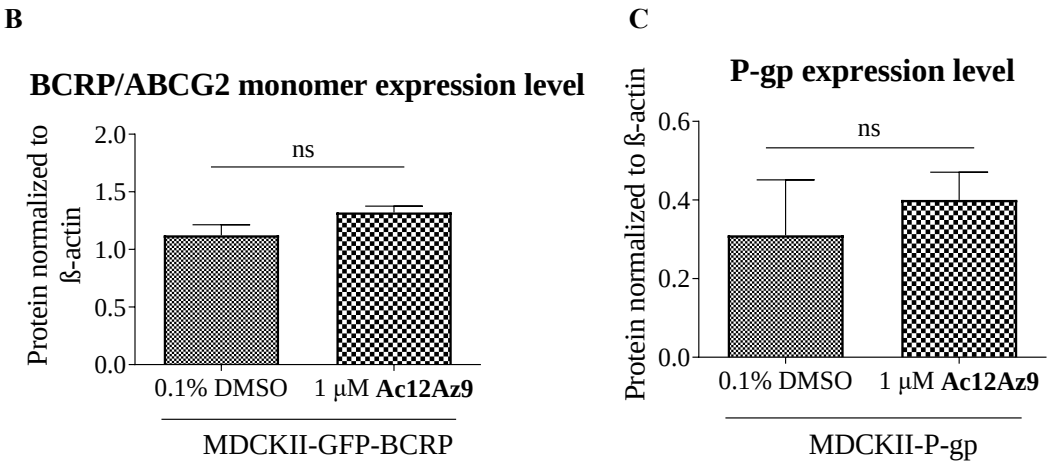

Figure 3-6 Effect of Ac12Az9 on BCRP/ABCG2 and P-gp protein expression in MDCKII-WT, MDCKII-GFP-BCRP, and MDCKII-P-gp cells

(A) Western blot analysis of BCRP/ABCG2 and P-gp protein; (B) Normalized BCRP/ABCG2 protein level of MDCKII-GFP-BCRP cells; (C) Normalized P-gp protein level of MDCKII-P-gp cells.

The MDCKII cells were incubated with 1 μM of **Ac12Az9** for 2 days, respectively. The P-gp and BCRP/ABCG2 protein levels were analyzed by western blot. Details can be found in **Methodology 2.2.10**. N = 2-3 independent experiments. The data was presented as mean ± SD. 0.1% of DMSO was used as a solvent control.

3.3 Discussion

BBB has long been a challenge in the treatment of GBM. BCRP/ABCG2 and P-gp are two clinically significant BBB efflux transporters that work together to block the entry of xenobiotics, such as drugs, and consequently alter their PK, therapeutic efficacy, and safety [147]. BCRP/ABCG2 and/or P-gp inhibition were used as a strategy to increase the brain permeability of anticancer medications to manage CNS disorders.

Membrane transporter inhibitor research has currently advanced from the first generation to the third generation. Third-generation P-gp inhibitors included tariquidar [162], GF120918 (elacridar) [163], and zosuquidar [164], which had high P-gp-modulating activity and minimal pharmacokinetic interactions. Clinical trials, however, have not been able to demonstrate that cancer medications improve treatment with the use of these third-generation P-gp inhibitors, and some even revealed harmful effects. Thus, more focus has been placed on the identification of effective and safe natural products [166-168] or inhibitors with dual selectivity for P-gp and BCRP/ABCG2 [169-171].

Ac12Az9 is the fifth-generation synthetic flavonoid dimer developed from the natural product apigenin in our lab [178]. **Ac12Az9** was shown to be a potent dual-selective inhibitor of BCRP/ABCG2 and P-gp. It can modulate P-gp-mediated PTX resistance with an EC_{50} of 200 nM in LCC6MDR cells and modulate BCRP/ABCG2-mediated TPT resistance with an EC_{50} of 1 nM in HEK293/R2 cells or 1.6 nM in MCF7-MX100 cells.

All *in vitro* cellular uptake, cellular efflux, and transepithelial transport experiments, using MDCKII-WT, MDCKII-P-gp, or MDCKII-GFP-BCRP cells, demonstrated that sorafenib was a better BCRP/ABCG2 substrate than P-gp. This was consistent with the knockout study in which the *Bcrp (-/-)* mice resulted in a 3.8-fold increase in brain accumulation of sorafenib, but the *Mdr1a/b (-/-)* mice had almost no effect [140]. **Ac12Az9** not only inhibited BCRP/ABCG2-mediated efflux of sorafenib, increasing intracellular sorafenib from 54% to 108% ($p < 0.001$), but it also blocked P-gp-mediated efflux of sorafenib in MDCKII-P-gp cells, increasing intracellular sorafenib from 70% to 78% ($p < 0.01$). The

transepithelial transport assay further demonstrated that **Ac12Az9** can reduce the BCRP/ABCG2- or P-gp-mediated *Papp* B-to-A of sorafenib by 81% ($p < 0.01$) or 8%, respectively, suggesting that **Ac12Az9** was a stronger inhibitor of BCRP/ABCG2 than P-gp. Taken together, considering that sorafenib was a better BCRP/ABCG2 substrate than P-gp, it was predicted that **Ac12Az9**, a greater BCRP/ABCG2 inhibitor than P-gp, would have a significant effect on sorafenib transport at the BBB. In addition, these effects were not mediated by affecting the protein level of P-gp or BCRP/ABCG2.

3.4 Conclusion

In conclusion, **Ac12Az9** was shown to be a safe and potent dual-selective inhibitor of BCRP/ABCG2 and P-gp. **Ac12Az9** can inhibit BCRP/ABCG2- and P-gp-mediated sorafenib efflux to improve sorafenib cell accumulation and permeability without affecting the protein expression of P-gp and BCRP/ABCG2.

Chapter 4 PK and toxicity study of sorafenib and Ac12Az9 in BALB/c mice

4.1 Introduction

PK plays a significant role in the development and discovery of new drugs. PK studies are carried out to evaluate how medications are disposed of within the body, including absorption, distribution, metabolism, and excretion [196]. The physicochemical property of a drug, its administration (dose, route, and schedule), and host factors all greatly influence these four PK phases [197]. The understanding of the distribution of a drug to the brain is another focus when developing CNS drugs. The therapeutic effect of a drug primarily depends on its high brain penetration and long exposure duration in the brain. Drug physicochemical properties (molecular weight and lipophilicity), as well as the transporters at the BBB, can influence how permeable a drug is to the brain [198]. It has been well demonstrated that inhibiting efflux transporters at the BBB are an efficient strategy to boost brain accumulation of conventional anticancer drugs, which is typically reflected by an increased drug's brain-to-plasma ratio in PK studies [199, 200].

UPLC-ESI-QqQ-MS/MS (UPLC-MS/MS), which has good specificity and high sensitivity, is widely utilized in PK investigations. There are many well-developed techniques for preparing biological samples, such as protein precipitation, liquid-liquid extraction, phospholipid removal media, solid phase extraction, etc., that can not only remove proteins, lipids, and other contaminants but also enhance the chromatographic performance to guarantee the precision and accuracy of sample detection [201]. Protein precipitation is one of the most popular techniques that has the advantages of simplicity, minimal loss of sample, and high extraction efficiency.

The evaluation of *in vivo* toxicity is also important in the new drugs development. Its objectives are to investigate the connection between drug exposure and toxicity in animal models, to identify potential toxic effects on different organs, and to forecast the safety of medication use. Blood tests, especially those for liver and kidney function, can help quickly

identify disorders and damage to the liver and kidneys. Liver function tests measure the blood's levels of several proteins and enzymes, such as ALT, AST, ALP, Albumin, total protein, etc. Kidney function tests look for the level of waste products, such as CRE and BUN, in blood.

This chapter investigated the effect of **Ac12Az9** on the PK and tissue distribution profiles of sorafenib, as well as the toxicity of this combination in BALB/c mice. Initially, to ensure the reliability and accuracy of biological sample detection, a reliable and specific UPLC-MS/MS method was developed and validated to detect sorafenib and **Ac12Az9** in murine plasma and brain (see **Methodology 2.2.12**). A suitable formulation for **Ac12Az9** was selected for animal experiments. The PK characteristics and toxicity assessment of the combination of sorafenib and **Ac12Az9** would provide foundational support for further efficacy evaluation in orthotopic GBM PDX models.

4.2 Results

4.2.1 Formulation optimization of Ac12Az9 for PK studies

Formulation of a drug ensures the delivery of a drug to the site of action to generate the desired therapeutic effect. To obtain an optimal formulation for **Ac12Az9**, different formulations were used to study their effects on the PK and brain accumulation of **Ac12Az9** in BALB/c mice. There were eight formulations in this study, including **A** (EtOH: CrEL: 5% Tween-80 = 5: 5: 90), **B** (DMSO: CrEL: 5% Tween-80 = 5: 5: 90), **C** (NMP: CrEL: 5% Tween-80 = 5: 5: 90), **D** (NMP: 20% Tween-80 = 5: 95), **E** (NMP: Solutol: 5% Tween-80 = 5: 10: 85), **F** (NMP: Solutol: Saline = 5: 10: 85), **G** (NMP: PEG400: 10% Tween-80 = 5: 30: 65), and **H** (NMP: CrEL: 5% Tween-80 = 10: 10: 80).

The UPLC-MS/MS method for **Ac12Az9** determination in biological samples was validated, which was described in **Methodology 2.2.12**. When the PK experiment was performed on **Ac12Az9** dissolved in different formulations, it was found that formulation **H** yielded the highest brain $AUC_{15\text{-}240}$ (75,862.1 ng·min/g), making it the preferred solvent for **Ac12Az9 (Figure 4-1A)**. Although the formulations **D** and **G** could yield a similarly high level of brain accumulation, with 59,807.8 and 45,376.5 ng·min/g respectively, some mice were found dead after a single intravenous dose. This might be due to hemolytic activity triggered by a high concentration of surfactant Tween-80 used [202]. Besides, NMP was found to be more suitable than EtOH and DMSO for **Ac12Az9**, with formulation **C** having a larger brain $AUC_{15\text{-}240}$ (40,659.2 ng·min/g) than formulations **A** (18,264.9 ng·min/g) and **B** (35,918.7 ng·min/g). CrEL and PEG400 were better solubilizers than solutol, with higher brain $AUC_{15\text{-}240}$ in formulations **C** (40,659.2 ng·min/g) and **G** (45,376.5 ng·min/g) than those in formulations **E** (17,035.2 ng·min/g) and **F** (10,548.3 ng·min/g).

Compared with the PK profiles of **Ac12Az9** in the brain, the PK profiles of **Ac12Az9** in blood varied a lot in different formulations, with the plasma $AUC_{15\text{-}240}$ ranging from 2,564.0 to 585,134.4 ng·min/mL (**Figure 4-1B**). The plasma **Ac12Az9** levels in formulations **B** and **G** were below the lower limit of quantification (LLOQ) 30 mins after

administration.

Taken together, the formulation **H** (NMP: CrEL: 5% Tween-80 = 10: 10: 80) with the highest level of **Ac12Az9** accumulation in the brain and moderate level of **Ac12Az9** in the plasma was preferred over others. Formulation **H** would be used in subsequent *in vivo* studies.

A

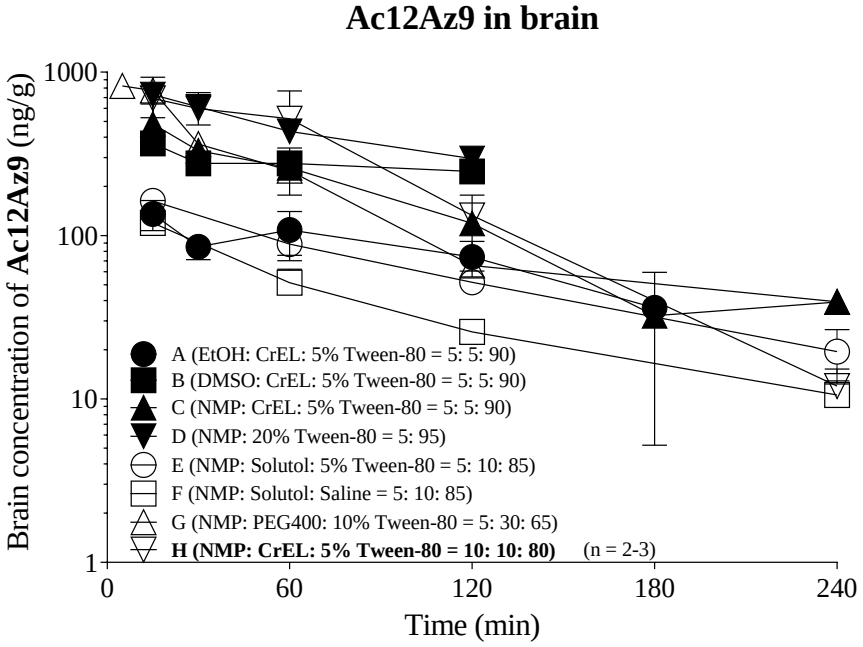

Groups	Brain $AUC_{15\text{-}t}$ (ng-min/g)
A (EtOH : CrEL : 5% Tween-80 = 5 : 5 : 90)	18,264.9
B (DMSO : CrEL : 5% Tween-80 = 5 : 5 : 90)	35,918.7
C (NMP : CrEL : 5% Tween-80 = 5 : 5 : 90)	40,659.2
D (NMP : 20% Tween-80 = 5 : 95)	59,807.8
E (NMP : Solutol : 5% Tween-80 = 5 : 10 : 85)	17,035.2
F (NMP : Solutol : Saline = 5 : 10 : 85)	10,548.3
G (NMP : PEG400 : 10% Tween-80 = 5 : 30 : 65)	45,376.5
H (NMP : CrEL : 5% Tween-80 = 10 : 10 : 80)	**75,862.1**

B

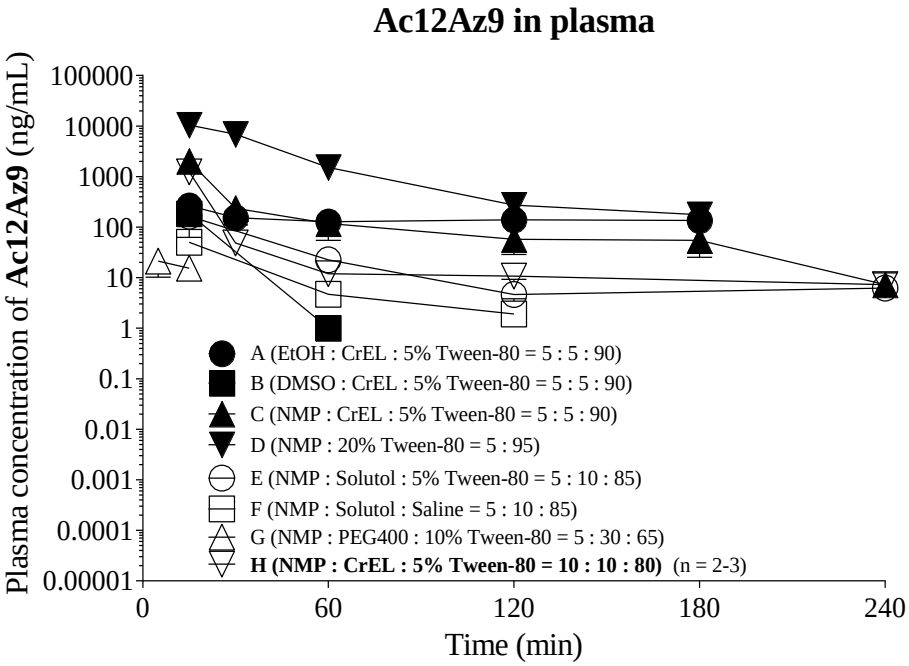

Groups	Plasma $AUC_{15\text{-}t}$ (ng-min/mL)
A (EtOH : CrEL : 5% Tween-80 = 5 : 5 : 90)	27,259.3
B (DMSO : CrEL : 5% Tween-80 = 5 : 5 : 90)	-
C (NMP : CrEL : 5% Tween-80 = 5 : 5 : 90)	101,556.5
D (NMP : 20% Tween-80 = 5 : 95)	585,134.4
E (NMP : Solutol : 5% Tween-80 = 5 : 10 : 85)	9,421.2
F (NMP : Solutol : Saline = 5 : 10 : 85)	2,564.0
G (NMP : PEG400 : 10% Tween-80 = 5 : 30 : 65)	-
H (NMP : CrEL : 5% Tween-80 = 10 : 10 : 80)	**70,464.8**

Figure 4-1 Effect of different formulations on the PK of Ac12Az9 in BALB/c mice
(A) Brain concentration-time curves of **Ac12Az9**; (B) Plasma concentration-time curves of **Ac12Az9**. Mice were given eight different formulations of **Ac12Az9** (1.5 mg/mL) intravenously through the tail vein, respectively. Blood and brain samples were collected respectively at various time points (5 min, 15 min, 30 min, 1 h, 2 h, 3 h, and 4 h). Plasma and brain concentrations of **Ac12Az9** were determined by UPLC-MS/MS. The data was presented as mean ± SEM (n = 2-3). A non-compartmental analysis of **Ac12Az9** was performed using PK Solutions 2.0.3 software (Ashland, OH44805, USA) to calculate the AUC values. Part of the experiments shown here were conducted by Dr. Xuesen Hu [195].

4.2.2 Effect of Ac12Az9 on the PK and brain distribution profiles of sorafenib in BALB/c mice

The brain distribution and plasma PK of **Ac12Az9** or GF120918 were studied. When given at a dose of 20 mg/kg, the $AUC_{5\text{-}360}$ of GF120918 in the brain (9,328,200 $ng \cdot min \cdot g^{-1}$) was 24-fold higher than that of **Ac12Az9** in the brain (385,617 $ng \cdot min \cdot g^{-1}$) (**Figure 4-2A**). Plasma $AUC_{5\text{-}360}$ of GF120918 (477,863 $ng \cdot min \cdot mL^{-1}$) was 8-fold higher than that of **Ac12Az9** (58,877 $ng \cdot min \cdot mL^{-1}$) (**Figure 4-2B**). The brain-to-plasma ratios of **Ac12Az9** (20 mg/kg) remained over 15 between 15 and 360 mins after administration and even reached 128 at 120 mins, but the brain-to-plasma ratios of GF120918 (20 mg/kg) were 11 to 21 at all time points (**Figure 4-2C**). These findings implied that GF120918 and **Ac12Az9** can pass the BBB and considerably accumulate in the brain.

The effect of **Ac12Az9** or GF120918 on the brain accumulation of sorafenib in BALB/c mice was investigated. It was found that **Ac12Az9** (10 or 20 mg/kg) or GF120918 (20 mg/kg) can elevate sorafenib levels in the brain to therapeutic concentrations greater than its *in vitro* IC_{50} towards U87MG-RedFluc cells (8 μM) (**Figure 4-2D**). The plasma sorafenib concentration remained unchanged when sorafenib was co-administered with **Ac12Az9** or GF120918 (**Figure 4-2E**), indicating that this combination might not cause drug-drug interaction (DDI). The brain-to-plasma ratio of sorafenib was elevated from 0.15 in the sorafenib alone group to 0.25, 0.37, or 0.7, respectively, when combined with **Ac12Az9** (10 or 20 mg/kg) or GF120918 (20 mg/kg) (**Figure 4-2F**). These data suggested that **Ac12Az9** can effectively enhance the bran penetration of sorafenib *in vivo*.

PK parameters were summarized in **Figure 4-2G**. Dose-normalized brain C_{max} of sorafenib (C_{max}/dose) were 99 $ng \cdot g^{-1}/mg \cdot kg^{-1}$ in sorafenib alone group. **Ac12Az9** (10 and 20 mg/kg) can increase the C_{max}/dose values of sorafenib to 173 (1.7-fold over sorafenib alone) and 207 (2.1-fold over sorafenib alone) $ng \cdot g^{-1}/mg \cdot kg^{-1}$, respectively. GF120918 (20 mg/kg) can enhance the C_{max}/dose values of sorafenib to 461 $ng \cdot g^{-1}/mg \cdot kg^{-1}$ (4.6-fold over sorafenib alone).

Dose-normalized $AUC_{15\text{-}480}$ of sorafenib in the brain (AUC_{brain}/dose) was 32,251 ng·min·g^{-1}/mg·kg^{-1} in sorafenib alone group. **Ac12Az9** (10 or 20 mg/kg) can increase the AUC_{brain}/dose of sorafenib to 49,148 ng·min·g^{-1}/mg·kg^{-1} (1.5-fold over sorafenib alone) and 59,177 (1.8-fold over sorafenib alone), respectively. GF120918 can increase the AUC_{brain}/dose of sorafenib to 147,461 ng·min·g^{-1}/mg·kg^{-1} (4.6-fold over sorafenib alone). Correspondingly, the dose-normalized $AUC_{15\text{-}480}$ of sorafenib in plasma (AUC_{plasma}/dose) was 253,045 ng·min·mL^{-1}/mg·kg^{-1}.

Ac12Az9 (10, 20 mg/kg) can increase the AUC_{brain}/AUC_{plasma} of sorafenib by 1.4- (from 0.13 to 0.19) and 1.8-fold (from 0.13 to 0.22), respectively (**Figure 4-2G**). Furthermore, GF120918 (20 mg/kg) can increase the AUC_{brain}/AUC_{plasma} of sorafenib by 3.9-fold (from 0.13 to 0.51) (**Figure 4-2G**).

A

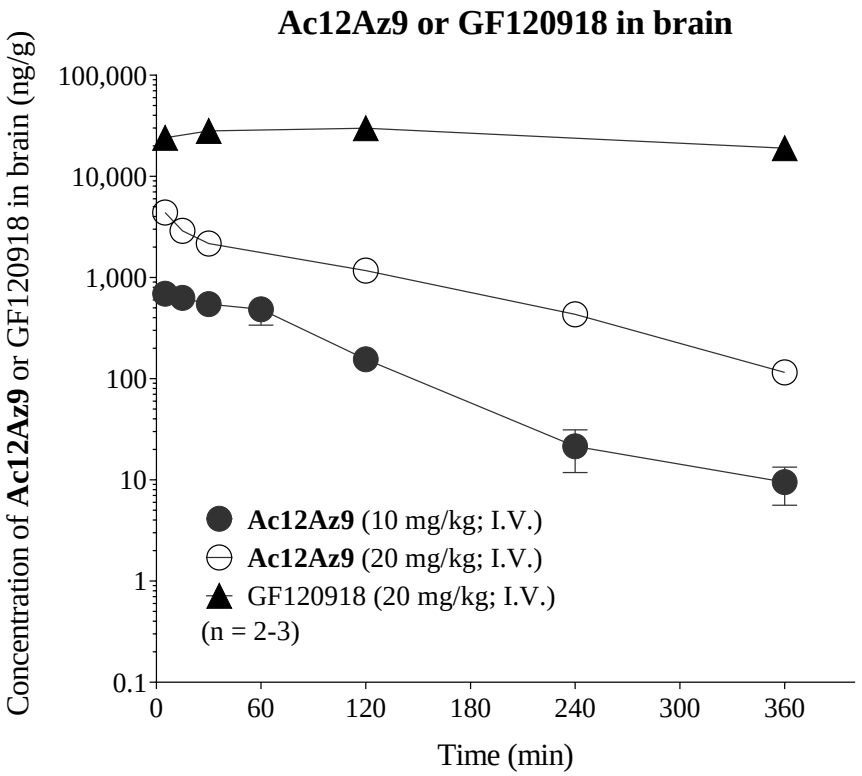

Pharmacokinetic parameters	**Ac12Az9**		GF120918
	10 mg/kg, I.V.	20 mg/kg, I.V.	20 mg/kg, I.V.
Brain C_{max} (ng/g)	693	4,391	29,940
Brain C_{max}/dose ($ng \cdot g^{-1}/mg \cdot kg^{-1}$)	69	220	1,497
Brain AUC (ng·min/g)	66,404	385,617	9,328,200
Brain AUC/dose ($ng \cdot min \cdot g^{-1}/mg \cdot kg^{-1}$)	6,640	19,281	466,410

B

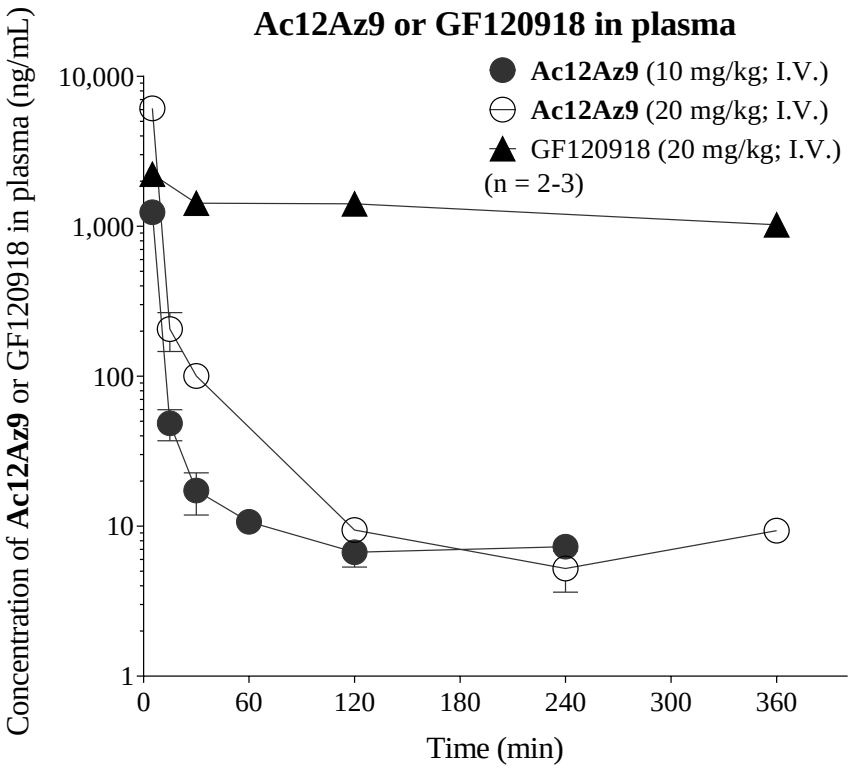

Pharmacokinetic parameters	**Ac12Az9**		GF120918
	10 mg/kg, I.V.	20 mg/kg, I.V.	20 mg/kg, I.V.
Plasma C_{max} (ng/mL)	1,243	6,110	2,230
Plasma C_{max}/dose ($ng \cdot mL^{-1}/mg \cdot kg^{-1}$)	124	305	111
Plasma AUC (ng·min/mL)	13,007	58,877	477,863
Plasma AUC/dose ($ng \cdot min \cdot mL^{-1}/mg \cdot kg^{-1}$)	1,301	2,944	23,893

C

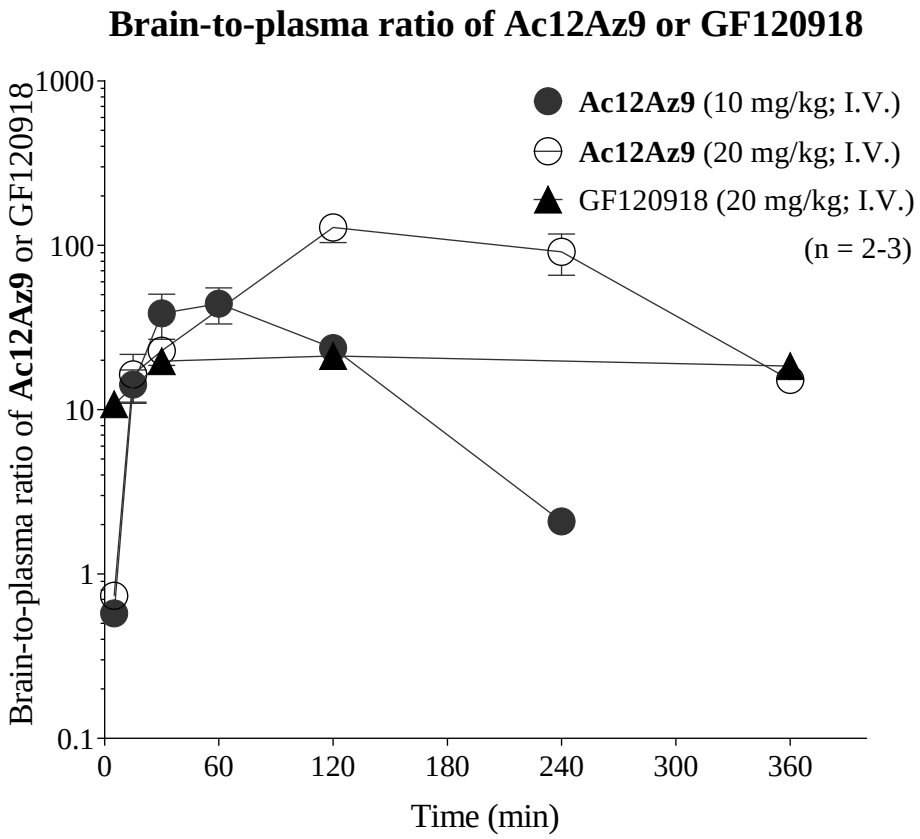
Brain-to-plasma ratio of Ac12Az9 or GF120918
Brain-to-plasma ratio of Ac12Az9 or GF120918
1000
100
10
1
0.1
0
60
120
180
240
300
360
Time (min)
Ac12Az9 (10 mg/kg; I.V.)
Ac12Az9 (20 mg/kg; I.V.)
GF120918 (20 mg/kg; I.V.)
(n = 2-3)

D

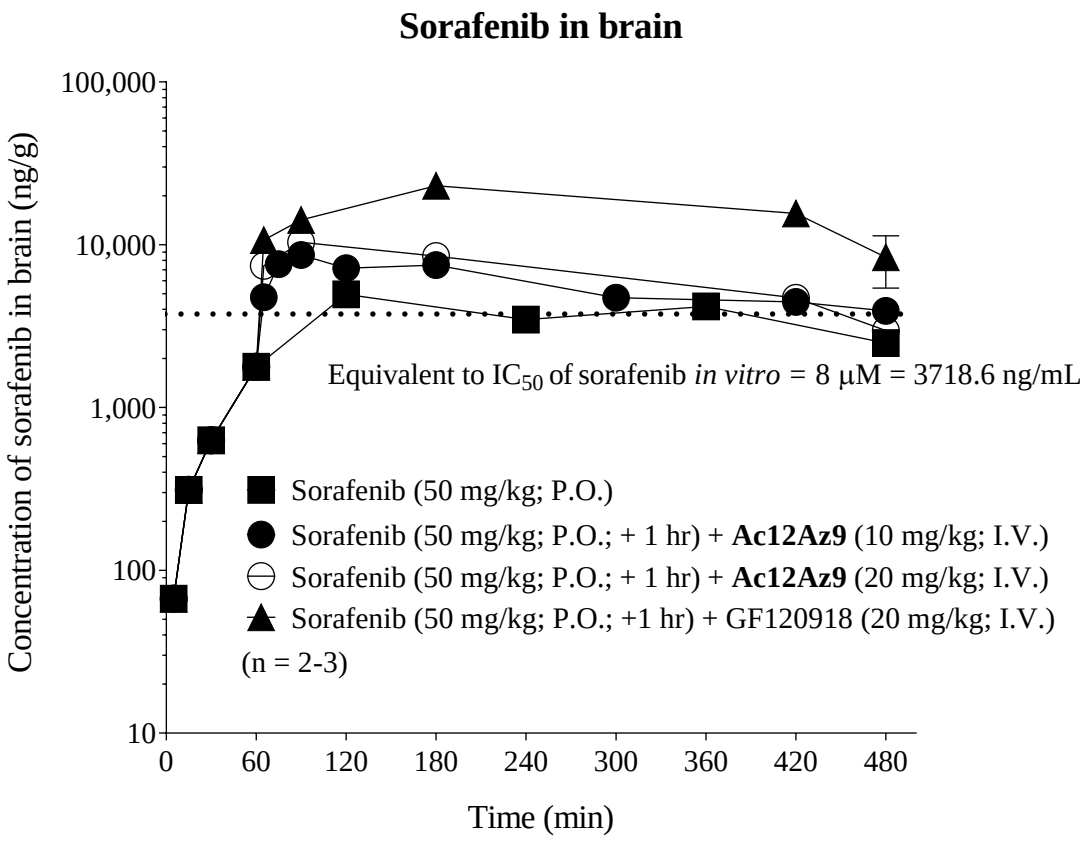
Sorafenib in brain
Concentration of sorafenib in brain (ng/g)
100,000
10,000
1,000
100
10
0
60
120
180
240
300
360
420
480
Time (min)
Equivalent to IC50 of sorafenib in vitro = 8 μM = 3718.6 ng/mL
Sorafenib (50 mg/kg; P.O.)
Sorafenib (50 mg/kg; P.O.; + 1 hr) + Ac12Az9 (10 mg/kg; I.V.)
Sorafenib (50 mg/kg; P.O.; + 1 hr) + Ac12Az9 (20 mg/kg; I.V.)
Sorafenib (50 mg/kg; P.O.; +1 hr) + GF120918 (20 mg/kg; I.V.)
(n = 2-3)

E

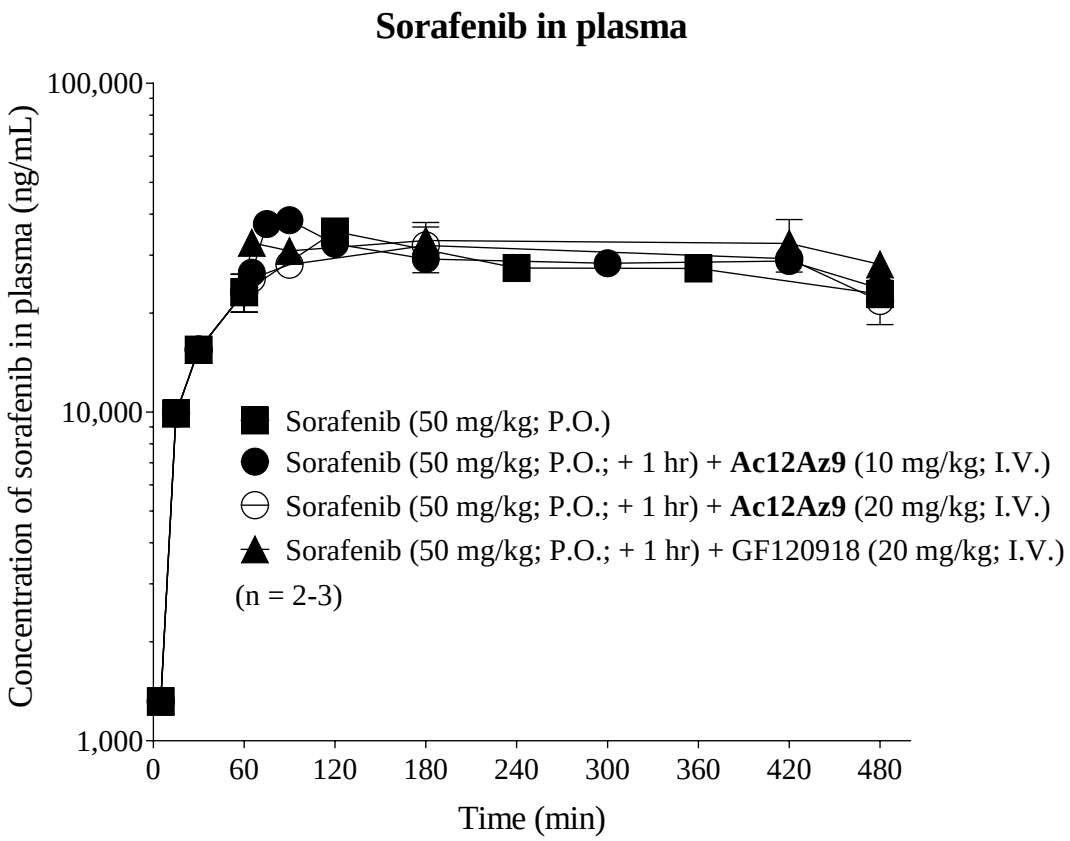
Sorafenib in plasma
Concentration of sorafenib in plasma (ng/mL)
100,000
10,000
1,000
0
60
120
180
240
300
360
420
480
Time (min)
Sorafenib (50 mg/kg; P.O.)
Sorafenib (50 mg/kg; P.O.; + 1 hr) + Ac12Az9 (10 mg/kg; I.V.)
Sorafenib (50 mg/kg; P.O.; + 1 hr) + Ac12Az9 (20 mg/kg; I.V.)
Sorafenib (50 mg/kg; P.O.; + 1 hr) + GF120918 (20 mg/kg; I.V.)
(n = 2-3)

F

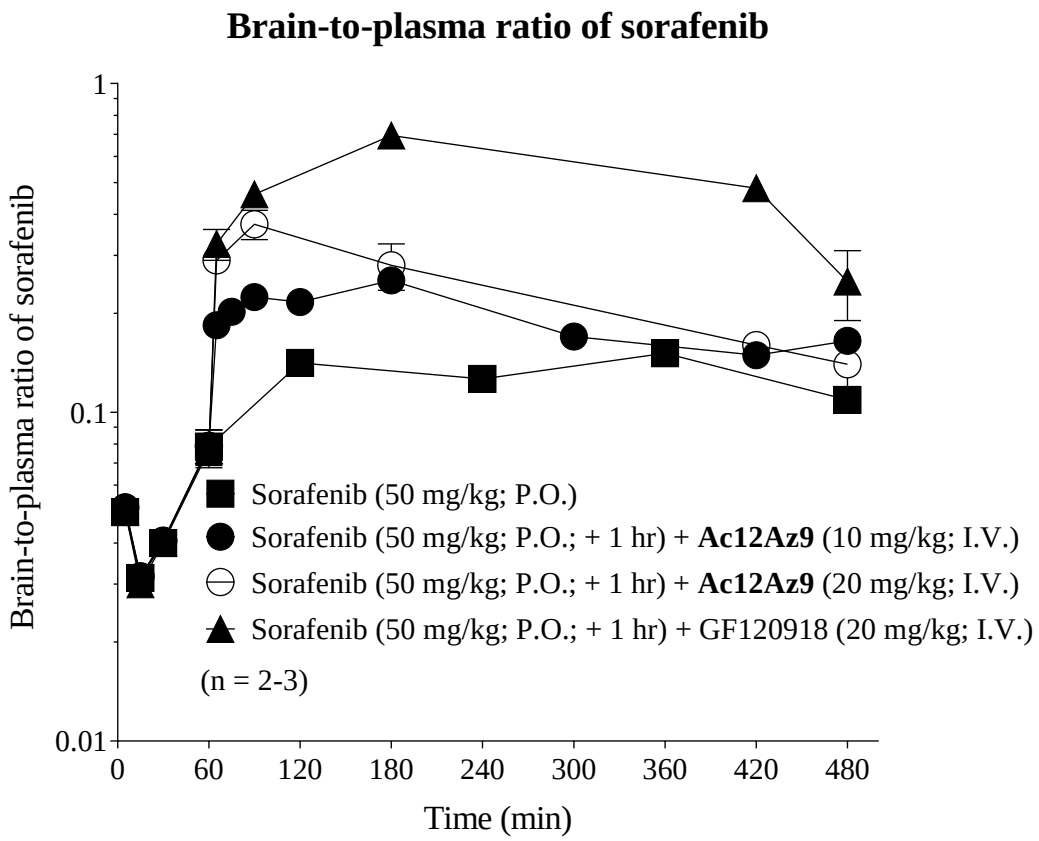
Brain-to-plasma ratio of sorafenib
Brain-to-plasma ratio of sorafenib
1
0.1
0.01
0
60
120
180
240
300
360
420
480
Time (min)
Sorafenib (50 mg/kg; P.O.)
Sorafenib (50 mg/kg; P.O.; + 1 hr) + Ac12Az9 (10 mg/kg; I.V.)
Sorafenib (50 mg/kg; P.O.; + 1 hr) + Ac12Az9 (20 mg/kg; I.V.)
Sorafenib (50 mg/kg; P.O.; + 1 hr) + GF120918 (20 mg/kg; I.V.)
(n = 2-3)

G

Adminstration route	**P.O.**		**P.O., 1 hr, I.V.**		**P.O., 1 hr, I.V.**		**P.O., 1 hr, I.V.**	
Sorafenib (mg/kg)	**50**		**50**		**50**		**50**	
Ac12Az9 (mg/kg)	**-**		**10**		**20**		**-**	
GF120918 (mg/kg)	**-**		**-**		**-**		**20**	
C_{max}/dose [brain] ng·g^{-1}/(mg·kg^{-1}) (fold)	99	(1.0 X)	173	(1.7 X)	207	(2.1 X)	461	(4.6 X)
AUC_{15-480}/dose [brain] ng·min·g^{-1}/(mg·kg^{-1}) (fold)	32,251	(1.0 X)	49,148	(1.5 X)	59,177	(1.8 X)	147,461	(4.6 X)
AUC_{15-480}/dose [plasma] ng·min·ml^{-1}/(mg·kg^{-1}) (fold)	253,045	(1.0 X)	264,261	(1.0 X)	264,602	(1.0 X)	287,407	(1.1 X)
AUC_{15-480}/dose [brain]/AUC_{15-480}/dose [plasma] (fold)	0.13	(1.0 X)	0.19	(1.4 X)	0.22	(1.8 X)	0.51	(3.9 X)

Figure 4-2 Effect of Ac12Az9 and GF120918 on PK and brain distribution profiles of sorafenib in BALB/c mice
(A) Brain concentration-time curves of **Ac12Az9** and GF120918; (B) Plasma concentration-time curves of **Ac12Az9** and GF120918; (C) Brain-to-plasma ratio of **Ac12Az9** and GF120918; (D) Brain concentration-time curves of sorafenib with or without modulators; (E) Plasma concentration-time curves of sorafenib with or without modulators; (F) Brain-to-plasma ratio of sorafenib with or without modulators; (G) Calculated PK parameters of sorafenib.
Mice in the sorafenib alone group received 50 mg/kg of sorafenib orally, whereas mice in the co-administration group received intravenous injections of **Ac12Az9** (10, 20 mg/kg) or GF120918 (20 mg/kg), respectively, one hour after receiving sorafenib orally. Blood and brain samples were taken at different intervals (5 min, 15 min, 30 min, 1 h, 2 h, 4 h, 6 h, and 8 h, respectively). Plasma and brain concentration of sorafenib were determined by UPLC-MS/MS. The data was presented as mean ± SEM (n = 2-3). A non-compartmental analysis was performed using PK Solutions 2.0.3 software (Ashland, OH44805, USA) to calculate the C_{max} and AUC values.

4.2.3 Effect of Ac12Az9 on the tissue accumulation of sorafenib in BALB/c mice

P-gp or BCRP/ABCG2 was expressed in the kidneys and liver [203]. The effect of **Ac12Az9** on sorafenib accumulation in these organs of BALB/c mice was also investigated. As shown in **Figure 4-3A-B**, the $AUC_{65\text{-}420}$ of sorafenib in kidneys and liver was 21,637,88 and 34,120,480 ng·min/g, respectively. **Ac12Az9** did not affect the accumulation of sorafenib in the kidneys and liver, with kidneys $AUC_{65\text{-}420}$ of 21,535,175 ng·min/g (1.0-fold over sorafenib alone) and liver $AUC_{65\text{-}420}$ of 30,562,517 ng·min/g (0.9-fold over sorafenib alone). This suggested that **Ac12Az9** should not impose any toxicity on the kidneys or liver.

A

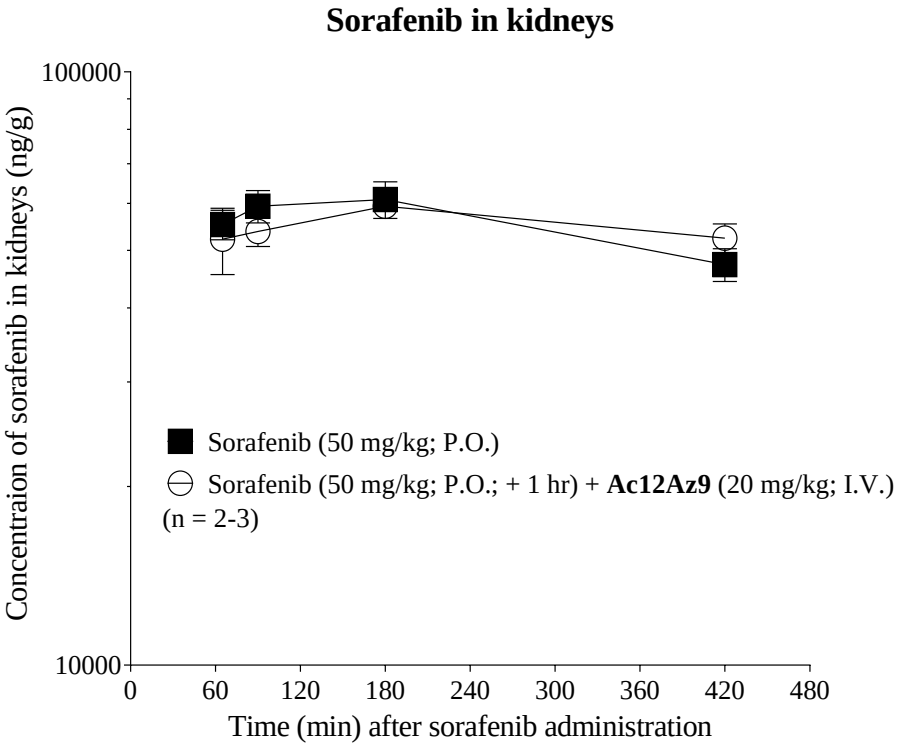

Adminstration route	**P.O.**		**P.O., 1 hr, I.V.**	
Sorafenib (mg/kg)	**50**		**50**	
Ac12Az9 (mg/kg)	**-**		**20**	
$AUC_{65\text{-}420}$ [kidneys] ng·min/g (fold)	21,637,888	(1.0 X)	21,535,175	(1.0 X)

B

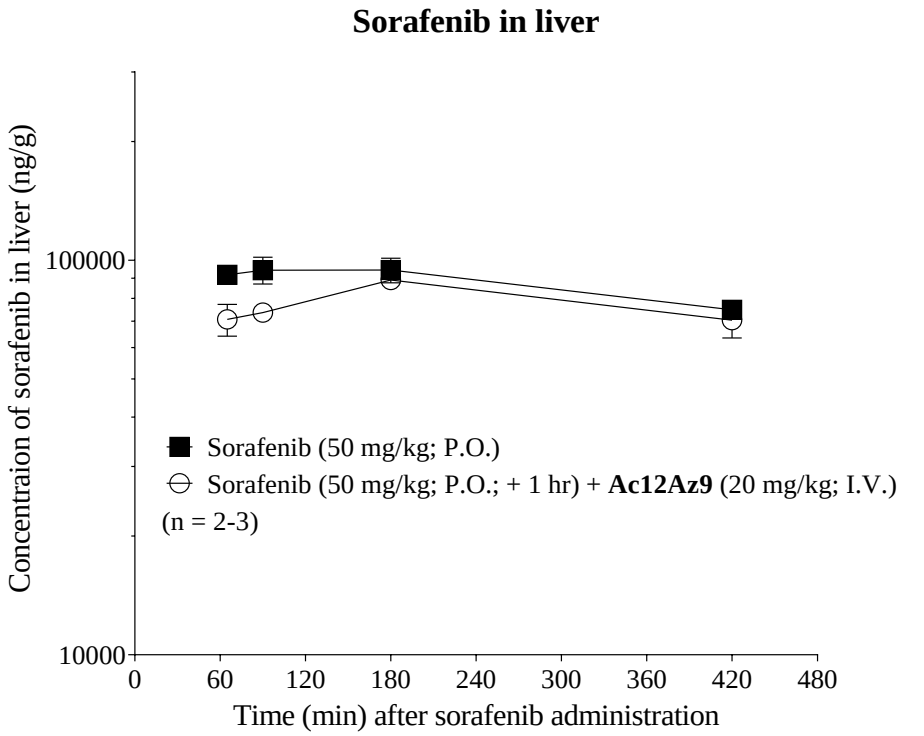

Adminstration route	**P.O.**		**P.O., 1 hr, I.V.**	
Sorafenib (mg/kg)	**50**		**50**	
Ac12Az9 (mg/kg)	**-**		**20**	
$AUC_{65\text{-}420}$ [liver] ng·min/g (fold)	34,120,480	(1.0 X)	30,562,517	(0.9 X)

Figure 4-3 Effect of Ac12Az9 on tissue accumulation of sorafenib in BALB/c mice
(A) Kidneys concentration-time curves of sorafenib with or without **Ac12Az9**; (B) Liver concentration-time curves of sorafenib with or without **Ac12Az9**.
Mice in the sorafenib alone group received 50 mg/kg of sorafenib orally, whereas mice in the co-administration group received intravenous injections of **Ac12Az9** (20 mg/kg), respectively, one hour after receiving sorafenib orally. Kidneys and liver samples were collected at various time points (60 min, 95 min, 180 min, and 420 min), respectively. The concentration of sorafenib was determined by UPLC-MS/MS. The data was presented as mean ± SEM (n = 2-3). A non-compartmental analysis was performed using PK Solutions 2.0.3 software (Ashland, OH44805, USA) to calculate the AUC values.

4.2.4 *In vivo* toxicity evaluation studies of sorafenib combined with Ac12Az9 in BALB/c mice

The toxicity of multiple doses of sorafenib (50 mg/kg, P.O.) without or with **Ac12Az9** (20 mg/kg, I.V.) was evaluated in BALB/c mice. Seven groups (n = 4) of BALB/c mice (6-8 weeks) received a total of nine treatments every other day (q.o.d. x 9). They were (1) untreated control, (2) sorafenib solvent (P.O.), (3) **Ac12Az9** solvent (I.V.), (4) sorafenib solvent (P.O.; 1 hr) + **Ac12Az9** solvent (I.V.), (5) sorafenib (50 mg/kg, P.O.; + 1 hr) + **Ac12Az9** solvent (I.V.), (6) sorafenib solvent (P.O.; + 1 hr) + **Ac12Az9** (20 mg/kg, I.V.), and (7) sorafenib (50 mg/kg, P.O.; + 1 hr) + **Ac12Az9** (20 mg/kg, I.V.).

Figure 4-4A-B demonstrated that all treatment groups saw an increase in body weight at the end of the experiment that ranged from 2.82% to 12.07%. No mice died during or after the treatment period from day 0 to 20. Blank solvent for sorafenib, solvent for **Ac12Az9**, or the combination of these two solvents did not affect the liver-to-body weight ratio, with values of 0.056, 0.054, or 0.051 compared to 0.056 in the untreated control (**Figure 4-4B**). **Ac12Az9** alone and the combination of sorafenib and **Ac12Az9** decreased the liver-to-body weight ratio to 0.047 ($p < 0.05$ over double blank solvent) and 0.048 ($p < 0.05$ over double blank solvent), respectively (**Figure 4-4B**). The plasma levels of ALT and AST did not significantly increase in all treatment groups compared to the untreated or solvent control group (**Figure 4-4B**), indicating that the liver functions of the mice were unaffected. The kidneys-to-body weight ratio showed no significant change across groups, with the ratios ranging from 0.016 to 0.018 (**Figure 4-4B**). The plasma levels of BUN and CRE showed no significant difference among groups, with values ranging from 13.31 to 16.19 mmol/L and from 21.98 to 28.46 μmol/L (**Figure 4-4B**), respectively, indicating that the renal functions were normal in mice.

A

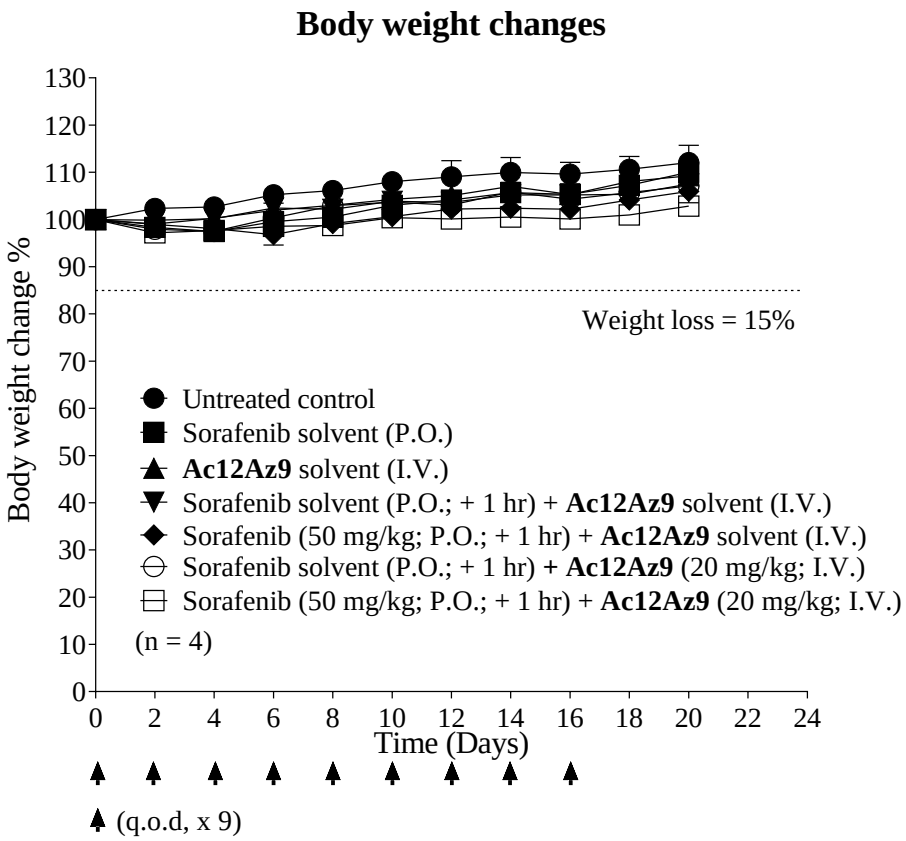
Body weight changes
Body weight change %
130
120
110
100
90
80
70
60
50
40
30
20
10
0
Weight loss = 15%
Untreated control
Sorafenib solvent (P.O.)
Ac12Az9 solvent (I.V.)
Sorafenib solvent (P.O.; + 1 hr) + Ac12Az9 solvent (I.V.)
Sorafenib (50 mg/kg; P.O.; + 1 hr) + Ac12Az9 solvent (I.V.)
Sorafenib solvent (P.O.; + 1 hr) + Ac12Az9 (20 mg/kg; I.V.)
Sorafenib (50 mg/kg; P.O.; + 1 hr) + Ac12Az9 (20 mg/kg; I.V.)
(n = 4)
0 2 4 6 8 10 12 14 16 18 20 22 24
Time (Days)
(q.o.d, x 9)

B

Groups	Treatment	Deaths	Weight changes (%)	Liver-to-body weight ratio	ALT (U/L)	AST (U/L)	Kidney-to-body weight ratio	BUN (mmol/L)	CRE (μmol/L)
1	Untreated control (P.O. + I.V.)	0/4	12.07 ± 7.29	0.056 ± 0.004	4.00 ± 2.46	4.42 ± 0.54	0.016 ± 0.002	15.88 ± 0.89	24.66 ± 5.60
2	Sorafenib solvent (P.O.)	0/4	10.03 ± 4.86	0.056 ± 0.006	4.97 ± 2.24	4.81 ± 0.20	0.017 ± 0.001	14.56 ± 1.49	21.98 ± 5.89
3	**Ac12Az9** solvent (I.V.)	0/4	9.27 ± 1.98	0.054 ± 0.001	2.83 ± 1.10	3.85 ± 0.47	0.017 ± 0.001	16.19 ± 1.15	28.46 ± 6.61
4	Sorafenib solvent (P.O.) + **Ac12Az9** solvent (I.V.)	0/4	7.52 ± 3.84	0.051 ± 0.001	2.76 ± 1.42	4.00 ± 0.66	0.018 ± 0.002	15.37 ± 1.96	26.82 ± 3.50
5	Sorafenib (50 mg/kg; P.O.) + **Ac12Az9** solvent (I.V.)	0/4	5.97 ± 4.78	0.050 ± 0.001	3.59 ± 1.10	3.58 ± 0.23	0.017 ± 0.000	13.31 ± 1.19	28.28 ± 3.65
6	Sorafenib solvent + **Ac12Az9** (20 mg/kg; I.V.)	0/4	7.12 ± 1.92	0.047 ± 0.002[b]	3.35 ± 1.68	4.25 ± 0.88	0.017 ± 0.001	15.20 ± 1.99	24.71 ± 7.33
7	Sorafenib (50 mg/kg; P.O.) + **Ac12Az9** (20 mg/kg; I.V.)	0/4	2.82 ± 0.88	0.048 ± 0.002[b]	2.62 ± 0.82	4.04 ± 0.70	0.017 ± 0.000	14.17 ± 1.98	22.43 ± 2.84

Figure 4-4 *In vivo* toxicity evaluation of sorafenib combined with Ac12Az9 in BALB/c mice

(A) Body weight changes of BALB/c mice after repeated administration of sorafenib with or without **Ac12Az9**; (B) The deaths, percentage weight changes, and levels of ALT, AST, BUN, and CRE in mice plasma.

Sorafenib (50 mg/kg) was administered orally, and **Ac12Az9** (20 mg/kg) was administered intravenously an hour later. Arrows in the figure represented the drug administration 9 times in total. The solvent for sorafenib was NMP: CrEL: 5% Tween-80 (5: 5: 90), while the solvent for **Ac12Az9** was NMP: CrEL: 5% Tween-80 (10: 10: 80). From day 0 to day 20, animal weight changes and activity were observed, and toxicity-related deaths were noted. The levels of AST, ALT, CRE, and BUN were measured using various blood test kits. Data was shown in mean ± SD (n = 4). Student's t-test was used to compare the means of two different sets of data. [a]: significance difference was compared with the untreated control group (Group 1) ($p < 0.05$). [b]: significance difference was compared with double solvent control (Group 5) ($p < 0.05$).

4.3 Discussion

In this chapter, a reliable UPLC-MS/MS method for simultaneous quantification of sorafenib and **Ac12Az9** in murine plasma and tissue homogenate was developed and validated (**Methodology 2.2.12**). The optimized UPLC-MS/MS method was applied to the PK study and tissue accumulation of sorafenib and **Ac12Az9**.

Formulation **H** - NMP: CrEL: 5% Tween-80 (10: 10: 80) was chosen as the optimal formulation because it can improve the solubility of **Ac12Az9**, yielded the highest brain distribution of **Ac12Az9,** and was safe to administer. **Ac12Az9** was very hydrophobic with a maximum solubility of 2 mg/mL in this formulation. **Ac12Az9** dissolved in formulation **H** yielded the greatest brain penetration, by producing a brain $AUC_{15\text{-}240}$ of 75,862.1 ng·min/g, which was 1.3-7.2 folds higher than that of the other formulations (**Figure 4-1A**). Besides, formulation **H** was well tolerated in BALB/c mice, resulting in no animal deaths or activity slowdown following a single intravenous dose of **Ac12Az9**.

PK studies indicated that **Ac12Az9** can help sorafenib to penetrate through the BBB and accumulate more in the brain. Administration of **Ac12Az9** (10 or 20 mg/kg) can increase the AUC_{brain}/AUC_{plasma} of sorafenib by 1.4- or 1.8-fold, respectively, reaching a therapeutic level equivalent to its *in vitro* IC_{50} against U87MG-RedFluc cells (8 μM). This result suggested that dual inhibition of BCRP/ABCG2 and P-gp can increase the brain penetration of sorafenib. Furthermore, **Ac12Az9** had an advantage over other P-gp or BCRP/ABCG2 inhibitors in that it did not affect the distribution of sorafenib in plasma, kidneys, and liver. This is significant given previous reports that P-gp inhibitors, such as quercetin [204] and curcumin [205], may generate unexpected systemic toxicity *in vivo*.

In vivo toxicity study also demonstrated the safety of sorafenib combined with **Ac12Az9** after multiple doses in BALB/c mice. The body weight gains in all treatment groups ranged from 2.82% to 12.07% at the end of the experiment. The liver and kidney function tests also showed that none of the treatment regimens resulted in hepatotoxicity or nephrotoxicity in mice.

4.4 Conclusion

Ac12Az9, a dual P-gp and BCRP/ABCG2 inhibitor could enhance the penetration of sorafenib to the brain without any undesirable systematic toxicity in BALB/c mice. Co-administration of **Ac12Az9** with sorafenib was expected to be effective against GBM.

Chapter 5 Establishment of orthotopic GBM PDX models for efficacy evaluation of sorafenib and Ac12Az9

5.1 Introduction

Laboratory animal tumor models are crucial for anticancer drug development. The cell-line-derived tumor xenografts (CDTXs), despite the ease of establishing, a high rate of tumor formation, and a short cycle, were shown to have lower clinical relevance [206-208]. Long-term *in vitro* culture of cancer cell lines has changed their ability to proliferate and invade as well as resulted in changes to their genetic information [209, 210]. PDX, a more recent cancer model, was developed for preclinical efficacy research. It was developed by implanting fresh tumor samples or cancer cells directly from patients into immunodeficient mice (BALB/c nude mice, NOD/SCID, etc) [211, 212]. This model preserved the original diversity of tumors and mimicked the original environment in which tumor cells develop within the human body. It can accurately predict how a tumor will react to chemotherapeutics. In this chapter, orthotopic GBM PDX models were developed for efficacy studies.

The *in vivo* bioluminescence imaging (BLI) technology was frequently used for the detection of tumors *in situ*. Bioluminescence refers to the emission of light when a luciferin substrate is oxidized by the enzyme luciferase [213]. FLuc gene (consisting of 554 amino acids, or roughly 50 kD), can be integrated into the genome for expression. Stable luciferase transfected cells produced bioluminescence within minutes *in vivo* after reacting with the luciferin substrate [214]. It is important to verify that the expression of luciferase does not affect tumor growth in mice [215]. In preclinical cancer research, BLI is used as an efficient and non-invasive detection approach for the long-term monitoring of tumor development and therapeutic response in small animal models.

In this study, orthotopic GBM PDX models were established. Initially, PDX G22 (TMZ-sensitive) and G28 (TMZ-resistant) cells (from the Mayo Clinic, USA [216]) were transduced with lentiviral vectors expressing FLuc to generate G22-FLuc and G28-FLuc cells. G22-FLuc or G28-FLuc cells were subsequently intracranially implanted into BALB/c nude mice to develop orthotopic GBM PDX models that were either TMZ-sensitive or TMZ-resistant. These models would be used to assess the efficacy of sorafenib and **Ac12Az9**.

5.2 Results

5.2.1 PDX xenograft information

PDX GBM 22 and 28 xenograft lines originated from tumors in several patients. **Table 5-1** listed the patient information, tumor characteristics, and xenograft gene alterations [217, 218].

Table 5-1 Patient characteristics and xenograft gene alterations

Xenograft lines	Age (y)/sex	Diagnosis	Types of xenografts	Therapies prior to xenograft	EGFR status	p53 status	PTEN status
22	80/M	Gliosarcoma	Primary	No	No amplification	Mutant, 273: arg > cys	Wide-type
28	67/M	Gliosarcoma	Primary	No	No amplification	Mutant, 246: met > thr	Mutant, 132: gly > asp

5.2.2 Stable expression of FLuc in PDX GBM cells *in vitro*

Short-term explant cultures from the xenograft tissues (G22 and G28) were genetically engineered to stably express FLuc (G22-FLuc and G28-FLuc).

As shown in **Figure 5-1A**, bioluminescence signals of G22-FLuc or G28-FLuc cells increased by 9 or 10 folds, respectively, compared to G22 or G28. The cellular bioluminescence signal *in vitro* correlated with the cell number, with linear regression coefficient (R^2) values of 0.9423 and 0.9945, respectively (**Figure 5-1B**). Expression of FLuc did not affect the cell proliferation rates of G22-FLuc and G28-FLuc, with cell doubling times of 1.70 and 1.99 days for G22-FLuc and G28-FLuc, respectively, compared to 1.83 days for G22 and 2.10 days for G28 (**Figure 5-1C**).

A

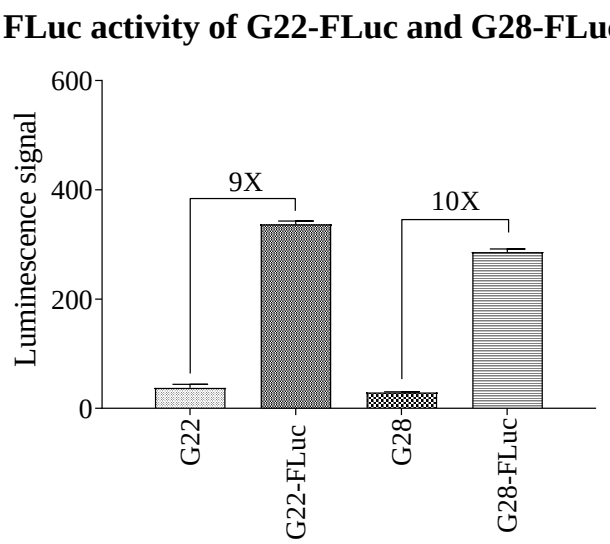

B

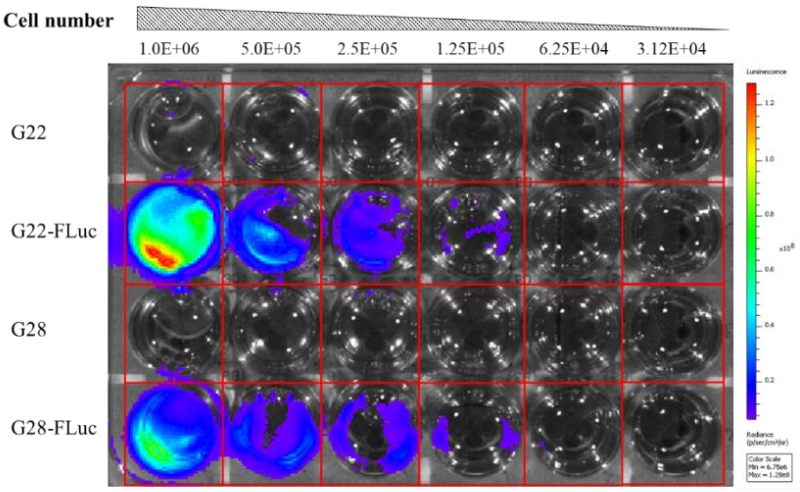

Luminescence (photon/sec/cm²)

G22-FLuc	1.89E+09	5.00E+08	2.85E+08	1.40E+08	5.19E+07	3.60E+07
G28-FLuc	9.22E+08	4.30E+08	2.77E+08	1.11E+08	5.03E+07	2.71E+07

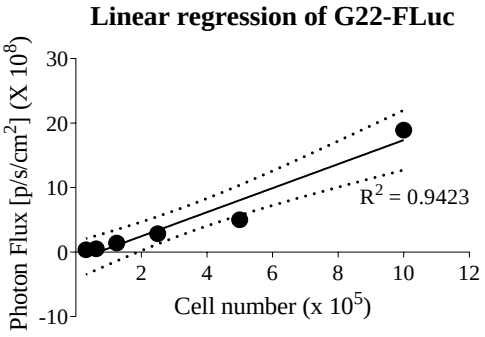

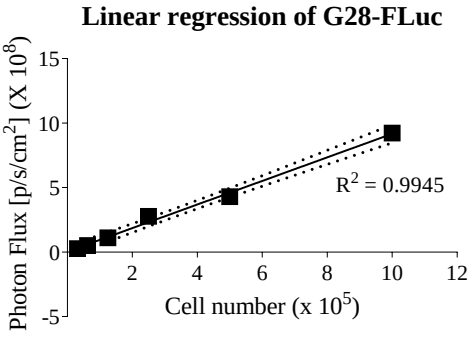

C

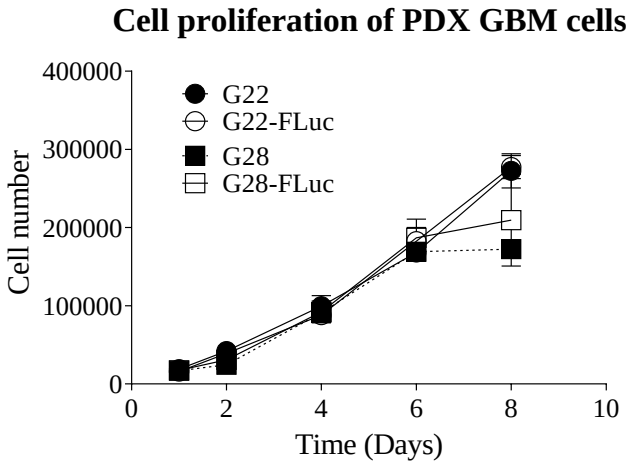

GBM cell lines	G22	G22-FLuc	G28	G28-FLuc
Doubling time (days)	1.83 ± 0.26	1.70 ± 0.02	2.10 ± 0.06	1.99 ± 0.33

Figure 5-1 FLuc activity and cell proliferation rates of PDX G22, G28, G22-FLuc, and G28-FLuc cells

(A) FLuc activity in G22, G28, G22-FLuc, and G28-FLuc cells; (B) Linearity between bioluminescent signal and cell density; (C) Comparison of cell proliferation between G22 and G22-FLuc, G28 and G28-FLuc.

(A) Cells were seeded into a 96-well plate with 1 x 10^4 cells/well. Each well received 20 µL of luciferin (D-Luciferin, 20 mg/mL). After 1 min of incubation protected from light, the cellular luciferase activity was determined using CLARIO Star Microplate Reader.

(B) Cell numbers decreased by 2 from left to right, from 1.0 x 10^6 cells/well to 3.12 x 10^4 cells/well. Each well received 10 µL of luciferin (D-Luciferin, 20 mg/mL. Bioluminescence (photon/sec/sr/cm^2) was evaluated by IVIS after 1 min of incubation under protection from light. Linear regression was analyzed using Prism software.

(C) A total of 2 x 10^4 cells were seeded into a 6-well plate. At different times - days 2, 4, 6, and 8 - the cells were trypsinized and counted manually. The number of cells was recorded, and the growth curve was plotted. Data was present as mean ± SD (n = 2-3).

5.2.3 Cytotoxicity of TMZ and sorafenib towards GBM PDX cells

The sensitivity of PDX GBM cells towards TMZ and sorafenib was measured *in vitro*. U87MG-RedFluc cell line, a TMZ-sensitive cell line both *in vitro* and *in vivo* [195], was employed as a control for TMZ sensitivity. It was found that G22 was sensitive to TMZ, with a lower IC_{50} (160.8 µM) than U87MG-RedFluc (257.3 µM) (**Figure 5-2A, C**). In contrast, G28 had a higher IC_{50} for TMZ (1201.5 µM) than U87MG-RedFluc

(257.3 μM) (**Figure 5-2A, C**), demonstrating that it was TMZ-resistant. U87MG-RedFluc and PDX GBM cells were more sensitive to sorafenib than TMZ. The IC_{50} values of sorafenib were 6.9-10.56 μM compared with 144.8-1201.5 μM for TMZ (**Figure 5-2A-C**). However, both TMZ-sensitive (U87MG-RedFluc, G22, and G22-FLuc) and TMZ-resistant (G28 and G28-FLuc) cells were equally sensitive to sorafenib, with IC_{50} values ranging from 6.48 to 10.56 μM (**Figure 5-2B-C**).

Expression of FLuc did not affect the cytotoxic effect of TMZ and sorafenib in PDX GBM cells. Similar IC_{50} values for TMZ were observed in G22 and G22-FLuc cells (160.8 and 144.8 μM) and in G28 and G28-FLuc cells (1180.5 and 1201.5 μM) (**Figure 5-2A, C**). Similarly, FLuc did not affect the cytotoxic effect of sorafenib in PDX GBM cells. The IC_{50}s of sorafenib in G22 and G22-FLuc cells were similar (10.56 and 8.65 μM), and the same was true for G28 and G28-FLuc cells (10.29 and 6.48 μM) (**Figure 5-2B-C**). In addition, **Ac12Az9** alone showed no cytotoxicity toward any of the GBM cells.

A

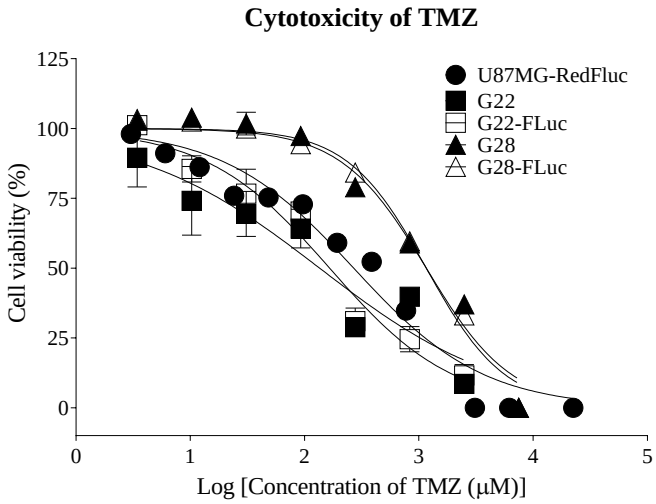

B

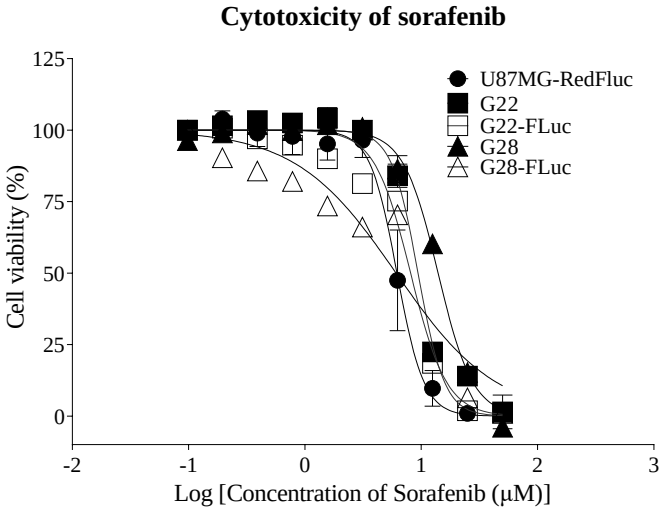

C

Anticancer drugs	IC_{50} (μM) of compounds towards different GBM cell lines				
	U87MG-RedFluc	G22	G22-FLuc	G28	G28-FLuc
TMZ	257.3 ± 20.4	160.8 ± 24.8	144.8 ± 11.2	1201.5 ± 54.4	1180.5 ± 3.54
Sorafenib	6.90 ± 0.20	10.56 ± 1.33	8.65 ± 1.67	10.29 ± 1.02	6.48 ± 1.81
Ac12Az9	> 100	> 100	> 100	> 100	> 100

Figure 5-2 Cytotoxicity of TMZ, sorafenib, and Ac12Az9 towards U87MG-RedFluc and PDX GBM cells

MTS assay of (A) TMZ; (B) sorafenib; (C) IC_{50} values of TMZ, sorafenib, and **Ac12Az9** towards U87MG-RedFluc and PDX GBM cells.

Cells were seeded into a 96-well plate with 4500 cells/well. Sorafenib and TMZ were added into

wells at varying concentrations (0, 0.027, 0.082, 0.25, 0.74, 2.2, 6.7, and 20 μM each for sorafenib and 0, 3.4, 10.3, 30.9, 92.6, 277.8, 833.3, and 2500 μM each for TMZ), respectively. Cell viability was measured after 4 days of incubation. Data was present as mean ± SD (n = 2-3). IC_{50} values of anticancer drugs were calculated by PRISM software.

5.2.4 Bioluminescence measurement of G22-FLuc and G28-FLuc in BALB/c nude mice

Expression of FLuc in G22-FLuc and G28-FLuc cells was further examined *in vivo*. PDX GBM cells (G22-FLuc or G28-FLuc) were implanted intracranially in the BALB/c nude mice (See **Methodology 2.3.3** for animal intracranial implantation). The tumor-bearing mice did not receive any medication throughout the observation period. Bioluminescence was used to quantify the tumor volume. Animal death was recorded once they become moribund. Bioluminescence signals in both G22-FLuc and G28-FLuc tumors were detectable, and these signals were found to be correlated with tumor progression (**Figure 5-3A-C**). Expression of FLuc did not affect the survival times of tumor-bearing mice; they were 26 and 33 days (p = 0.1010) for G22 and G22-FLuc, respectively, and 67 and 63 days (p = 0.8980) for G28 and G28-FLuc (**Figure 5-3D**). The findings suggested that G22-FLuc and G28-FLuc may be used reliably and accurately for *in vivo* efficacy studies.

A

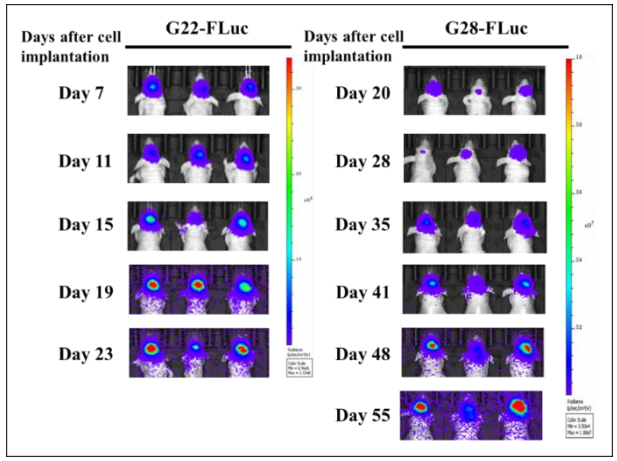

B

Bioluminescence signals of intracranial G22-FLuc tumor

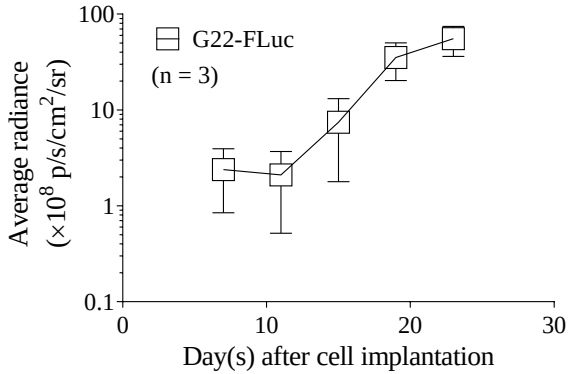

C

Bioluminescence signals of intracranial G28-FLuc tumor

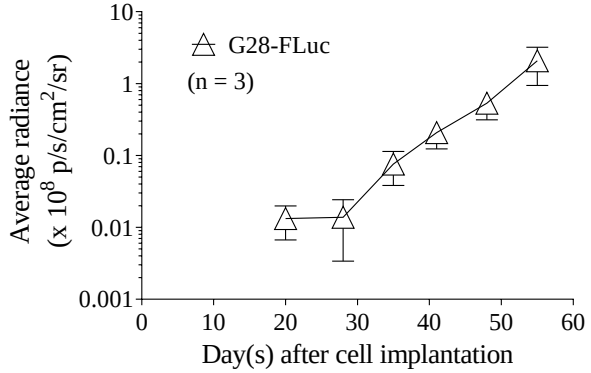

D

Survival times of tumor-bearing nude mice with different PDX GBM tumors

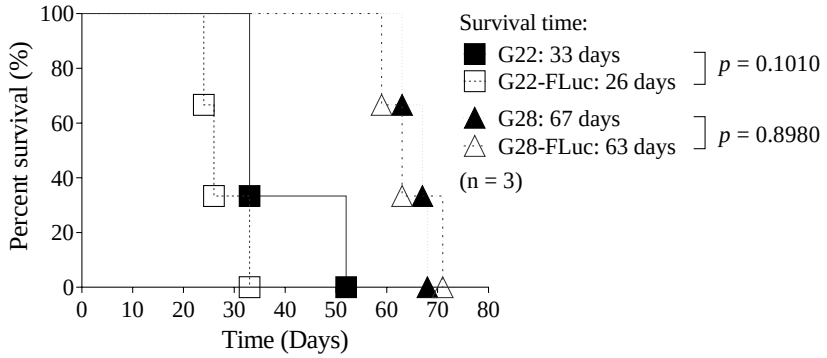

Figure 5-3 IVIS imaging and survival times of BALB/c nude mice with intracranial G22, G28, G22-FLuc, and G28-FLuc tumors (n = 3)

(A) IVIS Images of mice brain tumors after cell implantation; (B) Quantification of intracranial G22-FLuc tumor volume; (C) Quantification of intracranial G28-FLuc tumor volume; (D) Survival analysis of tumor-bearing nude mice with G22, G22-FLuc, G28, and G28-FLuc cells.

A total of 3 x 10^5 PDX GBM cells were implanted intracranially in BALB/c nude mice. Mice were anesthetized by isopropanol inhalation before each bioluminescence test, and then D-luciferin (150 mg/kg) was injected intraperitoneally. Bioluminescence signals were measured using IVIS. The mice were put to death when they were in a terminal condition, and their length of survival was noted. Log-rank test was used to compare the survival time between the G22 and G22-FLuc and between G28 and G28-FLuc. Statistics were deemed significant if the *p*-value was less than 0.05.

5.2.5 Evaluation of TMZ efficacy in orthotopic PDX GBM xenografts

The BALB/c nude mice implanted with intracranial G22-FLuc or G28-FLuc tumors were treated with either (1) untreated control, (2) TMZ (10 mg/kg, I.V.), or (3) TMZ (10 mg/kg, P.O.). Drug was administered to the mice every other day for a total of 10 doses (q.o.d, x 10).

It was found that TMZ when administered intravenously or orally, can completely reduce the tumor sizes of G22-FLuc by 100% (p = 0.0357) compared to the untreated group (**Figure 5-4A-B**). Overall survival of the TMZ groups (94 or 85 days) was significantly better than that of the untreated group (25 days, p = 0.0246 or 0.0246, respectively) (**Figure 5-4C**). Besides, mice in the TMZ group, either via intravenous injection or oral administration, did not lose body weight during or after the treatment period (**Figure 5-4D**), suggesting that TMZ was safe to use in GBM treatment.

In contrast, G28-FLuc tumors were more resistant to TMZ than G22-FLuc tumors. TMZ inhibited tumor growth of G28-FLuc by 92.25% compared to the untreated group, but this difference was not statistically significant (p = 0.2373) (**Figure 5-5B (1)**). TMZ did not extend the survival time of tumor-bearing mice, with 61 days (p = 0.4855) in both the untreated group and the TMZ treatment group (**Figure 5-5C**). Multiple doses of TMZ did not cause body weight loss in the G28-FLuc animal xenograft (**Figure 5-5D**).

To obtain an animal model with higher TMZ tolerance, G28-FLuc tumors were isolated from the animal after one round of TMZ treatment. These G28-FLuc cells were cultured *in vitro* and named "TMZ-selected G28-FLuc" (**Figure 5-5B**). It was found that TMZ-selected G28-FLuc cells were more resistant to TMZ *in vitro* (IC_{50} = 1691-1573 μM) compared to the naïve G28-FLuc cells (IC_{50} = 1180.5 μM) (**Figure 5-5B (2)**). Importantly, different passages of TMZ-selected G28-FLuc cells retained sensitivity

towards sorafenib (IC_{50} = 8.4-9.3 μM) similar to that of naïve G28-FLuc cells (IC_{50} = 8.5 μM) (**Figure 5-5B (3)**). To confirm that the TMZ-selected G28-FLuc cells were indeed TMZ-resistant, these cells were reinoculated intracranially into another BALB/c nude mice. It was found that TMZ treatment can only inhibit the tumor volume of TMZ-selected G28-FLuc by 52.46% (p = 0.4293) compared to the untreated group (**Figure 5-5B (4)**), but that it could reduce tumor volume of G28-FLuc by 92.25% (p = 0.2373 versus the untreated group) prior to selection (**Figure 5-5B (1)**).

Taken together, intracranial G22-FLuc and TMZ-selected G28-FLuc cells could be used to develop TMZ-sensitive and -resistant PDX GBM animal models. These models would be used to evaluate the efficacy of the **Ac12Az9** and sorafenib combination.

A

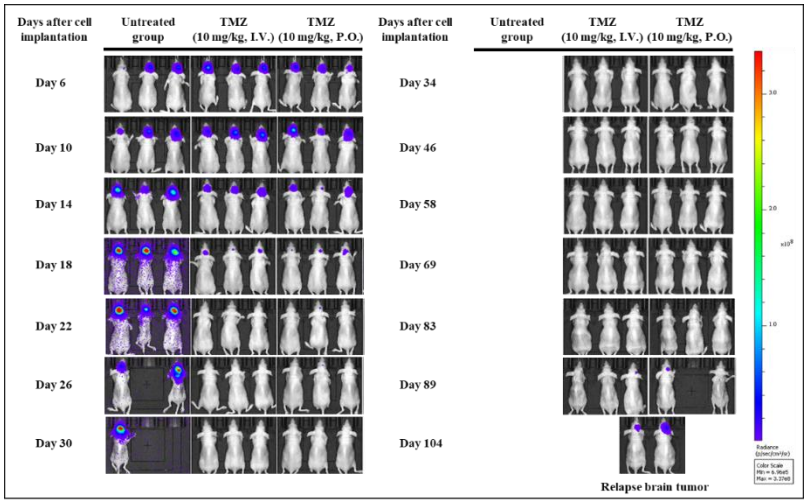
Days after cell implantation
Untreated group
TMZ (10 mg/kg, I.V.)
TMZ (10 mg/kg, P.O.)
Day 6
Day 10
Day 14
Day 18
Day 22
Day 26
Day 30
Day 34
Day 46
Day 58
Day 69
Day 83
Day 89
Day 104
Relapse brain tumor

B

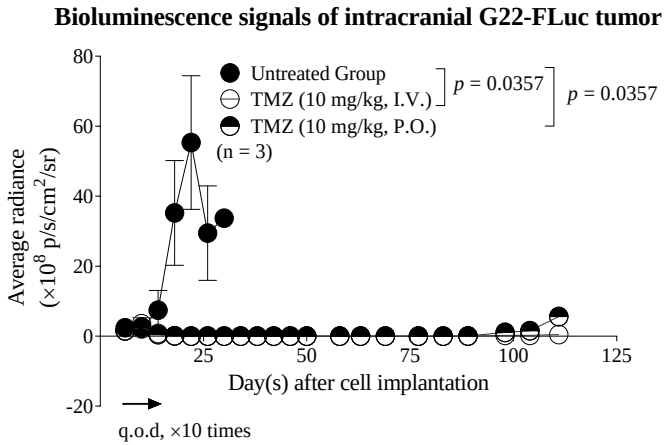
Bioluminescence signals of intracranial G22-FLuc tumor
Untreated Group
TMZ (10 mg/kg, I.V.)
TMZ (10 mg/kg, P.O.)
(n = 3)
p = 0.0357
p = 0.0357
Average radiance (×10^8 p/s/cm^2/sr)
Day(s) after cell implantation
q.o.d, ×10 times

C

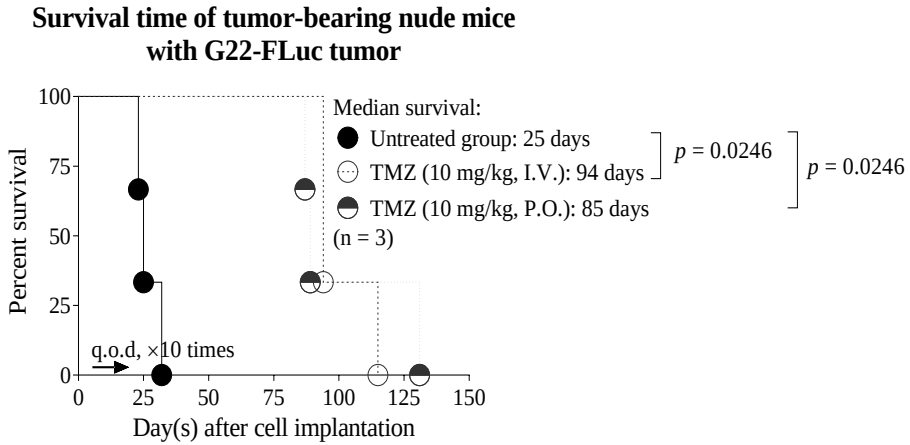
Survival time of tumor-bearing nude mice with G22-FLuc tumor
Median survival:
Untreated group: 25 days
TMZ (10 mg/kg, I.V.): 94 days
TMZ (10 mg/kg, P.O.): 85 days
(n = 3)
p = 0.0246
p = 0.0246
Percent survival
Day(s) after cell implantation
q.o.d, ×10 times

D

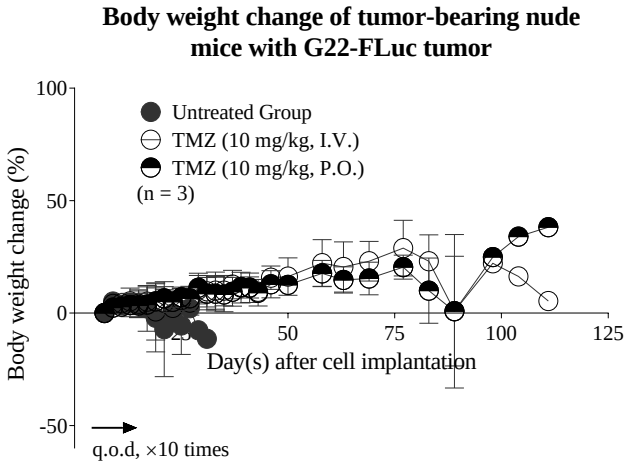
Body weight change of tumor-bearing nude mice with G22-FLuc tumor
Untreated Group
TMZ (10 mg/kg, I.V.)
TMZ (10 mg/kg, P.O.)
(n = 3)
Body weight change (%)
Day(s) after cell implantation
q.o.d, ×10 times

Figure 5-4 *In vivo* efficacy evaluation of TMZ in an intracranial model of G22-FLuc in BALB/c nude mice (n = 3-4)

(A) IVIS Images of mice brain tumors after cell implantation; (B) Bioluminescence signals of intracranial G22-FLuc tumor; (C) Survival times of tumor-bearing nude mice with G22-FLuc cells; (D) Body weight changes of mice with G22-FLuc tumors.

Mice implanted with intracranial G22-FLuc tumors were treated (q.o.d, x 10) with either (1) untreated control, (2) TMZ (10 mg/kg, I.V.), or (3) TMZ (10 mg/kg, P.O.) group. The horizontal arrow denoted the length of the treatment. BLIs were collected from day 6 to day 104 post-cell implantation by IVIS. The animal's weight was recorded during the experiment. The mice were put to death when they were in a terminal condition, and their length of survival was noted. Student's t-test was used to compare the differences in BLIs of tumors between the two groups, while the log-rank was utilized to examine the significant differences in survival time. Statistics were deemed significant if the *p*-value was less than 0.05.

A

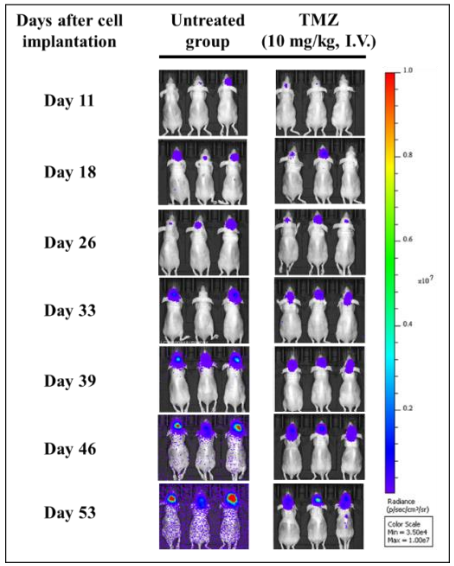
Days after cell implantation
Untreated group
TMZ (10 mg/kg, I.V.)
Day 11
Day 18
Day 26
Day 33
Day 39
Day 46
Day 53

B

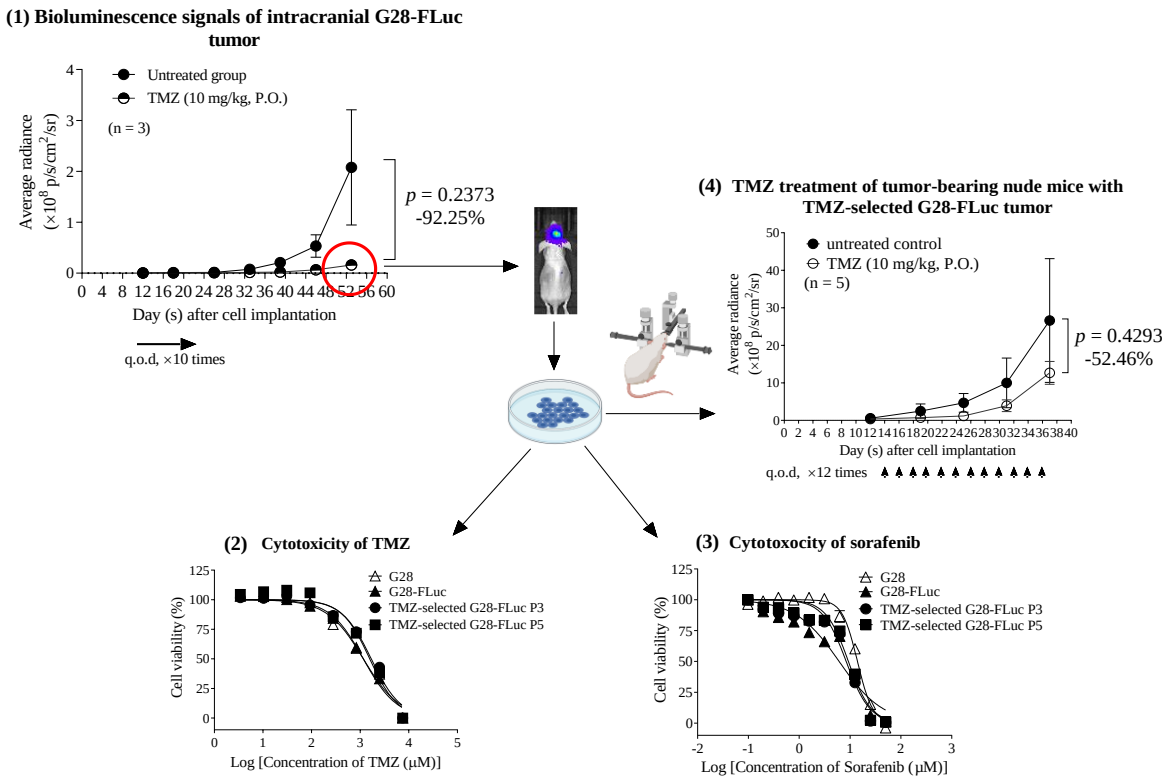
(1) Bioluminescence signals of intracranial G28-FLuc tumor
Untreated group
TMZ (10 mg/kg, P.O.)
(n = 3)
Average radiance (×10^8 p/s/cm^2/sr)
p = 0.2373
-92.25%
Day (s) after cell implantation
q.o.d, ×10 times
(4) TMZ treatment of tumor-bearing nude mice with TMZ-selected G28-FLuc tumor
untreated control
TMZ (10 mg/kg, P.O.)
(n = 5)
Average radiance (×10^6 p/s/cm^2/sr)
p = 0.4293
-52.46%
Day (s) after cell implantation
q.o.d, ×12 times
(2) Cytotoxicity of TMZ
G28
G28-FLuc
TMZ-selected G28-FLuc P3
TMZ-selected G28-FLuc P5
Cell viability (%)
Log [Concentration of TMZ (μM)]
(3) Cytotoxocity of sorafenib
Log [Concentration of Sorafenib (μM)]

C

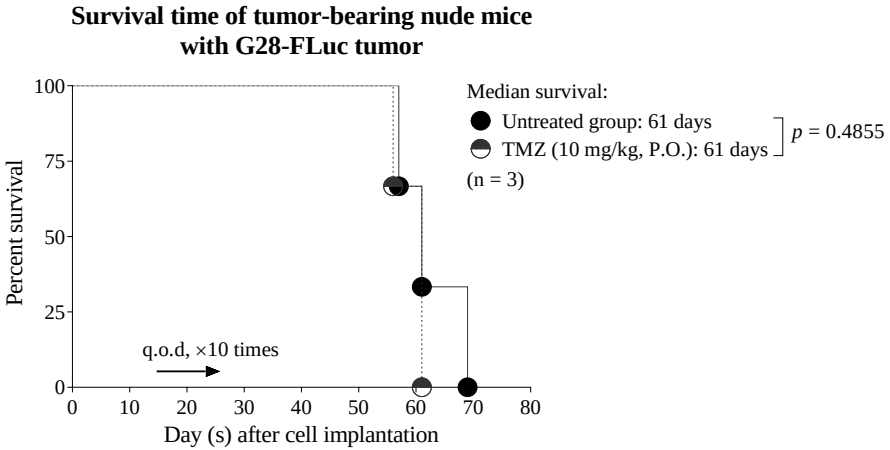

D

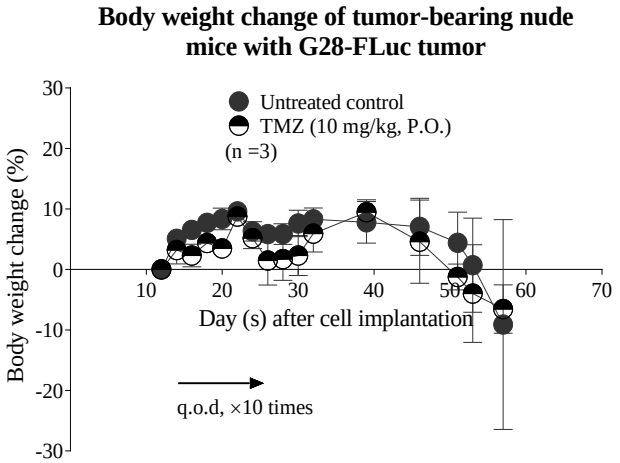

Figure 5-5 *In vivo* efficacy evaluation of TMZ in an intracranial model of G28-FLuc in BALB/c nude mice

(A) IVIS Images of mice brain tumors after cell implantation; (B) Bioluminescence signal of intracranial G28-FLuc tumor, and cytotoxicity test, subsequent inoculation, and TMZ treatment of TMZ-selected G28-FLuc cells both *in vitro* and *in vivo*; (C) Survival times of tumor-bearing nude mice with G28-FLuc cells; (D) Body weight changes of mice with G28-FLuc tumors.

Mice implanted with intracranial G28-FLuc tumors were treated (q.o.d, x 10) with either (1) untreated control, (2) TMZ (10 mg/kg, I.V.), or (3) TMZ (10 mg/kg, P.O.) group. The horizontal arrow denoted the length of the treatment. BLIs were measured after cell implantation by IVIS. The animal's weight was recorded during the experiment. The mice were put to death when they were in a terminal condition, and their length of survival was noted. Student's t-test was used to compare the differences in BLIs of tumors between the two groups, while the log-rank was utilized to examine the significant differences in survival time. Statistics were deemed significant if the *p*-value was less than 0.05.

5.2.6 *In vivo* efficacy study of sorafenib combined with Ac12Az9 in orthotopic G22-FLuc PDX model

BALB/c nude mice were intracranially implanted with G22-FLuc cells. They were treated (q.o.d. x 9) with either (1) solvent control, (2) sorafenib alone, or (3) sorafenib (+ 1 hr) + **Ac12Az9**. Overall survival of the combination group of sorafenib and **Ac12Az9** (28 days) was significantly better than that of the solvent control group (19 days, $p < 0.001$) and the sorafenib alone group (24 days, $p = 0.014$) (**Figure 5-6A**). Co-treatment of sorafenib and **Ac12Az9** can inhibit the tumor growth better than the solvent control group by 56.7% ($p = 0.13$) or the sorafenib alone group by 48.5% ($p = 0.18$) (**Figure 5-6B**). The lack of statistical significance may be due to the death of some mice in the solvent control group and sorafenib alone group. This result demonstrated the efficacy of sorafenib combined with **Ac12Az9** in the treatment of GBM.

Sorafenib alone led to body weight loss in orthotopic tumor-bearing mice for unknown reasons (**Figure 5-6C**). Fortunately, **Ac12Az9** did not aggravate such weight loss in tumor-bearing mice (**Figure 5-6C**), which further demonstrated its safety in combination use. The weight loss in the later stage of the treatment was accompanied by the progression of cancer, but the treatment group of sorafenib and **Ac12Az9** did not lose as much weight as the sorafenib alone group, and the solvent control group did. This result also suggested that the co-treatment of sorafenib and **Ac12Az9** could slow the progression of GBM.

A

Survival times of tumor-bearing nude mice with G22-FLuc tumor

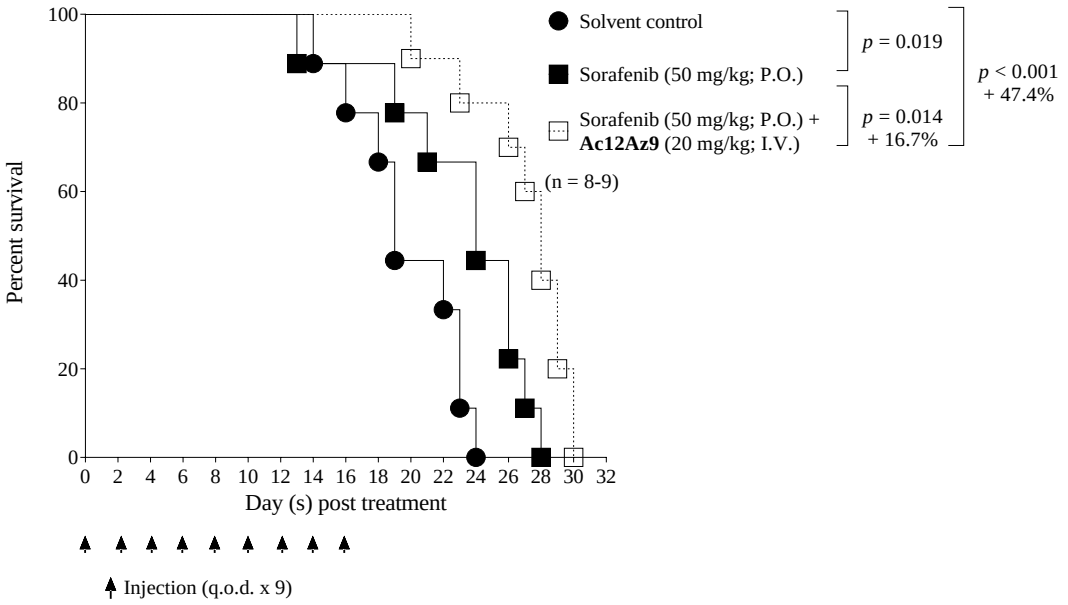

B

Bioluminescence signals of intracranial G22-FLuc tumor

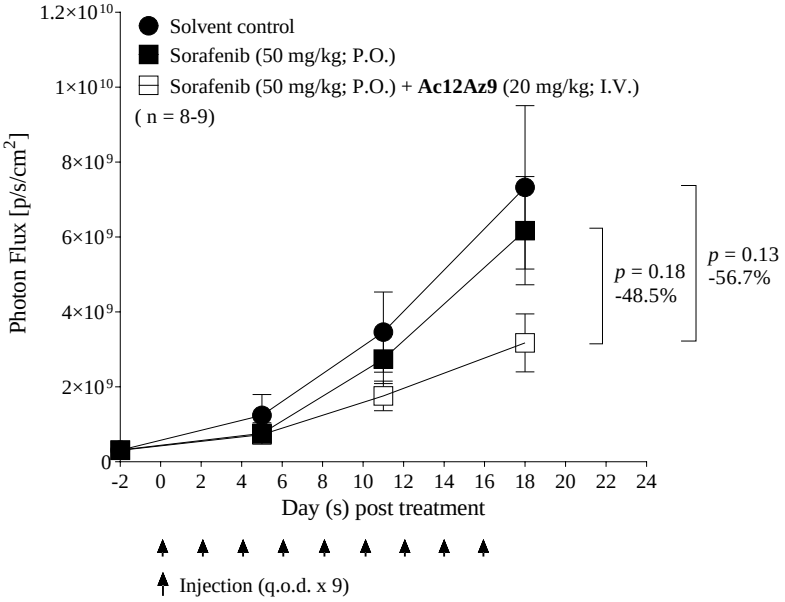

C

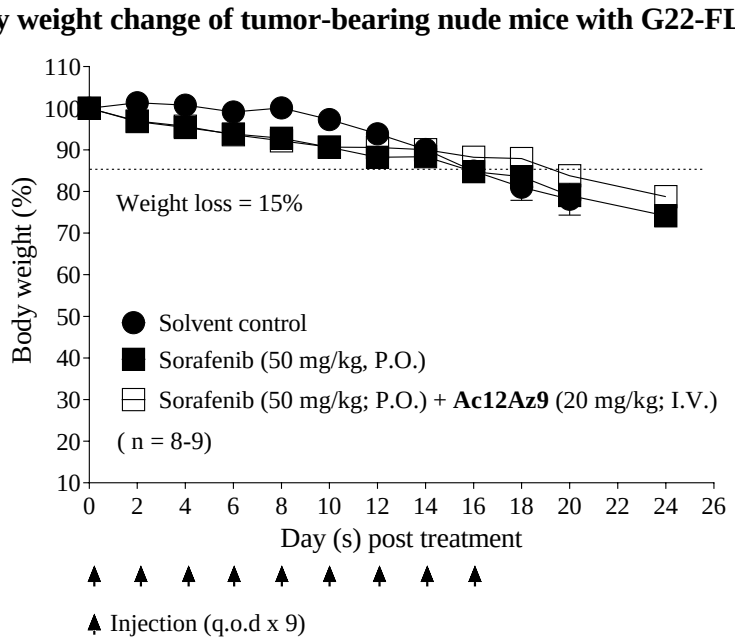

Figure 5-6 *In vivo* efficacy evaluation of sorafenib and Ac12Az9 in an intracranial model of PDX GBM G22-FLuc cells (n = 8-9)

(A) Survival times of tumor-bearing nude mice with G22-FLuc cells; (B) Bioluminescence signals of intracranial G22-FLuc tumor; (C) Body weight changes of mice with G22-FLuc tumors.

Mice implanted with intracranial G22-FLuc tumors were treated (q.o.d, x 9) with either (1) solvent control, (2) sorafenib (50 mg/kg, P.O.) group or (3) sorafenib (50 mg/kg, P.O.) + **Ac12Az9** (20 mg/kg, I.V.). BLIs were collected post-cell implantation by IVIS. The animal's weight was recorded during the experiment. The mice were put to death when they were in a terminal condition, and their length of survival was noted. Student's t-test was used to compare the differences in BLIs of tumors between the two groups, while the log-rank was utilized to examine the significant differences in survival time. Statistics were deemed significant if the *p*-value was less than 0.05.

5.2.7 *In vivo* efficacy study of sorafenib combined with Ac12Az9 in orthotopic TMZ-selected G28-FLuc PDX model

The BALB/c nude mice implanted with intracranial TMZ-selected G28-FLuc tumors were treated (q.o.d. x 10) with either (1) solvent control, (2) sorafenib alone, (3) sorafenib (+ 1 hr) + **Ac12Az9**, or (4) sorafenib (+ 1 hr) + GF120918. All the treatment groups (sorafenib alone, sorafenib + **Ac12Az9**, and sorafenib + GF120918) were found to marginally inhibit tumor growth by 36.5%-44.7% (p = 0.4405-0.5790) compared to the solvent control **(Figure 5-7A)**. Unexpectedly, **Ac12Az9** did not improve the inhibitory effect of sorafenib on TMZ-selected G28-FLuc tumor (**Figure 5-7A**). Even GF120918, a known dual P-gp and BCRP/ABCG2 inhibitor, failed to enhance the tumor inhibition of sorafenib (**Figure 5-7A**).

Each group experienced a body weight reduction between 8.5% and 13.5% following treatment, demonstrating that the drug intervention did not lessen the tumor burden of mice (**Figure 5-7B**).

A

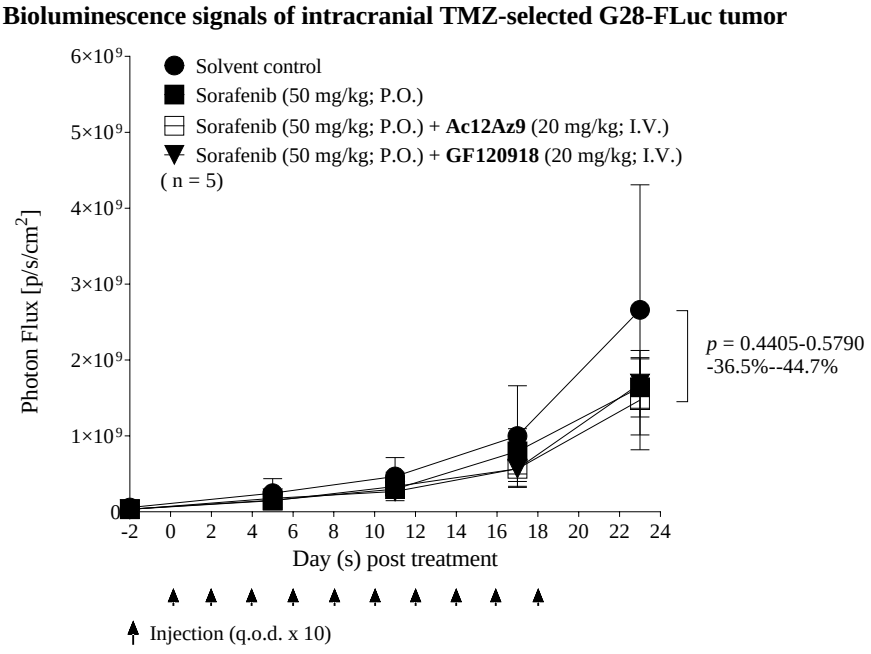

B

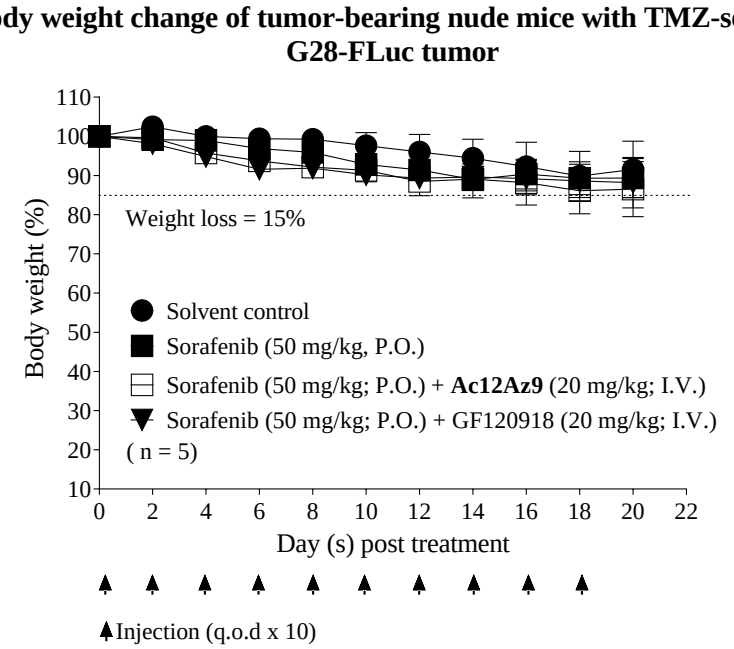

Figure 5-7 *In vivo* efficacy evaluation of sorafenib and Ac12Az9 in an intracranial model of TMZ-selected G28-FLuc in BALB/c nude mice (n = 5)

(A) Bioluminescence signals of intracranial TMZ-selected G28-FLuc tumor; (B) Body weight changes of mice with TMZ-selected G28-FLuc tumors.

Mice implanted with intracranial TMZ-selected G28-FLuc tumors were treated (q.o.d, x 10) with either (1) solvent control, (2) sorafenib (50 mg/kg, P.O.) group, (3) sorafenib (50 mg/kg, P.O.) + **Ac12Az9** (20 mg/kg, I.V.), or (4) sorafenib (50 mg/kg, P.O.) + GF120918 (20 mg/kg, I.V.). BLIs were collected post-cell implantation by IVIS. The animal's weight was recorded during the experiment. The mice were put to death when they were in a terminal condition. Student's t-test was used to compare the differences in BLIs of tumors between the two groups. Statistics were deemed significant if the *p*-value was less than 0.05.

5.3 Discussion

U87MG-human brain GBM has been widely used for *in vivo* efficacy evaluation of potential GBM therapies. However, it was different from PDX GBM models [219]. The use of this model usually resulted in a discrepancy between preclinical efficacy and clinical response for GBM. The GBM PDXs retained the histological, genetic, and epigenetic features of the parental tumor in the early passages [220, 221], allowing it to recapitulate the molecular heterogeneity of their original clinical samples. Thus, GBM PDX models in mice can be used to predict therapeutic outcomes accurately.

The short-term explant cultures of two PDX GBM xenograft lines - G22 and G28 (from the Mayo Clinic, USA [222]) were established, and their responses to TMZ and sorafenib were evaluated. When compared to U87MG-RedFluc (IC_{50} = 257.3 μM), G22 had a lower IC_{50} of 160.8 μM and was more sensitive to TMZ, whereas G28 had a higher IC_{50} of 1201.5 μM and was more resistant to TMZ. The IC_{50} values of sorafenib towards U87MG-RedFluc, G22, and G28 were between 6.90-10.56 μM, indicating that they were all sensitive to sorafenib.

The PDX GBM xenograft lines - G22 and G28 were further genetically engineered to stably express FLuc (G22-FLuc and G28-FLuc). The bioluminescence signals of the G22-FLuc and G28-FLuc cell cultures were positively correlated with the cell number *in vitro*. Expression of FLuc did not affect the cell proliferation rates of G22-FLuc and G28-FLuc. Besides, the cellular FLuc expression had no impact on the cytotoxic effect of TMZ and sorafenib on PDX GBM cells.

PDX G22-FLuc and G28-FLuc cells were implanted intracranially in the athymic nude mice to establish orthotopic GBM PDX models. The bioluminescence signals of G22-FLuc and G28-FLuc were found to correlate with tumor volume *in vivo*. Besides, expression of FLuc did not significantly affect the survival times of tumor-bearing nude

mice, with 26 days for G22-FLuc (p = 0.1010) compared to 33 days for G22 and 63 days for G28-FLuc (p = 0.8980) compared to 67 days for G28.

The established GBM PDX models (G22-FLuc and G28-FLuc) were further found to be TMZ-sensitive and -resistant, respectively, in the animal model. It was found that TMZ (10 mg/kg, I.V., or P.O.) not only inhibited the growth of G22-FLuc tumors by 100% (p = 0.0357), but it also significantly extended the survival time of tumor-bearing mice, increasing it to 94 (p = 0.0246) and 85 (p = 0.0246) days, respectively, as opposed to 25 days in the untreated group. In contrast, TMZ did not prolong the survival of nude mice bearing G28-FLuc tumors despite decreasing tumor growth (p = 0.2373 versus the untreated group).

To obtain a more TMZ-resistant model, the tumor cells from the TMZ-treated G28-FLuc tumor were isolated and renamed TMZ-selected G28-FLuc cells. TMZ-selected G28-FLuc cells (IC_{50} = 1691-1573 μM) were more resistant to TMZ compared to parental G28-FLuc cells (IC_{50} = 1180.5 μM). Furthermore, TMZ failed to suppress an orthotopic GBM model established with TMZ-selected G28-FLuc cells. As a result, the TMZ-sensitive and -resistant GBM PDX models were successfully developed, and they would be utilized to evaluate the efficacy of the sorafenib and **Ac12Az9** combination.

In an orthotopic G22-FLuc xenograft model, co-administration of **Ac12Az9** and sorafenib could suppress tumor growth by 56.7% (p = 0.13) and prolong the life span of tumor-bearing nude mice by 47.4% (p = 0.01) when compared to the solvent control group. However, this combination was not effective in the TMZ-resistant model of G28-FLuc cells. Even sorafenib and GF120918 (a well-known P-gp and BCRP/ABCG2 inhibitor) failed to stop the growth of the TMZ-selected G28-FLuc tumor. The above efficacy results led me to the following analysis: *In vitro* cytotoxicity studies with sorafenib were effective against both G22-FLuc and TMZ-selected G28-FLuc cells, with IC_{50} values of 8.4-9.3 μM. However, unlike the culture setting *in vitro*,

the *in vivo* tumor microenvironment has a more complex effect on the growth and proliferation of cancer cells. As a result, the cytotoxic effect of anticancer drugs *in vitro* does not always accurately predict the tumor response *in vivo*. To be specific, as a tumor grows *in vivo*, many distinct genes are altered, which could result in the formation of new cell types or even the expansion of sorafenib-resistant cell subsets. This may also be the reason why sorafenib and **Ac12Az9** are unsuccessful in the treatment of TMZ-selected G28-FLuc cancers. Additionally, further verification of the second experiment would be necessary because the sorafenib and **Ac12Az9** efficacy evaluation experiment in the TMZ-selected G28-FLuc model was only performed once and the initial intervention time and administration times were not optimized.

5.4 Conclusion

FLuc was stably expressed in PDX G22 and G28 cells, allowing the real-time monitoring of intracranial tumors in mice by BLI. The TMZ-sensitive (G22-FLuc) and -resistant (TMZ-selected G28-FLuc) PDX models were successfully developed and applied in the efficacy evaluation of the sorafenib and **Ac12Az9** combination. Co-administration of **Ac12Az9** with sorafenib was effective against TMZ-sensitive PDX orthotopic animal models. This study demonstrated the feasibility of blocking P-gp and BCRP/ABCG2 at BBB to increase the brain level of the conventional ABC transporter substrate anticancer drugs thereby enhancing their therapeutic effect on GBM.

Chapter 6 Structure-based modification of Ac12Az9 to improve its plasma stability and activity in reversing multidrug resistance mediated by BCRP/ABCG2

6.1 Introduction

Plasma stability is important when developing new medication. Unstable compounds frequently show a quick clearance and short half-life in PK experiments, leading to little retention in the body. Many compounds with promising pharmacological properties ultimately fail to advance to clinical trials due to poor plasma stability. Therefore, improving the plasma stability of molecules is an important issue in the search for potential drug candidates.

Chemical modification is one of the important strategies to improve the plasma stability of compounds. The bioisosteric substitution can improve the plasma stability of compounds with a small structural change while retaining the majority of its pharmacological activity [223]. For example, compound **1** (**Figure 6-1**) was a protein kinase B inhibitor (IC_{50} (PKB-α) = 5 nM) developed by Roche Pharmaceutical Co., LTD [224]. The ester group in compound **1** was exceedingly unstable in plasma, with a plasma half-life $t_{1/2}$ of less than 1 min. The plasma half-life $t_{1/2}$ of compound **2** could be increased to 69 h if the ester group was substituted by an amide group, while maintaining the inhibitory activity against PKB-α, with IC_{50} (PKB-α) of 4 nM (**Figure 6-1**). Although the replacement by an ether or an amine (compounds **3** and **4**) can increase the plasma stability (half-life $t_{1/2}$ = 29 and 161 h), the inhibitory activity of the compounds was noticeably lowered (IC_{50} (PKB-α) = 355 nM and 3 μM, respectively) (**Figure 6-1**).

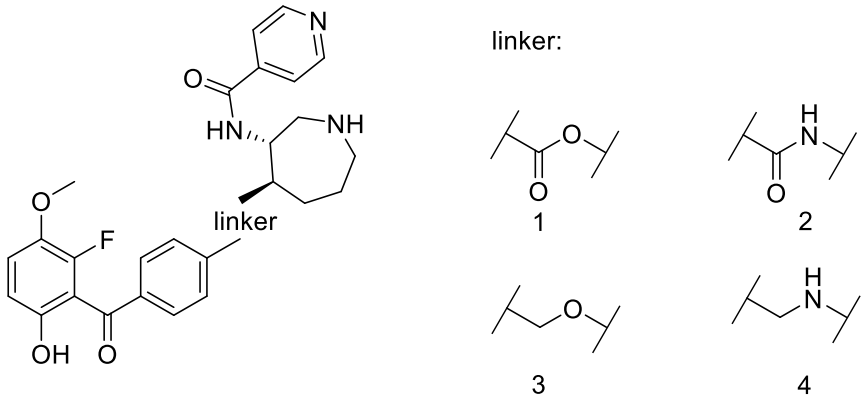

Inhibitor	$t_{1/2}$	IC_{50} (PKB-α)	IC_{50} (PKA)
1	< 1min	5 nM	5 nM
2	69 h	4 nM	2 nM
3	29 h	355 nM	39 nM
4	161 h	3 μM	800 nM

Figure 6-1 Chemical structure, plasma stability, and protein kinase B inhibitory activity of PKB inhibitors [224]

Increasing steric hindrance is another method to reduce the affinity between the compounds and the hydrolase, thereby increasing plasma stability. For example, compound **5** was a cathepsin C inhibitor developed by GlaxoSmithKline [225]. Due to the poor plasma stability of compound **5** (**Figure 6-2**), its benzene ring was derivatized to create compounds **6** and **7** (**Figure 6-2**), of which cathepsin C inhibitory activity was enhanced but plasma stability was not. The cyano group in the structure caused plasma instability, thus an aldehyde group or a tert-butoxy carbonyl group was used to substitute the cyan group to produce compounds **8** and **9**. The plasma stability of compounds **8** and **9** was improved, but the inhibitory activity of the compounds against cathepsin C was lost. In compound **10**, the addition of methyl group to the C-5 position of the pyrrole ring and para bromine at the benzene ring increased the steric hindrance of the o-site and reduced the electrophilicity of the cyan group, which not only improved the plasma stability of **10** but also enhanced its inhibitory activity against cathepsin C.

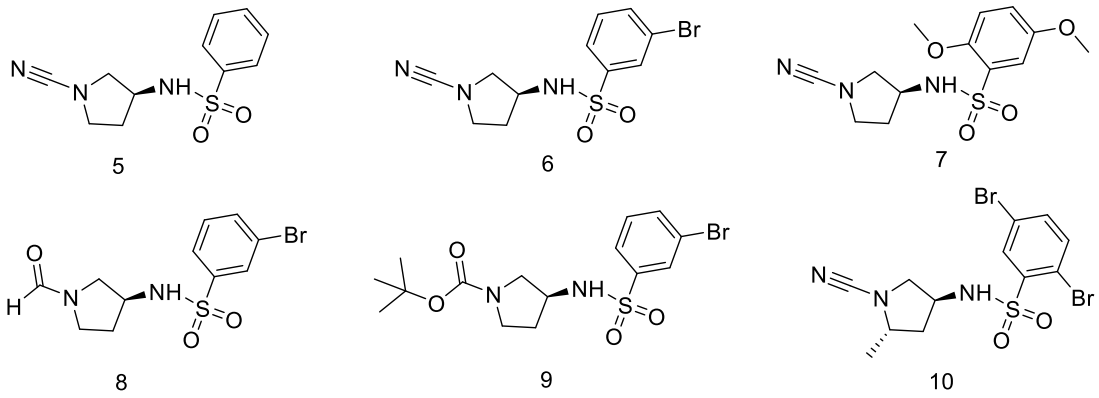

Compounds	Cat C pIC_{50}	Rat Plasma % left @ 30 min
5	6.5	30
6	8.1	18
7	8	23
8	< 4.6	95
9	< 4.6	> 100
10	8.7	88

Figure 6-2 Chemical structure, plasma stability, and cathepsin C inhibitory activity of cathepsin C inhibitors [225]

This part of the project focuses on discovering more stable, potent, and non-toxic P-gp or BCRP/ABCG2 inhibitors by modifying the chemical structure of **Ac12Az9**. First, **Ac12Az9** metabolite (**M1**, **Ac12Az9-COOH**) was successfully identified in plasma and was demonstrated to be inactive. After demonstrating that the methyl ester group in **Ac12Az9** was unstable, 11 derivatives of **Ac12Az9** (**D1-D11**) were generated via bioisosteric substitution, increasing steric resistance, lowering the electrophilicity of the active group, and deuterated substitution. **Ac12Az9** derivatives were screened for their plasma stability and activity in inhibiting P-gp and BCRP/ABCG2-mediated drug resistance *in vitro*. Compound **D6**, with improved plasma stability and inhibitory activity of BCRP/ABCG2 *in vitro*, was selected for efficacy investigation in the HEK293/R2 xenograft model.

6.2 Results

6.2.1 Metabolite identification of Ac12Az9 in plasma

To understand the rapid clearance of **Ac12Az9** in plasma, metabolite identification using UPLC-MS/MS was conducted on the PK plasma samples (from the PK study as discussed in **Chapter Four**). It was hypothesized that the methyl ester group in **Ac12Az9** will undergo ester hydrolysis when exposed to esterase in plasma [226]. **Ac12Az9-COOH** (**M1**) was predicted to be a metabolite of **Ac12Az9** (**Figure 6-3A)**. The product ions of **M1** were also predicted based on the bond cleavage at the active oxygen linked to a benzene ring, as shown in **Figure 6-3A**. The expected metabolite **M1** was found at a retention time of 5.39 min in the MRM mode of m/z 864.3 -> 626.2 and m/z 864.3 -> 492.1 in the positive ionization mode (**Figure 6-3B**). The identity of a metabolite of **Ac12Az9** (**M1**) was validated by the synthesis of the **M1** standard. As shown in **Figure 6-3C**, the product ion spectrum of the synthesized **M1** standard showed an identical fragmentation pattern with parent ion at m/z 864.3 and product ion at m/z 626.2, 492.1. A perfect superposition was observed between the peaks of the PK plasma sample and blank plasma spiked with standards (**Figure 6-3B, D**).

The UPLC-MS/MS method was further applied to quantify **M1** in previous PK samples. Protein precipitation was used to extract **M1**. As shown in **Figure 6-3E**, plasma concentrations of **M1** were higher than those of **Ac12Az9**, and its degradation rate over time was slower. The calculated plasma $AUC_{5\text{-}360\ min}$ of **M1** was 5-fold higher than that of **Ac12Az9** when **Ac12Az9** was administered at doses of 10 mg/kg or 20 mg/kg. **M1** and **Ac12Az9** were 170,378.4 and 30,145.7 ng·min/mL, respectively, in the 10 mg/kg group and 350,474.2 and 70,430.5 ng·min/mL, respectively, in the 20 mg/kg group. The above results suggested that **Ac12Az9** was largely bio-transformed into its metabolite **M1**. The brain PK result was shown in **Figure 6-3F**. **M1** was also found in the brain but at a lower concentration. The brain $AUC_{5\text{-}360min}$ of **M1** was 48,336.4 ng·min/g and 50,833.8 ng·min/g in the 10 mg/kg and 20 mg/kg groups, respectively, which were

lower than those of **Ac12Az9**, with 49,421.9 ng·min/g and 417,445.1 ng·min/g, respectively. The result implied that the modulator-induced increase in brain penetration of sorafenib observed in **Chapter Four** might be primarily caused by **Ac12Az9** rather than **M1**.

A

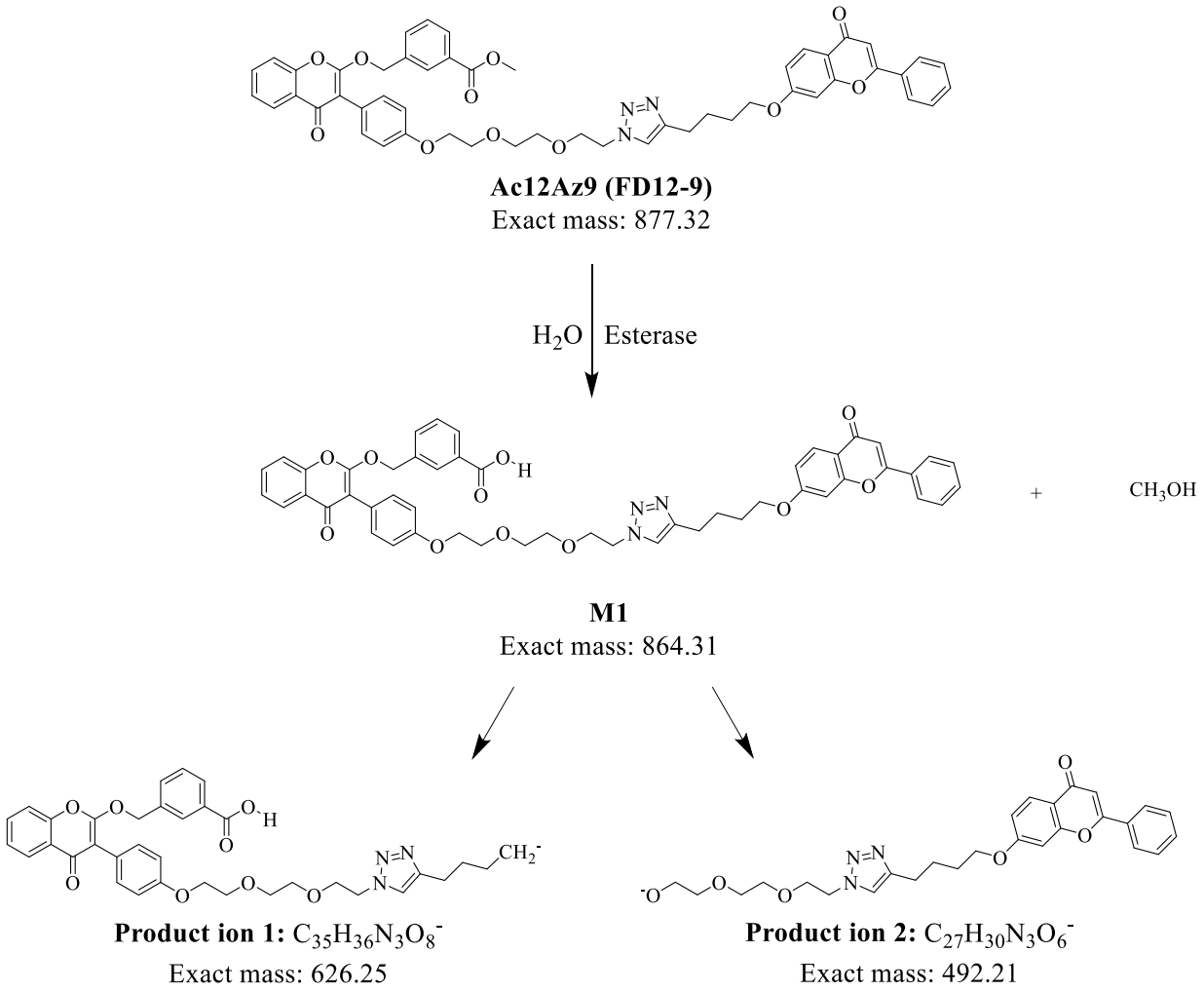
Ac12Az9 (FD12-9)
Exact mass: 877.32
H2O
Esterase
M1
Exact mass: 864.31
+
CH3OH
Product ion 1: C35H36N3O8-
Exact mass: 626.25
Product ion 2: C27H30N3O6-
Exact mass: 492.21

B

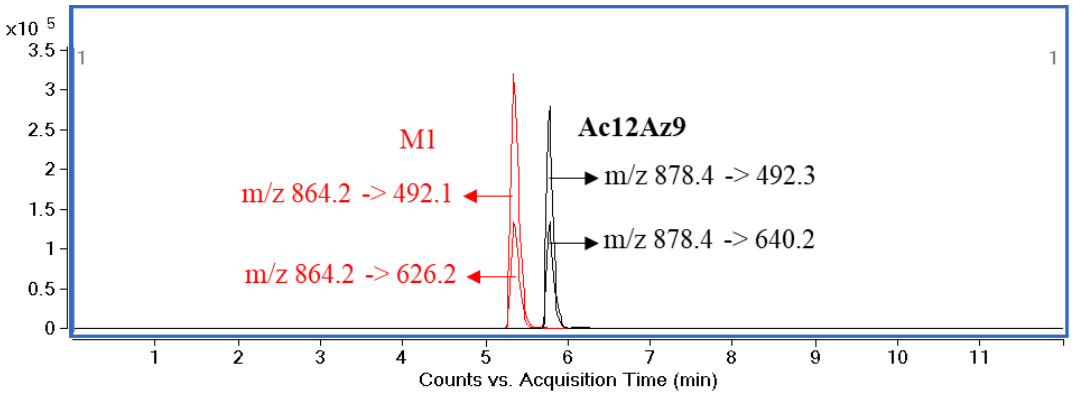
x10 5
3.5
3
2.5
2
1.5
1
0.5
0
M1
m/z 864.2 -> 492.1
m/z 864.2 -> 626.2
Ac12Az9
m/z 878.4 -> 492.3
m/z 878.4 -> 640.2
1 2 3 4 5 6 7 8 9 10 11
Counts vs. Acquisition Time (min)

C

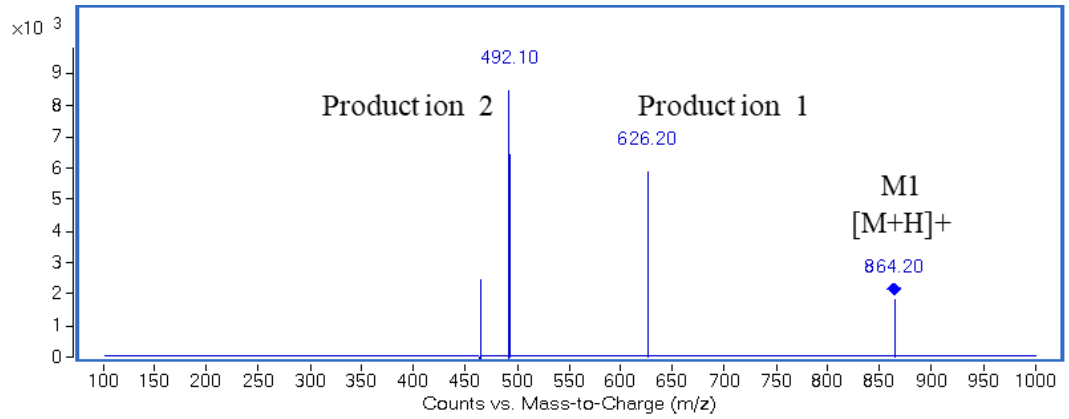
x10 3
9
8
7
6
5
4
3
2
1
0
492.10
Product ion 2
Product ion 1
626.20
M1
[M+H]+
864.20
100 150 200 250 300 350 400 450 500 550 600 650 700 750 800 850 900 950 1000
Counts vs. Mass-to-Charge (m/z)

D

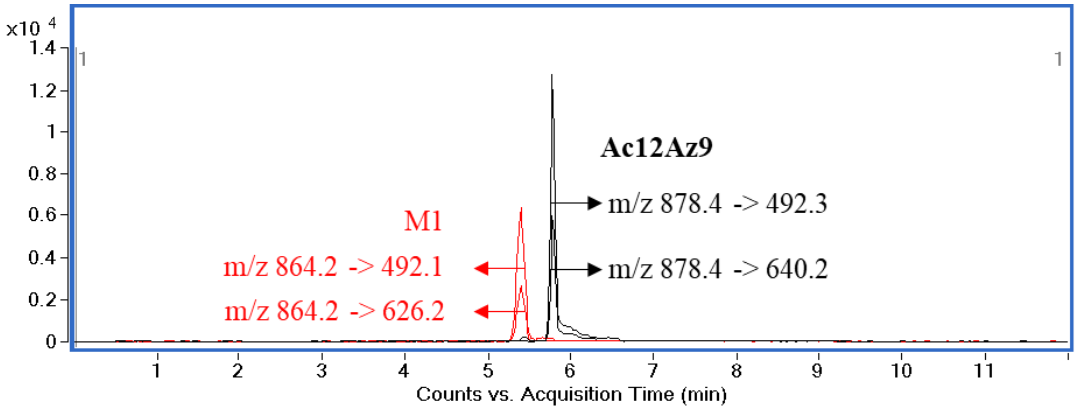
x10 4
1.4
1.2
1
0.8
0.6
0.4
0.2
0
Ac12Az9
m/z 878.4 -> 492.3
m/z 878.4 -> 640.2
M1
m/z 864.2 -> 492.1
m/z 864.2 -> 626.2
1 2 3 4 5 6 7 8 9 10 11
Counts vs. Acquisition Time (min)

E

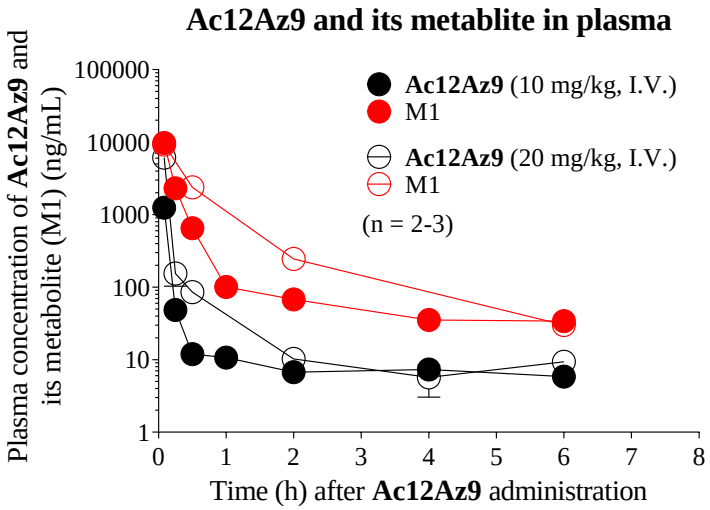

PK parameters	**Ac12Az9** 10 mg/kg I.V.		**Ac12Az9** 20 mg/kg, I.V.	
	Ac12Az9	**M1**	**Ac12Az9**	**M1**
Plasma AUC (ng-min/mL)	30,145.7	170,378.4	70,430.5	350,474.2
Plasma AUC/dose	3,014.6	17,037.8	3,521.5	17,523.7
CL (ml/min/kg)	301.3	55.7	119.0	28.3
$t_{1/2}$ (D/A phase) (min)	7.0	11.1	6.7	16.2

F

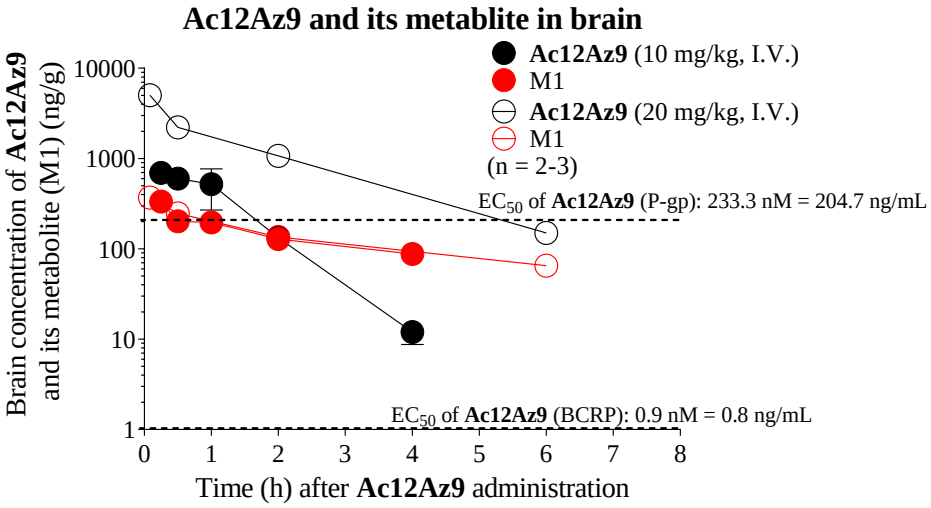

PK parameters	**Ac12Az9** 10 mg/kg, I.V.		**Ac12Az9** 20 mg/kg, I.V.	
	Ac12Az9	**M1**	**Ac12Az9**	**M1**
Brain AUC (ng-min/mL)	49,421.9	48,336.4	417,445.1	50,833.8
Brain AUC/dose	4,942.2	4,833.6	20,872.3	2,541.7
CL (ml/min/kg)	197.9	132.8	45.9	277.1
$t_{1/2}$ (D/A phase) (min)	16.2	11.6	9.0	23.3

Figure 6-3 Identification and quantitation analysis of Ac12Az9 metabolite (M1) in plasma and

brain

(A) Hypothetical hydrolysis of **Ac12Az9** in plasma and proposed fragmentation scheme of **Ac12Az9** metabolite (m/z 864.3 -> 626.2, 864.3 -> 492.2); (B) A representative chromatogram of PK plasma sample; (C) Product ion spectrum of synthesized **M1** standard; (D) A representative chromatogram of blank plasma spiked with **Ac12Az9** and **M1**; (E-F) The plasma and brain concentration-time curves of **Ac12Az9** and **M1** after single intravenous **Ac12Az9** administration (10 or 20 mg/kg) in BALB/c mice (n = 3).

PK samples or blank plasma that had been spiked with the **Ac12Az9** standard and the **M1** standard were deproteinized with 300 uL of ACN. After vortex mixing and centrifugation, the samples were analyzed by UPLC-MS/MS.

6.2.2 *In vitro* plasma stability of Ac12Az9

To further verify the enzymatic hydrolysis of **Ac12Az9**, plasma stability assays were performed *in vitro*. PMSF is a protease and esterase inhibitor that was widely used in the metabolic study of compounds [227, 228]. As seen in **Figure 6-4**, the level of **Ac12Az9** decreased very rapidly when incubated with plasma without PMSF in the first 15 mins, which was accompanied by a rapid rise of the **M1** level. In contrast, **Ac12Az9** remained at a high level for up to 120 mins in plasma while a low level of **M1** was detected if PMSF was added to the incubation. The above results indicated that **Ac12Az9** was hydrolyzed to **M1** by the plasma enzyme (eg, carboxylesterase) in plasma.

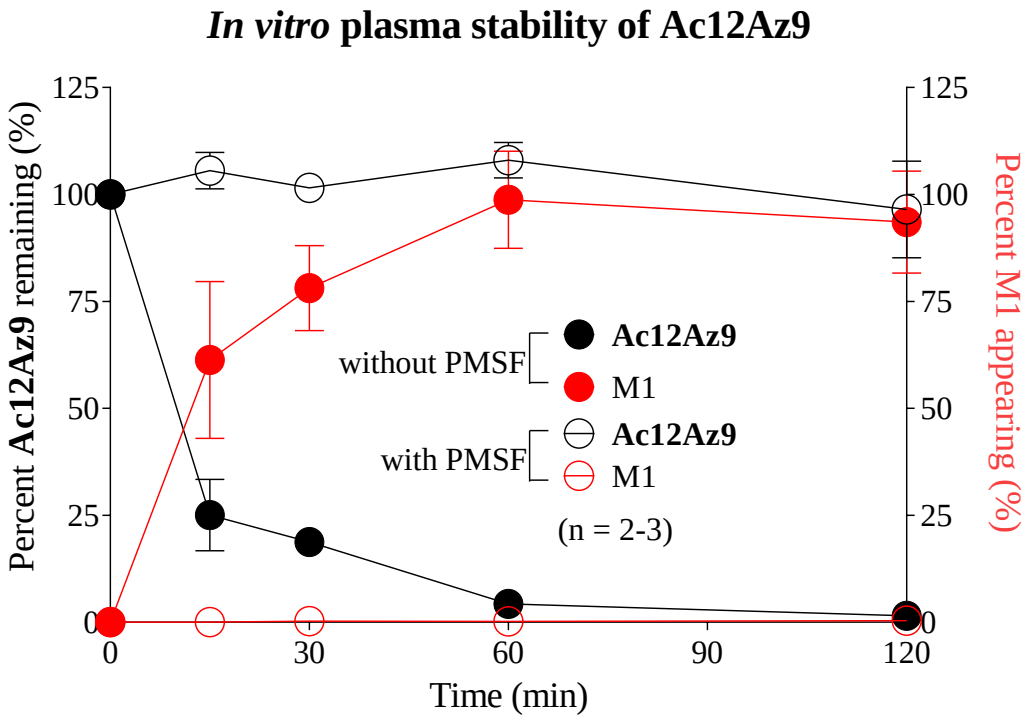

Figure 6-4 *In vitro* plasma stability of Ac12Az9

5 μL of **Ac12Az9** (20 μg/mL in DMSO) were incubated with 100 μL of freshly prepared plasma with or without 5 mM PMSF for various times (0, 15, 30, 60, and 120 min) at 37℃. The reaction was terminated by adding a 3-fold volume of ACN. **Ac12Az9** and its metabolite (**M1**) remaining in plasma were quantified by UPLC-MS/MS. The percentage of test compounds left at each time point relative to the 0-min sample was reported.

6.2.3 Chemical modification of Ac12Az9

The above result has demonstrated that **Ac12Az9** was unstable in plasma. We hypothesized that ester-based chemical modification of **Ac12Az9** could improve its plasma stability and *in vivo* performance in PK and efficacy. The schematic diagram of the chemical modification of **Ac12Az9** was shown in **Figure 6-5**. The strategies for ester-based modification mainly included: a. replacing the methyl ester group [229]; b. increasing the steric hindrance around the ester group [230]; c. reducing the electron density of ester [230]; d. incorporating deuterium at methyl ester [231]. As a result, eleven compounds, including **Ac12Az9-methoxy** (**D1**), **-methoxymethyl** (**D2**), **-methyl amide** (**D3**), **- trifluoromethoxy** (**D4**), **-ethyl** (**D5**), **-tertiary butyl** (**D6**), **-chlorine** (**D7**), **-fluorine** (**D8**), **-para-methoxy** (**D9**), and deuterium substituted compounds (**D10, D11**), were synthesized and characterized for their reversal activity of P-gp and BCRP/ABCG2-mediated drug resistance. These compounds were synthesized by Dr. Ma Cong's group (Hong Kong Polytechnic University, Hong Kong, SAR).

The physicochemical properties and P-gp-, BCRP/ABCG2-modulating activity of **Ac12Az9** and its derivatives were shown in **Table 6-1**. It was found that **M1** exhibited weak inhibition on P-gp and BCRP/ABCG2, with EC_{50} values of >1000 nM for reversing PTX resistance in LCC6MDR cells and 470 nM for reversing TPT resistance in HEK293/R2 cells, respectively, indicating that **Ac12Az9** lost activity after hydrolysis.

It was discovered that the substitution of the methyl ester with a methoxy ($-OCH_3$) and methyl methoxy ($-C_2H_5O$) group did not affect the inhibitory activity of **Ac12Az9** on P-gp. The EC_{50} values of **D1** and **D2** in reversing PTX resistance in LCC6MDR were 268.3 and 291.7 nM, respectively, which were comparable to **Ac12Az9** (EC_{50} = 233.3 nM); however, their inhibitory effects on BCRP/ABCG2 were noticeably weakened, and the EC_{50} value of **D1-D4** in reversing TPT resistance increased to 11.5-22.5 nM in HEK293/R2 cells and 26.0-109.2 nM in MCF7-MX100 cells, respectively, compared

to the 0.9 or 1.5 nM of **Ac12Az9**. This finding showed that the ester group was crucial to the inhibiting effect of **Ac12Az9** on BCRP/ABCG2.

D5 and **D6** with preserved ester groups and higher steric hindrance exhibited not only high BCRP/ABCG2-modulating activity but also good selectivity for BCRP/ABCG2. The EC_{50} values of **D5** and **D6** for reversing TPT resistance were 0.4 and 1.2 nM in HEK293/R2 cells and 4.3 and 1.3 nM in MCF7-MX100 cells, compared to **Ac12Az9**, which had an EC_{50} of 0.9 nM in HEK293/R2 cells and 1.5 nM in MCF7-MX100 cells. However, the P-gp inhibition of **D5** and **D6** was reduced by 3-4 folds, with EC_{50} values of 600 and 912.5 nM in reversing PTX resistance in LCC6MDR cells, respectively, compared to 233.3 nM of **Ac12Az9**.

Besides, the deuterium substitution product **D10** of **Ac12Az9** demonstrated strong P-gp and BCRP/ABCG2 inhibition, and its EC_{50} for reversing PTX resistance in LCC6MDR cells was 243.7 nM, while the EC_{50} for reversing TPT resistance in HEK293/R2 and MCF7-MX100 cells was 1.0 and 2.9 nM, respectively.

The relationship between the EC_{50}s and physicochemical descriptors was investigated. These included molecular weight (MW), octanol-water partition coefficient (clogP), and topological polar surface area (tPSA). The cLogP and tPSA were predicted by ChemDraw 18.0, which were used as indicators for the lipophilicity and cell permeability of compounds. It was found that the EC_{50}s for reversing TPT resistance in HEK293/R2 cells were significantly negatively correlated with the compounds' MW ($R^2 = 0.8621$, $p < 0.0001$), cLogP ($R^2 = 0.6532$, $p = 0.0005$) and tPSA ($R^2 = 0.8093$, $p < 0.0001$) (**Figure 6-6**). In contrast, the EC_{50}s for reversing PTX resistance in LCC6MDR cells were moderately positively correlated to the compounds' MW ($R^2 = 0.3466$, $p = 0.0268$) and tPSA ($R^2 = 0.4398$, $p = 0.0097$), and had no association with cLogP ($R^2 = 0.1714$, $p = 0.1411$) (**Figure 6-6**). Taken together, the inhibition of **Ac12Az9** and its derivatives on BCRP/ABCG2 could be improved but at the expense

of the loss of P-gp inhibition.

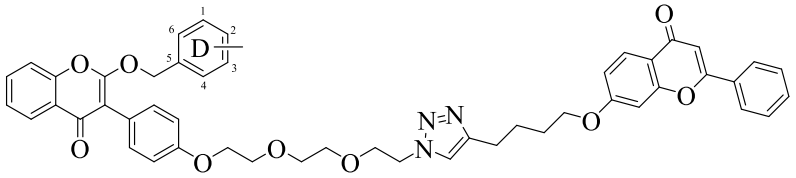

Ac12Az9: R = 3-$COOCH_3$

M1: R = 3-COOH

Substitutions of ester group

D1: R = 3-OCH_3

D2: R = 3-CH_2OCH_3

D3: R = 3-$CONHCH_3$

D4: R = 3-OCF_3

Different ester group

D5: R = 3-$COOCH_2CH_3$

D6: R = 3-$COOC(CH_3)_4$

Substitutions on D-ring

D7: R = 2-Cl, 3-$COOCH_3$

D8: R = 2-F, 3-$COOCH_3$

D9: R = 3-$COOCH_3$, 6-OCH_3

Deuteration

D10: R = 3-$COOCD_3$

D11: R = 3-OCD_3

Figure 6-5 Schematic diagram of chemical modification of Ac12Az9

Table 6-1 The molecular weight, clogP, tPSA, and P-gp- and BCRP/ABCG2 modulating activity of Ac12Az9 and its derivatives

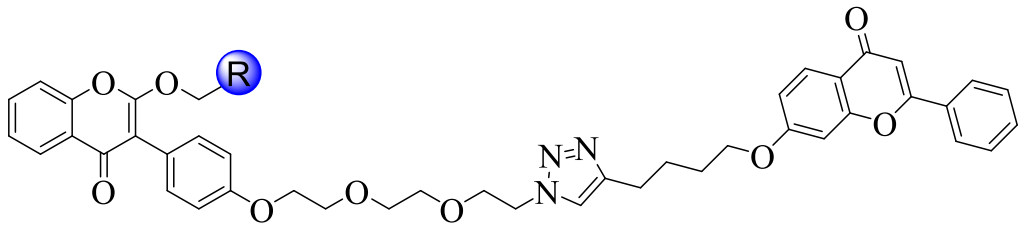

Compounds	R	Molecular weight (g/mol)	cLogP	tPSA (Å²)	EC_{50} (nM) for reversing MDR			BCRP/ABCG2 selectivity	
					LCC6MDR P-gp-mediated PTX resistance	HEK293/R2 BCRP/ABCG2-mediated TPT resistance	MCF7-MX100 BCRP/ABCG2-mediated TPT resistance	Relative to P-gp inhibition HEK293/R2	MCF7-MX100
Ac12Az9	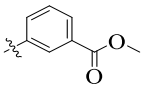	878.0	8.8	163.6	233.3 ± 48.0	0.9 ± 0.1	1.5 ± 0.1	259	156
M1	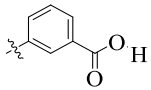	863.9	8.6	174.6	>1000	470.0 ± 56.6	ND	ND	ND
D1	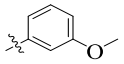	849.9	8.7	146.5	268.3 ± 74.2	11.5 ± 0.7	26.0 ± 5.9	23	10
D2	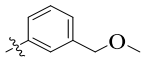	864.0	8.7	146.5	291.7 ± 67.9	16.5 ± 2.1	28.8 ± 12.4	18	10
D3	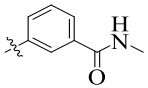	877.0	8.2	166.4	628.3 ± 92.2	22.5 ± 7.8	109.2 ± 26.5	28	6
D4	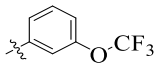	903.9	9.1	146.5	539.7 ± 40.0	16.2 ± 6.2	32.8 ± 7.4	33	16

Continued on Next Page

Compounds	R	Molecular weight (g/mol)	cLogP	tPSA (Å²)	EC_{50} (nM) for reversing MDR			BCRP/ABCG2 selectivity	
					LCC6MDR	HEK293/R2	MCF7-MX100	Relative to P-gp inhibition	
					P-gp-mediated PTX resistance	BCRP/ABCG2-mediated TPT resistance	BCRP/ABCG2-mediated TPT resistance	HEK293/R2	MCF7-MX100
D5	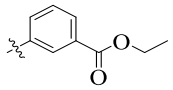	892.0	8.9	163.6	600.0 ± 14.1	0.4 ± 0.1	4.3 ± 0.4	1500	140
D6	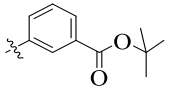	920.0	9.2	163.6	912.5 ± 17.7	1.2 ± 0.1	1.3 ± 0.1	760	702
D7	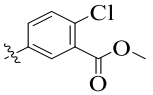	912.4	8.9	163.6	328.7 ± 12.4	7.4 ± 0.2	132.5 ± 46	44	2
D8	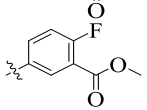	895.9	8.7	163.6	885.0 ± 49.5	7.2 ± 0.8	35.8 ± 6.29	123	25
D9	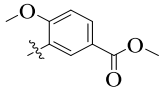	908.0	8.8	172.9	787.5 ± 123.7	2.7 ± 0.9	167.5 ± 58.4	292	5
D10	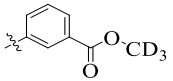	880.9	8.8	163.6	243.7 ± 10.8	1.0 ± 0.1	2.9 ± 0.1	244	84
D11	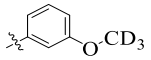	852.9	8.7	146.5	381.7 ± 10.1	10.3 ± 2.9	37.4 ± 3.2	37	10
Ko143	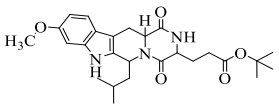	469.3	3.6	97.0	1060.0 ± 120.1	8.7 ± 2.2	9.0 ± 1.5	122	118

A total of 6500 cells were seeded into of a 96-well plate, including LCC6MDR, HEK293/R2, or MCF7-MX100 cells, respectively. Cells were treated with different doses of PTX or TPT together with either no modulator or different modulator dosages (**Ac12Az9**, **Ac12Az9** derivatives, and ko143). Cell viability was measured after 4-5 days of incubation. PRISM software was used to calculate the IC_{50} of several anticancer medications and the EC_{50} of various modulators. The data was presented as mean ± SD (n = 3). Ko143 and **Ac12Az9** were used as positive controls.

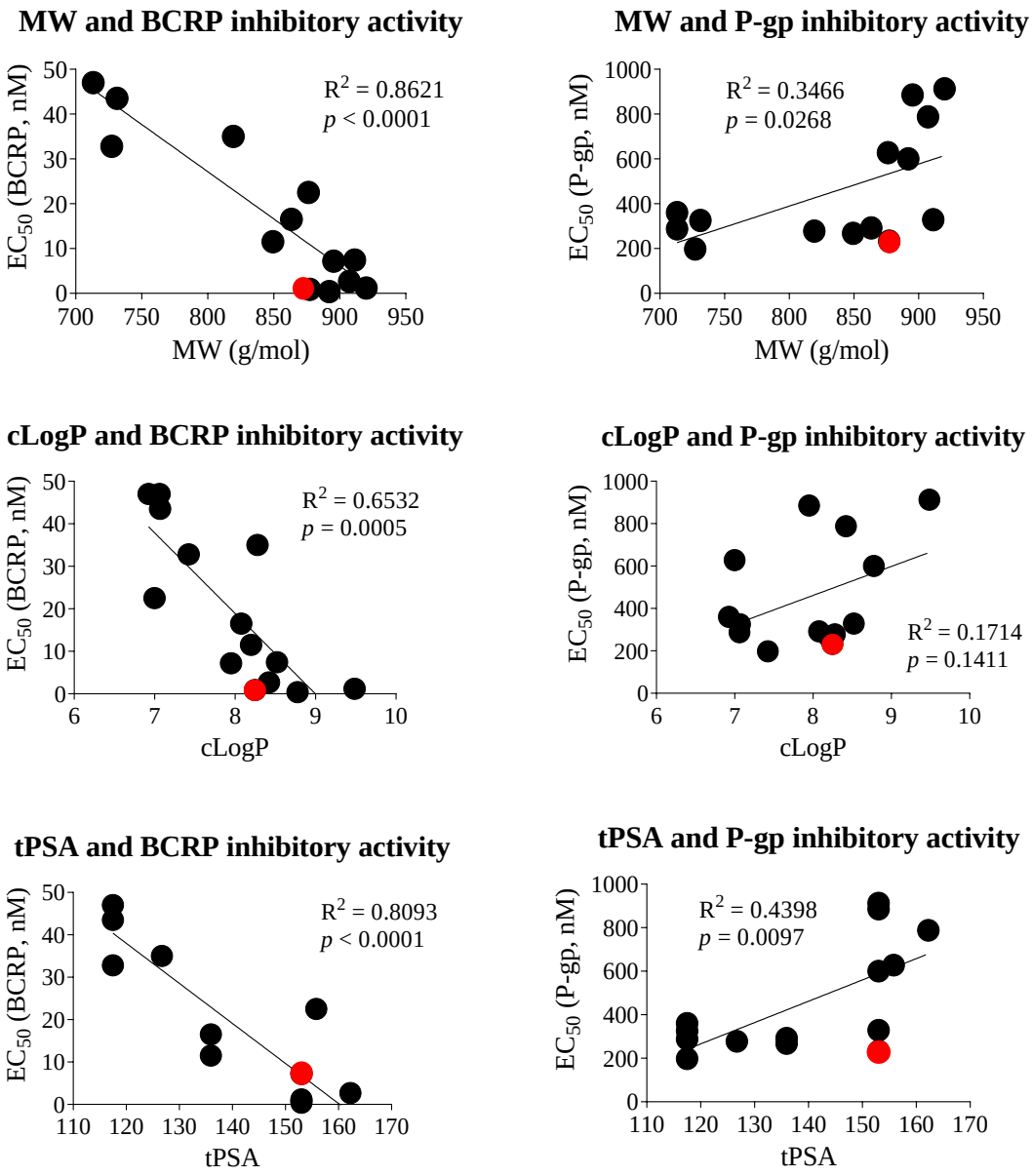

Figure 6-6 Correlation between the molecular weight, clogP, or tPSA of Ac12Az9 and its derivatives and their BCRP/ABCG2 and P-gp inhibitory activity

The physicochemical parameters, including MW, clogP, and tPSA, were calculated using ChemDraw 18.0. All the regression equations were derived using PRISM software. Linear regression coefficient (R^2) was indicated. *$p < 0.05$, **$p < 0.01$, ***$p < 0.001$.

6.2.4 *In vitro* plasma stability of Ac12Az9 and its derivatives

The plasma stability of **Ac12Az9** derivatives (**D1-D11**) was investigated. It was found that **D1**, **D2**, **D3**, **D4**, **D6**, and **D11** exhibited improved plasma stability with $t_{1/2}$ of 270-330 min or higher than 360 min compared to **Ac12Az9** ($t_{1/2}$ < 60 min) (**Figure 6-7**). However, the $t_{1/2}$ of **D5**, **D7**, **D8**, **D9**, and **D10** remained at 60 min below (**Figure 6-7**), which was comparable to that of **Ac12Az9**.

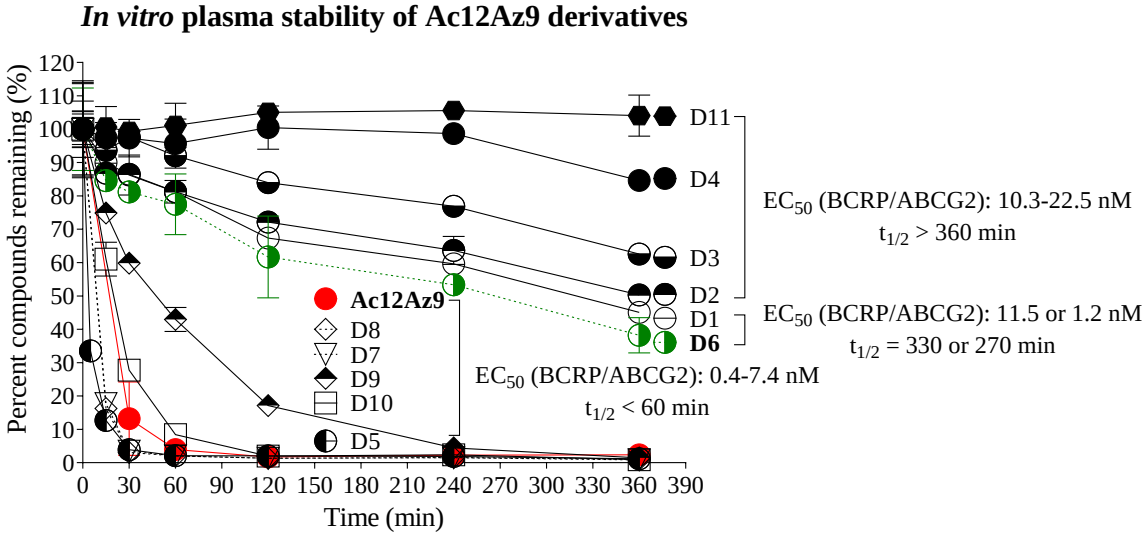

Figure 6-7 *In vitro* plasma stability of Ac12Az9 and its derivatives (D1-D11)
5 µL of **Ac12Az9** and its derivatives (20 µg/mL in DMSO) were incubated with 100 µL of freshly prepared plasma at various times (0, 15, 30, 60, 120, 240, and 360 min) at 37°C. The reaction was terminated by adding a 3-fold volume of ACN. **Ac12Az9** and its derivatives remaining in plasma were quantified by UPLC-MS/MS. The percentage of test compounds left at each time point relative to the 0-min sample was reported. The half-life ($t_{1/2}$), which measures how long it takes for a drug's blood concentration to drop by 50%, was used to assess the plasma stability of compounds.

6.2.5 Effect of Ac12Az9 and its derivatives on sorafenib accumulation in MDCKII-GFP-BCRP cells

We investigated whether the derivatives of **Ac12Az9** can increase sorafenib accumulation in the MDCKII-GFP-BCRP cells. It was found that MDCKII-GFP-BCRP cells accumulated 2.4-fold ($p < 0.001$) less sorafenib compared to its wild type (**Figure 6-8**). Treatment of MDCKII-GFP-BCRP cells with 1 µM of **Ac12Az9** or **D6**

significantly increased the low intracellular sorafenib accumulation by 2.4-fold ($p < 0.001$), respectively, in MDCKII-GFP-BCRP cells. This result suggested that **Ac12Az9** and its derivatives inhibited the BCRP/ABCG2 and restored the intracellular sorafenib concentration to the parental level.

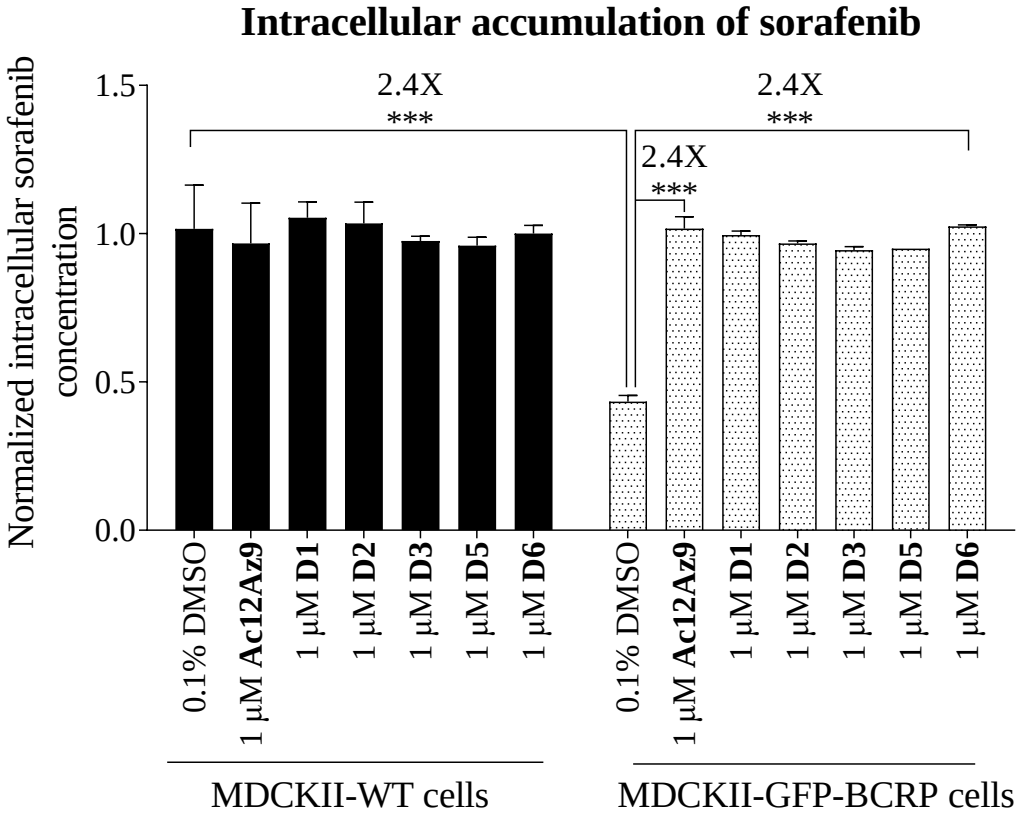

Figure 6-8 Effects of Ac12Az9 and its derivatives on intracellular accumulation of sorafenib in MDCKII-WT and MDCKII-GFP-BCRP cells

1 x 10^6 cells of MDCKII-WT or MDCKII-GFP-BCRP cells were collected in 1.5 mL Eppendorf tubes and treated with 2.5 μM sorafenib and 1 μM modulators at 37°C with shaking at 250 rpm for 1 hr. 0.1% DMSO solution was used as a negative control. The cells were collected by centrifugation (1,500 rpm, 3 mins) followed by washing with PBS. The cell pellets were re-suspended in 100 μL Milli-Q water and lysed through three freeze-thaw cycles (the tubes could be thawed quickly at 37°C in a water bath and frozen again in liquid nitrogen). The intracellular sorafenib level was determined by UPLC-MS/MS. All the data was shown as mean ± SD (n = 4). *** $p < 0.001$.

6.2.6 PK study and tissue accumulation of Ac12Az9 derivatives in BALB/c mice

The tissue distribution and plasma PK of **Ac12Az9** or its derivatives were studied.

Following intravenous administration of **Ac12Az9** (20 mg/kg), **M1** was shown to be abundant and widely distributed in the blood and several important organs (liver, kidneys, and lung) (**Figure 6-9A-D)**. **M1** can also cross the BBB and accumulate in the brain (**Figure 6-9E**). Other derivatives (**D1**, **D2**, **D3**, **D5**, and **D6**) can also be found in various organs, except for **D5**, which cannot be found in the liver (**Figure 6-9A-E**).

PK parameters were summarized in **Figure 6-9F**. **Ac12Az9** had an 8.2 times greater brain $AUC_{0\text{-}360\ min}$ than **M1**, with 426.08 μg·min/g for **Ac12Az9** versus 52.06 μg·min/g for **M1**. However, the plasma and liver $AUC_{5\text{-}360\ min}$ of **M1** were 57.7 and 167.2 times greater than those of **Ac12Az9**, with **M1**'s plasma $AUC_{5\text{-}360\ min}$ of 352.35 μg·min/mL compared to **Ac12Az9**'s being 6.11 μg·min/mL, and **M1**'s liver $AUC_{5\text{-}360\ min}$ being 5085.18 μg·min/g over **Ac12Az9**'s being 30.42 μg·min/g.

The plasma $AUC_{5\text{-}360\ min}$ of the other derivatives **(D1-D3**, **D5**, and **D6**), which were 195.79, 218.68, 360.91, and 330.5 μg·min/mL, respectively, were significantly higher than the plasma $AUC_{5\text{-}360\ min}$ of 6.11 μg·min/mL for **Ac12Az9**, which was compatible with the *in vitro* plasma stability test results. Similarly, **D1**, **D2**, **D3**, and **D6** had higher liver, kidney, and lung $AUC_{5\text{-}360\ min}$ than those of **Ac12Az9**. Particularly, the $AUC_{5\text{-}360\ min}$ for the liver, kidneys, or lungs in **D6** was 757.5, 2657.14, or 1164.23 μg·min/g, respectively, which were 25, 11, and 8 times higher than the comparable $AUC_{5\text{-}360\ min}$ in **Ac12Az9**, respectively.

Contrary to the findings in the liver, kidneys, and lung, the brain $AUC_{5\text{-}360\ min}$ of derivatives (**D1-D3**, **D5**, and **D6**) was lower than the brain **Ac12Az9** $AUC_{5\text{-}360\ min}$ of 426.08 μg·min/g, with values of 129.78, 76.84, 33.92, 25.61, and 38.46 μg·min/g, respectively.

A

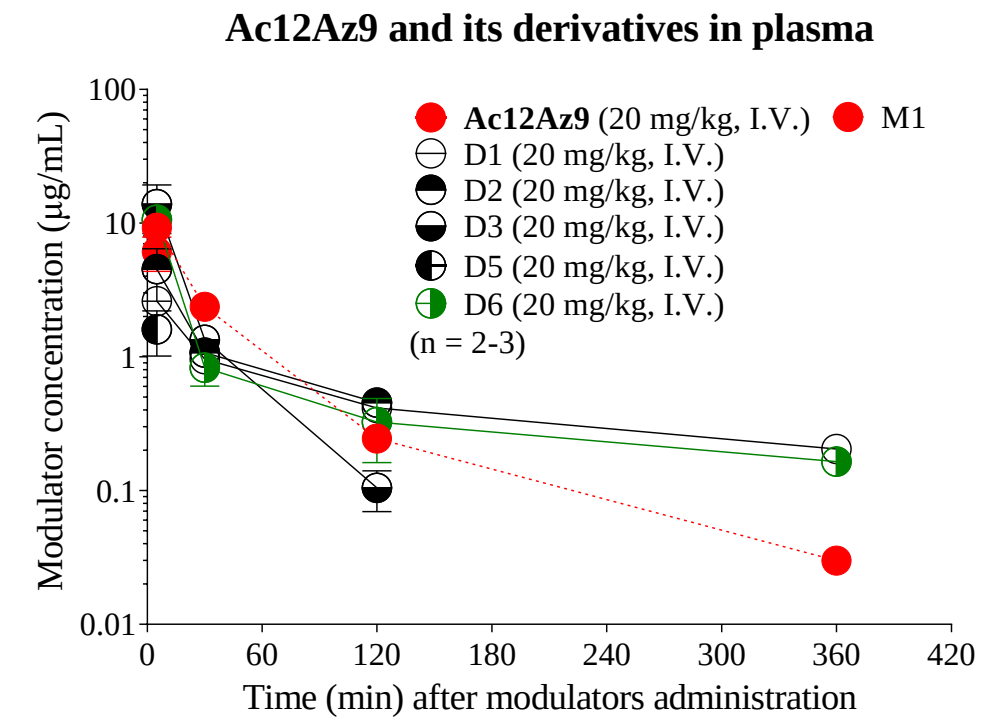
Ac12Az9 and its derivatives in plasma
Ac12Az9 (20 mg/kg, I.V.)
M1
D1 (20 mg/kg, I.V.)
D2 (20 mg/kg, I.V.)
D3 (20 mg/kg, I.V.)
D5 (20 mg/kg, I.V.)
D6 (20 mg/kg, I.V.)
(n = 2-3)
Modulator concentration (µg/mL)
100
10
1
0.1
0.01
0
60
120
180
240
300
360
420
Time (min) after modulators administration

B

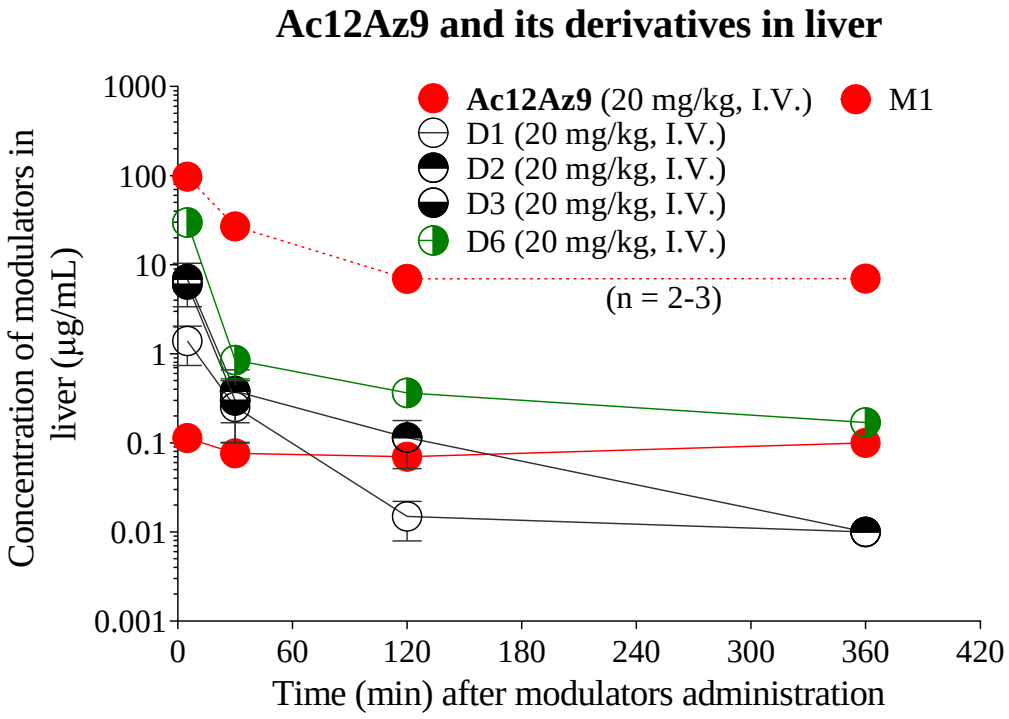
Ac12Az9 and its derivatives in liver
Ac12Az9 (20 mg/kg, I.V.)
M1
D1 (20 mg/kg, I.V.)
D2 (20 mg/kg, I.V.)
D3 (20 mg/kg, I.V.)
D6 (20 mg/kg, I.V.)
(n = 2-3)
Concentration of modulators in liver (µg/mL)
1000
100
10
1
0.1
0.01
0.001
0
60
120
180
240
300
360
420
Time (min) after modulators administration

C

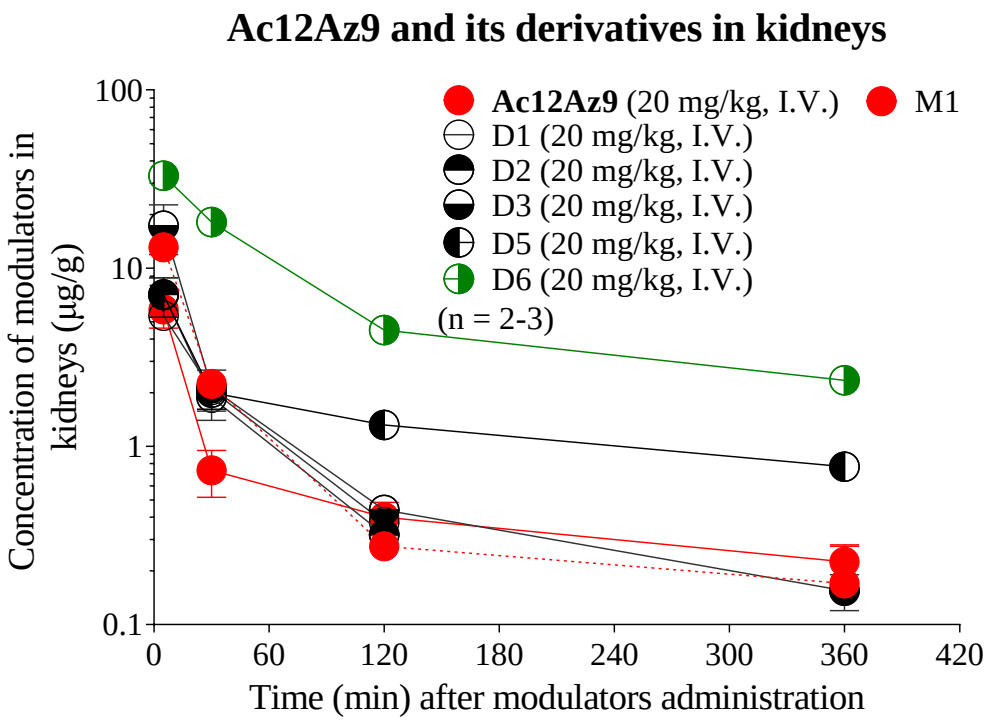
Ac12Az9 and its derivatives in kidneys
Ac12Az9 (20 mg/kg, I.V.)
M1
D1 (20 mg/kg, I.V.)
D2 (20 mg/kg, I.V.)
D3 (20 mg/kg, I.V.)
D5 (20 mg/kg, I.V.)
D6 (20 mg/kg, I.V.)
(n = 2-3)
Concentration of modulators in kidneys (µg/g)
100
10
1
0.1
0
60
120
180
240
300
360
420
Time (min) after modulators administration

D

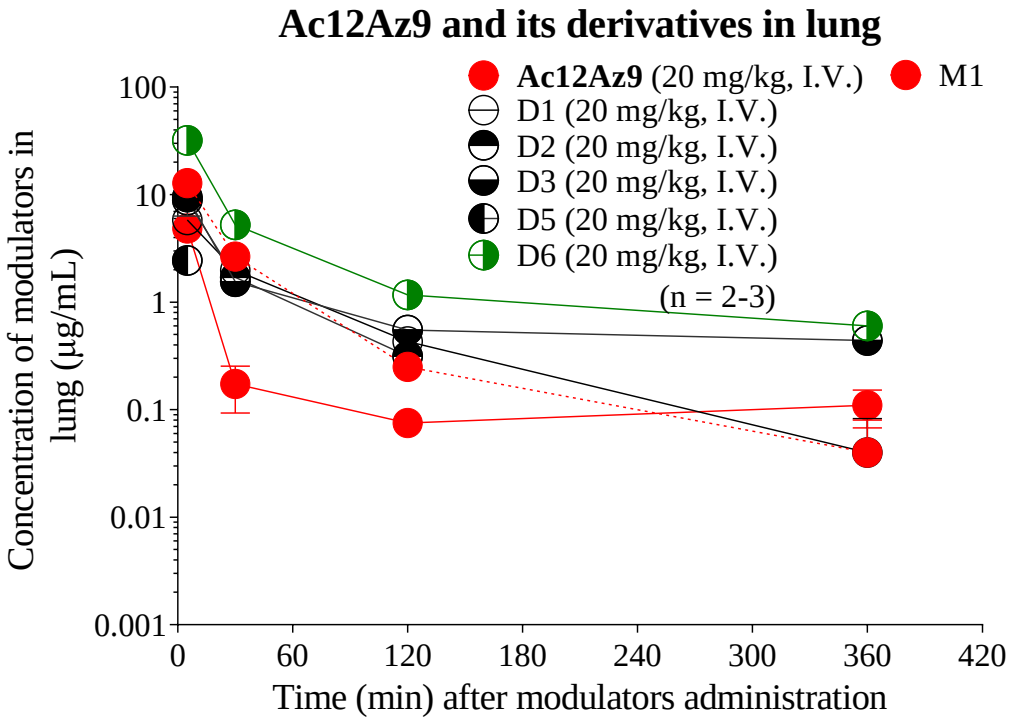
Ac12Az9 and its derivatives in lung
Ac12Az9 (20 mg/kg, I.V.)
M1
D1 (20 mg/kg, I.V.)
D2 (20 mg/kg, I.V.)
D3 (20 mg/kg, I.V.)
D5 (20 mg/kg, I.V.)
D6 (20 mg/kg, I.V.)
(n = 2-3)
Concentration of modulators in lung (µg/mL)
100
10
1
0.1
0.01
0.001
0
60
120
180
240
300
360
420
Time (min) after modulators administration

E

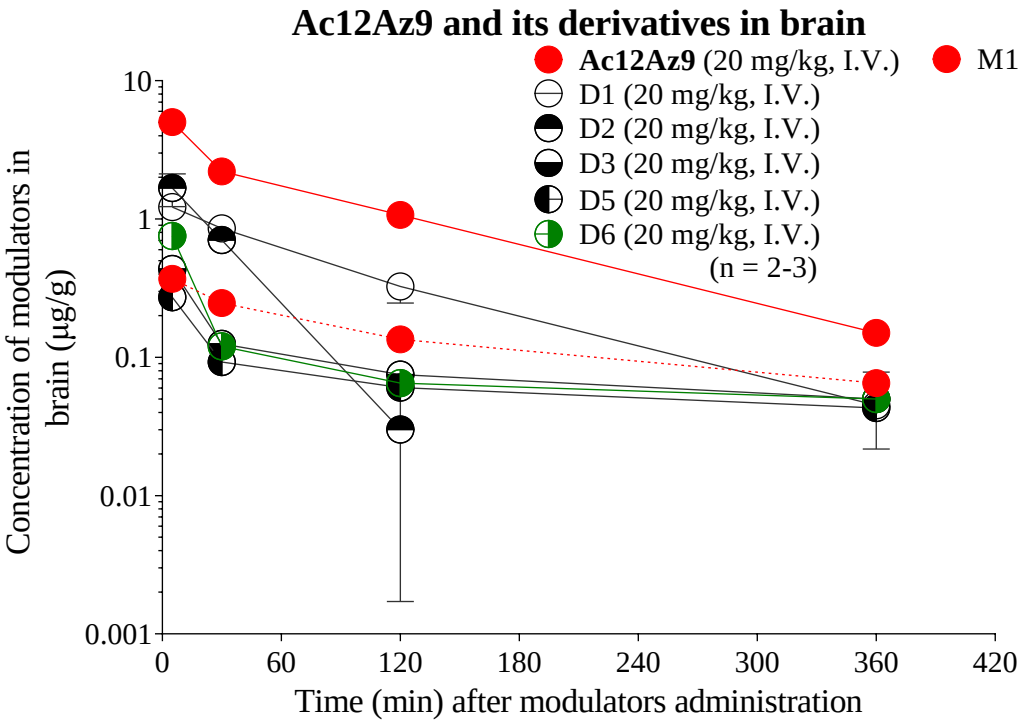
Ac12Az9 and its derivatives in brain
Ac12Az9 (20 mg/kg, I.V.)
D1 (20 mg/kg, I.V.)
D2 (20 mg/kg, I.V.)
D3 (20 mg/kg, I.V.)
D5 (20 mg/kg, I.V.)
D6 (20 mg/kg, I.V.)
(n = 2-3)
M1
Concentration of modulators in brain (μg/g)
10
1
0.1
0.01
0.001
0
60
120
180
240
300
360
420
Time (min) after modulators administration

F

Groups (20 mg/kg, I.V.)	Analyte	*In vitro* Half life $t_{1/2}$ (min)	*In vivo* $AUC_{5\text{-}360\ min}$ (μg·min/mL, μg·min/g)				
		Plasma	Plasma	Liver	Kidneys	Lung	Brain
Ac12Az9	**Ac12Az9**	<15	6.11 ± 1.75	30.42 ± 1.08	247.23 ± 20.38	144.89 ± 22.97	426.08 ± 32.91
	M1	-	352.35 ± 45.33	5085.18 ± 113.11	430.78 ± 16.83	395.15 ± 30.53	52.06 ± 2.75
D1	**D1**	325	195.79 ± 2.04	52.07 ± 16.50	285.36 ± 15.29	294.88 ± 37.21	129.78 ± 11.64
D2	**D2**	360	218.68 ± 30.62	188.28 ± 101.03	289.31 ± 67.8	320.04 ± 45.44	76.84 ± 11.78
D3	**D3**	> 360	360.91 ± 96.42	145.19 ± 12.38	476.46 ± 49.00	412.28 ± 54.91	33.92 ± 1.46
D5	**D5**	<15	1.61 ± 0.59	0	559.69 ± 48.21	2.45 ± 0.42	25.61 ± 0.24
D6	**D6**	263	330.5 ± 69.8	757.50 ± 30.83	2657.14 ± 125.79	1164.23 ± 102.91	38.46 ± 1.75

Figure 6-9 PK study and tissue accumulation of Ac12Az9 or its derivatives in BALB/c mice

(A) Plasma concentration-time curves of **Ac12Az9** or its derivatives; (B) Liver concentration-time curves of **Ac12Az9** or its derivatives; (C) Kidney concentration-time curves of **Ac12Az9** or its derivatives; (D) Lung concentration-time curves of **Ac12Az9** or its derivatives; (E) Brain concentration-time curves of **Ac12Az9** or its derivatives; (F) Calculated PK parameters of **Ac12Az9** or its derivatives.

Ac12Az9 (2 mg/mL) or its derivatives (2 mg/mL) were prepared in the formulation of NMP, CrEL, and 5% Tween-80 (10: 10: 80), respectively. **Ac12Az9** (20 mg/kg) or its derivatives were administered intravenously to mice, respectively. Blood and tissue samples (brain, liver, kidneys, and lung) samples were collected, respectively, at various time points (5 min, 30 min, 120 min, and 360 min). Plasma and tissue concentration of **Ac12Az9** or its derivatives were determined by UPLC-MS/MS. The data was presented as mean ± SD (n = 2-3). A non-compartmental analysis was performed using PK Solutions 2.0.3 software (Ashland, OH44805, USA) to calculate the AUC values.

6.2.7 Effect of D6 on the TPT accumulation in HEK293/R2 tumor

The above findings confirmed that **D6** was more potent in inhibiting the transport activity of BCRP/ABCG2 *in vitro*, having better stability, and accumulating more in the target organs in *in vivo* PK studies. Here, **D6** was investigated for its activity in increasing the accumulation of TPT in tumors.

The HEK293/R2 xenograft model was established and validated for its high and stable expression of BCRP/ABCG2 (**Figure 6-10A**). The BALB/c nude mice implanted with subcutaneous HEK293/R2 tumors were treated with either (1) TPT (6 mg/kg, I.P.) or (2) TPT (6 mg/kg, I.P.) + **D6** (20 mg/kg, I.V.) (simultaneously but in separate injections, single dose). It was found that **D6** can significantly increase the tumor accumulation of TPT by 2-fold (p = 0.0028) compared to the TPT alone group (**Figure 6-10B**).

A

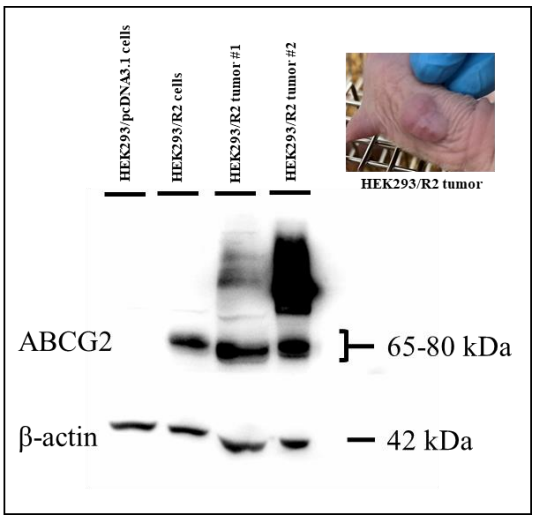

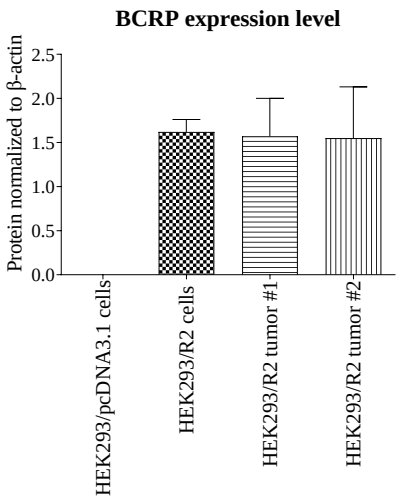

B

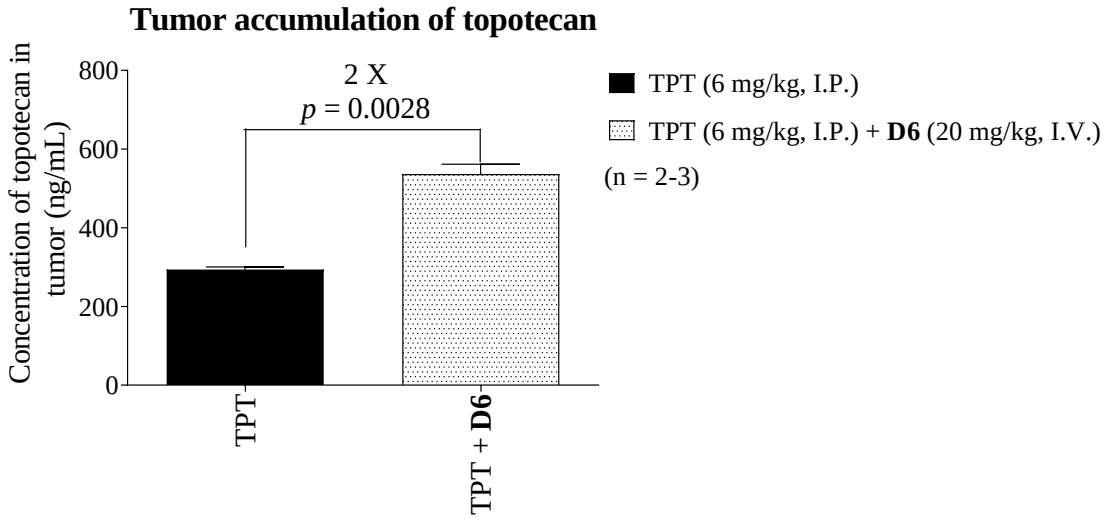

Figure 6-10 Effect of D6 on the tumor accumulation of TPT in the HEK293/R2 xenograft model

(A) Expression of BCRP/ABCG2 in HEK293/R2 tumor; (B) Effect of **D6** on the accumulation of TPT in the HEK293/R2 tumor.

For western blot analysis, each 0.1g of the tumor sample received 100 μL of lysis buffer. After being homogenized with a homogenizer, the tumor sample was then placed on ice for a further 10 minutes. The supernatant was separated by centrifugation and the protein concentration was determined. 20 μg of protein was run for western blot analysis. **Methodology 2.2.10** provided a full description of the Western blot process.

For the animal experiments, the tumor-bearing nude mice were treated with either (1) TPT or (2) TPT + D6. Tumors were excised, PBS-washed, weighed, and homogenized with PBS at a ratio of 1:3 two hours after drug administration. Concentration of TPT was determined using UPLC/MS-MS analysis following the processing of biological samples, which was described in detail in **Methodology 2.2.13**.

6.3 Discussion

Ac12Az9 was a safe, potent, and dual inhibitor of BCRP/ABCG2 and P-gp, with an EC_{50} of 0.9 nM in reversing TPT resistance in HEK293/R2 cells and 233.3 nM in reversing PTX resistance in LCC6MDR cells. The PK study of **Ac12Az9**, however, revealed that it had a short half-life $t_{1/2}$ and rapid clearance, potentially limiting its use in an efficacy study.

Ac12Az9-COOH (**M1**), a metabolite of **Ac12Az9**, was identified in murine plasma but was found to be inactive in reversing BCRP/ABCG2-mediated TPT resistance in HEK293/R2 cells (EC_{50} > 1000 nM) and P-gp-mediated PTX resistance in LCC6MDR cells (EC_{50} = 470 nM). The low plasma stability of **Ac12Az9** was attributed to the protease and esterase activity in the plasma.

The methyl ester group in **Ac12Az9** was responsible for its low plasma stability. A methoxy group (-OCH_3), methyl methoxy group (-C_2H_5O), methyl amide group (-$CONHCH_3$), and trifluoromethoxy (-OCF_3) were substituted for the methyl ester group to produce compounds **D1**, **D2**, **D3**, and **D4**. The plasma stability of **D1-D4** was improved (half-life $t_{1/2}$ > 360 min versus < 60 min for **Ac12Az9**), but their BCRP/ABCG2 inhibitory activity was diminished, with EC_{50} values of 11.5-22.5 nM in reversing TPT resistance in HEK293/R2 cells and 26.0-109.2 nM in MCF7-MX100 cells, compared to the EC_{50} of 0.9 or 1.5 nM of **Ac12Az9**. This indicated that the ester group was critical to the inhibitory effect of **Ac12Az9** on BCRP/ABCG2.

The introduction of the ethyl group, tertiary butyl group, *ortho* chlorine, *ortho* fluorine, and *para* methoxy to the ester group produced compounds **D5**, **D6**, **D7**, **D8**, and **D9**. **D5** has an improved selectivity for BCRP/ABCG2 (selectivity index = 1500 and 140) and stronger BCRP/ABCG2-modulating activity (EC_{50} = 0.4 and 4.3 nM for reversing TPT resistance in HEK293/R2 and MCF7-MX100 cells), but it did not affect plasma

stability (half-life $t_{1/2}$ < 60 min). **D6** displayed increased plasma stability, with a half-life $t_{1/2}$ of 270 min, while maintaining the good selectivity (selectivity index = 760 and 702) and inhibitory activity of BCRP/ABCG2, with an EC_{50} of 1.2 nM and 1.3 nM, respectively, for reversing TPT resistance in HEK293/R2 and MCF7-MX100 cells. This indicated that the tertiary butyl group, which was bulkier than the ethyl group, can effectively slow down the hydrolysis of the ester group. The structure-activity relationship (SAR) analysis of **Ac12Az9** derivatives and BCRP/ABCG2-inhibitory activity also supported this, showing that the increase in the steric bulk at the C-3 on the benzine ring D can improve **Ac12Az9**'s activity to inhibit BCRP/ABCG2. **D7-D9** remained sensitive to the hydrolysis of ester groups (half-life $t_{1/2}$ < 60 min), and they were less active in inhibiting BCRP/ABCG2 (EC_{50} values of 2.7-7.4 nM in reversing TPT resistance in HEK293/R2 cells and 35.8-167.5 nM in MCF7-MX100 cells, respectively, compared to the EC_{50} of 0.9 or 1.5 nM of **Ac12Az9**). SAR also predicted that decreasing the steric bulk around the benzine ring D would enhance **Ac12Az9**'s inhibitory effect on BCRP/ABCG2.

Deuterium may be strategically incorporated at the possible metabolic weak points to increase the compound stability [232, 233]. The deuterium substitution product **D10** retained its strong P-gp and BCRP/ABCG2 inhibition, with an EC_{50} of 243.7 nM for reversing PTX resistance in LCC6MDR cells and 1.0 and 2.9 nM for reversing TPT resistance in HEK293/R2 and MCF7-MX100 cells, respectively. However, the plasma stability of **D10** remained unchanged, with a half-life $t_{1/2}$ of 60 min below. This result clearly demonstrated that the low plasma stability of **Ac12Az9** was due to hydrolysis in the ester group (-COOR).

The relationship between the physicochemical descriptors (MW, clogP, and tPSA) of **Ac12Az9** and its derivative and their P-gp and BCRP/ABCG2 inhibitory activity showed that **Ac12Az9** could not be modified to produce better dual P-gp and BCRP/ABCG2 modulator; any increase in BCRP/ABCG2 inhibitory activity comes at

the expense of P-gp inhibitory activity. Therefore, **D6** with good stability and strong specific inhibition of BCRP/ABCG2 was selected from **D1-D11** for *in vivo* PK study and efficacy evaluation in combination with TPT in the HEK293/R2 xenograft model.

PK studies and tissue accumulation indicated that **D6** was stable and widely distributed throughout the body following a single I.V. injection (20 mg/kg). The $AUC_{5\text{-}360\ min}$ values of D6 were 330.5, 757.5, 2657.14, and 1164.23 μg·min/g (or mL) in the plasma, liver, kidneys, and lung, respectively, which were 54, 25, 11, and 8 times higher than the comparable $AUC_{5\text{-}360\ min}$ of **Ac12Az9**, respectively. This finding demonstrated that the enhanced plasma stability of **D6** did produce the expected *in vivo* results.

In a subcutaneous HEK293/R2 xenograft model, co-administration of **D6** and TPT at a single dose increased the tumor accumulation of TPT by 2-fold ($p = 0.0028$) compared to TPT alone. This result further suggested that repeated doses of **D6** and TPT can potentially inhibit tumor growth in the HEK293/R2 xenograft model, opening up further possibilities for cancer treatment in the future.

6.4 Conclusion

In conclusion, **Ac12Az9** was unstable in plasma with a fast clearance and a short half-life *in vivo*. To address the poor plasma stability of **Ac12Az9**, modification at the ester bond, including replacing the methyl ester group, increasing the steric hindrance around the ester group, reducing the electron density of ester, and incorporating deuterium at methyl ester, was employed. **D6** stood out from **D1-D11** with improved plasma stability, potent BCRP/ABCG2 inhibitory activity, and favorable PK performance. **D6** can significantly increase the tumor accumulation of TPT in the HEK293/R2 xenograft model, which implied that **D6** might be a promising option for more research into combination therapy for the treatment of BCRP/ABCG2-overexpressing tumors.

Chapter 7 Dual inhibition of P-gp and BCRP/ABCG2 to increase the brain penetration of AZD1775 in BALB/c mice

7.1 Introduction

Adavosertib (AZD1775, MK-1775, see **Figure 7-1**) was an investigational anticancer drug candidate developed by Merck & Co. and licensed to AstraZeneca [234]. It is a small-molecule inhibitor of the Wee1 tyrosine kinase [235]. Through Wee1 inhibition, AZD1775 can cause G2 checkpoint escape, thereby enhancing the apoptotic effects of radiotherapy or DNA-damaging agents [236]. AZD1775 has been evaluated in phase I/II clinical studies for the treatment of ovarian carcinoma [237, 238], uterine serous carcinoma [239], pancreatic cancer [240], breast cancer [241], head and neck squamous cell carcinoma [242], and GBM [116, 243, 244].

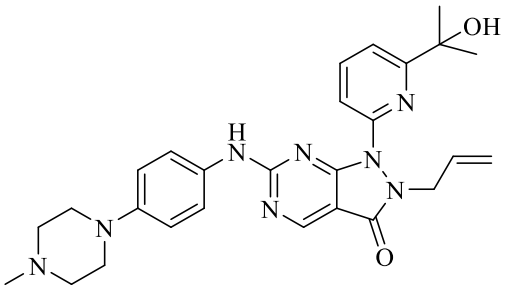

Adavosertib (AZD1775, MK1775)
Chemical Formula: $C_{27}H_{32}N_8O_2$
Molecular Weight: 500.61

Figure 7-1 Chemical structure of Adavosertib (AZD1775)

Brain accumulation of AZD1775, however, was low with a brain-to-plasma ratio of 4%-5% [245] possibly due to the presence of P-gp (ABCB1) and BCRP (ABCG2) at the BBB [141]. No therapeutic effect was observed in the Phase 0/I clinical trials of AZD1775 on GBM patients, possibly due to its low brain penetration [116, 243, 244].

P-gp and BCRP/ABCG2 at the BBB can prevent most xenobiotics from reaching the CNS by actively transporting them into blood [138]. Brain-to-plasma ratio of AZD1775

in Abcb1a/b$^{-/-}$Abcg2$^{-/-}$ mice was 25-fold higher compared to wild-type mice [141]. This illustrated the importance of inhibiting P-gp and BCRP/ABCG2 simultaneously to increase AZD1775 brain accumulation.

Previous chapters have demonstrated that **Ac12Az9** can increase the brain accumulation of sorafenib by inhibiting both P-gp and BCRP/ABCG2 at the BBB. Combination of **Ac12Az9** and sorafenib was effective in treating GBM. In this chapter, the effect of **Ac12Az9** on the cellular accumulation, efflux, and brain accumulation of AZD1775 in mice was investigated to determine whether the combination of **Ac12Az9** and AZD1775 might be used to treat GBM.

7.2 Results

7.2.1 Cytotoxicity of AZD1775 towards different GBM PDX cells

The cytotoxicity of AZD1775 was evaluated *in vitro* in various PDX GBM cells. It was found that AZD1775 was cytotoxic to different GBM cells, with IC_{50} values of 1.14, 0.59, and 0.90 μM for U87MG-RedFLuc, G22-FLuc, and TMZ-selected G28-FLuc cells, respectively (**Figure 7-2A-B**).

A

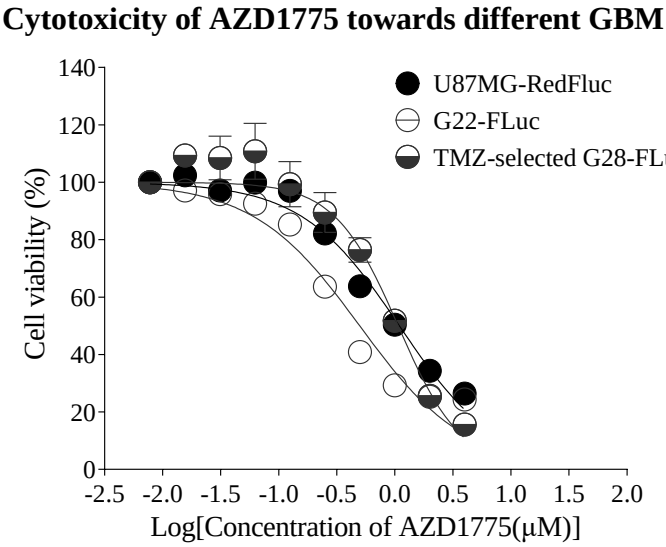

B

IC_{50} (μM) of AZD1775 towards different GBM lines		
U87MG-RedFLuc	G22-FLuc	TMZ-selected G28-FLuc
1.14 ± 0.08	0.59 ± 0.13	0.90 ± 0.24

Figure 7-2 Cytotoxicity of AZD1775 towards U87MG-RedFluc and PDX GBM cells
(A) MTS assay of cells treated with AZD1775; (B) IC_{50}s of AZD1775 towards U87MG-RedFluc and PDX GBM cells.
Cells were seeded into a 96-well plate with 4500 cells/well. AZD1775 at different doses (0, 0.016, 0.03, 0.062, 0.125, 0.25, 0.5, 1, 2, and 4 μM) were added into wells, respectively. Cell viability was measured after 4 days of incubation. Data was present as mean ± SD (n = 2-3). IC_{50} values of AZD1775 were calculated by PRISM software.

7.2.2 Effect of Ac12Az9 and its derivatives on AZD1775 accumulation in MDCKII-WT, MDCKII-P-gp, and MDCKII-GFP-BCRP cells

Accumulation of AZD1775 in MDCKII cells overexpressing either P-gp (MDCKII-P-gp cells) or BCRP/ABCG2 (MDCKII-GFP-BCRP cells) were examined with or without **Ac12Az9**. It was found that MDCKII-P-gp cells accumulated less AZD1775 compared to their wild type ($p < 0.001$) (**Figure 7-3A**). **Ac12Az9** and its derivatives significantly and dose-dependently increased the low intracellular AZD1775 accumulation in MDCKII-P-gp cells ($p < 0.05$, $p < 0.01$, or $p < 0.001$) (**Figure 7-3A**). 1 μM of **D1**, **D5**, and **D7** greatly increased the intracellular concentration of AZD1775 to a level similar to that of MDCKII-WT cells, reaching 106%, 90.65%, and 92.92%, respectively, in MDCKII-P-gp cells; such effects were better than **Ac12Az9** (71%) and similar to GF120918 (109.19%) (**Figure 7-3A**).

MDCKII-GFP-BCRP cells also accumulated less AZD1775 compared to their wild type ($p < 0.001$) (**Figure 7-3B**). **Ac12Az9** and its derivatives significantly increased the intracellular AZD1775 accumulation in MDCKII-GFP-BCRP cells in a dose-dependent manner (**Figure 7-3B**). 1 μM of **D1**, **D5**, **D6**, and **D7** significantly increased the intracellular concentration of AZD1775 to that of MDCKII-WT cells, reaching 131%, 135%, 105%, and 116%, respectively, in MDCKII-GFP-BCRP cells; which was similar to that of **Ac12Az9** (118%) and GF120918 (118%) (**Figure 7-3B**).

A

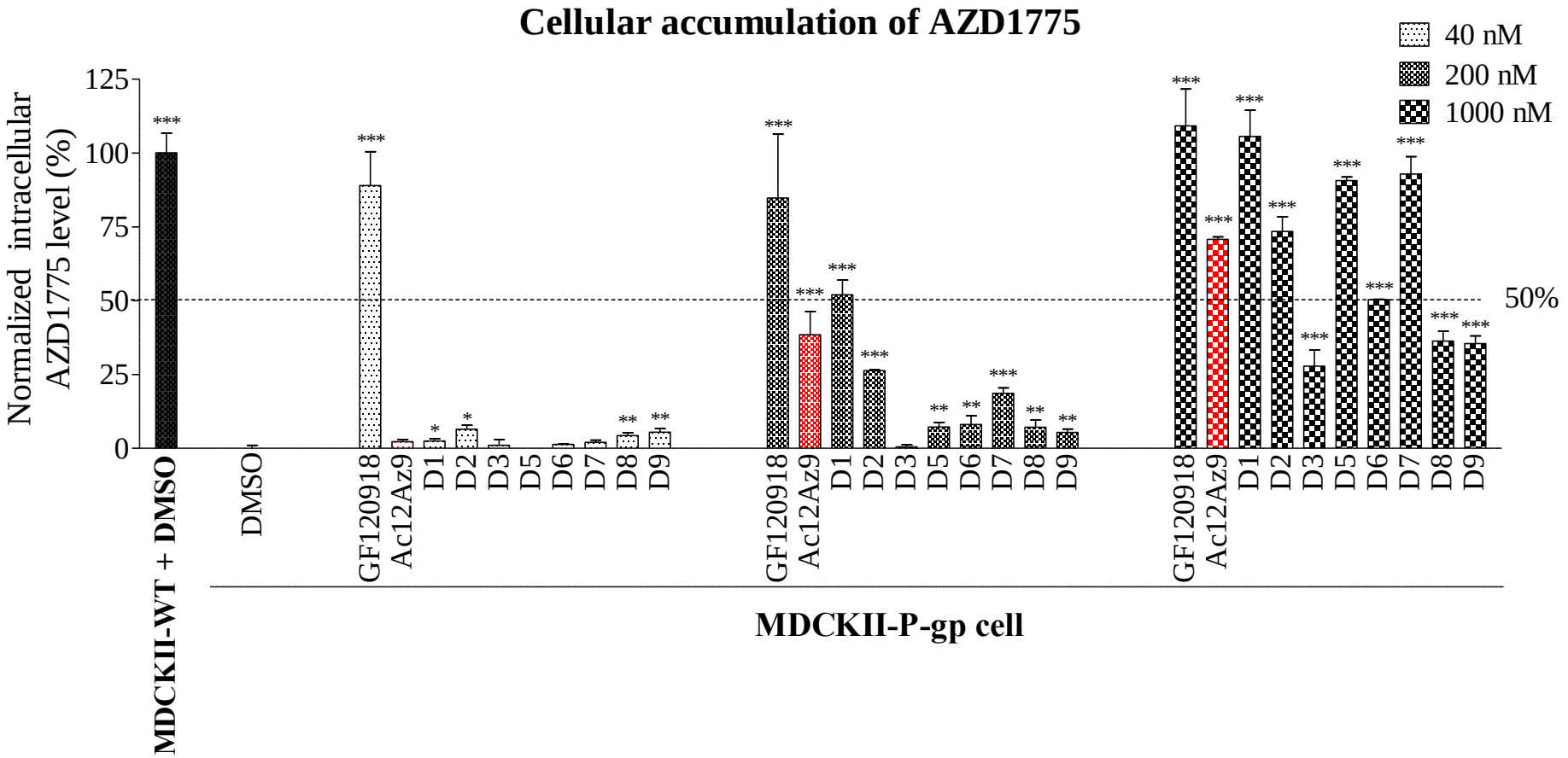
Cellular accumulation of AZD1775
40 nM
200 nM
1000 nM
Normalized intracellular AZD1775 level (%)
125
100
75
50
25
0
50%
MDCKII-WT + DMSO
DMSO
GF120918
Ac12Az9
D1
D2
D3
D5
D6
D7
D8
D9
MDCKII-P-gp cell

B

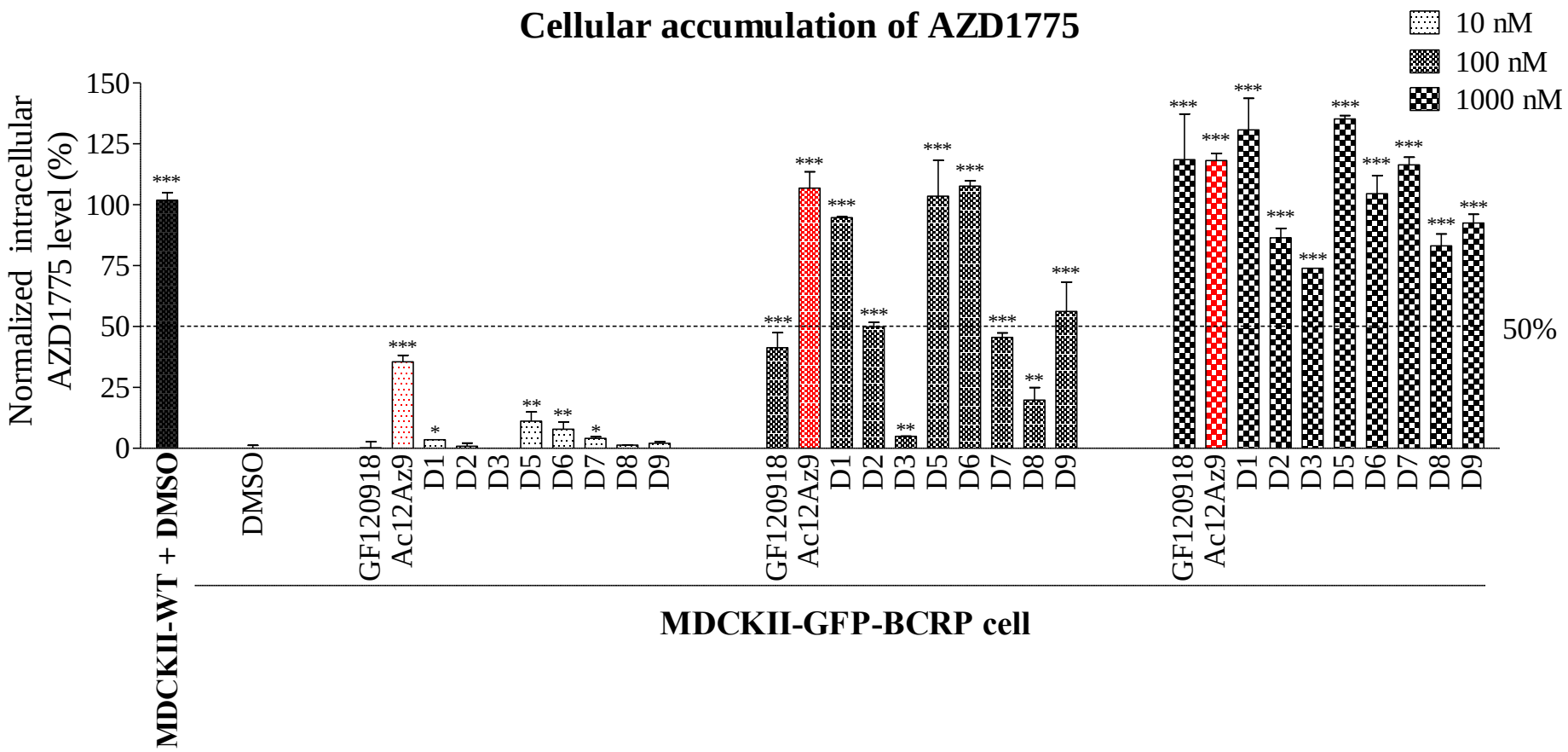

Figure 7-3 Effects of Ac12Az9 and its derivatives on the intracellular accumulation of AZD1775 in MDCKII-WT, MDCKII-P-gp, and MDCKII-GFP-BCRP cells

(A) Intracellular AZD1775 levels in MDCKII-WT and MDCKII-P-gp cells with or without modulators; (B) Intracellular AZD1775 levels in MDCKII-WT and MDCKII-GFP-BCRP cells with or without modulators.

The cells were incubated with 1 μM AZD1775 for 60 mins at 37°C with or without **Ac12Az9** (1 μM), GF120918 (1 μM), or **Ac12Az9** derivatives (1 μM). DMSO (0.1%) was used as a negative control. Intracellular levels of AZD1775 were determined by UPLC-MS/MS. Data was presented as the normalized AZD1775 %. Normalization was done by setting MDCKII-WT (0.1% DMSO) group to 100% and MDCKII-P-gp (0.1% DMSO) or MDCKII-GFP-BCRP (0.1% DMSO) group to 0%. After that, the remaining groups were converted to the matching percentage of AZD1775. The values were presented as mean ± SD and compared by student's t-test. *, $p < 0.05$, **, $p < 0.01$, ***, $p < 0.001$.

7.2.3 Effect of Ac12Az9 on AZD1775 efflux in MDCKII-WT, MDCKII-P-gp, and MDCKII-GFP-BCRP cells

Ac12Az9 can inhibit the efflux of AZD1775 in either P-gp (MDCKII-P-gp cells) or BCRP/ABCG2 (MDCKII-GFP-BCRP cells). 88%, 49%, and 42% of AZD1775 remained in MDCKII-WT, MDCKII-P-gp, and MDCKII-GFP-BCRP cells after 30 mins, respectively (**Figure 7-4**). **Ac12Az9** showed no effect on the efflux of AZD1775 in MDCKII-WT cells, with the intracellular AZD1775 remaining at 86%. **Ac12Az9** inhibited the P-gp-mediated AZD1775 efflux in MDCKII-P-gp cells, raising the intracellular AZD1775 from 49% to 80% ($p < 0.001$) (**Figure 7-4**). **Ac12Az9** also blocked the BCRP/ABCG2-mediated AZD1775 efflux, raising the intracellular AZD1775 from 42% to 102% ($p < 0.001$) in MDCKII-GFP-BCRP cells (**Figure 7-4**). This finding indicated that **Ac12Az9** increased the AZD1775 accumulation in MDCKII-P-gp and MDCKII-GFP-BCRP cells by inhibiting P-gp- and BCRP/ABCG2-mediated drug efflux.

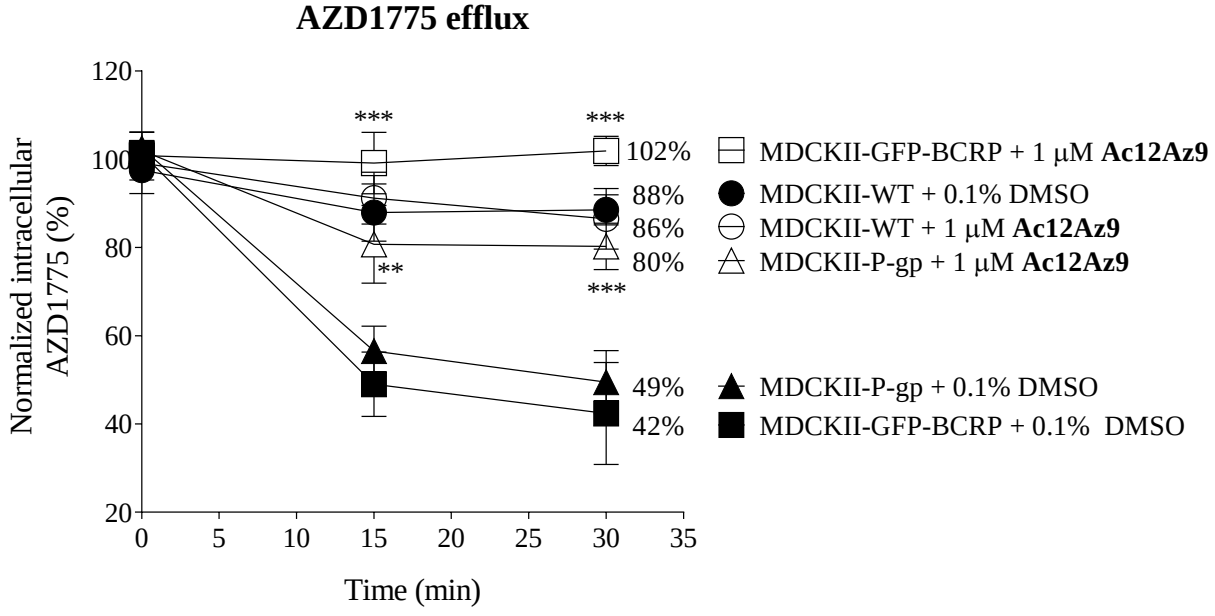

Figure 7-4 Effect of Ac12Az9 on AZD1775 efflux in MDCKII-WT, MDCKII-P-gp, and MDCKII-GFP-BCRP cells

Cells preloaded with AZD1775 were incubated with or without modulator **Ac12Az9** (1 μM) at 37 °C. Cells were taken at 0, 15, and 30 mins, and UPLC-MS/MS was used to determine the intracellular

AZD1775 concentration. All the data was shown as the normalized percentages of intracellular AZD1775 level and presented as mean ± SD (n = 4). Student's t-test was used to compare statistical differences between cells with and without **Ac12Az9** at various time points. **, $p < 0.01$, ***, $p < 0.001$.

7.2.4 Effect of Ac12Az9 on the PK and brain accumulation of AZD1775 in BALB/c mice

The effect of **Ac12Az9** on the brain accumulation of AZD1775 was studied in BALB/c mice. AZD1775 was given an hour before **Ac12Az9.** The PK experimental design was shown in **Figure 7-5A**. It was found that the brain level of AZD1775 peaked at the first time point (414 ng/g), and then it gradually decreased to only 28 ng/g at 300 min. Administration of **Ac12Az9** slowed down the decline of AZD1775 in the brain, increasing the level of AZD1775 to 131 ng/g in the brain after 300 min (**Figure 7-5B**). The increased brain level of AZD1775 was higher than its *in vitro* IC_{50} against both G22-FLuc and TMZ-selected G28-FLuc cells (**Figure 7-5B**). Unexpectedly, **Ac12Az9** decreased the plasma level of AZD1775 from 2047 ng/mL (at the first time point) in the AZD1775 alone group to 302 ng/mL, and this anomalous decline continued throughout the measurement period (**Figure 7-5C**). The brain-to-plasma ratio of AZD1775 was elevated from 0.2 in the AZD1775 alone group to 1.0 in the presence of **Ac12Az9** and remained above 1.0 ever since. (**Figure 7-5D**). These data suggested that **Ac12Az9** can enhance the brain penetration of AZD1775 *in vivo*.

PK parameters were summarized in **Figure 7-5E**. Dose-normalized brain C_{max} of AZD1775 (C_{max}/dose) was 8.28 $ng \cdot g^{-1}/mg \cdot kg^{-1}$ in AZD1775 alone group, and it can be increased by **Ac12Az9** to 12.10 $ng \cdot g^{-1}/mg \cdot kg^{-1}$ (1.5-fold over AZD1775 alone). Dose-normalized $AUC_{65\text{-}300}$ of AZD1775 in the brain (AUC_{brain}/dose) was 844.8 $ng \cdot min \cdot g^{-1}/mg \cdot kg^{-1}$ in AZD1775 alone group, and **Ac12Az9** can increase it to 1369.7 $ng \cdot min \cdot g^{-1}/mg \cdot kg^{-1}$ (1.6-fold over AZD1775 alone). Unexpectedly, the dose-normalized $AUC_{65\text{-}300}$ of AZD1775 in plasma (AUC_{plasma}/dose) was 6847 $ng \cdot min \cdot mL^{-1}/mg \cdot kg^{-1}$, and it was decreased by **Ac12Az9** to 674.12 $ng \cdot min \cdot mL^{-1}/mg \cdot kg^{-1}$ (10-fold decrease). Overall,

Ac12Az9 can increase the AUC_{brain}/AUC_{plasma} of AZD1775 from 0.12 to 2.03 (a 16.5-fold increase).

A

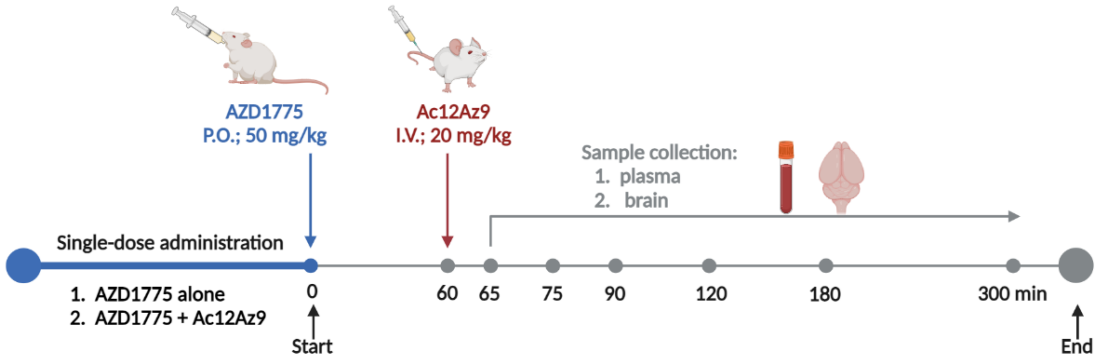

B

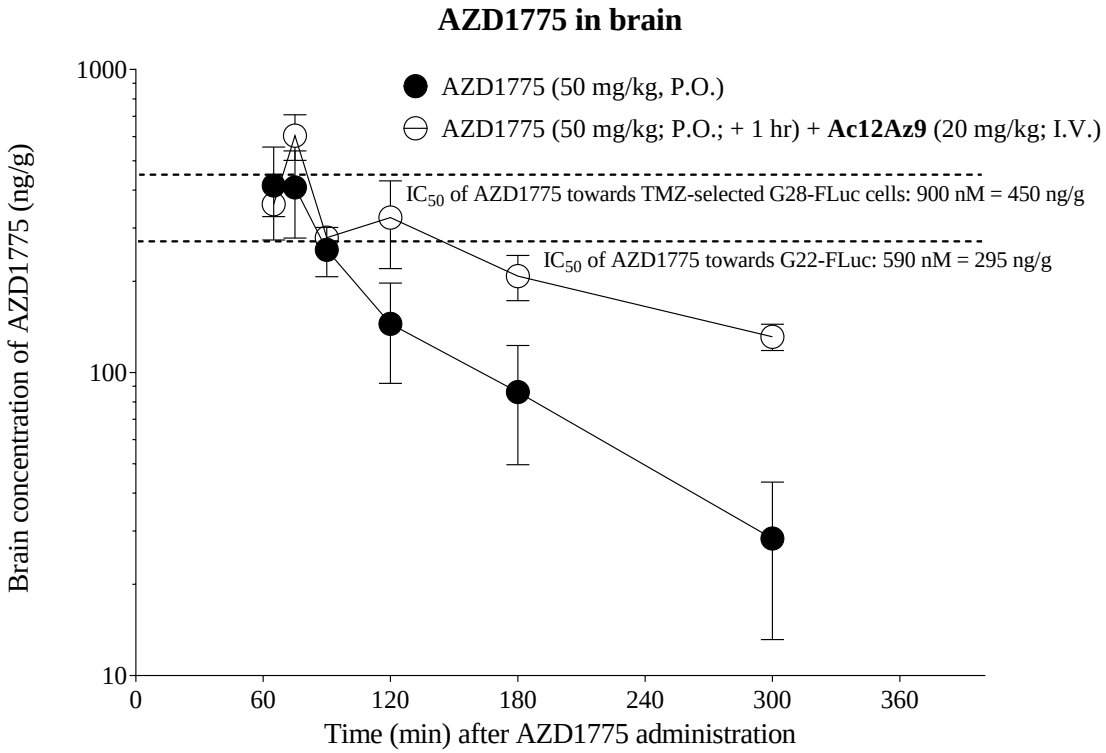

C

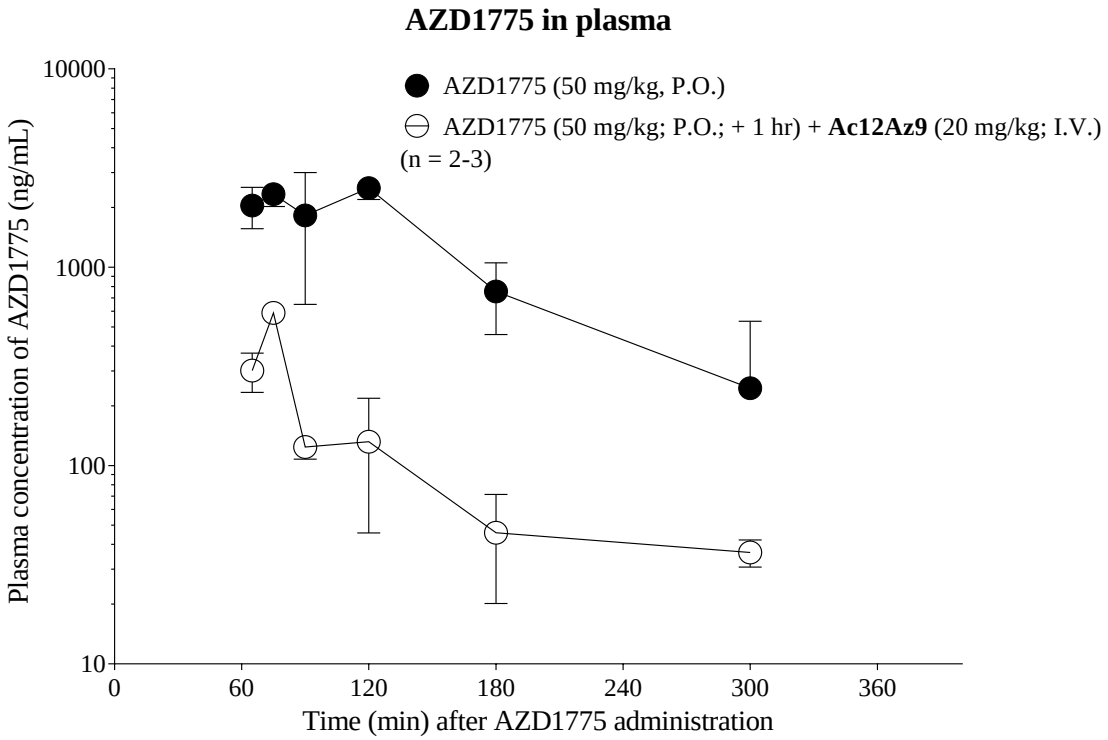
AZD1775 in plasma
AZD1775 (50 mg/kg, P.O.)
AZD1775 (50 mg/kg; P.O.; + 1 hr) + Ac12Az9 (20 mg/kg; I.V.)
(n = 2-3)
Plasma concentration of AZD1775 (ng/mL)
10000
1000
100
10
0
60
120
180
240
300
360
Time (min) after AZD1775 administration

D

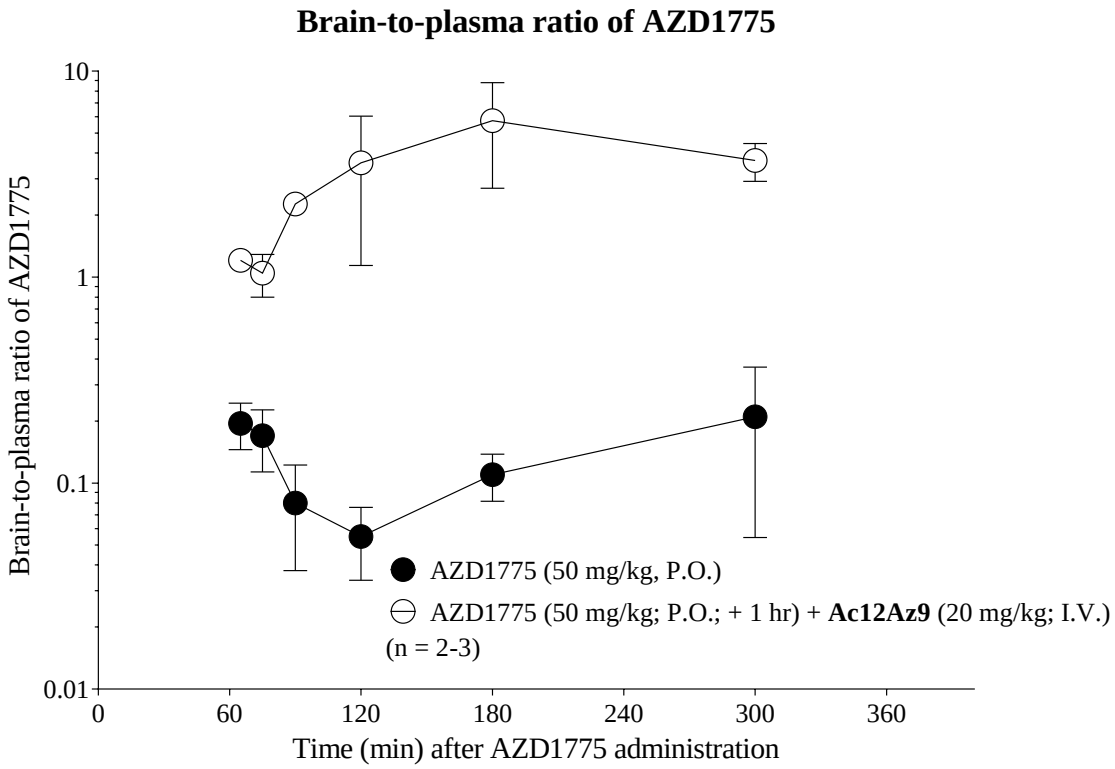
Brain-to-plasma ratio of AZD1775
Brain-to-plasma ratio of AZD1775
10
1
0.1
0.01
AZD1775 (50 mg/kg, P.O.)
AZD1775 (50 mg/kg; P.O.; + 1 hr) + Ac12Az9 (20 mg/kg; I.V.)
(n = 2-3)
0
60
120
180
240
300
360
Time (min) after AZD1775 administration

E

Adminstration route	**P.O.**		**P.O., 1 hr, I.V.**	
AZD1775 (mg/kg)	**50**		**50**	
Ac12Az9 (mg/kg)	**0**		**20**	
C_{max}/dose [brain] ng·g^{-1}/(mg·kg^{-1}) (fold)	8.28	(1.0 X)	12.10	(1.5 X)
$AUC_{65\text{-}300}$/dose [brain] ng·min·g^{-1}/(mg·kg^{-1}) (fold)	844.8	(1.0 X)	1369.7	(1.6 X)
$AUC_{65\text{-}300}$/dose [plasma] ng·min·mL^{-1}/(mg·kg^{-1}) (fold)	6847.0	(1.0 X)	674.12	(0.1 X)
$AUC_{65\text{-}300}$/dose [brain]/$AUC_{65\text{-}300}$/dose [plasma] (fold)	0.12	(1.0 X)	2.03	(16.5 X)

Figure 7-5 Effect of Ac12Az9 on PK and brain distribution profiles of AZD1775 in BALB/c mice

(A) Schematic diagram of PK studies of AZD1775 and **Ac12Az9**; (B) Brain concentration-time curves of AZD1775 with or without **Ac12Az9**; (C) Plasma concentration-time curves of AZD1775 with or without **Ac12Az9**; (D) Brain-to-plasma ratio of AZD1775 with or without **Ac12Az9**; (E) Calculated PK parameters of AZD1775.

AZD1775 (2.5 mg/mL) or **Ac12Az9** (2 mg/mL) were prepared in the formulation of NMP, CrEL, and 5% Tween-80 (10: 10: 80), respectively. Mice in the AZD1775 alone group received 50 mg/kg of AZD1775 orally, whereas mice in the co-administration group received intravenous injections of **Ac12Az9** (20 mg/kg) one hour after receiving AZD1775 orally. Blood and whole brain samples were collected at various time points (65, 75, 90, 120, 180, and 300 min) after the administration of AZD1775. Plasma and brain concentration of AZD1775 was determined by UPLC-MS/MS. The data was presented as mean ± SEM (n = 2-3). A non-compartmental analysis was performed using PK Solutions 2.0.3 software (Ashland, OH44805, USA) to calculate the AUC values.

7.2.5 Effect of solvent on the PK and tissue accumulation of AZD1775 in BALB/c mice

The previous section demonstrated that **Ac12Az9** led to an unexpected drop in the plasma level of AZD1775. The solvent used to dissolve **Ac12Az9** consisted of a combination of NMP, CrEL, Tween-80, and Milli-Q water (10: 10: 4: 76). Here, the effects of Milli-Q water, NMP, CrEL, Tween-80, and **Ac12Az9** on the plasma and tissue levels of AZD1775 were investigated in BALB/c mice. The design of the PK experiment design was shown in **Figure 7-6A**.

The plasma concentration of AZD1775 was 2927 ng/mL when combined with Milli-Q water (**Figure 7-6B**). 10% NMP did not affect the plasma concentration of AZD1775, with only a 10% (p = 0.6088) reduction in AZD1775 compared to Milli-Q water. 10% CrEL, 4% Tween-80, or solvent for **Ac12Az9** dramatically reduced the plasma concentration of AZD1775 by 98% (p = 0.0153), 97% (p = 0.0158), and 94% (p = 0.0023), respectively, compared to Milli-Q water (**Figure 7-6B**). Additionally, **Ac12Az9** significantly decreased the blood level of AZD1775 by 98% (p = 0.0033) compared to Milli-Q water (**Figure 7-6B)**. These results suggested that the two solvents, CrEL and Tween-80, were responsible for the abnormal decline in the plasma level of AZD1775.

The level of AZD1775 in the liver and kidney was also measured to see if the aberrant drop in AZD1775 plasma levels could be attributed to the distribution of AZD1775 to other organs. The level of AZD1775 in the kidney was 19952.4 ng/g when combined with Milli-Q water (**Figure 7-6C**). 10% NMP had no impact on the kidney concentration of AZD1775, which remained at 20784.3 ng/g compared to Milli-Q water. 10% CrEL, 4% Tween-80, solvent for **Ac12Az9**, and **Ac12Az9** dramatically reduced the kidney concentration of AZD1775 by 98% (p = 0.0025), 78% (p = 0.0118), 91% (p = 0.0032), and 88% (p = 0.0033), respectively, compared to Milli-Q water (**Figure 7-6C**). Solvent and **Ac12Az9** had an identical impact on AZD1775 distribution in the

liver as they did in the kidney. The liver concentration of AZD1775 was 35830.6 ng/g when combined with Milli-Q water (**Figure 7-6D**). 10% NMP did not affect the liver concentration of AZD1775, and the liver concentration of AZD1775 only decreased by 16% ($p = 0.4556$) compared to the Milli-Q water (**Figure 7-6D**). 10% CrEL, 4% Tween-80, solvent for **Ac12Az9**, and **Ac12Az9** dramatically reduced the kidney concentration of AZD1775 by 88% ($p = 0.0258$), 73% ($p = 0.0375$), 74% ($p = 0.0363$), and 85% ($p = 0.0277$), respectively, compared to Milli-Q water (**Figure 7-6D**). Together, these findings suggested that the abnormal drop in AZD1775 blood levels may be due to degradation, precipitation, or other unknown reasons that made it undetectable by UPLC-MS/MS.

The brain concentration of AZD1775 was also investigated in the BALB/c mice. The brain concentration of AZD1775 was 214.53 ng/g when combined with Milli-Q water (**Figure 7-6E**). According to our earlier PK data (**Figure 7-5B**), **Ac12Az9** did not affect the concentration of AZD1775 in the brain at the first time point (65 mins) after administration. Here, 10% NMP, 4% Tween-80, **Ac12Az9** solvent, and **Ac12Az9** also did not alter the concentration of AZD1775 in the brain, with AZD1775 brain levels of 259.9, 233.1, 179.6, and 212.8 ng/g, respectively, compared to 214.53 ng/g when combined with Milli-Q water (**Figure 7-6E**). However, 10% CrEL decreased the brain level of AZD1775 by 72% ($p = 0.0055$) compared to the Milli-Q water group.

A

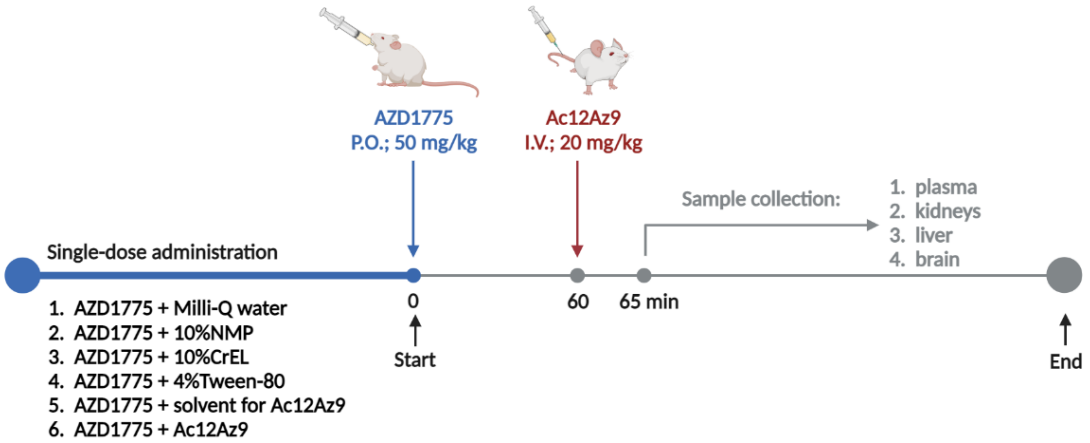

B

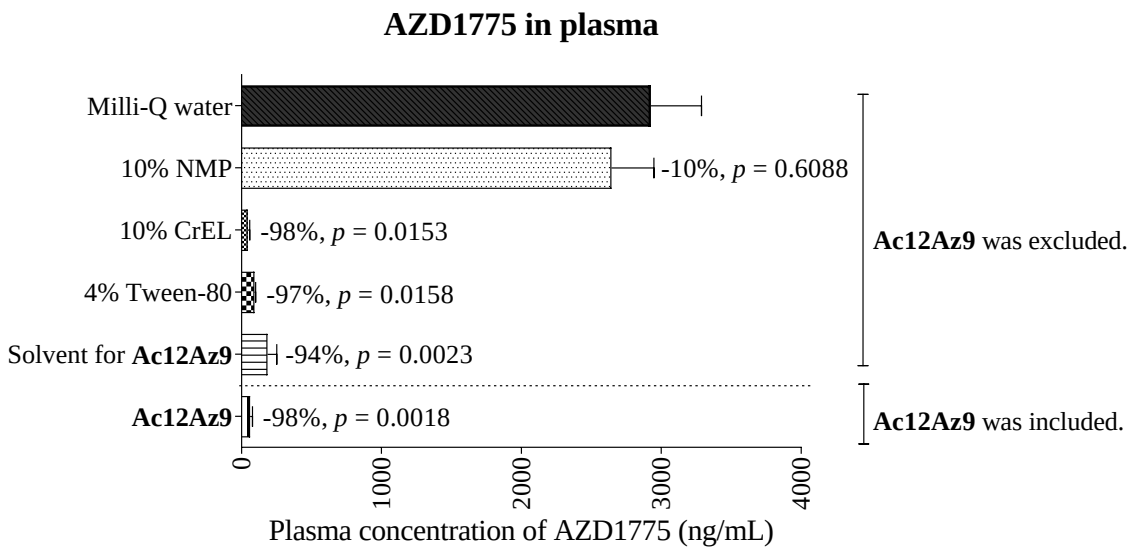
AZD1775 in plasma
Milli-Q water
10% NMP
10% CrEL
4% Tween-80
Solvent for Ac12Az9
Ac12Az9
-10%, p = 0.6088
-98%, p = 0.0153
-97%, p = 0.0158
-94%, p = 0.0023
-98%, p = 0.0018
Ac12Az9 was excluded.
Ac12Az9 was included.
0
1000
2000
3000
4000
Plasma concentration of AZD1775 (ng/mL)

C

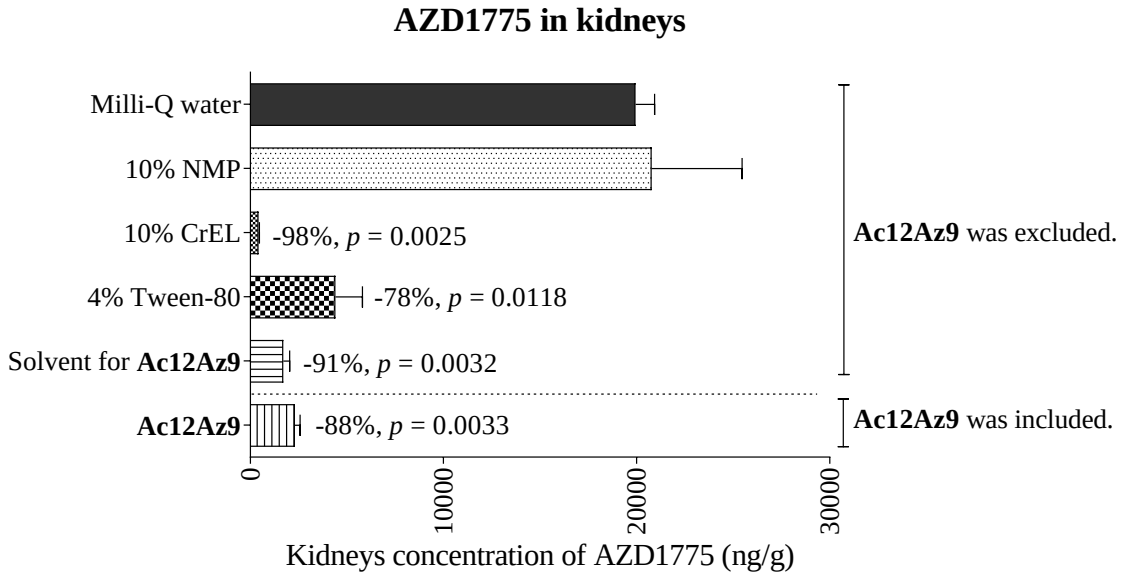
AZD1775 in kidneys
Milli-Q water
10% NMP
10% CrEL
4% Tween-80
Solvent for Ac12Az9
Ac12Az9
-98%, p = 0.0025
-78%, p = 0.0118
-91%, p = 0.0032
-88%, p = 0.0033
Ac12Az9 was excluded.
Ac12Az9 was included.
0
10000
20000
30000
Kidneys concentration of AZD1775 (ng/g)

D

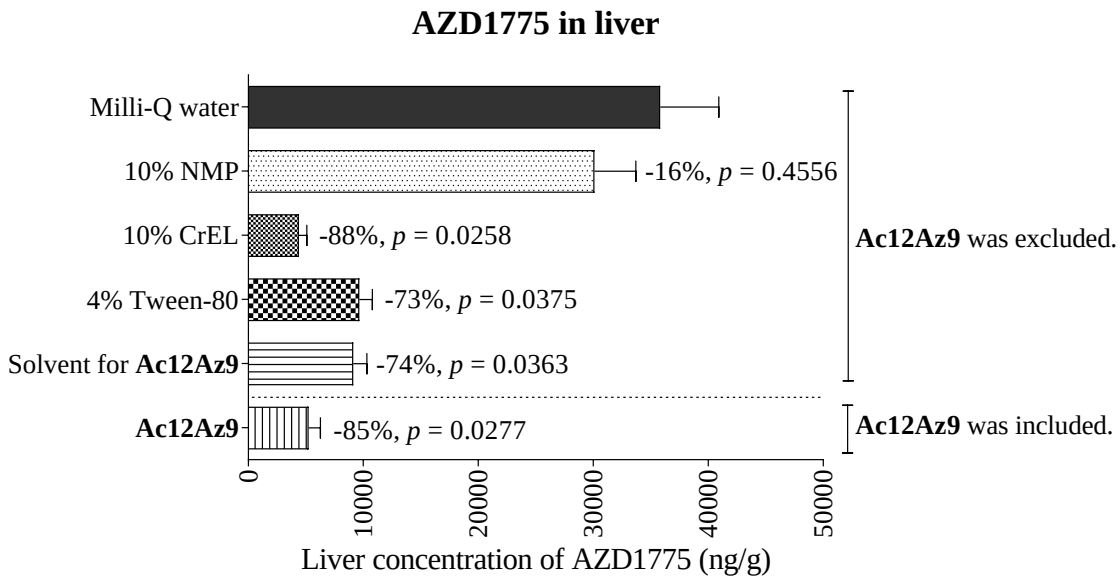

E

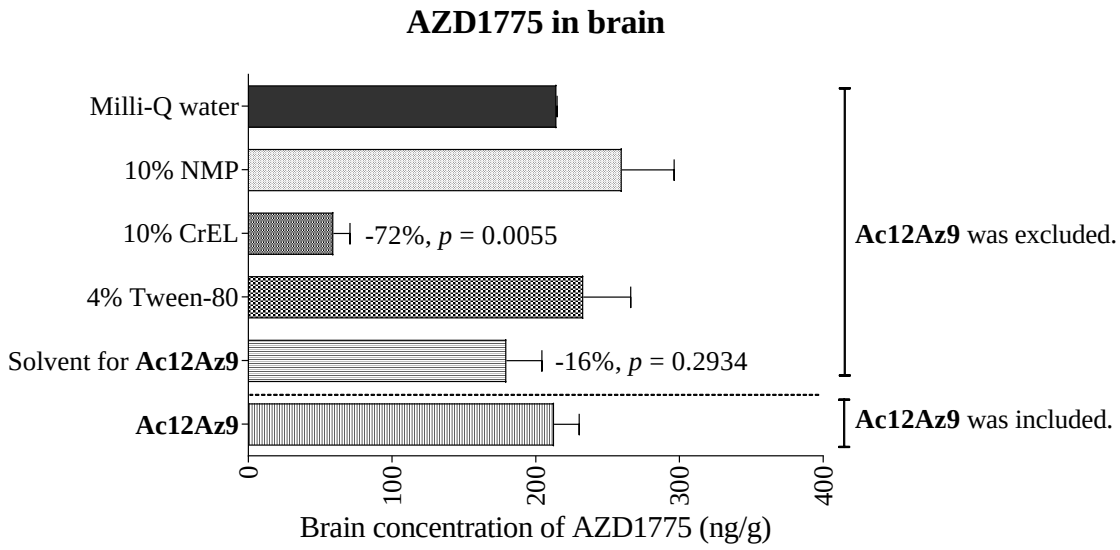

Figure 7-6 Effects of Ac12Az9 and its solvent on the plasma and tissue accumulation of AZD1775 in BALB/c mice

(A) Schematic diagram of *in vivo* studies of AZD1775 and **Ac12Az9**; (B) Plasma concentration of AZD1775 65 mins after administration of AZD1775 with or without the addition of other factors; (C) Kidneys concentration of AZD1775 65 mins after administration of AZD1775 with or without the addition of other factors; (D) Liver concentration of AZD1775 65 mins after administration of AZD1775 with or without the addition of other factors; (E) Brain concentration of AZD1775 65 mins after administration of AZD1775 with or without the addition of other factors.

AZD1775 (2.5 mg/mL) or **Ac12Az9** (2 mg/mL) were prepared in the formulation of NMP, CrEL, and 5% Tween-80 (10: 10: 80), respectively. Mice in the AZD1775 alone group received oral administration of AZD1775 (50 mg/kg), whereas mice in the co-administration group were intravenously injected with a range of solutions or **Ac12Az9** (20 mg/kg), including Milli-Q water,

10%NMP, 10%CrEL, 4%Tween-80, **Ac12Az9** solvent, and **Ac12Az9**, one hour after receiving an oral dosage of AZD1775 (50 mg/kg). Blood and tissue samples were collected, respectively, at 65 min after the administration of AZD1775. AZD1775 concentration was determined by UPLC-MS/MS. The data was presented as mean ± SEM (n = 2-3).

7.2.6 Effect of solvent on AZD1775 levels *in vitro*

The above results suggested that the **Ac12Az9** solvent, rather than **Ac12Az9** itself, was the source of aberrant plasma PK data of AZD1775. Additionally, it was demonstrated that the significant decrease of AZD1775 in plasma did not result in an increase in the distribution of AZD1775 in other organs (liver or kidneys). Here, the effects of solvents on the solubility of AZD1775 were examined by mixing AZD1775 with mouse plasma first, followed by Milli-Q water or different components of **Ac12Az9** solvent.

Similar to the *in vivo* plasma PK result (**Figure 7-6B**), 10% NMP had no impact on the concentration of AZD1775 in plasma, with 96% of AZD1775 remaining in the plasma compared to the Milli-Q water group (**Figure 7-7A**). The solvents, including 10% CrEL, 4% Tween-80, and **Ac12Az9** solvent, substantially decreased the level of AZD1775 remaining in plasma by 95% ($p < 0.001$), 95% ($p < 0.001$), and 97% ($p < 0.001$), respectively, compared to Milli-Q water (**Figure 7-7A**).

The media was changed from plasma to water to further determine if the surfactant (CrEL and Tween-80) still had an effect on the concentration of AZD1775 in Milli-Q water without the biological factors. It was found that 10% NMP had no impact on the level of AZD1775, which remained at 98% compared to the Milli-Q water group (**Figure 7-7B**). The solvents, including 10% CrEL, 4% Tween-80, and **Ac12Az9** solvent, substantially decreased the level of AZD1775 by 77% ($p < 0.001$), 71% ($p < 0.001$), and 60% ($p < 0.001$), respectively, compared to Milli-Q water (**Figure 7-7B**).

Taken together, the concentration of AZD1775 in the Milli-Q water significantly decreased with the addition of the surfactants (CrEL and Tween-80) for an unknown reason. It is hypothesized that the anomalous drop in AZD1775 concentration may be caused by alterations in solubility or other unidentified reasons that make it challenging to detect by UPLC-MS/MS.

A

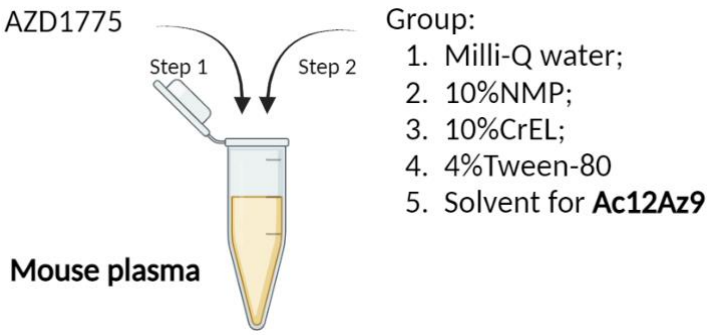
AZD1775
Step 1
Step 2
Mouse plasma
Group:
1. Milli-Q water;
2. 10%NMP;
3. 10%CrEL;
4. 4%Tween-80
5. Solvent for **Ac12Az9**

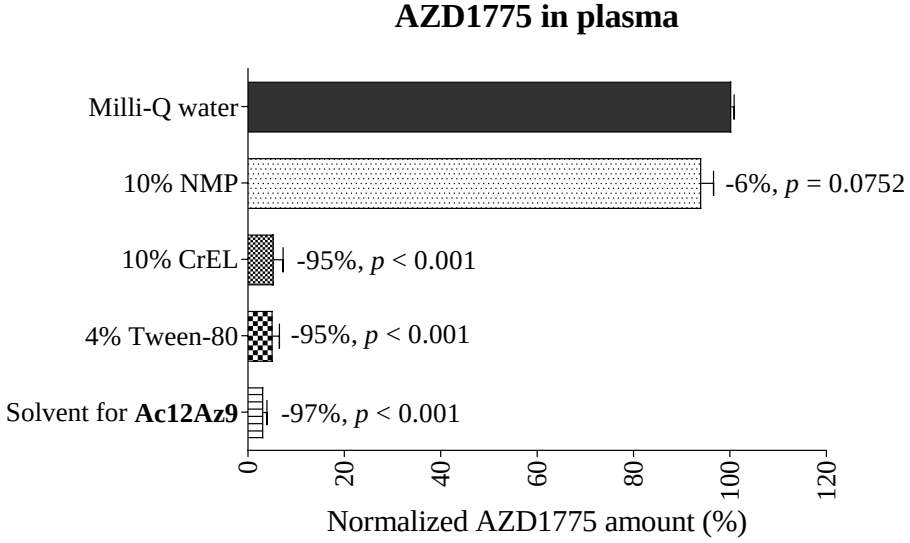
AZD1775 in plasma
Milli-Q water
10% NMP
10% CrEL
4% Tween-80
Solvent for **Ac12Az9**
-6%, p = 0.0752
-95%, p < 0.001
-95%, p < 0.001
-97%, p < 0.001
0
20
40
60
80
100
120
Normalized AZD1775 amount (%)

B

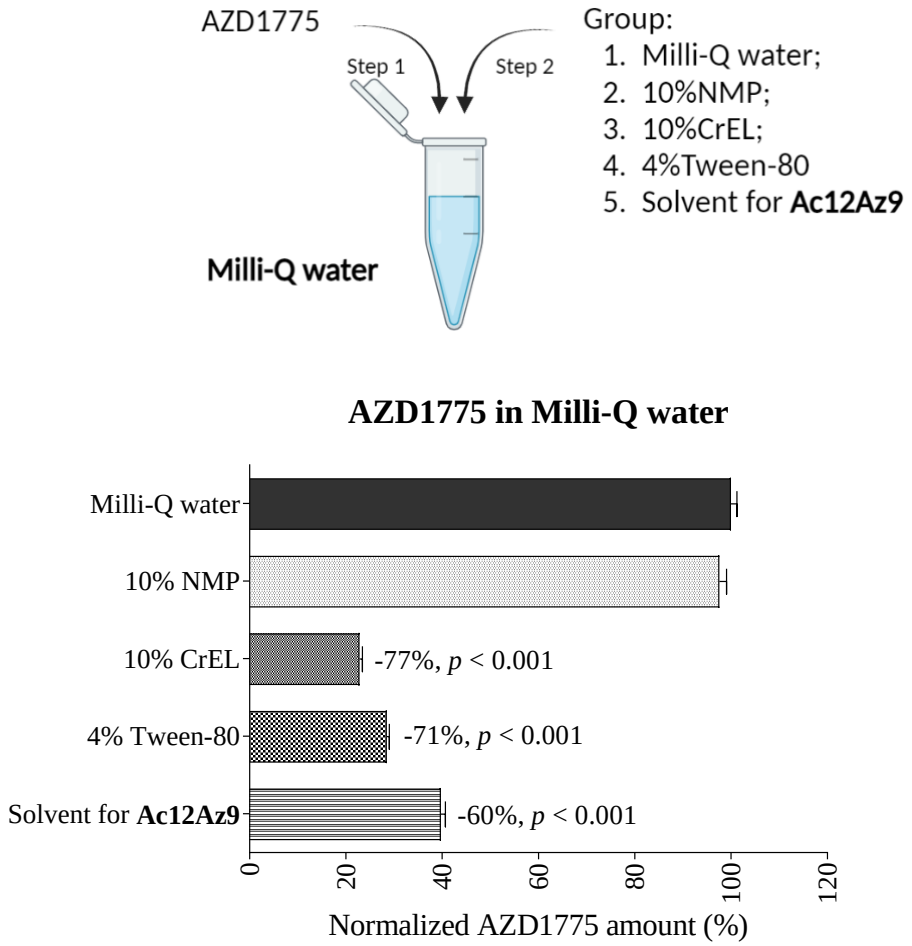

Figure 7-7 Effects of solvents on the solubility of AZD1775 in mouse plasma or Milli-Q water
(A) Concentration of AZD1775 in plasma with different solvents; (B) Concentration of AZD1775 in Milli-Q water with different solvents.
5 μL of AZD1775 (0.2 mg/mL in DMSO) were added into 200 μL of freshly prepared plasma or Milli-Q water. Following brief vortex mixing, 20 μL of each of the following solvents (MilliQ-water, 10% NMP, 10% CrEL, 4% Tween-80, or solvent for **Ac12Az9**) were added into the mixture, respectively. After 15 min of co-incubation at room temperature, the samples were added with a 3-fold volume of ACN. The compounds remaining in plasma or Milli-Q water were quantified by UPLC-MS/MS. The percentage of remaining AZD1775 relative to the Milli-Q water group was reported. The data was presented as mean ± SEM (n = 2-3).

7.2.7 Effect of Ac12Az9 on the PK and tissue accumulation of AZD1775 in BALB/c mice

The surfactant (CrEL and Tween-80) can greatly increase the solubility of **Ac12Az9**, but it also contributed to the unexpected decline in blood levels of AZD1775. Since a better solvent for **Ac12Az9** has yet to be developed, an alternative approach would be to try an early intravenous injection of **Ac12Az9**, hopefully, to reduce the effect of solvent on AZD1775 in the blood (by dilution). The design of PK experiments design was shown in **Figure 7-8A**.

It was found that pre-administration of **Ac12Az9** can still increase the brain of AZD1775 to therapeutic levels that were higher than its *in vitro* IC_{50} against G22-FLuc cells (0.59 μM) (**Figure 7-8B**). However, pre-administration of **Ac12Az9** still decreased the plasma level of AZD1775, from 3332.6 ng/mL (in the AZD1775 alone group at the first time point) to 348.2 ng/mL; and this abnormal decrease remained throughout the measurement period (**Figure 7-8C**). The brain-to-plasma ratio of AZD1775 was elevated from 0.02 in the AZD1775 alone group to around 1.0 in the presence of **Ac12Az9** (**Figure 7-8D**). These data suggested that pre-administration of **Ac12Az9** can still enhance the bran penetration of AZD1775 *in vivo*, even though the plasma level of AZD1775 remained unexpectedly decreased.

PK parameters were summarized in **Figure 7-8E**. Dose-normalized brain C_{max} of AZD1775 (C_{max}/dose) was 1.8 $ng \cdot g^{-1}/mg \cdot kg^{-1}$ in AZD1775 alone group. **Ac12Az9** can increase the C_{max}/dose values of AZD1775 to 7.8 $ng \cdot g^{-1}/mg \cdot kg^{-1}$ (4.2-fold over AZD1775 alone). Dose-normalized $AUC_{60\text{-}180}$ of AZD1775 in the brain (AUC_{brain}/dose) was 173 $ng \cdot min \cdot g^{-1}/mg \cdot kg^{-1}$ in AZD1775 alone group. **Ac12Az9** can increase the AUC_{brain}/dose of AZD1775 to 743 $ng \cdot min \cdot g^{-1}/mg \cdot kg^{-1}$ (4.3-fold over AZD1775 alone). Correspondingly, the dose-normalized $AUC_{60\text{-}180}$ of AZD1775 in plasma (AUC_{plasma}/dose) was 9451 $ng \cdot min \cdot mL^{-1}/mg \cdot kg^{-1}$. However, **Ac12Az9** decreased the AUC_{plasma}/dose of AZD1775 from 9451 $ng \cdot min \cdot mL^{-1}/mg \cdot kg^{-1}$ in the AZD1775 alone

group to 1254 ng·min·mL^{-1}/mg·kg^{-1} (decreased by7.5-fold). Overall, **Ac12Az9** can increase the AUC_{brain}/AUC_{plasma} of AZD1775 by 29-fold, raising from 0.02 to 0.59.

A

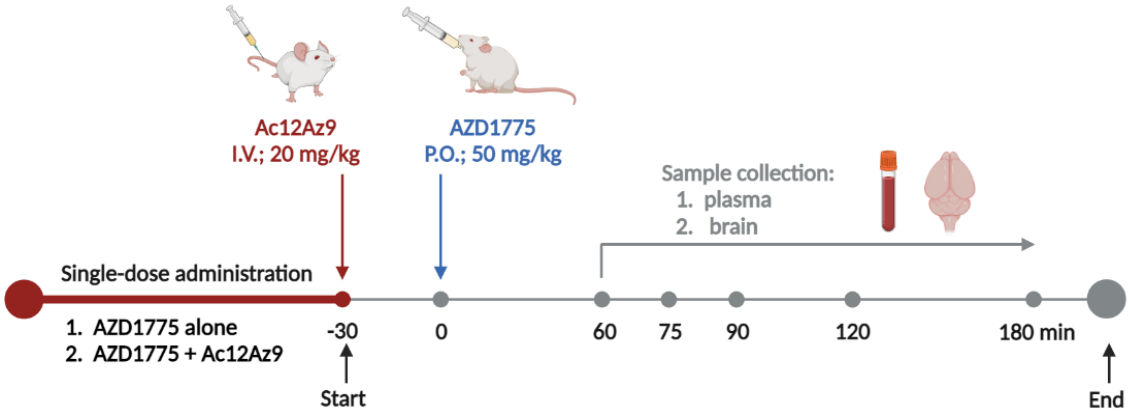

B

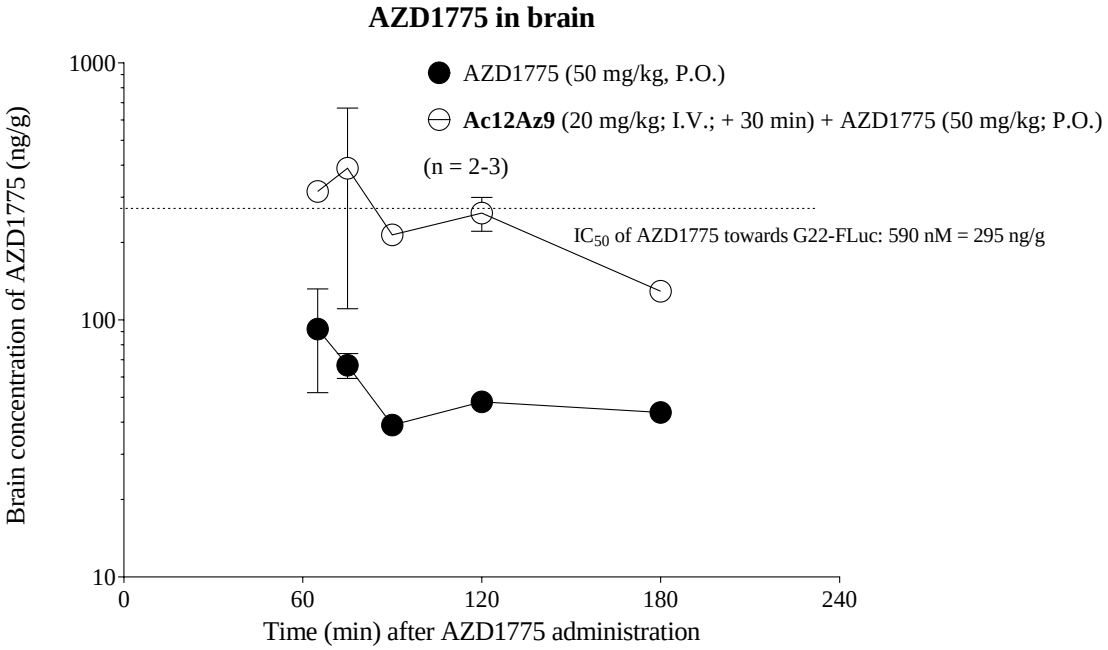

C

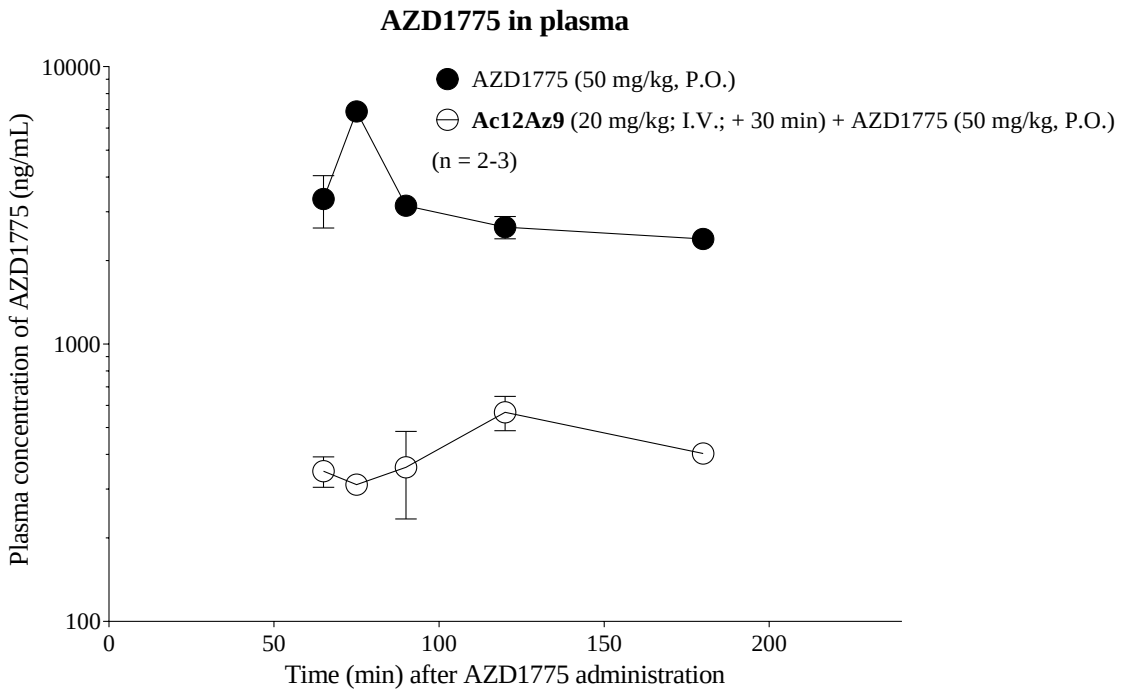
AZD1775 in plasma
AZD1775 (50 mg/kg, P.O.)
Ac12Az9 (20 mg/kg; I.V.; + 30 min) + AZD1775 (50 mg/kg, P.O.)
(n = 2-3)
Plasma concentration of AZD1775 (ng/mL)
10000
1000
100
0
50
100
150
200
Time (min) after AZD1775 administration

D

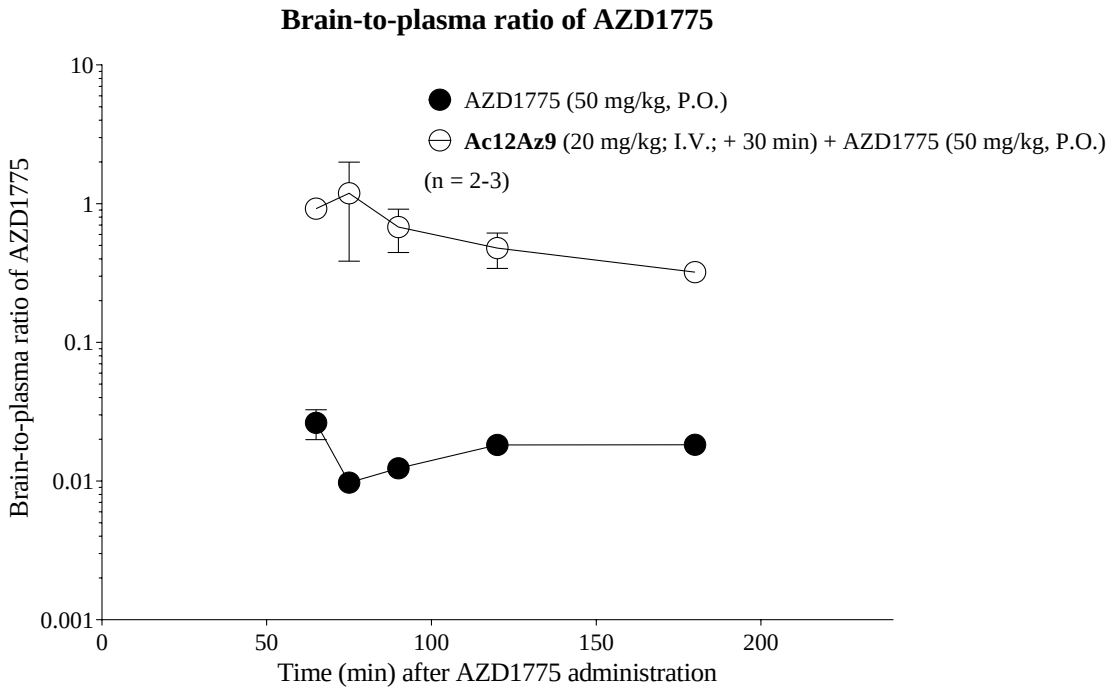
Brain-to-plasma ratio of AZD1775
AZD1775 (50 mg/kg, P.O.)
Ac12Az9 (20 mg/kg; I.V.; + 30 min) + AZD1775 (50 mg/kg, P.O.)
(n = 2-3)
Brain-to-plasma ratio of AZD1775
10
1
0.1
0.01
0.001
0
50
100
150
200
Time (min) after AZD1775 administration

E

Adminstration route	**I.V.**		**I.V., 30 mins, P.O.**	
Ac12Az9 (mg/kg)	**0**		**20**	
AZD1775 (mg/kg)	**50**		**50**	
C_{max}/dose [brain] ng·g^{-1}/(mg·kg^{-1}) (fold)	1.8	(1.0 X)	7.8	(4.2 X)
$AUC_{60\text{-}180}$/dose [brain] ng·min·g^{-1}/(mg·kg^{-1}) (fold)	173	(1.0 X)	743	(4.3 X)
$AUC_{60\text{-}180}$/dose [plasma] ng·min·mL^{-1}/(mg·kg^{-1}) (fold)	9451	(1.0 X)	1254	(0.1 X)
$AUC_{60\text{-}180}$/dose [brain]/$AUC_{60\text{-}180}$/dose [plasma] (fold)	0.02	(1.0 X)	0.59	(29 X)

Figure 7-8 Effect of Ac12Az9 on PK and brain distribution profiles of AZD1775 in BALB/c mice

(A) Schematic diagram of PK studies of AZD1775 and **Ac12Az9**; (B) Brain concentration-time curves of AZD1775 with or without **Ac12Az9**; (C) Plasma concentration-time curves of AZD1775 with or without **Ac12Az9**; (D) Brain-to-plasma ratio of AZD1775 with or without **Ac12Az9**; (E) Calculated PK parameters of AZD1775.

AZD1775 (2.5 mg/mL) or **Ac12Az9** (2 mg/mL) were prepared in the formulation of NMP, CrEL, and 5% Tween-80 (10: 10: 80), respectively. Mice in the AZD1775 alone group received oral administration of 50 mg/kg AZD1775, whereas mice in the combination group received AZD1775 orally 30 min after receiving **Ac12Az9** intravenously. Blood and brain were collected, respectively, after the administration of AZD1775 at different time points (60, 75, 90, 120, and 180 min). Plasma and brain concentration of AZD1775 was determined by UPLC-MS/MS. The data was presented as mean ± SEM (n = 2-3). A non-compartmental analysis was performed using PK Solutions 2.0.3 software (Ashland, OH44805, USA) to calculate the AUC values.

7.3 Discussion

Despite numerous attempts at novel treatment development, the survival outcomes for individuals with GBM have not improved significantly in the previous few years. The difficulty stemmed not only from the heterogeneity of brain tumors [113, 114] but also from the BBB, which prevented medications from reaching their effective concentrations in the brain [246].

Wee1 kinase is a molecular target for GBM treatment because it is overexpressed and inversely correlated with OS [247]. Wee1 kinase inhibitors can cause a mitotic disaster by forcing GBM cells past G2 arrest [248]. Given that, 87% of GBMs lack a functioning p53 pathway [249], GBM cells treated with Wee1 inhibitors should be more vulnerable to inducing DNA damage as a result of genetic and pharmacological loss of the G1 and G2 checkpoints, respectively. Our *in vitro* data indicated that AZD1775 (IC_{50} = 0.59-1.14 μM) was more effective than TMZ (IC_{50} = 144.8-1201.5 μM) and sorafenib (IC_{50} = 6.48-10.56 μM) (**Figure 5-2C**) in killing GBM cells, including U87MG-RedFluc, PDX G22-FLuc, and G28-FLuc cells. This finding suggested that AZD1775 may have a therapeutic potential toward GBM.

Here AZD1775 was demonstrated to be a good substrate for both P-gp and BCRP/ABCG2. This was consistent with the knockout mice study in which the brain-to-plasma ratio of AZD1775 can be increased by 25-fold in Abcb1a/b$^{-/-}$Abcg2$^{-/-}$ mice compared to wild-type mice and by 6-fold compared to Abcb1a/b$^{-/-}$ animals, indicating that both P-gp and BCRP/ABCG2 were crucial for the efflux of AZD1775 across the BBB [141]. **Ac12Az9** and its derivatives can increase the cellular accumulation of AZD1775 in MDCKII-P-gp or MDCKII-GFP-BCRP cells in a dose-dependent manner. Among them, 1 μM of **Ac12Az9**, **D1**, **D5**, or **D7** can increase the low levels of AZD1775 in MDCKII-P-gp or MDCKII-GFP-BCRP cells to the level of AZD1775 in wild-type cells. Additionally, **Ac12Az9** can reduce the P-gp- or BCRP/ABCG2-

mediated efflux of AZD1775 by 63% or 143%, respectively, suggesting that **Ac12Az9** was a stronger inhibitor of BCRP/ABCG2 than P-gp. Taken together, it was anticipated that **Ac12Az9**, a dual BCRP/ABCG2 and P-gp inhibitor, would have a significant effect on AZD1775 transport at the BBB.

According to PK studies, **Ac12Az9** can increase the brain-to-plasma ratios of AZD1775 by 16.5 or 29 times, when given either after or before oral administration of AZD1775, reaching a therapeutic level equivalent to its *in vitro* IC_{50} against PDX G22-FLuc (0.59 μM). However, the plasma level of AZD1775 was reduced unexpectedly, which may cause an overestimation of the brain-to-plasma ratio of AZD1775, but AZD1775 distribution in the brain can still be increased by **Ac12Az9**. The unexpected drop in the plasma concentration of AZD1775 was not due to the re-distribution of AZD1775 into other tissues. Taken together, **Ac12Az9** played an important role in enhancing the brain penetration of AZD1775.

Nonionic surfactants like CrEL [250] and Tween-80 [251] are widely used to improve the solubility and distribution of medicines. However, the results in this Chapter demonstrated that the addition of CrEL or Tween-80 directly led to a reduction in the plasma concentration of AZD1775 when mixed with either plasma or water. The reason for this is still under investigation. One future experiment that can be done was to use other techniques, instead of using these solvents, to increase the solubility of **Ac12Az9**, such as particle size reduction [252], nanosuspension technology [253], solid dispersion [254, 255], etc.

7.4 Conclusion

In summary, AZD1775, a Wee1 kinase inhibitor, was demonstrated to be cytotoxic to GBM cells. The dual P-gp and BCRP/ABCG2 inhibitor **Ac12Az9** can increase the brain level of AZD1775 to a therapeutic level. Co-administration of **Ac12Az9** with AZD1775 was expected to be successful in the treatment of GBM.

Chapter 8 Conclusions and suggestions for future research

GBM has a very poor prognosis due to frequent relapses. TMZ is a first-line chemotherapeutic medication for the treatment of GBM. Resistance to TMZ, however, is frequent, particularly in patients with recurrent GBM. Many conventional anticancer drugs have minimal brain penetration due to drug efflux by P-gp and BCRP/ABCG2 at the BBB, which ultimately results in treatment failure of GBM. Inhibition of P-gp and/or BCRP/ABCG2 was used to improve the delivery of anticancer drugs to brain tumors, thereby treating GBM.

Our *in vitro* data indicated that sorafenib (IC_{50} = 6.48-10.56 μM) was more effective than TMZ (IC_{50} = 257.3-1201.5 μM) in killing GBM cells, including U87MG-RedFluc, PDX G22, G22-FLuc, G28, and G28-FLuc cells (**Figure 5-2**). Furthermore, sorafenib is approved for treating RCC [256] and HCC [95], making it a logical candidate for treating GBM. However, sorafenib alone did not improve the OS compared with other treatments like radiation therapy, TMZ, erlotinib, or BVZ [257-259]. This may be associated with the limited brain penetration of sorafenib as a result of P-gp- and BCRP/ABCG2-mediated efflux of sorafenib at the BBB [188-190].

All *in vitro* cellular uptake, cellular efflux, and transepithelial transport experiments using MDCKII cells expressing either P-gp or BCRP/ABCG2 indicated that sorafenib was a better BCRP/ABCG2 substrate than P-gp. This was consistent with the knockout study in which the *Bcrp (-/-)* mice resulted in a 3.8-fold increase in brain accumulation of sorafenib, but the *Mdr1a/b (-/-)* mice had almost no effect [140].

From an in-house library of 74-member of triazole-bridged flavonoid dimer, we have identified a highly potent and nontoxic dual inhibitor, **Ac12Az9**, with an EC_{50} of 285 nM and 0.9-1.4 nM for reversing P-gp- and BCRP/ABCG2-mediated drug resistance *in vitro*, respectively [178]. **Ac12Az9,** not only inhibited BCRP/ABCG2-mediated

efflux of sorafenib, increasing intracellular sorafenib from 54% to 108% ($p < 0.001$), but it also blocked P-gp-mediated efflux of sorafenib in MDCKII-P-gp cells, increasing intracellular sorafenib from 70% to 78% ($p < 0.01$) (**Figure 3-4**). The transepithelial transport assay further demonstrated that **Ac12Az9** can reduce the BCRP/ABCG2- or P-gp-mediated *Papp* B-to-A of sorafenib by 81% ($p < 0.01$) or 8%, respectively, suggesting that **Ac12Az9** was a stronger inhibitor of BCRP/ABCG2 than P-gp (**Figure 3-5**). Taken together, considering that sorafenib was a better BCRP/ABCG2 substrate than P-gp, it was predicted that **Ac12Az9**, a greater BCRP/ABCG2 inhibitor than P-gp, would have a significant effect on sorafenib transport at the BBB. In addition, the inhibiting effects of **Ac12Az9** were not mediated by affecting the protein level of P-gp or BCRP/ABCG2 (**Figure 3-6**).

PK studies indicated that **Ac12Az9** can help sorafenib to penetrate through the BBB and accumulate more in the brain. Administration of **Ac12Az9** (10 or 20 mg/kg) can increase the AUC_{brain}/AUC_{plasma} of sorafenib by 1.4- or 1.8-fold, respectively, reaching a therapeutic level equivalent to its *in vitro* IC_{50} against U87MG-RedFluc cells (8 μM) (**Figure 4-2D**). This result suggested that dual inhibition of BCRP/ABCG2 and P-gp can increase the brain penetration of sorafenib. Furthermore, **Ac12Az9** had an advantage over other P-gp or BCRP/ABCG2 inhibitors in that it did not affect the distribution of sorafenib in plasma, kidneys, and liver (**Figure 4-2E, Figure 4-3**). This is significant given previous reports that P-gp inhibitors, such as quercetin [204] and curcumin [205], may generate unexpected systemic toxicity *in vivo*. Furthermore, the repeated doses of sorafenib combined with **Ac12Az9** did not show any hepatotoxicity or nephrotoxicity in mice (**Figure 4-4**).

The GBM PDXs retained the histological, genetic, and epigenetic features of the parental tumor in the early passage [220, 221], allowing it to recapitulate the molecular heterogeneity of their original clinical samples. GBM PDX models in mice can be used to predict therapeutic outcomes accurately. The short-term explant cultures of two PDX

GBM xenograft lines - G22 and G28 (from the Mayo Clinic, USA [222]) were established. G22 had a lower IC_{50} of 160.8 μM and was more sensitive to TMZ, whereas G28 had a higher IC_{50} of 1201.5 μM and was more resistant to TMZ (**Figure 5-2**). FLuc was stably expressed in G22 and G28 cells, yielding G22-FLuc and G28-FLuc cells, respectively, for the purpose of real-time bioluminescence imaging monitoring of brain tumors in mice.

In an orthotopic G22-FLuc PDX model, co-administration of **Ac12Az9** and sorafenib could suppress tumor growth by 56.7% ($p = 0.13$) and prolong the life span of tumor-bearing nude mice by 47.4% ($p = 0.01$) when compared to the solvent control group (**Figure 5-6A-B**). This result demonstrated the feasibility of using the combination of **Ac12Az9** with sorafenib in treating clinical GBM cases.

The combination of **Ac12Az9** and sorafenib was not effective in another orthotopic TMZ-selected G28-FLuc model we developed here. Our TMZ-selected G28-FLuc model was established by a single round of TMZ treatment. The tumor cells from the TMZ-treated G28-FLuc tumors were isolated and renamed TMZ-selected G28-FLuc cells. TMZ-selected G28-FLuc cells (IC_{50} = 1691-1573 μM) were more resistant to TMZ compared to parental G28-FLuc cells (IC_{50} = 1180.5 μM) (**Figure 5-5B**). Furthermore, TMZ failed to suppress an orthotopic GBM model established with TMZ-selected G28-FLuc cells. More importantly, these TMZ-selected G28-FLuc cells remained sensitive to sorafenib *in vitro*. Our findings indicated that neither co-administration of **Ac12Az9** with sorafenib nor co-administration of GF120918 with sorafenib failed to stop the growth of the TMZ-selected G28-FLuc tumor (**Figure 5-7A**). The cause of this is still under investigation, but further verification of the second experiment would be necessary because the sorafenib and **Ac12Az9** efficacy evaluation experiment in the TMZ-selected G28-FLuc model was only performed once and the initial intervention time and administration times were not optimized.

Understanding *in vivo* metabolism of **Ac12Az9** can help us use it more successfully and provide it with a better function. Our findings demonstrated that under esterase, **Ac12Az9** can hydrolyze to the metabolite **M1**, which has no inhibitory effects on P-gp or BCRP/ABCG2. This further emphasizes the need of maintaining **Ac12Az9** stability *in vivo*. After demonstrating that the methyl ester group in **Ac12Az9** was unstable, eleven derivatives of **Ac12Az9** (**D1-D11**) were generated via bioisosteric substitution, increasing steric resistance, lowering the electrophilicity of the active group, and deuterated substitution (**Figure 6-5**). All derivatives **D1-D11** have been demonstrated to be effective for reversing P-gp- and BCRP/ABCG2-mediated drug resistance in cancer cells to different degrees (**Table 6-1**), and many of them, including **D1-D4**, **D6**, and **D11**, exhibited improved plasma stability *in vitro* (**Figure 6-7**). However, the relationship between the physicochemical descriptors (MW, clogP, and tPSA) of **Ac12Az9** and its derivatives and their P-gp and BCRP/ABCG2 inhibitory activity revealed that **Ac12Az9** could not be modified to produce better dual P-gp and BCRP/ABCG2 inhibitory activity; any increase in BCRP/ABCG2 inhibitory activity would only be at the expense of P-gp inhibitory activity. As a result, compound **D6**, with good stability (half-life $t_{1/2}$ = 270 min versus < 60 min for **Ac12Az9**) and strong specific inhibition of BCRP/ABCG2 (EC_{50}s of 1.2-1.3 nM), was selected for *in vivo* PK study and efficacy evaluation in combination with TPT in the HEK293/R2 xenograft model. PK studies indicated that **D6** was stable and widely distributed throughout the body's organs following a single I.V. injection (20 mg/kg) (**Figure 6-9**). In a subcutaneous HEK293/R2 xenograft model, co-administration of **D6** and TPT could increase the tumor accumulation of TPT by 2-fold (p = 0.0028) compared to TPT alone (**Figure 6-10**). This result further suggested that **D6** might be a promising option for more research into combination therapy for the treatment of BCRP/ABCG2-overexpressing tumors.

In a different investigation, **Ac12Az9** was found to increase brain permeability not only for sorafenib but also for AZD1775, a Wee1 inhibitor. AZD1775 was not only found to

be efficient against GBM cells (IC_{50} = 0.59-1.14 μM) (**Figure 7-2**), but it was also found to be a substrate for P-gp and BCRP/ABCG2. The knockout mice study indicated that the brain-to-plasma ratio of AZD1775 can be increased by 25-fold in Abcb1a/b$^{-/-}$Abcg2$^{-/-}$ mice compared to wild-type mice and by 6-fold compared to Abcb1a/b$^{-/-}$ animals, indicating that both P-gp and BCRP/ABCG2 were crucial for the efflux of AZD1775 across the BBB [141]. Likewise, **Ac12Az9** not only inhibited BCRP/ABCG2-mediated efflux of AZD1775, increasing intracellular AZD1775 from 42% to 102% ($p < 0.001$), but it also blocked P-gp-mediated efflux of AZD1775 in MDCKII-P-gp cells, increasing intracellular AZD1775 from 49% to 80% ($p < 0.001$) (**Figure 7-4**). As a result, **Ac12Az9** was also anticipated to have a greater effect on AZD1775 transport at BBB. PK studies indicated that **Ac12Az9** can increase the brain-to-plasma ratios of AZD1775 by 16.5 or 29 times, reaching a therapeutic level equivalent to its *in vitro* IC_{50} against PDX G22-FLuc (0.59 μM) (**Figure 7-5B**, **Figure 7-8B**). **Ac12Az9** did have the potential to improve brain distribution of AZD1775, even if the effect of the surfactant in the formulation on AZD1775 hasn't been studied.

In summary, sorafenib and AZD1775 were more cytotoxic than TMZ against GBM cells. To overcome the poor brain penetration of sorafenib or AZD1775, a safe and effective dual inhibitor of P-gp and BCRP/ABCG2 (**Ac12Az9**) was designed and synthesized. **Ac12Az9** can increase the brain level of sorafenib or AZD1775 to a therapeutic level. Co-administration of **Ac12Az9** and sorafenib was even effective against GBM PDX orthotopic animal model. Our study demonstrated the feasibility of blocking P-gp and BCRP/ABCG2 at BBB to increase the brain level of the conventional ABC transporter substrate anticancer drugs. Additionally, **Ac12Az9** derivative - **D6**, a specific inhibitor of BCRP/ABCG2, might be another promising option for combination therapy for the treatment of BCRP/ABCG2-overexpressing tumors.

Finally, this project can be further expanded in the following aspects, including:

1. To establish a PDX model that is TMZ-resistant except for G28-FLuc, investigate the effectiveness of sorafenib and **Ac12Az9** in the treatment of relapsed GBM, and work to gain a more thorough assessment of the combined efficacy of these drugs.
2. To evaluate the effectiveness of co-administration of **D6** and TPT in the treatment of the HEK293/R2 xenograft animal model, providing new therapeutic options for future cancer treatment.
3. To investigate the impact of the surfactant on AZD1775 or to develop a more suitable solvent for **Ac12Az9**, so that it can be combined with AZD1775 and tested for effectiveness in various GBM animal models.

All in all, the clinical management of GBM will reach a new high point if it is demonstrated that **Ac12Az9** can inhibit the efflux transporters P-gp and BCRP/ABCG2 at the BBB, opening the door to the use of additional anticancer drugs.

Reference

1. Ostrom, Q.T., et al., *CBTRUS statistical report: Primary brain and other central nervous system tumors diagnosed in the United States in 2015–2019.* Neuro-oncology, 2022. **24**(Supplement_5): p. v1-v95.
2. Torp, S.H., O. Solheim, and A.J. Skjulsvik, *The WHO 2021 Classification of Central Nervous System tumours: a practical update on what neurosurgeons need to know—a minireview.* Acta Neurochirurgica, 2022. **164**(9): p. 2453-2464.
3. Salvati, M., et al., *Radiation-induced gliomas: report of 10 cases and review of the literature.* Surgical neurology, 2003. **60**(1): p. 60-67.
4. Schwartzbaum, J.A., et al., *Epidemiology and molecular pathology of glioma.* Nature clinical practice Neurology, 2006. **2**(9): p. 494-503.
5. Bralten, L.B. and P.J. French, *Genetic alterations in glioma.* Cancers, 2011. **3**(1): p. 1129-1140.
6. Zhang, W., et al., *Association between dietary nitrite intake and glioma risk: a systematic review and dose-response meta-analysis of observational studies.* Frontiers in Oncology, 2022. **12**.
7. McFaline-Figueroa, J.R. and P.Y. Wen, *The viral connection to glioblastoma.* Current infectious disease reports, 2017. **19**: p. 1-5.
8. Zhang, Y., et al., *The p53 pathway in glioblastoma.* Cancers, 2018. **10**(9): p. 297.
9. Mao, H., et al., *Deregulated signaling pathways in glioblastoma multiforme: molecular mechanisms and therapeutic targets.* Cancer investigation, 2012. **30**(1): p. 48-56.
10. Van Meir, E.G., et al., *Exciting new advances in neuro-oncology: the avenue to a cure for malignant glioma.* CA: a cancer journal for clinicians, 2010. **60**(3): p. 166-193.
11. Balss, J., et al., *Analysis of the IDH1 codon 132 mutation in brain tumors.* Acta neuropathologica, 2008. **116**: p. 597-602.
12. Nobusawa, S., et al., *IDH1 mutations as molecular signature and predictive factor of secondary glioblastomas.* Clinical Cancer Research, 2009. **15**(19): p. 6002-6007.
13. Du, X. and H. Hu, *The roles of 2-hydroxyglutarate.* Frontiers in Cell and Developmental Biology, 2021. **9**: p. 651317.
14. Yan, H., et al., *IDH1 and IDH2 mutations in gliomas.* New England journal of medicine, 2009. **360**(8): p. 765-773.
15. Tran, A.N., et al., *Increased sensitivity to radiochemotherapy in IDH1 mutant glioblastoma as demonstrated by serial quantitative MR volumetry.* Neuro-oncology, 2014. **16**(3): p. 414-420.
16. Guo, J., et al., *Biological roles and therapeutic applications of IDH2 mutations in human cancer.* Frontiers in Oncology, 2021. **11**: p. 644857.
17. Gilbert, M.R., et al., *Dose-dense temozolomide for newly diagnosed glioblastoma: a randomized phase III clinical trial.* Journal of clinical oncology, 2013. **31**(32): p. 4085.
18. Cohen, M.H., J.R. Johnson, and R. Pazdur, *Food and Drug Administration Drug approval summary: temozolomide plus radiation therapy for the treatment of newly diagnosed glioblastoma multiforme.* Clinical Cancer Research, 2005. **11**(19): p. 6767-6771.

19. Lee, S.Y., *Temozolomide resistance in glioblastoma multiforme.* Genes & diseases, 2016. **3**(3): p. 198-210.
20. Stupp, R., et al., *Promising survival for patients with newly diagnosed glioblastoma multiforme treated with concomitant radiation plus temozolomide followed by adjuvant temozolomide.* Journal of Clinical Oncology, 2002. **20**(5): p. 1375-1382.
21. Stupp, R., et al., *Radiotherapy plus concomitant and adjuvant temozolomide for glioblastoma.* New England journal of medicine, 2005. **352**(10): p. 987-996.
22. Hegi, M.E., et al., *MGMT gene silencing and benefit from temozolomide in glioblastoma.* New England Journal of Medicine, 2005. **352**(10): p. 997-1003.
23. Stupp, R., et al., *Effects of radiotherapy with concomitant and adjuvant temozolomide versus radiotherapy alone on survival in glioblastoma in a randomised phase III study: 5-year analysis of the EORTC-NCIC trial.* The lancet oncology, 2009. **10**(5): p. 459-466.
24. Stupp, R., et al., *Maintenance therapy with tumor-treating fields plus temozolomide vs temozolomide alone for glioblastoma: a randomized clinical trial.* Jama, 2015. **314**(23): p. 2535-2543.
25. Stupp, R., et al., *Effect of tumor-treating fields plus maintenance temozolomide vs maintenance temozolomide alone on survival in patients with glioblastoma: a randomized clinical trial.* Jama, 2017. **318**(23): p. 2306-2316.
26. Tan, A.C., et al., *Management of glioblastoma: State of the art and future directions.* CA: a cancer journal for clinicians, 2020. **70**(4): p. 299-312.
27. Wolbers, J.G., *Novel strategies in glioblastoma surgery aim at safe, supra-maximum resection in conjunction with local therapies.* Chinese journal of cancer, 2014. **33**(1): p. 8.
28. Lacroix, M., et al., *A multivariate analysis of 416 patients with glioblastoma multiforme: prognosis, extent of resection, and survival.* Journal of neurosurgery, 2001. **95**(2): p. 190-198.
29. Laurent, D., et al., *Impact of extent of resection on incidence of postoperative complications in patients with glioblastoma.* Neurosurgery, 2020. **86**(5): p. 625.
30. Gandhi, S., et al., *Survival outcomes among patients with high-grade glioma treated with 5-aminolevulinic acid–guided surgery: A systematic review and meta-analysis.* Frontiers in oncology, 2019. **9**: p. 620.
31. Stummer, W., et al., *Fluorescence-guided surgery with 5-aminolevulinic acid for resection of malignant glioma: a randomised controlled multicentre phase III trial.* The lancet oncology, 2006. **7**(5): p. 392-401.
32. Bömers, J.P., et al., *Sodium fluorescein shows high surgeon-reported usability in glioblastoma surgery.* The Surgeon, 2020. **18**(6): p. 344-348.
33. Cho, S.S., R. Salinas, and J.Y. Lee, *Indocyanine-green for fluorescence-guided surgery of brain tumors: evidence, techniques, and practical experience.* Frontiers in surgery, 2019. **6**: p. 11.
34. Buszek, S.M., et al., *Optimal timing of radiotherapy following gross total or subtotal resection of glioblastoma: a real-world assessment using the National Cancer Database.* Scientific reports, 2020. **10**(1): p. 4926.
35. Dhermain, F., *Radiotherapy of high-grade gliomas: current standards and new concepts, innovations in imaging and radiotherapy, and new therapeutic approaches.* Chinese journal of cancer, 2014. **33**(1): p. 16.

36. Walker, M.D., T.A. Strike, and G.E. Sheline, *An analysis of dose-effect relationship in the radiotherapy of malignant gliomas.* International Journal of Radiation Oncology* Biology* Physics, 1979. **5**(10): p. 1725-1731.
37. Bleehen, N. and S. Stenning, *A Medical Research Council trial of two radiotherapy doses in the treatment of grades 3 and 4 astrocytoma.* British journal of cancer, 1991. **64**(4): p. 769-774.
38. Nelson, D., et al., *Combined modality approach to treatment of malignant gliomas--re-evaluation of RTOG 7401/ECOG 1374 with long-term follow-up: a joint study of the Radiation Therapy Oncology Group and the Eastern Cooperative Oncology Group.* NCI monographs: a publication of the National Cancer Institute, 1988(6): p. 279-284.
39. Shin, K.H., et al., *Multiple daily fractionated radiation therapy and misonidazole in the management of malignant astrocytoma. A preliminary report.* Cancer, 1985. **56**(4): p. 758-760.
40. Chargari, C., et al., *Optimize and refine therapeutic index in radiation therapy: overview of a century.* Cancer treatment reviews, 2016. **45**: p. 58-67.
41. Nguyen, N.P., et al., *Potential applications of imaging and image-guided radiotherapy for brain metastases and glioblastoma to improve patient quality of life.* Frontiers in Oncology, 2013. **3**: p. 284.
42. Al Feghali, K.A., et al., *Phase II trial of proton therapy versus photon IMRT for GBM: secondary analysis comparison of progression-free survival between RANO versus clinical assessment.* Neuro-Oncology Advances, 2021. **3**(1): p. vdab073.
43. Hochberg, F.H., et al., *Quality and duration of survival in glioblastoma multiforme: combined surgical, radiation, and lomustine therapy.* Jama, 1979. **241**(10): p. 1016-1018.
44. Walker, M.D., et al., *Evaluation of BCNU and/or radiotherapy in the treatment of anaplastic gliomas: a cooperative clinical trial.* Journal of neurosurgery, 1978. **49**(3): p. 333-343.
45. Cohen, M.H., et al., *FDA drug approval summary: bevacizumab (Avastin®) as treatment of recurrent glioblastoma multiforme.* The oncologist, 2009. **14**(11): p. 1131-1138.
46. Das, P., S. McCaffrey, and D. Conkey, *Re-evaluating the Efficacy and Toxicity of Procarbazine, Lomustine and Vincristine (PCV) in Relapsed Glioblastoma in the Concurrent/Adjuvant Temozolamide Era.* J Cancer Prev Curr Res, 2016. **6**(3): p. 00204.
47. Ahn, S., et al., *Clinical feasibility of modified procarbazine and lomustine chemotherapy without vincristine as a salvage treatment for recurrent adult glioma.* Oncology Letters, 2022. **23**(4): p. 1-8.
48. Herrlinger, U., et al., *Lomustine-temozolomide combination therapy versus standard temozolomide therapy in patients with newly diagnosed glioblastoma with methylated MGMT promoter (CeTeG/NOA–09): a randomised, open-label, phase 3 trial.* The lancet, 2019. **393**(10172): p. 678-688.
49. Ren, X., et al., *Effectiveness of lomustine combined with bevacizumab in glioblastoma: A meta-analysis.* Frontiers in Neurology, 2021. **11**: p. 603947.
50. Bota, D.A., et al., *Interstitial chemotherapy with biodegradable BCNU (Gliadel®) wafers in the treatment of malignant gliomas.* Therapeutics and clinical risk management, 2007. **3**(5): p. 707-715.
51. Xiao, Z.-Z., et al., *Carmustine as a supplementary therapeutic option for glioblastoma: a*

systematic review and meta-analysis. Frontiers in neurology, 2020. **11**: p. 1036.
52. Klein, J., et al., *Safety and effectiveness of bis-chloroethylnitrosourea wafer chemotherapy in elderly patients with recurrent glioblastoma.* Oncology, 2017. **93**(1): p. 43-50.
53. Gazaille, C., et al., *Local delivery and glioblastoma: Why not combining sustained release and targeting?* Frontiers in Medical Technology, 2021: p. 67.
54. Detti, B., et al., *Bevacizumab in recurrent high-grade glioma: a single institution retrospective analysis on 92 patients.* La radiologia medica, 2021. **126**(9): p. 1249-1254.
55. Tsien, C.I., et al., *NRG oncology/RTOG1205: A randomized phase II trial of concurrent bevacizumab and Reirradiation versus bevacizumab alone as treatment for recurrent glioblastoma.* Journal of Clinical Oncology, 2022: p. JCO. 22.00164.
56. Lopes, I.C., S.C.B. de Oliveira, and A.M. Oliveira-Brett, *Temozolomide chemical degradation to 5-aminoimidazole-4-carboxamide–electrochemical study.* Journal of electroanalytical chemistry, 2013. **704**: p. 183-189.
57. Tisdale, M.J., *Antitumour imidazotetrazines—XV: Role of guanine O6 alkylation in the mechanism of cytotoxicity of imidazotetrazinones.* Biochemical pharmacology, 1987. **36**(4): p. 457-462.
58. Kanzawa, T., et al., *Role of autophagy in temozolomide-induced cytotoxicity for malignant glioma cells.* Cell Death & Differentiation, 2004. **11**(4): p. 448-457.
59. Alexander, B.M., et al., *Targeting DNA repair and the cell cycle in glioblastoma.* Journal of neuro-oncology, 2012. **107**: p. 463-477.
60. Woo, P.Y., et al., *A multifaceted review of temozolomide resistance mechanisms in glioblastoma beyond O-6-methylguanine-DNA methyltransferase.* Glioma, 2019. **2**(2): p. 68.
61. Gerson, S.L., *Clinical relevance of MGMT in the treatment of cancer.* Journal of Clinical Oncology, 2002. **20**(9): p. 2388-2399.
62. Stritzelberger, J., et al., *Acquired temozolomide resistance in human glioblastoma cell line U251 is caused by mismatch repair deficiency and can be overcome by lomustine.* Clinical and Translational Oncology, 2018. **20**: p. 508-516.
63. von Bueren, A.O., et al., *Mismatch repair deficiency: a temozolomide resistance factor in medulloblastoma cell lines that is uncommon in primary medulloblastoma tumours.* British journal of cancer, 2012. **107**(8): p. 1399-1408.
64. Tang, J.-b., et al., *N-methylpurine DNA glycosylase and DNA polymerase β modulate BER inhibitor potentiation of glioma cells to temozolomide.* Neuro-oncology, 2011. **13**(5): p. 471-486.
65. Luo, J., et al., *Role of micro-RNA (miRNA) in pathogenesis of glioblastoma.* Eur Rev Med Pharmacol Sci, 2015. **19**(9): p. 1630-1639.
66. Novakova, J., et al., *MicroRNA involvement in glioblastoma pathogenesis.* Biochemical and biophysical research communications, 2009. **386**(1): p. 1-5.
67. Bartel, D.P., *MicroRNAs: genomics, biogenesis, mechanism, and function.* cell, 2004. **116**(2): p. 281-297.
68. Mathupala, S.P., et al., *MicroRNA and brain tumors: a cause and a cure?* DNA and cell biology, 2007. **26**(5): p. 301-310.
69. Magee, P., L. Shi, and M. Garofalo, *Role of microRNAs in chemoresistance.* Annals of translational medicine, 2015. **3**(21).

70. Wong, S.T.S., et al., *MicroRNA-21 inhibition enhances in vitro chemosensitivity of temozolomide-resistant glioblastoma cells.* Anticancer research, 2012. **32**(7): p. 2835-2841.
71. Yang, J.-T., et al., *ADAM17 Confers Temozolomide Resistance in Human Glioblastoma Cells and miR-145 Regulates Its Expression.* International Journal of Molecular Sciences, 2023. **24**(9): p. 7703.
72. Wang, H., et al., *MicroRNA-195 reverses the resistance to temozolomide through targeting cyclin E1 in glioma cells.* Anti-cancer drugs, 2019. **30**(1): p. 81.
73. Ujifuku, K., et al., *MiR-195, miR-455-3p and miR-10a＊ are implicated in acquired temozolomide resistance in glioblastoma multiforme cells.* Cancer letters, 2010. **296**(2): p. 241-248.
74. Song, Y., et al., *Prognostic Role of MicroRNA 222 in Patients with Glioma: A Meta-analysis.* BioMed Research International, 2020. **2020**.
75. Ge, X., et al., *Hypoxia-mediated mitochondria apoptosis inhibition induces temozolomide treatment resistance through miR-26a/Bad/Bax axis.* Cell death & disease, 2018. **9**(11): p. 1128.
76. Munoz, J.L., et al., *Temozolomide competes for P-glycoprotein and contributes to chemoresistance in glioblastoma cells.* Cancer Letters, 2015. **367**(1): p. 69-75.
77. Schaich, M., et al., *A MDR1 (ABCB1) gene single nucleotide polymorphism predicts outcome of temozolomide treatment in glioblastoma patients.* Annals of Oncology, 2009. **20**(1): p. 175-181.
78. Zou, Y. and J. Wang, *TRPC5 mediates TMZ resistance in TMZ-resistant glioblastoma cells via NFATc3-P-gp pathway.* Translational Oncology, 2021. **14**(12): p. 101214.
79. Jawhari, S., M.-H. Ratinaud, and M. Verdier, *Glioblastoma, hypoxia and autophagy: a survival-prone 'menage-a-trois'.* Cell death & disease, 2016. **7**(10): p. e2434-e2434.
80. Muz, B., et al., *The role of hypoxia in cancer progression, angiogenesis, metastasis, and resistance to therapy.* Hypoxia, 2015. **3**: p. 83.
81. 謝佳宏, *Livin contributes to tumor hypoxia-induced resistance to cytotoxic therapies in glioblastoma multiforme.* CLINICAL CANCER RESEARCH, 2015. **21**(2): p. 1-11.
82. Kim, S.S., et al., *Biliverdin reductase plays a crucial role in hypoxia-induced chemoresistance in human glioblastoma.* Biochemical and Biophysical Research Communications, 2013. **440**(4): p. 658-663.
83. Piper, K., et al., *Glioma stem cells as immunotherapeutic targets: advancements and challenges.* Frontiers in Oncology, 2021: p. 92.
84. Auffinger, B., et al., *The role of glioma stem cells in chemotherapy resistance and glioblastoma multiforme recurrence.* Expert review of neurotherapeutics, 2015. **15**(7): p. 741-752.
85. Jiapaer, S., et al., *Potential strategies overcoming the temozolomide resistance for glioblastoma.* Neurologia medico-chirurgica, 2018. **58**(10): p. 405.
86. Li, Z., et al., *Hypoxia-inducible factors regulate tumorigenic capacity of glioma stem cells.* Cancer cell, 2009. **15**(6): p. 501-513.
87. Beier, D., et al., *Temozolomide preferentially depletes cancer stem cells in glioblastoma.* Cancer research, 2008. **68**(14): p. 5706-5715.
88. Gong, X., et al., *Neural stem/progenitors and glioma stem-like cells have differential sensitivity to chemotherapy.* Neurology, 2011. **76**(13): p. 1126-1134.

89. Valdés-Rives, S.A., et al., *Apoptotic signaling pathways in glioblastoma and therapeutic implications.* BioMed research international, 2017. **2017**.
90. Uribe, D., et al., *Multidrug resistance in glioblastoma stem-like cells: Role of the hypoxic microenvironment and adenosine signaling.* Molecular aspects of medicine, 2017. **55**: p. 140-151.
91. Zhang, Y., et al., *EGCG inhibits properties of glioma stem-like cells and synergizes with temozolomide through downregulation of P-glycoprotein inhibition.* Journal of neuro-oncology, 2015. **121**: p. 41-52.
92. Cruz Da Silva, E., et al., *A systematic review of glioblastoma-targeted therapies in phases II, III, IV clinical trials.* Cancers, 2021. **13**(8): p. 1795.
93. Fougner, V., et al., *Implementing targeted therapies in the treatment of glioblastoma: Previous shortcomings, future promises, and a multimodal strategy recommendation.* Neuro-Oncology Advances, 2022. **4**(1): p. vdac157.
94. Gabora, K., et al., *Current evidence on thyroid related adverse events in patients treated with protein tyrosine kinase inhibitors.* Drug metabolism reviews, 2019. **51**(4): p. 562-569.
95. Lang, L., *FDA approves sorafenib for patients with inoperable liver cancer.* Gastroenterology, 2008. **134**(2): p. 379.
96. Blumenthal, G.M., et al., *FDA approval summary: sunitinib for the treatment of progressive well-differentiated locally advanced or metastatic pancreatic neuroendocrine tumors.* The oncologist, 2012. **17**(8): p. 1108-1113.
97. Habeck, M., *FDA licences imatinib mesylate for CML.* The Lancet Oncology, 2002. **3**(1): p. 6.
98. Ward, J.E. and W.M. Stadler, *Pazopanib in Renal Cell CarcinomaPazopanib.* Clinical Cancer Research, 2010. **16**(24): p. 5923-5927.
99. Deshpande, H., et al., *Vandetanib (ZD6474) in the treatment of medullary thyroid cancer.* Clinical Medicine Insights: Oncology, 2011. **5**: p. CMO. S6197.
100. Tyler, T., *Axitinib: newly approved for renal cell Carcinoma.* Journal of the advanced practitioner in oncology, 2012. **3**(5): p. 333.
101. Siegelin, M.D., et al., *Sorafenib exerts anti-glioma activity in vitro and in vivo.* Neuroscience letters, 2010. **478**(3): p. 165-170.
102. Reardon, D.A., et al., *Effect of CYP3A-inducing anti-epileptics on sorafenib exposure: results of a phase II study of sorafenib plus daily temozolomide in adults with recurrent glioblastoma.* Journal of neuro-oncology, 2011. **101**: p. 57-66.
103. Forte, I.M., et al., *Targeted therapy based on p53 reactivation reduces both glioblastoma cell growth and resistance to temozolomide.* International journal of oncology, 2019. **54**(6): p. 2189-2199.
104. Miles, X., et al., *MDM2/X inhibitors as radiosensitizers for glioblastoma targeted therapy.* Frontiers in oncology, 2021. **11**: p. 703442.
105. Fang, Y., G. Liao, and B. Yu, *Small-molecule MDM2/X inhibitors and PROTAC degraders for cancer therapy: advances and perspectives.* Acta Pharmaceutica Sinica B, 2020. **10**(7): p. 1253-1278.
106. Wick, W., et al., *N2M2 (NOA-20) phase I/II trial of molecularly matched targeted therapies plus radiotherapy in patients with newly diagnosed non-MGMT hypermethylated glioblastoma.* Neuro-oncology, 2019. **21**(1): p. 95-105.

107. Hu, Y., et al., *Potential prospect of CDK4/6 inhibitors in triple-negative breast cancer.* Cancer Management and Research, 2021: p. 5223-5237.
108. Zhang, M., et al., *CDK inhibitors in cancer therapy, an overview of recent development.* American journal of cancer research, 2021. **11**(5): p. 1913.
109. Raheem, F., et al., *Abemaciclib: The First FDA-Approved CDK4/6 Inhibitor for the Adjuvant Treatment of HR+ HER2− Early Breast Cancer.* Annals of Pharmacotherapy, 2022. **56**(11): p. 1258-1266.
110. Beaver, J.A., et al., *FDA Approval: Palbociclib for the Treatment of Postmenopausal Patients with Estrogen Receptor–Positive, HER2-Negative Metastatic Breast CancerFDA Approval Summary for Palbociclib for ER+, HER2− MBC.* Clinical Cancer Research, 2015. **21**(21): p. 4760-4766.
111. Shah, A., et al., *FDA approval: ribociclib for the treatment of postmenopausal women with hormone receptor–positive, HER2-negative advanced or metastatic breast cancer.* Clinical Cancer Research, 2018. **24**(13): p. 2999-3004.
112. Cao, Y., et al., *CDK4/6 inhibition suppresses tumour growth and enhances the effect of temozolomide in glioma cells.* Journal of Cellular and Molecular Medicine, 2020. **24**(9): p. 5135-5145.
113. DeCordova, S., et al., *Molecular heterogeneity and immunosuppressive microenvironment in glioblastoma.* Frontiers in immunology, 2020. **11**: p. 1402.
114. Qazi, M., et al., *Intratumoral heterogeneity: pathways to treatment resistance and relapse in human glioblastoma.* Annals of Oncology, 2017. **28**(7): p. 1448-1456.
115. Baxter, P.A., et al., *A phase I/II study of veliparib (ABT-888) with radiation and temozolomide in newly diagnosed diffuse pontine glioma: a Pediatric Brain Tumor Consortium study.* Neuro-oncology, 2020. **22**(6): p. 875-885.
116. Romo, C.G., et al., *Intratumoral drug distribution of adavosertib in patients with glioblastoma: Interim results of phase I study*. 2020, American Society of Clinical Oncology.
117. Kim, M., et al., *Brain distribution of a panel of epidermal growth factor receptor inhibitors using cassette dosing in wild-type and Abcb1/Abcg2-deficient mice.* Drug Metabolism and Disposition, 2019. **47**(4): p. 393-404.
118. Becker, A.P., et al., *Tumor heterogeneity in glioblastomas: from light microscopy to molecular pathology.* Cancers, 2021. **13**(4): p. 761.
119. Han, M., et al., *Clinicopathological and prognostic significance of CD133 in glioma patients: a meta-analysis.* Molecular neurobiology, 2016. **53**: p. 720-727.
120. Brown, D.V., et al., *Expression of CD133 and CD44 in glioblastoma stem cells correlates with cell proliferation, phenotype stability and intra-tumor heterogeneity.* PLoS One, 2017. **12**(2): p. e0172791.
121. Kenney-Herbert, E., et al., *CD15 expression does not identify a phenotypically or genetically distinct glioblastoma population.* Stem cells translational medicine, 2015. **4**(7): p. 822-831.
122. Pratt, D., et al., *Expression of CD70 (CD27L) is associated with epithelioid and sarcomatous features in IDH-Wild-Type glioblastoma.* Journal of Neuropatholgy & Experimental Neurology, 2017. **76**(8): p. 697-708.
123. Chen, C., et al., *Intracavity generation of glioma stem cell–specific CAR macrophages*

primes locoregional immunity for postoperative glioblastoma therapy. Science Translational Medicine, 2022. **14**(656): p. eabn1128.
124. Jin, L., et al., *CD70, a novel target of CAR T-cell therapy for gliomas.* Neuro-oncology, 2018. **20**(1): p. 55-65.
125. Zhang, H., et al., *Novel insights into astrocyte-mediated signaling of proliferation, invasion and tumor immune microenvironment in glioblastoma.* Biomedicine & Pharmacotherapy, 2020. **126**: p. 110086.
126. Peereboom, D.M., et al., *Metronomic capecitabine as an immune modulator in glioblastoma patients reduces myeloid-derived suppressor cells.* JCI insight, 2019. **4**(22).
127. Daneman, R. and A. Prat, *The blood–brain barrier.* Cold Spring Harbor perspectives in biology, 2015. **7**(1): p. a020412.
128. Anderson, J.M. and C.M. Van Itallie, *Physiology and function of the tight junction.* Cold Spring Harbor perspectives in biology, 2009. **1**(2): p. a002584.
129. Mahringer, A. and G. Fricker, *ABC transporters at the blood–brain barrier.* Expert opinion on drug metabolism & toxicology, 2016. **12**(5): p. 499-508.
130. Sauna, Z.E., K. Nandigama, and S.V. Ambudkar, *Exploiting reaction intermediates of the ATPase reaction to elucidate the mechanism of transport by P-glycoprotein (ABCB1).* Journal of Biological Chemistry, 2006. **281**(36): p. 26501-26511.
131. Frank, G.A., et al., *Cryo-EM analysis of the conformational landscape of human P-glycoprotein (ABCB1) during its catalytic cycle.* Molecular pharmacology, 2016. **90**(1): p. 35-41.
132. Karthika, C., et al., *Multidrug resistance of cancer cells and the vital role of p-glycoprotein.* Life, 2022. **12**(6): p. 897.
133. Martin, C., et al., *The expression of P-glycoprotein does influence the distribution of novel fluorescent compounds in solid tumour models.* British journal of cancer, 2003. **89**(8): p. 1581-1589.
134. Pires, M.M., et al., *Inhibition of P-glycoprotein-mediated paclitaxel resistance by reversibly linked quinine homodimers.* Molecular pharmacology, 2009. **75**(1): p. 92-100.
135. Ni, Z., et al., *Structure and function of the human breast cancer resistance protein (BCRP/ABCG2).* Current drug metabolism, 2010. **11**(7): p. 603-617.
136. Oostendorp, R.L., et al., *The effect of P-gp (Mdr1a/1b), BCRP (Bcrp1) and P-gp/BCRP inhibitors on the in vivo absorption, distribution, metabolism and excretion of imatinib.* Investigational new drugs, 2009. **27**: p. 31-40.
137. Hua, W.J., W.X. Hua, and H.J. Fang, *The role of OATP1B1 and BCRP in pharmacokinetics and DDI of novel statins.* Cardiovascular therapeutics, 2012. **30**(5): p. e234-e241.
138. Agarwal, S., et al., *Breast cancer resistance protein and P-glycoprotein in brain cancer: two gatekeepers team up.* Current pharmaceutical design, 2011. **17**(26): p. 2793-2802.
139. Asakawa, C., et al., *[11C] Sorafenib: radiosynthesis and preliminary PET study of brain uptake in P-gp/Bcrp knockout mice.* Bioorganic & medicinal chemistry letters, 2011. **21**(8): p. 2220-2223.
140. Agarwal, S., et al., *The role of the breast cancer resistance protein (ABCG2) in the distribution of sorafenib to the brain.* Journal of Pharmacology and Experimental Therapeutics, 2011. **336**(1): p. 223-233.
141. de Gooijer, M.C., et al., *ATP-binding cassette transporters limit the brain penetration of*

Wee1 inhibitors. Investigational new drugs, 2018. **36**: p. 380-387.

142. Rappa, G., et al., *Evidence that the multidrug resistance protein (MRP) functions as a co-transporter of glutathione and natural product toxins.* Cancer research, 1997. **57**(23): p. 5232-5237.
143. Rothnie, A., et al., *Mechanistic differences between GSH transport by multidrug resistance protein 1 (MRP1/ABCC1) and GSH modulation of MRP1-mediated transport.* Molecular pharmacology, 2008. **74**(6): p. 1630-1640.
144. Eijdems, E.W., et al., *Mechanisms of MRP over-expression in four human lung-cancer cell lines and analysis of the MRP amplicon.* International journal of cancer, 1995. **60**(5): p. 676-684.
145. Hanssen, K.M., M. Haber, and J.I. Fletcher, *Targeting multidrug resistance-associated protein 1 (MRP1)-expressing cancers: Beyond pharmacological inhibition.* Drug Resistance Updates, 2021. **59**: p. 100795.
146. Dalla, C., et al., *Sex Differences in Blood–Brain Barrier Transport of Psychotropic Drugs.* Frontiers in Behavioral Neuroscience, 2022. **16**.
147. Bicker, J., et al., *Elucidation of the impact of p-glycoprotein and breast cancer resistance protein on the brain distribution of catechol-o-methyltransferase inhibitors.* Drug Metabolism and Disposition, 2017. **45**(12): p. 1282-1291.
148. Tsuruo, T., et al., *Overcoming of vincristine resistance in P388 leukemia in vivo and in vitro through enhanced cytotoxicity of vincristine and vinblastine by verapamil.* Cancer research, 1981. **41**(5): p. 1967-1972.
149. Solary, E., et al. *Mitoxantrone/Cytarabine with or without Quinine as a Potential MDR-Reversing Agent for the Treatment of Acute Leukemias*. in *Acute Leukemias V: Experimental Approaches and Management of Refractory Disease*. 1996. Springer.
150. Mendell, J., et al., *Drug-drug interaction studies of cardiovascular drugs involving P-glycoprotein, an efflux transporter, on the pharmacokinetics of edoxaban, an oral factor Xa inhibitor.* American Journal of Cardiovascular Drugs, 2013. **13**: p. 331-342.
151. Bartlett, N.L., et al., *Phase I trial of doxorubicin with cyclosporine as a modulator of multidrug resistance.* Journal of Clinical Oncology, 1994. **12**(4): p. 835-842.
152. Singh, S.N., et al., *Amiodarone in patients with congestive heart failure and asymptomatic ventricular arrhythmia.* New England Journal of Medicine, 1995. **333**(2): p. 77-82.
153. Infarction, D.S.G.o.V.i.M., *Verapamil in acute myocardial infarction.* European Heart Journal, 1984. **5**(7): p. 516-528.
154. Towpik, E. and J.W. Kupiec-Weglinski, *Use of cyclosporine in transplantation of nonprimarily vascularized tissues.* Transplantation Reviews, 1987. **1**: p. 85-100.
155. Ledwitch, K.V., et al., *Cooperativity between verapamil and ATP bound to the efflux transporter P-glycoprotein.* Biochemical pharmacology, 2016. **118**: p. 96-108.
156. Anglicheau, D., et al., *Role of P-glycoprotein in cyclosporine cytotoxicity in the cyclosporine–sirolimus interaction.* Kidney international, 2006. **70**(6): p. 1019-1025.
157. Tolcher, A., et al., *Phase I crossover study of paclitaxel with r-verapamil in patients with metastatic breast cancer.* Journal of clinical oncology, 1996. **14**(4): p. 1173-1184.
158. Gandhi, L., et al., *A phase II study of the safety and efficacy of the multidrug resistance inhibitor VX-710 combined with doxorubicin and vincristine in patients with recurrent small cell lung cancer.* Cancer: Interdisciplinary International Journal of the American

Cancer Society, 2007. **109**(5): p. 924-932.
159. Kolitz, J.E., et al., *P-glycoprotein inhibition using valspodar (PSC-833) does not improve outcomes for patients younger than age 60 years with newly diagnosed acute myeloid leukemia: Cancer and Leukemia Group B study 19808.* Blood, The Journal of the American Society of Hematology, 2010. **116**(9): p. 1413-1421.
160. Fischer, V., et al., *The multidrug resistance modulator valspodar (PSC 833) is metabolized by human cytochrome P450 3A: implications for drug-drug interactions and pharmacological activity of the main metabolite.* Drug Metabolism and Disposition, 1998. **26**(8): p. 802-811.
161. Ledwitch, K.V., R.W. Barnes, and A.G. Roberts, *Unravelling the complex drug–drug interactions of the cardiovascular drugs, verapamil and digoxin, with P-glycoprotein.* Bioscience reports, 2016. **36**(2).
162. Kelly, R.J., et al., *A Pharmacodynamic Study of Docetaxel in Combination with the P-glycoprotein Antagonist Tariquidar (XR9576) in Patients with Lung, Ovarian, and Cervical CancerPharmacodynamic Study of a Docetaxel-Tariquidar Combination.* Clinical Cancer Research, 2011. **17**(3): p. 569-580.
163. Kuppens, I.E., et al., *A phase I, randomized, open-label, parallel-cohort, dose-finding study of elacridar (GF120918) and oral topotecan in cancer patients.* Clinical Cancer Research, 2007. **13**(11): p. 3276-3285.
164. Sandler, A., et al., *A Phase I trial of a potent P-glycoprotein inhibitor, zosuquidar trihydrochloride (LY335979), administered intravenously in combination with doxorubicin in patients with advanced malignancy.* Clinical cancer research, 2004. **10**(10): p. 3265-3272.
165. Dufour, R., et al., *BCRP and P-gp relay overexpression in triple negative basal-like breast cancer cell line: a prospective role in resistance to Olaparib.* Scientific reports, 2015. **5**(1): p. 1-9.
166. Syed, S.B., et al., *Targeting P-glycoprotein: Investigation of piperine analogs for overcoming drug resistance in cancer.* Scientific reports, 2017. **7**(1): p. 1-18.
167. Dewanjee, S., et al., *Natural products as alternative choices for P-glycoprotein (P-gp) inhibition.* Molecules, 2017. **22**(6): p. 871.
168. Ravikumar Reddy, D., et al., *Natural flavonoids silymarin and quercetin improve the brain distribution of co-administered P-gp substrate drugs.* SpringerPlus, 2016. **5**(1): p. 1-9.
169. Lee, J., et al., *Dual inhibition of P-gp and BCRP improves oral topotecan bioavailability in rodents.* Pharmaceutics, 2021. **13**(4): p. 559.
170. Qiu, Q., et al., *Structure-based discovery of pyrimidine aminobenzene derivatives as potent oral reversal agents against P-gp-and BCRP-mediated multidrug resistance.* Journal of Medicinal Chemistry, 2021. **64**(9): p. 6179-6197.
171. Dei, S., et al., *Recent advances in the search of BCRP-and dual P-gp/BCRP-based multidrug resistance modulators.* Cancer Drug Resistance, 2019. **2**(3): p. 710.
172. Alvarez, A.I., et al., *Modulation of the activity of ABC transporters (P-glycoprotein, MRP2, BCRP) by flavonoids and drug response.* Journal of pharmaceutical sciences, 2010. **99**(2): p. 598-617.
173. Chan, K.F., et al., *Flavonoid dimers as bivalent modulators for P-glycoprotein-based multidrug resistance: synthetic apigenin homodimers linked with defined-length poly(ethylene glycol) spacers increase drug retention and enhance chemosensitivity in*

resistant cancer cells. J Med Chem, 2006. **49**(23): p. 6742-59.

174. Chan, K.F., et al., *Flavonoid dimers as bivalent modulators for p-glycoprotein-based multidrug resistance: structure-activity relationships.* ChemMedChem, 2009. **4**(4): p. 594-614.
175. Wong, I.L., et al., *Modulation of multidrug resistance protein 1 (MRP1/ABCC1)-mediated multidrug resistance by bivalent apigenin homodimers and their derivatives.* J Med Chem, 2009. **52**(17): p. 5311-22.
176. Boechat, N., et al., *Novel 1,2,3-triazole derivatives for use against Mycobacterium tuberculosis H37Rv (ATCC 27294) strain.* J Med Chem, 2011. **54**(17): p. 5988-99.
177. Wong, I.L., et al., *Discovery of Novel Flavonoid Dimers To Reverse Multidrug Resistance Protein 1 (MRP1, ABCC1) mediated drug resistance in cancers using a high throughput platform with "Click Chemistry".* Journal of Medicinal Chemistry, 2018. **61**(22): p. 9931-9951.
178. Zhu, X., et al., *Triazole bridged flavonoid dimers as potent, nontoxic, and highly selective breast cancer resistance protein (BCRP/ABCG2) inhibitors.* Journal of medicinal chemistry, 2019. **62**(18): p. 8578-8608.
179. Carlson, B.L., et al., *Establishment, maintenance, and in vitro and in vivo applications of primary human glioblastoma multiforme (GBM) xenograft models for translational biology studies and drug discovery.* Current protocols in pharmacology, 2011. **52**(1): p. 14.16. 1-14.16. 23.
180. Yan, C.S., et al., *A New Class of Safe, Potent, and Specific P-gp Modulator: Flavonoid Dimer FD18 Reverses P-gp-Mediated Multidrug Resistance in Human Breast Xenograft in Vivo.* Mol Pharm, 2015. **12**(10): p. 3507-17.
181. Hui Liu, W.Q., Tianyu Sun, Lei Wang, Chenxi Du, Yanyu Hu, Wenyuan Liu, Feng Feng, Yao Chen, Haopeng Sun, *Therapeutic strategies of glioblastoma (GBM): The current advances in the molecular targets and bioactive small molecule compounds.* Acta pharmaceutica Sinica. B, 2021: p. 1-24.
182. Kane, R.C., et al., *Sorafenib for the treatment of advanced renal cell carcinoma.* Clin Cancer Res, 2006. **12**(24): p. 7271-8.
183. Liu, L., et al., *Sorafenib blocks the RAF/MEK/ERK pathway, inhibits tumor angiogenesis, and induces tumor cell apoptosis in hepatocellular carcinoma model PLC/PRF/5.* Cancer research, 2006. **66**(24): p. 11851-11858.
184. Bronte, G., et al., *Sorafenib for the treatment of breast cancer.* Expert opinion on pharmacotherapy, 2017. **18**(6): p. 621-630.
185. Yosef, H., et al., *Exploring the efficacy and cellular uptake of sorafenib in colon cancer cells by Raman micro-spectroscopy.* Analyst, 2018. **143**(24): p. 6069-6078.
186. Zhang, J., K.A. Gold, and E. Kim, *Sorafenib in non-small cell lung cancer.* Expert opinion on investigational drugs, 2012. **21**(9): p. 1417-1426.
187. Wei, J., et al., *Small, smart, and LDLR-specific micelles augment Sorafenib therapy of Glioblastoma.* Biomacromolecules, 2021. **22**(11): p. 4814-4822.
188. Hottinger, A., et al., *Phase I study of sorafenib combined with radiation therapy and temozolomide as first-line treatment of high-grade glioma.* British journal of cancer, 2014. **110**(11): p. 2655-2661.
189. Lagas, J.S., et al., *Breast cancer resistance protein and P-glycoprotein limit sorafenib brain*

accumulation. Mol Cancer Ther, 2010. **9**(2): p. 319-26.
190. Sarkaria, J.N., et al., *Is the blood-brain barrier really disrupted in all glioblastomas? A critical assessment of existing clinical data.* Neuro Oncol, 2018. **20**(2): p. 184-191.
191. Den, R.B., et al., *A phase I study of the combination of sorafenib with temozolomide and radiation therapy for the treatment of primary and recurrent high-grade gliomas.* Int J Radiat Oncol Biol Phys, 2013. **85**(2): p. 321-8.
192. Löscher, W. and H. Potschka, *Drug resistance in brain diseases and the role of drug efflux transporters.* Nature Reviews Neuroscience, 2005. **6**(8): p. 591-602.
193. Begley, D.J., *ABC transporters and the blood-brain barrier.* Current pharmaceutical design, 2004. **10**(12): p. 1295-1312.
194. Xuezhen Zhu, I.L.K.W., Kin-Fai Chan, Jiahua Cui, Man Chun Law, Tsz Cheung Chong, Xuesen Hu, Larry M. C. Chow, Tak Hang Chan, *Triazole Bridged Flavonoid Dimers as Potent, Nontoxic, and Highly Selective Breast Cancer Resistance Protein (BCRP/ABCG2) Inhibitors.* Journal of Medicinal Chemistry, 2019. **62**(18): p. 8578-8608.
195. Hu, X., *Developing a novel strategy to treat glioblastoma: improving brain bioavailability of sorafenib with a synthetic flavonoid dimer to inhibit drug efflux in blood brain barrier.* 2018.
196. Subrahmanyam, V.V. and A.P. Tonelli, *Pharmacokinetics/ADME of small molecules.* DRUGS AND THE PHARMACEUTICAL SCIENCES, 2005. **152**: p. 99.
197. Jambhekar, S.S. and P.J. Breen, *Basic pharmacokinetics*. Vol. 76. 2009: Pharmaceutical press London.
198. Fong, C.W., *Permeability of the blood–brain barrier: molecular mechanism of transport of drugs and physiologically important compounds.* The Journal of membrane biology, 2015. **248**(4): p. 651-669.
199. Gampa, G., et al., *Enhancing Brain Retention of a Kif11 Inhibitor Significantly Improves Its Efficacy in a Mouse Model of Glioblastoma.* Neuro-Oncology, 2019. **21**: p. 274-274.
200. Wang, J., et al., *P-Glycoprotein (MDR1/ABCB1) Restricts Brain Accumulation of the Novel EGFR Inhibitor EAI045 and Oral Elacridar Coadministration Enhances Its Brain Accumulation and Oral Exposure.* Pharmaceuticals, 2022. **15**(9): p. 1124.
201. Stone, J., *A practical guide to sample preparation for liquid chromatography-tandem mass spectrometry in clinical research and toxicology.* Article, 2018. **30**: p. 15-21.
202. Bielawski, J., L. Mrówczynska, and M. Konarczak, *Hemolytic activity of the non-ionic detergents Tween 80 and Triton X-100.* Biological Bulletin of Poznań, 1995. **32**.
203. Taskar, K.S., et al., *Clinical Relevance of Hepatic and Renal P-gp/BCRP Inhibition of Drugs: An International Transporter Consortium Perspective.* Clinical Pharmacology & Therapeutics, 2022. **112**(3): p. 573-592.
204. S-Y Wang, K.-M.D., Y Li, Y Mei, H Sheng, H Liu, X Mei, W Ouyang, H-H Zhou, Z-Q Liu, *Effect of quercetin on P-glycoprotein transport ability in Chinese healthy subjects.* European Journal of Clinical Nutrition 2013. **67**: p. 390–394.
205. He X, M.L., Li Z.-Y, Tan Z.-R, Chen Y, Ouyang D.-S, *Effects of curcumin on the pharmacokinetics of talinolol in human with ABCB1 polymorphism.* Xenobiotica, 2012. **42**(12): p. 1248-1254.
206. Wytske M. van Weerden, J.C.R., *Use of nude mouse xenograft models in prostate cancer research.* The Prostate, 2000. **43**(4): p. 263-271.

207. Vivek A Bhadri, M.J.C., Warren Kaplan, Toby N Trahair and Richard B Lock, *Evaluation of the NOD/SCID xenograft model for glucocorticoid-regulated gene expression in childhood B-cell precursor acute lymphoblastic leukemia.* BMC genomics, 2011. **12**(1): p. 565-565.
208. Lisa Hutchinson, R.K., *High drug attrition rates-where are we going wrong?* Nature reviews. Clinical oncology, 2011. **8**(4): p. 189-190.
209. De Witt Hamer, P., et al., *The genomic profile of human malignant glioma is altered early in primary cell culture and preserved in spheroids.* Oncogene, 2008. **27**(14): p. 2091-2096.
210. Pandita, A.A., Kenneth D ; Zadeh, Gelareh ; Guha, Abhijit ; James, C. David, *Contrasting in vivo and in vitro fates of glioblastoma cell subpopulations with amplified EGFR.* GENES, CHROMOSOMES & CANCER, 2004. **39**(1): p. 29-36.
211. John J. Tentler, A.C.T., Colin D. Weekes, Antonio Jimeno, Stephen Leong, Todd M. Pitts, and W.A.M.a.S.G.E. John J. Arcaroli, *Patient-derived tumour xenografts as models for oncology drug development.* Nature reviews. Clinical oncology, 2012. **9**(6): p. 338-350.
212. Despina Siolas, G.J.H., *Patient-derived tumor xenografts: transforming clinical samples into mouse models.* Cancer Rearch, 2013. **73**(17): p. 5315-5319.
213. Mcelroy, W.D., *Properties of the reaction utilizing adenosinetriphosphate for bioluminescence.* The Journal of biological chemistry, 1951. **191**(2): p. 547-557.
214. Szentirmai Oszkar, B.C.H., Lin Ning, Szucs Szofia, Takahashi Masaya, Kiryu Shigeru, Kung Andrew L, Mulligan Richard C, Carter Bob S, *Noninvasive bioluminescence imaging of luciferase expressing intracranial U87 xenografts: correlation with magnetic resonance imaging determined tumor volume and longitudinal use in assessing tumor growth and antiangiogenic treatment effect.* Neurosurgery, 2006. **58**(2): p. 365-372.
215. Aaron J. Clark, S.F., Quanhong Ma, Rintaro Hashizume, *Bioluminescence Imaging of an Immunocompetent Animal Model for Glioblastoma.* Journal of Visualized Experiments, 2016(107): p. 53287-53287.
216. Brett L. Carlson, J.L.P., Mark A. Schroeder, Jann N. Sarkaria, *Establishment, Maintenance, and In Vitro and In Vivo Applications of Primary Human Glioblastoma Multiforme (GBM) Xenograft Models for Translational Biology Studies and Drug Discovery.* Current protocols in pharmacology, 2011. **52**(14): p. 1-14.
217. JannN. Sarkaria, B.L.C., MarkA. Schroeder, PatrickGrogan, PaulD. Brown, CaterinaGiannini, KarlaV. Ballman, GasparJ. Kitange, Abjahit Guha, Ajay Pandita, C. DavidJames, *Use of an Orthotopic Xenograft Model for Assessing the Effect of EGFR Amplification on Glioblastoma Radiation Response.* Clinical Cancer Research, 2006. **12**(7): p. 2264-2271.
218. Jann N. Sarkaria, L.Y., Patrick T. Grogan, Gaspar J. Kitange, Brett L. Carlson, Mark A. Schroeder, Evanthia Galanis, Caterina Giannini, Wenting Wu, Eduard B. Dinca, C. David James, *Identification of molecular characteristics correlated with glioblastoma sensitivity to EGFR kinase inhibition through use of an intracranial xenograft test panel.* Molecular Cancer Therapeutics, 2007. **6**(3): p. 1167-1174.
219. Aiguo Li, J.W., Yuri Kotliarov, Angela Center, Mary Ellen Steed, Susie J. Ahn, Mark Rosenblum, Tom Mikkelsen, Jean Claude Zenklusen, and a.H.A. Fine, *Genomic changes and gene expression profiles reveal that established glioma cell lines are poorly representative of primary human gliomas.* Molecular Cancer Research, 2008. **6**(1): p. 21-

30.
220. Vaubel, R.A., et al., *Genomic and Phenotypic Characterization of a Broad Panel of Patient-Derived Xenografts Reflects the Diversity of GlioblastomaCharacterization of Glioblastoma Patient-Derived Xenografts.* Clinical Cancer Research, 2020. **26**(5): p. 1094-1104.
221. Joo, K.M., et al., *Patient-specific orthotopic glioblastoma xenograft models recapitulate the histopathology and biology of human glioblastomas in situ.* Cell reports, 2013. **3**(1): p. 260-273.
222. Carlson, B.L., et al., *Establishment, maintenance and in vitro and in vivo applications of primary human glioblastoma multiforme (GBM) xenograft models for translational biology studies and drug discovery.* Curr Protoc Pharmacol, 2011. **Chapter 14**(14): p. Unit 14.16.
223. Bunch, L., *Bioisosteres in Medicinal Chemistry. Edited by Nathan Brown*. 2013, Wiley Online Library.
224. Breitenlechner, C.B., et al., *Structure-based optimization of novel azepane derivatives as PKB inhibitors.* Journal of medicinal chemistry, 2004. **47**(6): p. 1375-1390.
225. Laine, D., et al., *Discovery of novel cyanamide-based inhibitors of cathepsin C.* ACS medicinal chemistry letters, 2011. **2**(2): p. 142-147.
226. Berry, L.M., L. Wollenberg, and Z. Zhao, *Esterase activities in the blood, liver and intestine of several preclinical species and humans.* Drug Metabolism Letters, 2009. **3**(2): p. 70-77.
227. Wei, X.L., et al., *Stabilization of zeylenone in rat plasma by the presence of esterase inhibitors and its LC-MS/MS assay for pharmacokinetic study.* Biomedical Chromatography, 2013. **27**(5): p. 636-640.
228. T Williams, E., et al., *Investigation of the metabolism of rufinamide and its interaction with valproate.* Drug Metabolism Letters, 2011. **5**(4): p. 280-289.
229. Klein, V.G., et al., *Amide-to-ester substitution as a strategy for optimizing PROTAC permeability and cellular activity.* Journal of medicinal chemistry, 2021. **64**(24): p. 18082-18101.
230. Takahashi, M., et al., *Effects of steric hindrance and electron density of ester prodrugs on controlling the metabolic activation by human carboxylesterase.* Drug Metabolism and Pharmacokinetics, 2021. **38**: p. 100391.
231. Knutson, D.E., et al., *Design and synthesis of novel deuterated ligands functionally selective for the γ-aminobutyric acid type A receptor (GABAAR) α6 subtype with improved metabolic stability and enhanced bioavailability.* Journal of medicinal chemistry, 2018. **61**(6): p. 2422-2446.
232. Parcella, K., et al., *Improving metabolic stability with deuterium: the discovery of BMT-052, a pan-genotypic HCV NS5B polymerase inhibitor.* ACS Medicinal Chemistry Letters, 2017. **8**(7): p. 771-774.
233. Gajula, S.N.R., N. Nadimpalli, and R. Sonti, *Drug metabolic stability in early drug discovery to develop potential lead compounds.* Drug Metabolism Reviews, 2021. **53**(3): p. 459-477.
234. Chackalamannil, S., D. Rotella, and S. Ward, *Comprehensive medicinal chemistry III*. 2017: Elsevier.
235. Hirai, H., et al., *Small-molecule inhibition of Wee1 kinase by MK-1775 selectively sensitizes p53-deficient tumor cells to DNA-damaging agentsWee1 Inhibitor in Combination with*

DNA-Damaging Agents. Molecular cancer therapeutics, 2009. **8**(11): p. 2992-3000.

236. Indovina, P., et al., *Abrogating G2/M checkpoint through WEE1 inhibition in combination with chemotherapy as a promising therapeutic approach for mesothelioma.* Cancer biology & therapy, 2014. **15**(4): p. 380-388.
237. Takebe, N., et al., *Safety, Antitumor Activity, and Biomarker Analysis in a Phase I Trial of the Once-daily Wee1 Inhibitor Adavosertib (AZD1775) in Patients with Advanced Solid TumorsOnce-daily Adavosertib in Solid Tumors.* Clinical Cancer Research, 2021. **27**(14): p. 3834-3844.
238. Fu, S., et al., *Phase II trial of the Wee1 inhibitor adavosertib in advanced refractory solid tumors with CCNE1 amplification.* Cancer Research, 2021. **81**(13_Supplement): p. 974-974.
239. Liu, J.F., et al., *Phase II study of the WEE1 inhibitor adavosertib in recurrent uterine serous carcinoma.* Journal of Clinical Oncology, 2021. **39**(14): p. 1531-1539.
240. Cuneo, K.C., et al., *Dose escalation trial of the Wee1 inhibitor adavosertib (AZD1775) in combination with gemcitabine and radiation for patients with locally advanced pancreatic cancer.* Journal of Clinical Oncology, 2019. **37**(29): p. 2643.
241. Tutt, A., et al., *161O VIOLETTE: Randomised phase II study of olaparib (ola)+ ceralasertib (cer) or adavosertib (ada) vs ola alone in patients (pts) with metastatic triple-negative breast cancer (mTNBC).* Annals of Oncology, 2022. **33**: p. S194-S195.
242. Chera, B.S., et al., *Phase 1 trial of adavosertib (AZD1775) in combination with concurrent radiation and cisplatin for intermediate-risk and high-risk head and neck squamous cell carcinoma.* Cancer, 2021. **127**(23): p. 4447-4454.
243. Sanai, N., et al., *Phase 0 trial of AZD1775 in first-recurrence glioblastoma patients.* Clinical Cancer Research, 2018. **24**(16): p. 3820-3828.
244. Alexander, B.M., et al., *Phase I study of AZD1775 with radiation therapy (RT) and temozolomide (TMZ) in patients with newly diagnosed glioblastoma (GBM) and evaluation of intratumoral drug distribution (IDD) in patients with recurrent GBM*. 2017, American Society of Clinical Oncology.
245. Pokorny, J.L., et al., *The efficacy of the Wee1 inhibitor MK-1775 combined with temozolomide is limited by heterogeneous distribution across the blood–brain barrier in glioblastoma.* Clinical cancer research, 2015. **21**(8): p. 1916-1924.
246. Gomez-Zepeda, D., et al., *ABC transporters at the blood–brain interfaces, their study models, and drug delivery implications in gliomas.* Pharmaceutics, 2019. **12**(1): p. 20.
247. Mir, S.E., et al., *In silico analysis of kinase expression identifies WEE1 as a gatekeeper against mitotic catastrophe in glioblastoma.* Cancer cell, 2010. **18**(3): p. 244-257.
248. De Witt Hamer, P.C., et al., *WEE1 Kinase Targeting Combined with DNA-Damaging Cancer Therapy Catalyzes Mitotic CatastropheWEE1 Targeting Catalyzes Mitotic Catastrophe.* Clinical cancer research, 2011. **17**(13): p. 4200-4207.
249. 1, C.G.A.R.N.T.s.s.D.U.M.S.M.R.F.A.B.D., et al., *Comprehensive genomic characterization defines human glioblastoma genes and core pathways.* Nature, 2008. **455**(7216): p. 1061-1068.
250. Gelderblom, H., et al., *Cremophor EL: the drawbacks and advantages of vehicle selection for drug formulation.* European journal of cancer, 2001. **37**(13): p. 1590-1598.
251. Chen, L.R., et al., *Dissolution behavior of a poorly water soluble compound in the presence*

of Tween 80. Pharmaceutical research, 2003. **20**: p. 797-801.

252. Khadka, P., et al., *Pharmaceutical particle technologies: An approach to improve drug solubility, dissolution and bioavailability.* Asian journal of pharmaceutical sciences, 2014. **9**(6): p. 304-316.
253. Gunasekaran, T., et al., *Nanotechnology: an effective tool for enhancing bioavailability and bioactivity of phytomedicine.* Asian Pacific Journal of Tropical Biomedicine, 2014. **4**: p. S1-S7.
254. Sharma, D., *Solubility enhancement strategies for poorly water-soluble drugs in solid dispersions: a review.* Asian Journal of Pharmaceutics (AJP), 2007. **1**(1).
255. Thenmozhi, K. and Y.J. Yoo, *Enhanced solubility of piperine using hydrophilic carrier-based potent solid dispersion systems.* Drug development and industrial pharmacy, 2017. **43**(9): p. 1501-1509.
256. Kane, R.C., et al., *Sorafenib for the treatment of advanced renal cell carcinoma.* Clinical Cancer Research, 2006. **12**(24): p. 7271-7278.
257. Den, R.B., et al., *A phase I study of the combination of sorafenib with temozolomide and radiation therapy for the treatment of primary and recurrent high-grade gliomas.* International Journal of Radiation Oncology* Biology* Physics, 2013. **85**(2): p. 321-328.
258. Chen, H., et al., *Phase I/II study of sorafenib in combination with erlotinib for recurrent glioblastoma as part of a 3-arm sequential accrual clinical trial: NABTC 05-02.* Neuro-Oncology Advances, 2020. **2**(1): p. vdaa124.
259. Galanis, E., et al., *Phase II Study of Bevacizumab in Combination with Sorafenib in Recurrent Glioblastoma (N0776): A North Central Cancer Treatment Group TrialBevacizumab in Combination with Sorafenib for Treatment of Recurrent GBM.* Clinical Cancer Research, 2013. **19**(17): p. 4816-4823.